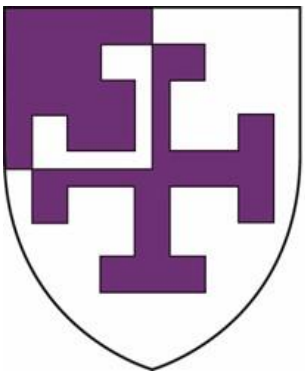
Advanced Cracking Catalysts for the Conversion of Naphtha into Light Olefins

Naif S. Almuqati

St Cross College, University of Oxford





Supervisor

Prof. Peter P. Edwards FRS ML

Prof. Michael A. Hayward

A thesis submitted to the Department of Chemistry, University of Oxford for the Degree of Doctor of Philosophy in Inorganic Chemistry

Trinity 2022

Contents

Declaration ---------- **VIII**

Dedication ---------- **IX**

Acknowledgements ---------- **X**

Proposed publications from this thesis ---------- **XIII**

Abstract ---------- **XIV**

List of Figures ---------- **XVI**

List of Tables ---------- **XXII**

List of abbreviations and symbols ---------- **XXIV**

Chapter 1 Overview of catalytic cracking ---------- **1**

1.1 General background ---------- 2

1.2 Applications of Light Olefins ---------- 2

1.2.1 Ethylene ---------- 2

1.2.2 Propylene ---------- 4

1.3 Commercial Processes for Producing Light Olefins ---------- 5

1.3.1 Steam Cracking (SC) ---------- 6

1.3.2 Catalytic Cracking ---------- 8

1.3.2.1 Mechanism ---------- 10

1.3.2.2 Thermodynamic aspects ---------- 13

1.3.2.3 Conventional Feedstocks for Catalytic Cracking ---------- 14

1.3.2.4 Catalysts employed in the Catalytic Cracking process ---------- 17

1.3.2.5 Structure and pore size of zeolite for catalytic cracking ---------- 17

1.3.2.6 Acidity ---------- 21

1.3.2.7 Conversion of hydrocarbons into olefins on ZSM-5 ---------- 22

1.3.2.8 Conversion of hydrocarbon into olefins on modified ZSM-5 ---------- 28

1.3.3 Industrial production of light olefins via catalytic cracking ---------- 32

1.3.3.1 Material and composition ---------- 34

1.3.3.2 ZSM-5 as a propylene yield-increasing additive in FCC catalysts ---------- 37

1.4 Other processes to produce light olefins ----- 38
1.4.1 The Methanol to Olefins Process ----- 38
1.4.2 Oxidative Coupling of Methane ----- 39
1.4.3 Paraffin Dehydrogenation ----- 41
1.5 Scope of the thesis ----- 41
1.6 References ----- 44
Chapter 2 Experimental methods, instrumentation, and fundamentals ----- 56
2.1 Introduction ----- 57
2.2 Catalyst Preparation ----- 58
2.3 Evaluation of Catalyst Performance ----- 59
2.3.1 Feedstock ----- 59
2.3.2 Catalyst performance test ----- 60
2.3.3 Calibration of reactants flowrates ----- 63
2.4 Products analysis ----- 64
2.4.1 Gas Chromatography (GC) ----- 64
2.4.2 Gas Chromatography-Mass Spectrometry (GC-MS) ----- 67
2.5 Calculating methods ----- 71
2.6 Catalyst characterization methods ----- 72
2.6.1 X-Ray Diffraction (XRD) ----- 72
2.6.2 Thermogravimetric Analysis (TGA) ----- 75
2.6.3 NH_3-temperature-Programmed Desorption (TPD) ----- 77
2.6.4 Brunauer, Emmett and Teller (BET) analysis ----- 78
2.6.5 Scanning Electron Microscopy (SEM) ----- 80
2.6.6 Energy dispersive X-ray analysis (EDX) ----- 82
2.6.7 Transmission Electron Microscopy (TEM) ----- 84
2.6.8 X-ray photoelectron spectroscopy (XPS) ----- 86

2.7 References----------90

Chapter 3 Effect of H-ZSM-5 with different Si/Al ratios and preparation methods for various CrO_x-H-ZSM-5 formulations on the catalytic cracking of *n*-heptane as a model compound for light naphtha----------94

Overview ----------95

3.1 Introduction ----------95

3.2 Experimental----------97

3.2.1 Preparation of catalysts ----------97

3.2.1.1 Impregnation method (IMP) ----------98

3.2.1.2 Mechanical mixture method (MM) ----------98

3.2.2 Characterisation of catalysts ----------99

3.2.3 Experimental conditions---------- 100

3.3 Results and Discussion ---------- 101

3.3.1 Effect of H-ZSM-5 with different Si/Al ratios on the cracking of *n*-heptane 101

3.3.1.1 Pre-reaction analysis of catalysts---------- 101

3.3.1.1.1 X-ray diffraction (XRD) analysis---------- 101

3.3.1.1.2 Thermogravimetric analysis (TGA) ---------- 103

3.3.1.2 Evaluation of catalyst performance ---------- 104

3.3.1.3 Post-reaction analysis of catalysts---------- 110

3.3.1.3.1 X-ray diffraction (XRD) analysis---------- 110

3.3.1.3.2 Thermogravimetric analysis (TGA) ---------- 111

3.3.2 Influence of metal oxide loading and preparation method for HZ80 zeolite on the cracking reaction of *n*-heptane ---------- 112

3.3.2.1 Pre-reaction analysis of catalysts---------- 112

3.3.2.1.1 X-ray diffraction (XRD) ---------- 112

3.3.2.1.2 Brunauer-Emmett-Teller (BET) analysis ---------- 115

3.3.2.1.3 Thermogravimetric analysis (TGA) ---------- 116

3.3.2.1.4 Scanning electron microscopy (SEM) ---------- 117

3.3.2.1.5 SEM-EDX elemental analysis---------- 118

3.3.2.1.6 X-ray photoelectron spectroscopy (XPS)---------- 121

3.3.2.2 Catalytic performance tests---------- 123

3.3.2.3 Post-reaction analysis of catalysts ---------- 130
3.3.2.3.1 X-ray diffraction analysis ---------- 130
3.3.2.3.2 Thermogravimetric measurement (TGA) ---------- 131
3.3.2.3.3 Brunauer-Emmentt-Teller (BET) analysis ---------- 134
3.3.2.3.4 X-ray photoelectron spectroscopy (XPS) ---------- 136
3.4 Conclusion ---------- 139
3.5 References ---------- 141
Chapter 4 Cracking of *n*-heptane on HZ23-support formulations: Effect of different supports ---------- 145
Overview ---------- 146
4.1 Introduction ---------- 146
4.2 Experimental ---------- 150
4.2.1 Preparation of catalysts ---------- 150
4.2.2 Characterisation of catalysts ---------- 150
4.2.3 Experimental condition ---------- 152
4.3 Results and Discussion ---------- 153
4.3.1 Pre-reaction analysis of catalysts ---------- 153
4.3.1.1 X-ray diffraction (XRD) ---------- 153
4.3.1.2 Brunauer-Emmentt-Teller (BET) analysis ---------- 154
4.3.1.3 Thermogravimetric analysis (TGA) ---------- 155
4.3.1.4 Scanning Electron Microscopy (SEM) ---------- 158
4.3.1.5 Transmission Electron Microscopy (TEM) ---------- 160
4.3.2 Catalytic performance tests ---------- 163
4.3.3 Post- reaction analysis of catalysts ---------- 169
4.3.3.1 X-ray diffraction analysis ---------- 169
4.3.3.2 Thermogravimetric measurement (TGA) ---------- 170
4.3.3.3 Brunauer-Emmentt-Teller (BET) analysis ---------- 174
4.4 Conclusion ---------- 176
4.5 References ---------- 178

Chapter 5 Cracking of *n*-heptane and naphtha on HZ23-kaolin formulations------ 183

Overview ---------- 184

5.1 Introduction ---------- 184

5.2 Experimental Methods ---------- 187

5.2.1 Materials ---------- 187

5.2.2 Preparation of catalysts ---------- 188

5.2.3 Characterisation of catalysts ---------- 188

5.2.4 Experimental conditions ---------- 190

5.3 Results and Discussion ---------- 191

5.3.1 Pre-reaction analysis of catalysts ---------- 191

5.3.1.1 X-ray diffraction (XRD) ---------- 191

5.3.1.2 Brunauer-Emmentt-Teller (BET) analysis ---------- 192

5.3.1.3 Scanning Electron Microscopy (SEM) ---------- 193

5.3.1.4 Transmission Electron Microscopy (TEM) ---------- 194

5.3.1.5 Acidity measurement ---------- 196

5.3.2 Catalytic performance test ---------- 198

5.3.2.1 Catalytic cracking of *n*-heptane on different HZ23-kaolin catalyst formulations ---------- 199

5.3.2.2 Catalytic cracking of light naphtha on different HZ23-kaolin catalyst formulations ---------- 201

5.3.2.3 Total olefin yield for HZ23-kaolin formulation for *n*-heptane and naphtha cracking 205

5.3.2.4 Effect of different weight hourly space velocities (WHSV) on catalytic cracking of *n*-heptane into light olefins ---------- 210

5.3.2.5 Study of the effect of reaction temperature and lifetime of 5 wt.% HZ23-kaolin catalyst in the catalytic cracking of *n*-heptane into light olefins ---------- 215

5.3.3 Post- reaction analysis of catalysts ---------- 219

5.3.3.1 X-ray diffraction analysis (XRD) ---------- 219

5.3.3.2 Thermogravimetric measurement (TGA) ---------- 220

5.3.3.3 Brunauer-Emmentt-Teller (BET) analysis ---------- 223

5.4 A preliminary discussion of the sustainability credentials of light olefins production ---------- 224

5.5 Conclusion ---------- 226

5.6 References ---------- 228

Chapter 6 Conclusions and Future Research ---------- 232

6.1 Concluding remarks ---------- 233

6.2 Future perspectives ---------- 238

Appendix ---------- 240

Estimation of Errors ---------- 240

Supplementary Information for Chapter 3 ---------- 242

Supplementary Information for Chapter 4 ---------- 246

Supplementary Information for Chapter 5 ---------- 250

Declaration

The work described in this thesis was carried out at Inorganic Chemistry Laboratory (ICL) at the University of Oxford between October 2018 and October 2022 under the supervision of Prof. Peter P. Edwards (2018-2021) and Prof. Michael A. Hayward (2021-2022). All the work presented herein is my own except where I have either acknowledged help from a named person or given reference to a published source. None of the work has been submitted by the author for any other degree at any other university.

Naif Almuqati
October 2022

Dedication

This work is dedicated to my parents, my father, who was the first person in my life to inspire and assist me to finish my education. And to my dearly adored mother, who prayed daily to Allah for me. May God protect my parents. Additionally, to my brothers and sisters, who have always encouraged and supported me in my pursuit of higher education. In conclusion, I would like to dedicate this work to my cherished wife, who gives me the unending care, support, and encouragement I need to accomplish my objective and be successful; also, I would like to dedicate this work to my dearest children, Zeyad and Dana, who are the source of my joy and happiness at home.

Acknowledgements

First and foremost, all praise and thanks are due to God the Almighty for giving me all the graces and blessings, health, strength, and skills I need to be successful and happy during my DPhil study.

It is an honour for me to be an employee of King Abdulaziz City for Science and Technology (KACST) and part of the projects between KACST and the University of Oxford (KOPRC). For this, I gratefully acknowledge to the president of King Abdulaziz City for Science and Technology (KACST) Dr .Munir Eldesouki, for his support to give me the chance to study at the University of Oxford and for all the help and generous support he provided to KOPRC to move forward and reach what we have achieved today.

When I look back on the four years that I spent studying and doing research in chemistry at Oxford, I felt an overwhelming sense of contentment. Not just about what I have accomplished, but also about what I have learned and experienced at this prestigious international institution, which has helped me decide what I want to do with the rest of my life.

I would like to convey my profound appreciation to my DPhil supervisor, Professor Peter P. Edwards, for his advice, encouragement, and support. His unwavering support has given me the opportunity to pick my study topics and plan and execute the whole experiment. This has allowed me to develop and study in a manner that has allowed me to become an autonomous young scientist, and I hope I have lived up to his confidence.

I would like to thank my supervisor, Professor Michael Hayward, for accepting me to join his group after Professor Peter's retirement, and also for the help and guidance throughout the last period of my study at Oxford.

I would like to express my gratitude to Professor Hamid Al-Megren for the assistance and guidance he provided me concerning the application procedure, for Dr. Mohammed Alotaibi, Dr. Raja Alotaibi and Dr. Faisal Alotaibi for the assistance and knowledge they provided, and for encouraging me to pursue this way.

I would like to thank Dr. Afrah Aldawasari for her support, help and for her encouragement during my study.

During my time at Oxford, I have had the honour of getting to know and collaborate with a number of very remarkable people. In a variety of ways, they were beneficial to both my life and my education. Every single one of them made genuine attempts to help me achieve my objectives and triumph over challenges. I shall discuss them in a historical context as follows:

I would like to extend my sincerest gratitude to Professor Jon Dilworth for all of the stimulating conversation and insightful comments that helped bring the level of my work to a higher level.

Dr. Sergio Gonzalez-Cortes, the exceptional team leader, and my friend at ICL, was the first person I talked with when I arrived. In the beginning, he introduced me to my lab mates and led me through my first days until I submitted my thesis. Thank you sincerely for your assistance and suggestions. Dr. Tugce Ayvali, thank you for your help and advice.

Mr. Sultan Alshuhri and Mr. Saud Aldress, my teammates from KACST and refined taste friends. We had great times together in the lab and in the office. They offered me all the support throughout my days in Oxford.

Dr. Robert Jacobs for the BET analysis. And Dr. Francisco in Spain for the acidity measurements.

The EPSRC National Facility for Photoelectron Spectroscopy (HarwellXPS), operated by Cardiff University and UCL under contract number PR16195 is acknowledged for help with the analysis of the XPS spectra.

To Mrs. Linda Webb, you have my utmost respect and gratitude from the bottom of my heart. I will never be able to adequately express my gratitude to you for all you have done to assist me over the whole of the study.

To all the people in the mechanical workshop at PTCL and the electronics workshop (Nenad and Alex) thanks for helping me to fix the reactor unit. Also, I would like to thank Mrs. Alison Chesworth-Wing who is our best receptionist at ICL, for everything did for me.

To all the members of the PPE group, thanks for the interesting discussions.

My UK friends, I'm so grateful to the place that brought us together, I know that I have brothers for life in UK.

Last and not least, I would want to convey my gratitude to my family, my wife and my children, for all the love, pleasure, and joy they have bestowed upon me, as well as for their unending support, encouragement, and patience; the term "thank you" does not adequately describe my gratitude.

Naif Almuqati

October 2022, Oxford, UK

Proposed publications from this thesis.

1- **Catalysts, Technologies, and Sustainability Credentials of Light Olefins Production.**
2- **High yield of light olefins via catalytic cracking of *n*-heptane and naphtha on combined HZSM-5-kaolin catalyst formulations.**
3- **Effect of various metal oxides or kaolin on HZ23 zeolite in *n*-heptane catalytic cracking.**

Advanced Cracking Catalysts for the Conversion of Naphtha into light Olefins

Naif S. Almuqati, St. Cross College

A thesis submitted to the Department of Chemistry, University of Oxford for the Degree of Doctor of Philosophy in Inorganic Chemistry

Abstract

To meet the current global warming limit of 1.5°C above pre-industrial levels, an urgent requirement is to develop advanced technologies fully- able to decarbonise the energy industry and other sectors. It is also expected that the demand for fossil of derived fuels will start declining in the coming years. Thereby, a significant fraction of the still vast resources of fossil hydrocarbons will be targeted towards the production of petrochemicals, notably to the production of light olefins, especially propene, and aromatics within an environmentally–friendly, climate-conscious perspective. The main scope of the project is to design and develop highly selective solid based catalysts and also to optimize the reaction conditions for converting the relatively high molecular weight hydrocarbons present in naphtha into the desired compounds.

ZSM-5 is the most efficient catalyst for naphtha cracking to light olefins. Our initial studies reveal that, for these catalytic processes, the SiO_2/Al_2O_3 ratio is not perhaps the primary criterion for the assessment of the performance of the zeolite catalyst.

When compared to the catalyst formulation that was created by the impregnation approach, Cr_2O_3 loading on HZSM-5 (SiO_2/Al_2O_3 = 80) zeolite using the mechanical mixing (MM) method results in a better *n*-heptane conversion (i.e., 95 wt.%) than the impregnation method (IMP). The inclusion of Cr had an effect on the physicochemical parameters of the catalysts, as well as their catalytic activity and selectivity. The optimum amount of Cr loading, which was 10% by weight, resulted in an increase in selectivity toward olefins, especially ethylene. In order to gain an understanding of the interaction mechanisms of the catalyst components and the role of support in the catalytic cracking of *n*-heptane over a hybrid of zeolite-matrix catalysts, it was investigated the effect of different matrix over ZSM-5 zeolite.

The advance made in this thesis is based on the designed combination of HZSM-5 with kaolin, the latter being a highly versatile catalyst and support matrix. This inert, inexpensive and earth-abundant material significantly improves the catalyst's sustainable features alongside the effective production of light olefins from *n*-heptane (a model compound) and naphtha (the actual petrochemical feedstock). The matrix alters the texture, morphology, surface density and strength of acid sites of HZSM-5 zeolite hence, enhancing

the production of light olefins, particularly propene, followed by ethene and in minor extension C_4H_8 compound.

This work highlights the favourable impact of carefully tuning the strength and surface density of acid sites in HZSM-5 by combining it with a natural clay! This strategy enhances the production of light alkenes, particularly propene, and even aromatics via the catalytic cracking of naphtha.

List of Figures

Figure 1.1. Major chemicals derived from ethylene [13, 14]. ---------- 3
Figure 1.2. Propylene supply and request, adapted from[7, 21].---------- 4
Figure 1.3. Propylene value chain adapted from[30]. ---------- 5
Figure 1.4. Simplified Plot of traditional steam cracking and catalytic olefin energy profiles. Adapted from[35].----------10
Figure 1.5. (a) Proposed Haag–Dessau cracking mechanism for an alkane molecule (RH) proceeding via a carbonium ion transition state. (b) Classical cracking mechanism for an alkane molecule (RH) consisting of a hydride transfer step to a smaller carbenium ion ($R1^+$) followed by β-scission, Adapted from[33]. (c) Reaction pathways for hydrocarbon cracking over zeolite. HZ and L stand for zeolite Brønsted and Lewis acid sites, respectively. Adapted from[46].----------12
Figure 1.6. The different fractions, carbon ranges and boiling points for crude oil, Adapted from[4] .----------15
Figure 1.7. Types of naphtha related to their boiling points and areas of hydrocarbon formation, Adapted from[66]. ----------16
Figure 1.8. Pore sizes for zeolite and other materials.----------18
Figure 1.9. ZSM-5 structure: a) Zig Zag pore structure and b) The channel structure in ZSM-5, Adapted from[73, 74]. ----------20
Figure 1.10. A schematic diagram of the formation of acidic sites in zeolite, Adapted from[78].----------22
Figure 1.11. Propylene yield based on the type of feedstock in FCC unit. Adapted from[4]. ----------33
Figure 1.12. Diagrammatic representation of FCC reactor and regenerator. Adapted from[4]. ----------34
Figure 1.13. Schematic representation of FCC catalyst formulation, adapted from[34].----36
Figure 2.1. Schematic representation of a fixed-bed tubular reactor used in the present investigations, which is routinely used for conducting small scale catalyst tests. ----------60
Figure 2.2. Schematic diagram of the reaction system. ----------61
Figure 2.3. MicroReactor 10A benchtop pilot plants used in this investigation. ----------63
Figure 2.4. Calibration of HPLC pump for liquid feedstock. ----------64
Figure 2.5. Schematic illustration of the Gas Chromatography (GC) apparatus used in this study. ----------65

Figure 2.6. Schematic representation of the GC-MS instrumentation used in this investigation.----------68
Figure 2.7. GC-MS calibration for a range of liquid products. ----------70
Figure 2.8. Illustration of Bragg's Law derived by treating layers of atom as reflecting planes.----------73
Figure 2.9. A typical XRD experiment on a thin film sample is shown in this diagram, where θ denotes the diffraction angle (Bragg angle). ----------74
Figure 2.10. TGA and DTG curves of ZSM-5 with rate of 10ºC.min^{-1} in air atmosphere. ----------76
Figure 2.11. The NH_3-temperature programed desorption instrument used in this investigation.----------78
Figure 2.12. The Brunauer, Emmentt and Teller (BET) instrument used in this investigation.----------80
Figure 2.13. A schematic illustration of a scanning electron microscope (SEM). Adapted from[45].----------81
Figure 2.14. A schematic illustration of a Transmission electron microscope (TEM). Adapted from[45].----------85
Figure 2.15. The energy distribution of the photoelectrons released in XPS. Adapted from [54].----------87
Figure 2.16. (a) Emission of a photoelectron in XPS, (b) Spin-orbit splitting j values and peak area ratios. Adapted from[56]. ----------89
Figure 3.1. Schematic representation of the Brønsted acid site formation via ammonium cation decomposition.----------97
Figure 3.2. Comparison of powder X-ray diffraction patterns of the H-ZSM-5 zeolite for fresh samples with SiO_2/Al_2O_3 (23, 30, 50, 80, and 280) molar ratios. ---------- 102
Figure 3.3. Comparison of X-ray powder diffraction patterns for fresh HZ23 catalyst and ZSM-5 reference (MFI type).---------- 103
Figure 3.4. Thermogravimetric analysis (TGA) samples under air flow for zeolite with different SiO_2/Al_2O_3 ratios. Inset plot shown the weight derivative thermogravimetry (DTG) curves (b) of the fresh H-ZSM-5 zeolite for fresh samples with SiO_2/Al_2O_3 (23, 30, 50, 80, and 280) molar ratios. ---------- 103
Figure 3.5. Effect of time-on-stream on *n*-heptane conversion (a), C_2H_4 selectivity (b), C_3H_6 selectivity (c) and C_4H_8 selectivity (d) over HZ23, HZ30, HZ50, HZ80 and HZ280 zeolite catalysts. The reactions were conducted at 550°C, atmospheric pressure (0.1 MPa), wight

hour space velocity (WHSV) 8.2 h^{-1}, and 20 $ml.min^{-1}$ N_2 flowrate. The estimated errors were between 3 and 6%.---------- 106
Figure 3.6. Selectivity of produced alkanes from the *n*-heptane catalytic cracking over HZ23, HZ30, HZ50, HZ80 and HZ280 zeolite catalysts. The reactions were conducted at 550°C, atmospheric pressure (0.1 MPa), wight hour space velocity (WHSV) 8.2 h^{-1} and 20 $ml.min^{-1}$ N_2 flowrate. The estimated errors were between 3 and 6%. ---------- 109
Figure 3.7. Comparison of powder X-ray diffraction patterns of the H-ZSM-5 zeolite for spent samples with SiO_2/Al_2O_3 (23, 30, 50, 80, and 280) molar ratios. ---------- 111
Figure 3.8. Thermogravimetric analysis (TGA) of spent samples under air for zeolites with different SiO_2/Al_2O_3 ratios. Inset plot shows the weight derivative thermogravimetry (DTG) curves of the fresh H-ZSM-5 zeolite for spent samples with SiO_2/Al_2O_3 (23, 30, 50, 80, and 280) molar ratios.---------- 112
Figure 3.9. Comparison of powder X-ray diffraction patterns of the HZ80, pure Cr_2O_3, and Cr oxide loading by different method for fresh samples. (MM = mechanical mixture, IMP = impregnation method). ---------- 113
Figure 3.10. TGA for fresh samples under air flow for different Cr oxide over HZ80 catalyst. Inset plot shown the weight derivative thermogravimetry (DTG) curves of the five catalysts under air flow. ---------- 116
Figure 3.11. Scanning electron microscopy (SEM) images of Cr loading over HZ80 synthesis by different methods. ---------- 117
Figure 3.12. SEM-EDX analysis of different loadings of Cr oxide on HZ80.---------- 120
Figure 3.13. Effect of Cr_2O_3 loading and preparation method over HZ80 zeolite catalyst on *n*-heptane conversion (a), C_2H_4 selectivity (b), C_3H_6 selectivity (c) and C_4H_8 selectivity (d). The reactions were conducted at 550°C, atmospheric pressure (0.1 MPa), wight hour space velocity (WHSV) 8.2 h^{-1} and 20 $ml.min^{-1}$ N_2 flow rate. The estimated error was between 3 and 6%. ---------- 125
Figure 3.14. Selectivity for alkanes for *n*-heptane catalytic cracking over Cr_2O_3/HZ80. The reactions were conducted at 550°C, atmospheric pressure (0.1 MPa), wight hour space velocity (WHSV) 8.2 h^{-1} and 20 $ml.min^{-1}$ N_2 flowrate. The estimated error was between 3 and 6%. ---------- 128
Figure 3.15. Comparison of powder X-ray diffraction patterns of the spent HZ80 zeolite, and Cr oxide-modified HZ80 catalysts prepared by impregnation and mechanical mixture. ---------- 131

Figure 3.16. (a)TGA for spent samples under Air flow. Inset plot shown the weight derivative thermogravimetry (DTG) curves of the five catalysts under air flow, (b) Coke content versus Cr oxide loading for the spent Cr_2O_3-HZ80 catalysts. ---------- 133
Figure 3.17. The relationship between the amount of coke and conversion in spent Cr_2O_3/HZ80 catalysts at 180 min of TOS. ---------- 134
Figure 3.18. The relationship between the amount of coke and surface area in spent Cr_2O_3/HZ80 catalysts. ---------- 136
Figure 3.19. Schematic representation of the influence of the synthesis methods of Cr_2O_3-HZ80 catalyst over the production of light alkenes and BTX through the catalytic cracking of *n*-heptane at fairly similar conversion. ---------- 138
Figure 4.1. Comparison of powder X-ray diffraction patterns of the H-ZSM-5 zeolite (HZ23), and 20 wt.% HZ23 on different supports for fresh samples. ---------- 154
Figure 4.2. The surface area (BET) analysis of the fresh 20 wt.% H-ZSM-5 (HZ23) over different supports for the selective cracking reaction of *n*-heptane toward light olefins. 155
Figure 4.3. (a**)** TGA for fresh samples under air flow for 20 wt.% HZ23 with different supports catalyst. (b) weight derivative thermogravimetric (DTG) curves of the five catalysts under air. ---------- 157
Figure 4.4. Scanning electron microscopy (SEM) images of 20 wt.% H-ZSM-5(HZ23) over different supports catalysis. ---------- 160
Figure 4.5. Transmission Electron Microscopy (TEM) image of 20 wt.% HZ23 over different supports. ---------- 162
Figure 4.6. Effect of HZ23-oxide/kaolin formulations on *n*-heptane conversion (a), C_2H_4 selectivity (b), C_3H_6 selectivity (c) and C_4H_8 selectivity (d). The reactions were conducted at 550°C, atmospheric pressure (0.1 MPa), wight hour space velocity (WHSV) 8.2 h^{-1} and 20 ml.min^{-1} N_2 flow rate. The estimated error was between 3 and 6%. ---------- 165
Figure 4.7. Selectivity of alkane on *n*-heptane catalytic cracking over HZ23-supports formulations. The reactions were conducted at 550°C, atmospheric pressure (0.1 MPa), wight hour space velocity (WHSV) 8.2 h^{-1} and 20 ml min^{-1} N_2 flowrate. The estimated error was between 3 and 6%. ---------- 169
Figure 4.8. Comparison of powder X-ray diffraction patterns of the spent samples of H-ZSM-5 zeolite (HZ23), and 20 wt.% HZ23 over different supports. ---------- 170
Figure 4.9. (a) TGA for spent samples under air flow for 20 wt.% HZ23 over different supports. (b) weight derivative thermogravimetry (DTG) curves of the five catalysts under air flow. ---------- 172

Figure 4.10. The surface area (BET) analysis of the spent 20 wt.% HZ23 on different supports for the selective cracking reaction of *n*-heptane to light olefins. ---------- 175
Figure 4.11. The loss of surface area of the spent hybrid of 20 wt.% HZ23 on different supports. ---------- 175
Figure 5.1. Illustration of the molecular structure of kaolinite. ---------- 185
Figure 5.2. Comparison of powder X-ray diffraction patterns of the various HZ23 zeolite/kaolin combinations for fresh samples. Kaolin is as received whilst kaolin @550 is treated at 550°C. ---------- 192
Figure 5.3. Scanning electron microscopy images (SEM) of six samples under study before the catalytic reaction. ZSM-5 (HZ23), Kaolin, 5% HZ23/Kaolin, 10% HZ23/Kaolin, 20% HZ23/Kaolin, and 30% HZ23/Kaolin. ---------- 194
Figure 5.4. HZ23 zeolite and kaolin structures alongside TEM images of different compositions of HZ23-kaolin catalyst at two magnifications (100 and 50 nm). The percentage in the left-hand side of the photographs corresponds to the zeolite content in wt.%. ---------- 195
Figure 5.5. Dependence of the turnover frequencies (rates normalized to the moles of NH_3 per mass of catalyst) and Brønsted/Lewis molar ratio with the surface acidity density of HZ23-kaolin catalysts in the production of light alkenes through the cracking reaction of *n*-heptane. The TOF errors was between 3-6%. ---------- 198
Figure 5.6. Effect of HZ23 zeolite loading on kaolin support on *n*-heptane conversion (a), C_2H_4 selectivity (b), C_3H_6 selectivity (c) and C_4H_8 selectivity (d). The reactions were conducted at 550°C, atmospheric pressure (0.1 MPa), wight hour space velocity (WHSV) 8.2 h^{-1}, and 20 ml.min-1 N_2 flow rate. The estimated error was between 3-6%. ---------- 200
Figure 5.7. Effect of HZ23 zeolite loading of kaolin catalyst on naphtha, C_2H_4 selectivity (a), C_3H_6 selectivity (b), C_4H_8 selectivity (c), and total alkane (d). The reactions were conducted at 550°C, atmospheric pressure (0.1 MPa), wight hour space velocity (WHSV) 8.2 h^{-1}, and 20 ml.min^{-1} N_2 flow rate. The estimated error was between 3-6%. ---------- 204
Figure 5.8. Effect of HZ23 zeolite loading over kaolin at 3-hour TOS on the *n*-heptane (a) and naphtha (b) cracking reaction for light olefins and BTX yield. The reactions were conducted at 550°C, atmospheric pressure (0.1 MPa), liquid hour space velocity (LHSV) 8.2 h^{-1}, and 20 ml min^{-1} N_2 flowrate. ---------- 206
Figure 5.9. The propylene/ethylene (P/E) ratio for two feedstocks on HZ23-kaolin catalysts with different compositions. ---------- 208

Figure 5.10. Catalytic cracking of *n*-heptane and distribution of olefins over HZ23-kaolin catalysts tested at different weight hourly space velocity (WHSV). (a) Influence of WHSV over conversion of *n*-heptane, (b) Effect of *n*-heptane conversion over ethene selectivity, (c) propene selectivity and (d) $C_4^=$ selectivity. The conversion of *n*-heptane and alkene selectivity correspond to a TOS of 3 h at 550°C, atmospheric pressure (0.1 MPa), 20 ml.min^{-1} N_2 flow rate and *n*-heptane flow rate between 0.075- and 0.8 ml.min^{-1}. ---------- 211
Figure 5.11. Effect of HZ23 loading on kaolin catalyst and olefins/alkane selectivity on different space velocities on the *n*-heptane conversion after 3-hour reaction.---------- 214
Figure 5.12. a) *n*-heptane conversion and light olefin yields (wt.%), and b) alkane and BTX yields (wt.%) over 5% HZ23-kaolin catalyst at different temperatures. The reactions were conducted at atmospheric pressure (0.1 MPa), and 20 ml.min^{-1} N_2 flowrate. ---------- 216
Figure 5.13. *n*-Heptane conversion over 5% HZ23 Zeolite-Kaolin catalysts in a 26-hour test reaction. The reactions were conducted at 550 °C, atmospheric pressure (0.1 MPa), and 20 ml.min^{-1} N_2 flowrate.---------- 217
Figure 5.14. The yield of light olefins over 5% HZ23 Zeolite-Kaolin catalysts on *n*-heptane cracking in a 26-hour catalytic test reaction. The reactions were conducted at 550 °C, atmospheric pressure (0.1 MPa), and 20 ml.min^{-1} N_2 flowrate. ---------- 218
Figure 5.15. Comparison of powder X-ray diffraction patterns for used HZ23 catalyst, kaolin, and different compositions of HZ23-kaolin catalyst. ---------- 219
Figure 5.16. Characterization of the catalysts after the catalytic cracking of *n*-heptane. a) TGA for used samples under air flow for different HZ23-kaolin catalyst. b) weight derivative profiles of the six used catalysts under air flow. Derivative data of HZ23 curve was divided by 4 to amplify the scale of the samples containing low loading of zeolite. The weight loss calculation considered the initial sample mass obtained at 250-300°C after the removal of adsorbed *n*-heptane. ---------- 221
Figure 5.17. Dependence of the total weight loss of the used catalysts with HZ23 content. ---------- 222
Figure 5.18. Schematic representation of the influence of HZ23-kaolin catalyst over the production of light alkenes through the catalytic cracking of *n*-heptane. ---------- 224

List of Tables

Table 1.1. Typical thermodynamic data for idealized reactions of importance in catalytic cracking of *n*-heptane. ----------14

Table 1.2. The conversion and selectivity for catalytic cracking of *n*-heptane over ZSM-5 at different temperatures and C/F=3 (Reproduced from[81]). ----------24

Table 1.3. The conversion and selectivity of catalytic cracking of *n*-heptane over ZSM-5 at different catalytic-to-feed (C/F) ratio and 550°C (Reproduced from[81]). ----------24

Table 1.4. The conversion, olefin selectivities, and olefin yields over H-ZSM-5 (Si/Al=150) for n-hexane, cyclohexane, and methylcyclohexane. (Reproduced from[82]) ----------25

Table 1.5. The conversion, and olefin yields over ZSM-5 (Si/Al=15 and 140) for 1-Hexene. (Reproduced from[29]) ----------27

Table 2.1. Summary of light naphtha composition.----------59

Table 2.2. The quantification of hydrocarbon types (wt.%) in light naphtha. ----------59

Table 3.1. Si/Al ratios and surface areas for ZSM-5 zeolites from Zeolyst International. 98

Table 3.2. Yield of hydrocarbon products from the catalytic cracking of *n*-heptane over HZ23, HZ30, HZ50, HZ80 and HZ280 zeolite catalysts. The reactions were conducted at 550°C, atmospheric pressure (0.1 MPa), wight hour space velocity (WHSV) 8.2 h^{-1} and 20 $ml.min^{-1}$ N_2 flowrate. The estimated errors were between 3 and 6%. ---------- 108

Table 3.3. The crystallite size of fresh and spent zeolite catalysts with different SiO_2/Al_2O_3 ratios determined from the X-ray peak at $2\theta = 23.3^{o}$. ---------- 110

Table 3.4. The average of particle size and loading amount for Cr_2O_3 from X-ray patterns for catalysts.---------- 114

Table 3.5. The surface area (BET) analysis of the fresh Cr_2O_3-HZ80 catalyst series for the selective cracking reaction of *n*-heptane toward light olefins.---------- 115

Table 3.6. The binding energies, FWHM and surface compositions (%) of HZ80 zeolite modified with Cr_2O_3 *via* impregnation and mechanical methods. ---------- 123

Table 3.7. Yield of hydrocarbon products for *n*-heptane cracking over Cr_2O_3-HZ80. The reactions were conducted at 550°C, atmospheric pressure (0.1 MPa), wight hour space velocity (WHSV) 8.2 h^{-1} and 20 ml min^{-1} N_2 flowrate. The estimated error was between 3 and 6%. ---------- 126

Table 3.8. Catalytic cracking of *n*-heptane and distribution of olefins over HZ80 modified by 10 wt.% Cr oxide loading using different preparation methods at a several weight hourly space velocities (WHSV). The conversion of *n*-heptane and alkene selectivity correspond

to a TOS of 3h at 550°C, atmospheric pressure (0.1 MPa), 20 ml min^{-1} N_2 flow rate and *n*-heptane flow rate between 0.05 and 0.7 mL. min^{-1} to have WHSV between 4.1 and 57.5 h^{-1}.---------- 129

Table 3.9. The surface area (BET) analysis of the spent Cr_2O_3-HZ80 catalyst series for the selective cracking reaction of n-heptane toward light olefins.---------- 135

Table 3.10. The binding energies, FWHM and surface compositions of various Cr oxide species for the spent 10 wt.% Cr_2O_3-HZ80 catalysts prepared by impregnation and mechanical methods.---------- 137

Table 4.1. Yields of hydrocarbon products from *n*-heptane cracking over HZ23-oxide/kaolin formulations. The reactions were conducted at 550°C, atmospheric pressure (0.1 MPa), wight hour space velocity (WHSV) 8.2 h^{-1} and 20 ml.min^{-1} N_2 flowrate. The estimated error was between 3 and 6%.---------- 167

Table 5.1. Surface area of the HZ23-kaolin catalyst series tested in the selective cracking reaction of *n*-heptane and naphtha toward light olefins.---------- 193

Table 5.2. Acidity of the HZ23-kaolin catalyst series. ---------- 197

Table 5.3. The **s**urface area of the spent HZ23-kaolin catalyst series was tested in the selective cracking reaction of *n*-heptane toward light olefins.---------- 223

List of abbreviations and symbols

SC	Steam Cracking
PE	Polyethylene
PET	Polyethylene terephthalate
PVC	Polyvinyl chloride
PS	Polystyrene
MTO	Methanol-to-olefins
FCC	Fluid Catalytic Cracking
HS-FCC	high-severity fluid catalytic cracking
DCC	deep catalytic cracking
LPG	Liquefied petroleum gas
VGO	Vacuum gas oil
VR	Vacuum residue
AR	Atmospheric residue
OCM	Oxidative coupling of methane
MTBE	Methyl tert-butyl ether
DME	Dimethyl ether
P/E	Propylene/Ethylene ratio
P+E	Propylene + Ethylene
BAS	Brønsted acid site
LAS	Lewis acid site
B/L	Brønsted acid/ Lewis acid
HDS	Hydrodesulfurization
HDN	Hydrodenitrogenation

IUPAC	International Union of Pure and Applied Chemistry
ZSM-5	Zeolite Socony Mobil-5
H-ZSM-5	H form-Zeolite Socony Mobil-5
NH_4-ZSM-5	NH_4 form-Zeolite Socony Mobil-5
MFI	The framework type of the ZSM-5
HZ23	H-ZSM-5 with SiO_2/Al_2O_3 ratio 23
HZ30	H-ZSM-5 with SiO_2/Al_2O_3 ratio 30
HZ50	H-ZSM-5 with SiO_2/Al_2O_3 ratio 50
HZ80	H-ZSM-5 with SiO_2/Al_2O_3 ratio 80
HZ280	H-ZSM-5 with SiO_2/Al_2O_3 ratio 280
USY	Ultra-Stabilized Zeolite Y
SAPO	Silico-Alumino-Phosphate
MCM-22	Mobil-Composition-of-Matter-22
RE	Rare earth
HY	Zeolite Y, H form
SCT-MAT	Short contact time micro activity testing unit
MAT	Micro activity testing unit
C/F	Catalyst/ feed ratio
LHHW	Langmuir-Hinshelwood-Hou-gen-Watson theory
LHSV	Liquid Hourly Space Velocity
Si/Al	Si to Al ration within the zeolite framework
TOS	Time-on-stream
WHSV	weight hourly space velocity
LCA	Lifecycle analysis
CSI	Catalyst Sensitivity Index

BTX	Benzene- Toluene - Xylene
NH_3-TPD	ammonia temperature-programmed desorption
XRD	X-ray powder diffraction
TEM	Transmission electron microscopy
SEM	Scanning electron microscopy
TGA	Thermogravimetric analysis
DTG	Derivative Thermogravimetry
BET	Brunauer, Emmett and Teller (BET) analysis
HPLC	High Performance Liquid Chromatography
EDX	Energy dispersive X-ray analysis
XPS	X-ray photoelectron spectroscopy
GC	Gas chromatography
GC-MC	Gas chromatography mass spectrometry
FID	Flame ionization detectors
TCD	Thermal conductivity detectors
IMP	Impregnation method
MM	Mechanical mixture method
WL	Weight loss
SAD	Surface acidity density
C_1-C_4	Paraffins from C_1 to C_4
$C_4^=$	Butene
ΔG	Gibbs free energy
ΔH	Heat of reaction
ΔS	Entropy change
Å	Angstrom

kV	Kilovolts
mA	Milliamperes
eV	Electron volts
MPa	Megapascal
nm	Nanometre
℃	Degree Celsius
2θ	2 theta
$M^2.g^{-1}$	Square meter/grams
$mmol.g^{-1}$	Millimole/ grams
$\mu mol.g^{-1}$	Micromoles/ grams
γ	Gamma
h	Hour
g	Gram
min	Minute
mL	Millilitre

Chapter 1

Overview of catalytic cracking

1.1 General background

Concerns about sustainable development and climate change have prompted chemical manufacturers to start seeking renewable feedstocks. Since oil reserves are finite and in high demand, it is essential to look for an alternative route, especially a sustainable one, to produce the widely used light olefins in a more efficient manner by minimizing energy input (or using renewable energy) and emission of CH_4 or CO_2 to the atmosphere.

Light olefins with carbon atoms between C_2 and C_4 are unsaturated hydrocarbons with a least one carbon-carbon double bond and have the chemical formula C_nH_{2n}. They include ethene (or ethylene) propene (or propylene), and butene. Ethylene and propylene, which are sometimes called the king and crown of chemicals respectively, are critical building blocks in the petrochemical industry, where demands for these light olefins have been continually increasing. These compounds serve a myriad of markets such as plastic manufacturing and processing, construction, automobiles, textile, and the furnishing sector, and many chemicals. Butene is used for synthetic rubber manufacturing, and pentene is the feedstock for high octane gasoline components. They are also essential feedstocks for the production of oxygenates used as octane boosting additives[1-10]. Thus, the range of applications for light olefins continues to expand globally across many industries. In particular, the demand for propylene is increasing rapidly in petrochemical industries[3, 4, 7, 11].

1.2 Applications of Light Olefins

1.2.1 Ethylene

The steam cracking of naphtha (SC) is the main chemical process used to produce ethylene[12, 13]. Ethylene can undergo many reactions such as polymerization, oxidation, hydrolysis, and alkylation. It is a key material in the manufacture of polymers such as

polyethylene (PE), polyethylene terephthalate (PET), polyvinyl chloride (PVC), polystyrene (PS) and fibers and other chemicals as shown in **Figure 1.1**[12-15].

Ethylene-based products are used in a wide variety of industrial and consumer contexts such as packaging, transportation, electrical/electronic devices, textile and construction industries as well as chemicals, coatings, and adhesives. It is also used in the manufacture of daily used commodities, such as grocery bags, shampoo bottles, children's toys, and even bulletproof vests amongst many other products.

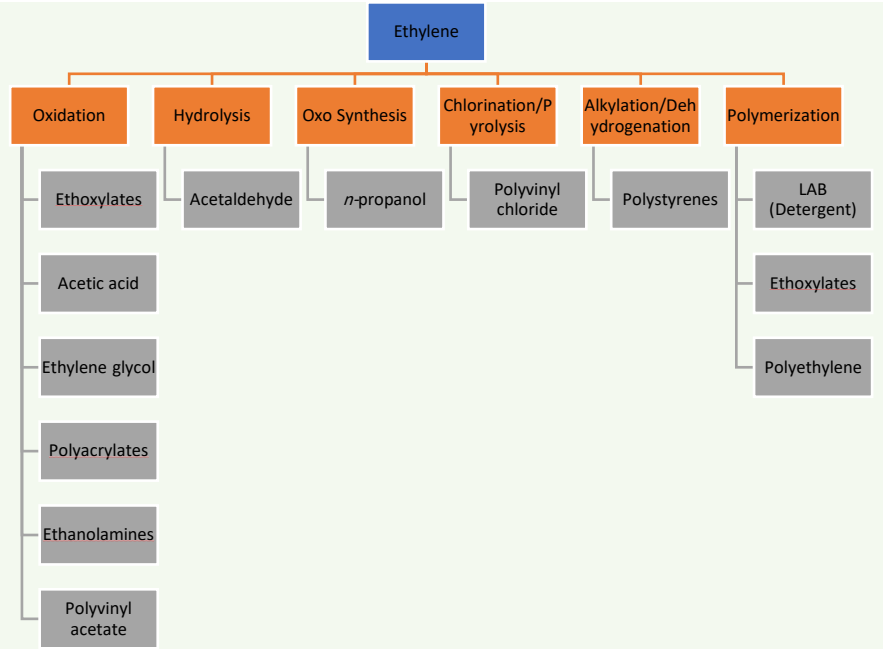


Figure 1.1. Major chemicals derived from ethylene [13, 14].

Ethylene can be produced by several processes with feedstocks such as oil or natural gas. The following processes generate ethylene[12, 16, 17]:

a) The steam cracking of heavy hydrocarbons.

b) The catalytic cracking of heavy hydrocarbons.

c) Fischer-Tropsch process.

d) Methanol- to olefins (MTO).

e) Catalytic dehydrogenation.

1.2.2 Propylene

Propylene is the second chemical most used in industry after ethylene. The demand for propylene is expanding rapidly as compared to ethylene, and according to the latest market analysis, the projected demand cannot meet the current supply[7, 18]. The apparent need for propylene reached 84 million tons annually in 2013, with an increase of 30% over 2009. In 2022, the propylene market is expected to increase by 85% compared to 2009[18, 19]. The global demand for ethylene and propylene reached 270 million tons in 2018, and this demand is expected to grow to 385 million tons by 2030, an increase of 42.6% over 2018[12, 20]. As displayed in **Figure 1.2**, propylene production cannot meet market demand. Therefore, there is urgent need for new technology to produce additional propylene to bridge the gap between supply and demand.

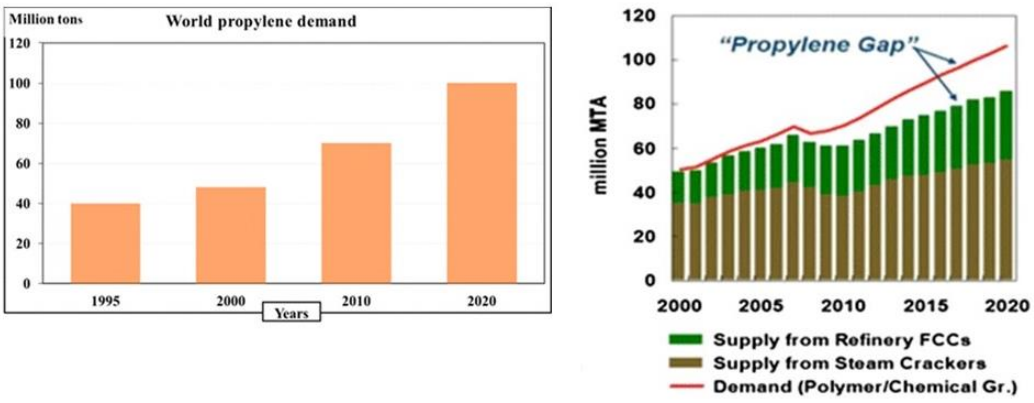


Figure 1.2. Propylene supply and request, adapted from[7, 21].

Propylene is mostly obtained as a co-product in ethane cracking plants. Like ethylene, propylene is highly reactive and is used to produce more valuable chemicals. Polypropylene, another very popular polymer, is used in the manufacture of plastic bottles, plastic toys, plastic films in packaging, acrylonitrile, acrylic acid, and other laboratory wares. The reaction for

producing polypropylene is similar to the production of polyethylene from ethylene[6, 22-26]. In **Figure 1.3**, we can see some of the most common chemicals obtained from propylene. The methods used to make propylene can be classified as commercial or non-commercial. The commercial processes include thermal and catalytic cracking processes such as steam cracking (SC) and fluid catalytic cracking processes, where propylene is a by-product. On the other hand, there are non-commercial processes for propylene production such as methanol reduction and propane dehydrogenation[18, 22, 27-29].

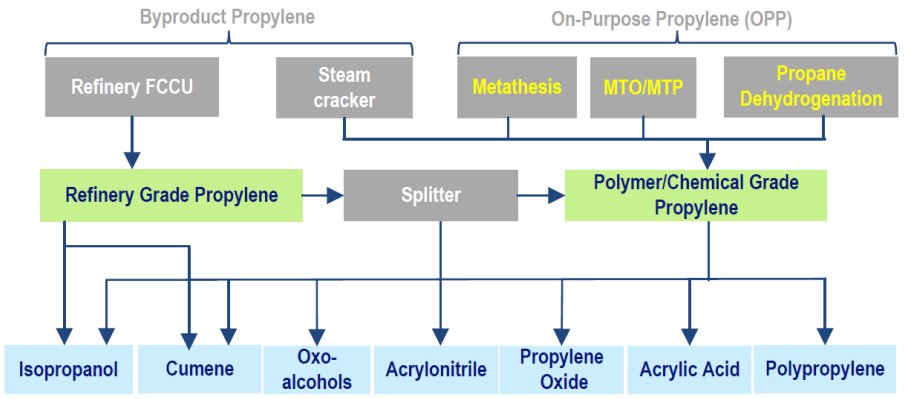


Figure 1.3. Propylene value chain adapted from[30].

1.3 Commercial Processes for Producing Light Olefins

All the methods described here result in the production of a range of major products and by-products. Currently, there are three principal processes for olefin production from petrochemicals: Steam Cracking of hydrocarbons (naphtha, crude oil, gas oil, and LPG), Fluid Catalytic Cracking (FFC) and paraffin dehydrogenation. In addition to these industrial processes, there are some non-commercial technologies under various phases of development, such as catalytic cracking, oxidative coupling of methane (OCM), oxidative dehydrogenation of paraffins, and methanol to olefins (MTO) conversion. Herein, mainly steam cracking, FCC processes and catalytic cracking will be described as they are well-established technologies.

Other processes such as the oxidative dehydrogenation of paraffins[31], and Fischer-Tropsch[15, 32], have been widely discussed elsewhere in the literature and are not included.

1.3.1 Steam Cracking (SC)

Steam cracking of hydrocarbons, also known as pyrolysis, is the leading and primary source of olefins. Ethylene is the first and foremost product of the steam cracking process with propylene as a by-product. Hydrocarbon feedstocks most often include crude oil, naphtha, and gas oil, although alkanes may be used. Regardless of the feedstock employed, the same process is used, although the amount of energy used, and cost vary depending on the type of feedstock and the desired product. While there are several configurations available to accomplish pyrolysis, essentially all begin with the introduction of hydrocarbon feed and steam into a tubular pyrolysis furnace. Usually, steam cracking is carried out in the absence of oxygen with the furnace at a cracking temperature of about 800-900°C. These conditions allow the C-C, C-S, C-O, and C-H bonds in large chain molecules to be broken down to give smaller molecules. To crack ethane a higher temperature is required than for the heavier feedstocks[4, 7, 8, 33-37].

Although steam-crackers have represented the most important source of light olefins for more than half a century, propylene supply is very limited due to the low propylene yield[4, 6]. The ethylene yield is 24-55%, while propylene yields are 1.5-18% depending greatly on the feedstock type and operating conditions. Steam-cracking is still the main route for the production of olefins but requires very high temperatures to get light olefins due to its endothermic character[33, 38]. Despite the improvements made in the steam cracking process, it is considered one of the most energy-consuming technologies in the petrochemical industry and results in a high amount of CO_2 emission[33, 38, 39]. Some 40% of the total annual energy consumption in petrochemical plants[18] is due to steam cracking. Furthermore, the ratio of propylene to ethylene (P/E) in the olefins resulting from thermal cracking and its direct

dependence on the type of feed cannot be easily controlled. Moreover, the global demand for propylene is increasing faster than for ethylene[4, 6, 8, 33, 36, 37].

The steam cracking reaction of hydrocarbons proceeds via free-radical intermediates from the homolytic breaking of C-C bonds to create alkyl radicals, as proposed by Rice and Kossiakoff [40]. It can be represented in the following manner[41]:

$$R - CH_2 - CH_2 - CH_2 - R \longrightarrow R - CH_2 - CH_2 - CH_2\bullet + \bullet R \qquad (1\text{-}1)$$

$$R - CH_2 - CH_2 - CH_2\bullet \longrightarrow RCH_2\bullet + CH_2 = CH_2 \qquad (1\text{-}2)$$

where 'R' is any alkyl group

The radicals undergo β-scission (cleavage of the C-C bond situated in the β position to the carbon with 1 hydrogen less) to create a terminal or alpha-olefin and another radical with the absence of one hydrogen atom. The β-scission from a fundamental radical produces ethylene and another radical that would create further ethylene without radical isomerisation. By progressive splitting, methyl and ethyl fragments react with H atoms to deliver methane, ethane, and new radicals that trigger the breaking (chain) response[4, 41, 42]. The termination of the breaking process can happen by the mixing and disproportionation of (extreme) alkyl radicals to create hydrogen and light alkanes. Several kinetic models have been suggested for the thermal splitting of gases and fluid catalytic cracking of hydrocarbons to light olefins[43-45].

Steam cracking of hydrocarbons is strongly endothermic reaction, requiring high temperatures and low pressures owing to the large stoichiometric ratio of gaseous products relative to the reactants (eq. (1-3)). The deep dehydrogenation of hydrocarbon produces carbon as given in eq. (1-4).

$$C_2H_6 \longrightarrow C_2H_4 + H_2 \qquad \Delta H_{590^\circ C} = +143 \text{ mol. } KJ^{-1} \qquad (1\text{-}3)$$

$$C_2H_6 \longrightarrow 2C + 3H_2 \qquad (1\text{-}4)$$

$$C + H_2O \longrightarrow CO + H_2 \qquad (1\text{-}5)$$

The partial pressure of the reactive hydrocarbons is reduced using hot steam. Carbon deposits generated by the pyrolysis of hydrocarbons at high temperatures are also reduced by hot steam as illustrated in eq. (1-5). Furthermore, steam as a diluent minimizes the odds of the hydrocarbons coming into contact at high temperature. While deposits inhibit heat transport via reactor tubes, steam mitigates this effect by interacting with the carbon residues (steam reforming reaction, (1-5))[41].

1.3.2 Catalytic Cracking

Catalytic cracking is a chemical conversion process that can be employed for a variety of feedstocks. This process occurs by catalytically converting long-chain hydrocarbons and compounds such as heavy oils and residues into olefins and fuels. The catalytic cracking process is carried out on a solid catalyst to moderate the cracking conditions, increase the desired products, and improve their selectivity. In 1915, McAfee at the Gulf Refining Company introduced the first technical model of catalytic cracking technology using an aluminum chloride catalyst. However, this process was abandoned because it was not economic and also because of the increasing popularity of the steam cracking units at that time[46]. The French scientist, Houdry, developed catalytic cracking technology in the Mobil Oil company in the USA (Previously the Socony-Vacum oil company) in 1936 to process 1500 barrels of oil per day using a fixed bed reactor. Sun Oil's refinery in the United States of America took advantage of the Houdry operation and operated the first commercial plant in 1937 by replacing the catalyst by silica-alumina. This process resulted in high-quality fuel in large quantities. The Houdry technology was developed quickly to manufacture large amounts of aviation fuel for the allies' efforts in World War II[24, 46].

In some ways, catalytic cracking is similar to steam cracking; however, catalytic cracking uses a catalyst to improve process efficiency. The catalytic cracking process is carried out at low temperatures ranging between 485 to 550℃ and pressures of 100 psi. In comparison, steam cracking requires very high temperatures of up to 900℃. Moreover, this is reflected in lower CO_2 emissions for the catalytic cracking process[47-50]. The relatively mild temperatures can also facilitate the control of the propylene-to-ethylene ratio to obtain values higher than 0.6, which is the maximum value obtained by steam cracking. Although steam cracking is still the leading commercial technology for light olefin production after more than half a century, it has significant drawbacks. One of the disadvantages of steam cracking is the difficulty in controlling the selectivity for light olefins. The low weight ratio (i.e., 0.5-0.6) of propylene/ethylene gives limited control over the P/E. The yield amount can be controlled in catalytic cracking, as the yield of ethylene and propylene ranged between 28-34% and 23-29%, respectively. It can also control the propylene/ethylene (P/E) ratio. Therefore much attention has been focused on developing more energy-efficient and reduced CO_2 emission processes[3, 33].

According to Ren *et al.*[35], 65% of the energy consumed in steam cracking involves the combustion process, with 75% of the total energy lost. The utilization of solid catalysts for producing olefins can reduce energy consumption by decreasing the activation energy, as shown in **Figure 1.4**.

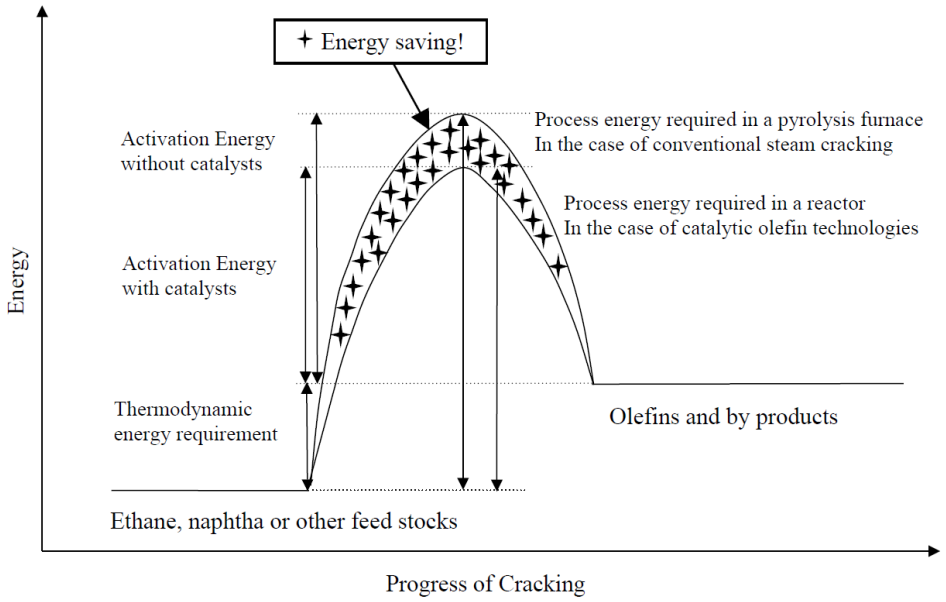


Figure 1.4. Simplified Plot of traditional steam cracking and catalytic olefin energy profiles. Adapted from[35].

Among the reasons why catalytic cracking saves energy compared to steam cracking are the following[35]:

- First, the catalysts have a lower activation energy barrier for C-C bond cleavage (see **Figure 1.4**), allowing the cracking process to be performed at lower temperatures and pressures compared to steam cracking.
- Second, the catalysts enhance the selectivity for the desired products such as propylene in particular and olefins in general, thus increasing the total yield of olefins.
- Third, catalysts decrease the amount of coke deposited. It is known that coke impedes heat transfer and reduces energy efficiency. Coke removal is achieved by air treatment of the spent catalyst at high temperatures or regeneration as in FCC technology.

1.3.2.1 Mechanism

A potential mechanistic approach for the catalytic cracking of hydrocarbons has been published[33, 51, 52]. It proposes a reaction scheme for catalytic cracking and defines the potential

contribution of several parameters on the mechanism. It is thought that the activation of alkanes can occur by two pathways: (1) Monomolecular and (2) Bimolecular. The monomolecular approach, also known as protolytic cracking, was suggested by Haag and Dessau[53]. It was proposed that alkanes were first protonated to generate carbonium ion transition states followed either by the cleavage of a single carbon-carbon bond to yield lower alkanes (such as ethane and methane) or by the scission of the carbon-hydrogen bond to yield carbenium ions and hydrogen. These carbenium ions would then react by donating back a proton to the zeolite to form alkenes (see **Figure 1.5a**). The bimolecular mechanism, on the other hand, occurs when branched alkylcarbenium ions (only secondary and tertiary ions), which come from the feedstock, are cleaved in a unique step of β-scission to yield smaller alkylcarbenium ions and alkenes (see **Figure 1.5b**). It is highly improbable that primary alkylcarbenium ions are formed in the bimolecular approach. Therefore, compounds such as methane, ethane, and ethylene could not be produced through this mechanistic pathway. Finally, it has been highlighted that those transfer reactions of bimolecular hydrides involving alkylcarbenium ions and alkanes have a knock-on effect, which produces further yields of (shorter) alkanes, thus capping the yield of olefins to around 50%[33, 51, 52].

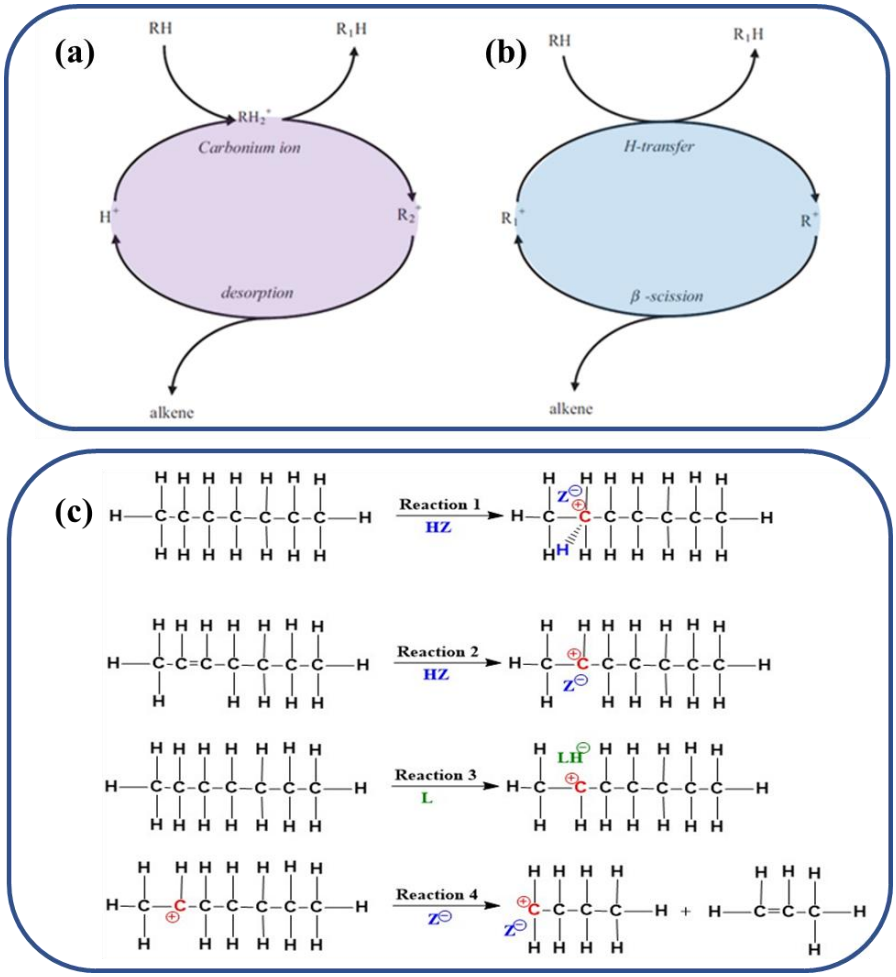


Figure 1.5. (a) Proposed Haag–Dessau cracking mechanism for an alkane molecule (RH) proceeding via a carbonium ion transition state. (b) Classical cracking mechanism for an alkane molecule (RH) consisting of a hydride transfer step to a smaller carbenium ion ($R1^+$) followed by β-scission, Adapted from[33]. (c) Reaction pathways for hydrocarbon cracking over zeolite. HZ and L stand for zeolite Brønsted and Lewis acid sites, respectively. Adapted from[46].

Several researchers have studied and discussed the mechanism of catalytic cracking reactions on zeolite[4, 46, 51, 52, 54-56] . **Figure 1.5c** shows a zeolite-assisted reaction network for hydrocarbon cracking and the formation of carbonium ions. The zeolite protolytic cracking forms a carbonium ion by transferring a proton from the zeolite Brønsted acid site (BAS) to the alkane (reaction 1). Carbenium ions are formed via proton transfer from zeolite to the alkene via reaction 2. Carbenium ions are also formed through hydride transfer from alkane into the zeolite structure (reaction 3). Alkene and a primary carbonium ion can be formed through the β-scission of a carbonium ion (reaction 4). The primary carbenium ion can take a proton from

a larger alkane molecule to produce an alkane or experiences a β-scission to desorb ethylene from the acid site. The molecular fragment of carbenium ion on zeolite sites can propagate the reaction. The primary carbonium ion can produce α-alkene and regenerate the Brønsted acid sites (BAS) by transferring a proton back to zeolite.

Overall, catalytic cracking involves the formation of carbonium ions through the following pathways:

1) Brønsted acid (BAS) and alkene which have been formed by thermal cracking for alkanes can donate protons to alkenes.
2) Lewis acid sites (LAS) and some strong Brønsted acid sites (BAS) can extract a hydride from an alkane and form dihydrogen.

1.3.2.2 Thermodynamic aspects

Naphtha is usually composed of a mixture of hydrocarbon molecules of 5-12 carbon atoms. These molecules include paraffin, olefins, naphthenes, and aromatics. The most significant reaction step in catalytic cracking is β-scission, which is not restricted by equilibrium; thus, the thermodynamics are of little use in adjusting operating parameters or estimating the magnitude of the reaction. Under cracking conditions, the cracking of long-chain olefins and paraffins may proceed to up to 95% completion. Moreover, dehydrogenation, isomerization, dealkylation, and transalkylation reactions are examples of hydrogen transfer processes that function similarly and serve as intermediates in the process of reaching equilibrium. **Table 1.1** shows the changes in Gibbs free energy (ΔG) and heat of reaction (ΔH) for various reactions.

The size and nature of such reactions have an impact on the unit's functioning and energy balance. For instance, if a catalyst with fewer hydrogen transfer properties is utilised, the net heat of the reaction will be more endothermic[57-61].

Table 1.1. Typical thermodynamic data for idealized reactions of importance in catalytic cracking of *n*-heptane.

Reaction		$\Delta G^{\circ}_{550°C}$ *(kJ.mol^{-1})*	$\Delta H^{\circ}_{550°C}$ *(kJ.mol^{-1})*	$\Delta S^{\circ}_{550°C}$ *(J.mol^{-1}K^{-1})*
Cracking	n-$C_7H_{16} \longrightarrow C_3H_6 + C_4H_{10}$	-84.1	136.4	267.9
	n-$C_7H_{16} \longrightarrow C_2H_4 + C_5H_{12}$	-21.6	107.4	156.7
	n-$C_7H_{16} \longrightarrow C_4H_8 + C_3H_8$	-80.4	137.4	264.6
Isomerization	n-$C_7H_{16} \longrightarrow$ 2-methyl-hexane	0.5	-6.2	-8.1
	n-$C_7H_{16} \longrightarrow$ 3-methyl-hexane	2.7	-3.9	-8.1
Transalkylation	n-$C_7H_{16} \longrightarrow C_7H_8 + 4H_2$	-134.9	308.3	538.4
Dealkylation	3-methyl-hexane $\longrightarrow C_6H_{12} + CH_4$	-49.8	84.5	163.0
Dehydrogenation	n-$C_7H_{16} \longrightarrow C_3H_6 + C_4H_8 + H_2$	-65.1	267.2	403.7
Coke formation	n-$C_7H_{16} \longrightarrow 7C + 8H_2$	-428.5	285.3	867.1

1.3.2.3 Conventional Feedstocks for Catalytic Cracking

Light olefins are currently produced from alkanes and from heavier hydrocarbon fractions, such as naphtha and gas oil[62]. The catalytic cracking of naphtha is a promising alternative to thermal steam cracking[6, 8, 33]. Due to the availability of naphtha, its low cost, and the possibility of obtaining high yields, it is widely used to produce olefins.

Naphtha is one of the most attractive feedstocks for the production of light olefins through catalytic or thermal cracking[33, 63]. Naphtha is a fraction of petroleum, typically occurring as 15-30% of crude oil. This complex mixture consists of hydrocarbon molecules

with 5-12 carbon atoms, including paraffin, olefins, naphthenes, and aromatics[64] and also small amounts of sulfur- and nitrogen- compounds[65]. Naphtha has a boiling point between 30°C and 200°C[64, 65]. There are two types of naphtha -light and heavy. Light naphtha is the fraction boiling from 30°C to 90°C, containing the C_5 and C_6 hydrocarbons. Heavy naphtha is the fraction boiling from 90°C to about 200°C [64, 65] as illustrated in **Figure 1.6**. The ranges of boiling points and numbers of carbon atoms for heavier fractions (e.g., kerosene, gas oil and vacuum residue) of crude oil are also given in **Figure 1.6**.

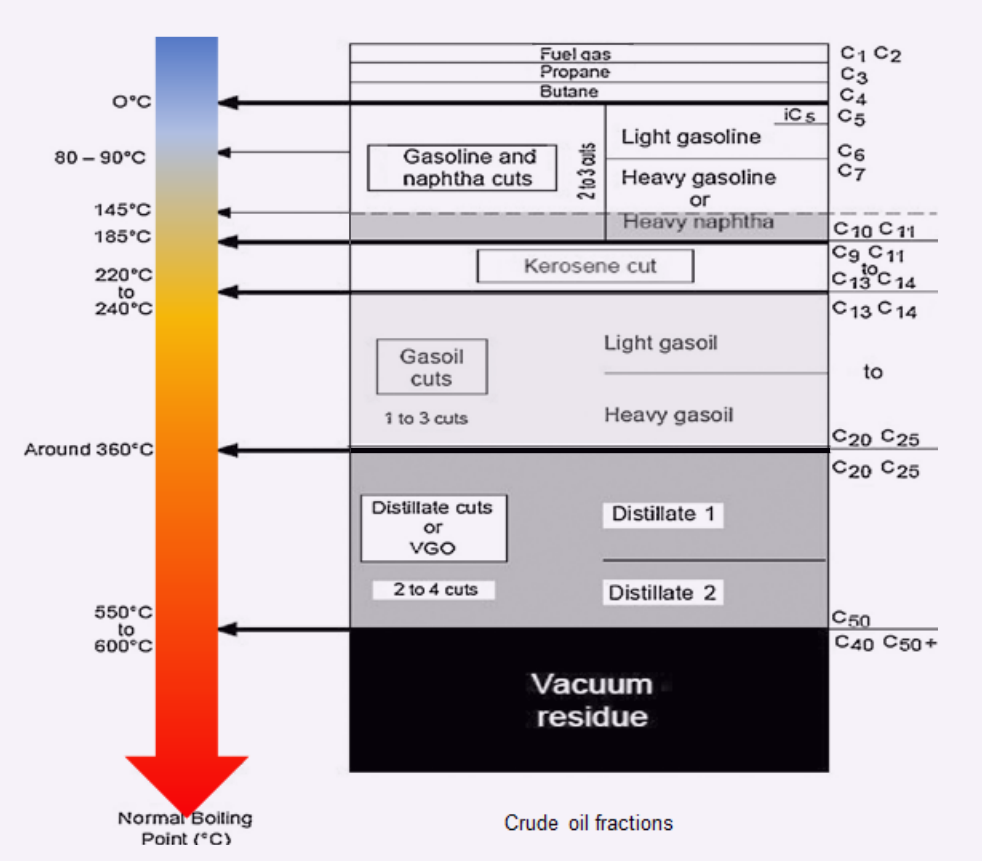


Figure 1.6. The different fractions, carbon ranges and boiling points for crude oil, Adapted from[4] .

As shown in **Figure 1.7**, paraffins are concentrated in the lower boiling point light naphtha, and their concentration decreases as the boiling point increases. The amounts of complex compounds in naphtha increase with rising boiling points in the heavy naphtha region due to the rise in the number of isomers and poly-naphthenes.

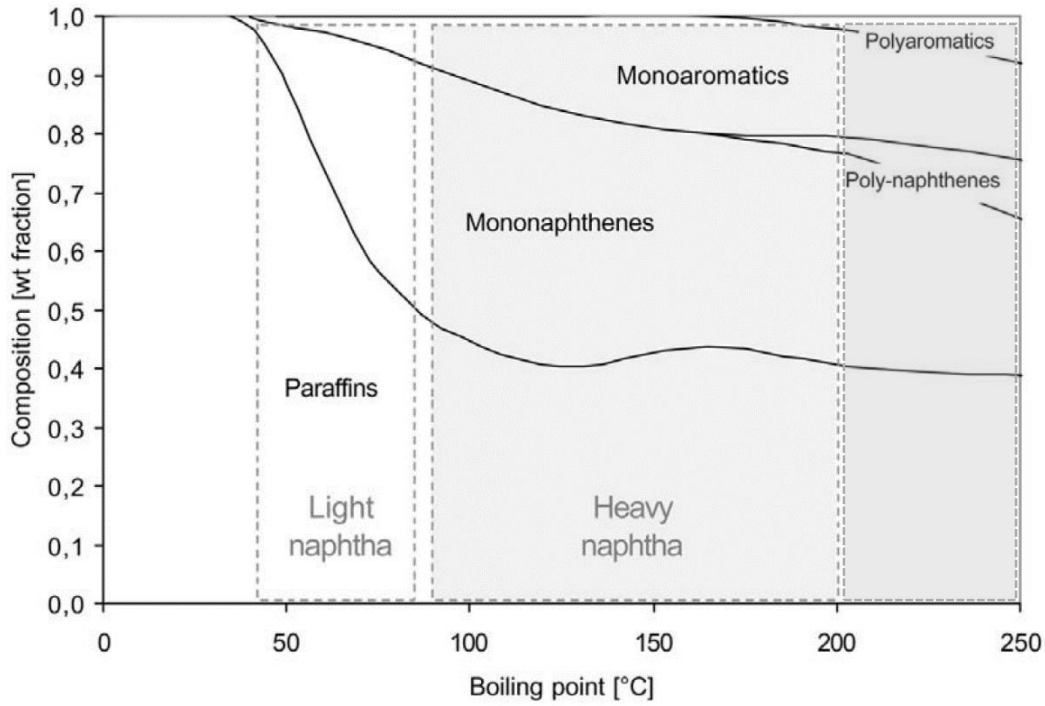


Figure 1.7. Types of naphtha related to their boiling points and areas of hydrocarbon formation, Adapted from[66].

Sulfur and nitrogen compounds must be removed from naphtha feeds to low levels before use in catalytic or thermal cracking [thermal cracking does not use a catalyst]. These elements affect the performance of the bi-functional noble metal catalyst used[38, 65]. Sulfur poisoning of the catalyst used in cracking increases the formation of unwanted sulfur oxide (SO_x) compounds during combustion. The nitrogen content is usually 10 to 100 times lower than that of sulfur, Moreover, certain nitrogen compounds present in the heavier cuts have a pronounced alkaline nature and poison the acid catalysts used in catalytic units. Sulfur and nitrogen are removed from the naphtha through a hydrotreatment process that involves hydrodesulfurization (HDS), hydrodenitrogenation (HDN) and hydrogenation reactions. The naphtha is treated with hydrogen or hydrogen-saturated gas (75% and above hydrogen concentration) over a fixed-bed of catalyst so that the sulfur/ nitrogen is converted to hydrogen sulfide/ nitride which can be removed by washing with an amine solution according to the general reaction[66]:

$$R - S - R + 2H_2 \rightarrow 2R - H + H_2S \qquad (1\text{-}6)$$

1.3.2.4 Catalysts employed in the Catalytic Cracking process

The catalyst used in catalytic cracking of high molecular weight hydrocarbons present in naphtha must possess several chemical and physical properties to be suitable for the production of light olefins[24]: high activity, high selectivity for light olefins, low selectivity for aromatics, and ease of regeneration.

Various kinds of materials such as basic catalysts, transition metal oxides, and acidic catalysts have all been studied for naphtha/hydrocarbons catalytic cracking to light olefins. Oxides of Ca, Al, Mg, Ti, Sr, Mn, Mn, Zr, K, and In have been used to produce olefins for more than a half-century. The yields of ethylene and propylene over metal oxide catalysts are between 24-40% and 15-22% respectively. The yields are also dependent on the feedstock type and reaction conditions[6, 33]. Different types of solid proton-donor acids, including zeolites, have also been investigated[6, 33]. Zeolites have been used extensively in the petroleum industry as catalytic cracking catalysts[4, 6]. ZSM-5 zeolite was found to be the most efficient for producing light olefins[4].

1.3.2.5 Structure and pore size of zeolite for catalytic cracking

According to the diameters of the pores, the International Union of Pure and Applied Chemistry (IUPAC) has divided the porosity of different types of materials into three distinct groups as shown in **Figure 1.8**. The zeolite pores are generally less than 2 nm in size and are categorised to be members of the microporous group. The maximum pore aperture of microporous zeolites may be used to categorise these materials further, which results in the following three distinct groups for these materials: small pore size which have 8 T-atoms per pore and ±0.30-0.45 nm diameter such as Linde type A (LTA, zeolite A), medium-pore size

coming with 10 T-atoms per pore and ±0.45-0.60nm diameter such as ZSM-5, large-pore size which have 12 T-atom per pore and ±0.60-0.80 nm diameter such as beta zeolite and faujasite zeolite, and extra-large pore size such as UTD-1 zeolite which has 14 T-atoms. Note that mesoporous materials have pore size between 2 and 50 nm such as MCM-41 and SBA-15 whilst pore sizes beyond are associated to macroporous materials[67-70].



Figure 1.8. Pore sizes for zeolite and other materials.

Zeolites have a three-dimensional crystal structure comprising aluminum, silicon, and oxygen atoms. They also have water and some metal species of elements such as sodium, potassium, and magnesium in limited quantities in their porous structures[71]. Zeolite is an important and active catalyst in the field of petroleum refining, petrochemicals and pollution control. ZSM-5 is the second most extensively used zeolite in cracking applications as it has textural and structural properties that make it an appropriate catalyst for catalytic cracking reactions. These include large surface area, high hydrothermal and thermal stability (resistance to deactivation) and high acidity. ZSM-5 is also used in the aromatization of hydrocarbons, alkylation and many other reactions[33, 38].

Furthermore, ZSM-5 has a cation-exchange capability, a well-ordered microporous network and molecular shape selectivity arising from a unique framework structure[33]. However, some significant limitations hinder the extensive use of ZSM-5 in cracking reactions. First, the high acidity of ZSM-5 zeolites decreases the lifetime of the zeolite due to an increase in coke formation. Secondly, the large crystal size limits the diffusion and transfer of reactants and product molecules. Thirdly narrow channels and relatively small pores in ZSM-5 lead to

diffusion limitations for large reactant molecules[4, 18]. Therefore, some modifications based on the generation of a hierarchical pore structures in the zeolite, optimization of acidity and particle size, incorporation of metals and even phosphorus treatment[4, 33, 38] need to be applied. These methods can enhance not only the ZSM-5 performance for light olefins but also the catalyst stability.

The ZSM-5 structure typically contains tetrahedral [SiO_4] and [AlO_4] units, which are bound together by sharing an oxygen atom. Zeolites and are represented chemically by the empirical formula[72]:

$M_{2/n}O \cdot Al_2O_3 \cdot ySiO_2 \cdot wH_2O$

Where:

M= the exchangeable cation, usually from the group I or II ions,

y = varies from 2 to ∞

n = represents the cation valence

w = corresponds to the number of water molecules confined in the voids of the zeolite per structural unit.

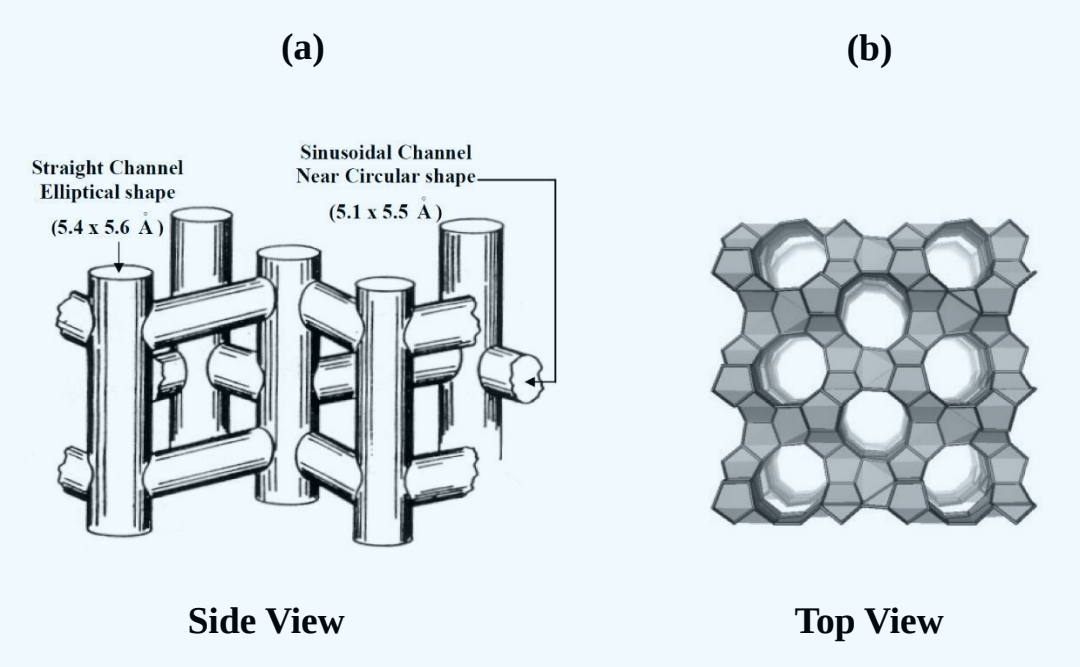


Figure 1.9. ZSM-5 structure: a) Zig Zag pore structure and b) The channel structure in ZSM-5, Adapted from[73, 74].

Figure 1.9 shows the structure of ZSM-5 containing a 10-member oxygen ring. ZSM-5 is made up of many pentasil units that are connected by oxygen bridges to create pentasil chains. These chains are joined by oxygen to produce corrugated sheets with 10-ring holes, which are connected by oxygen bridges to build a structure with parallel straight 10-ring channels and sinusoidal 10-ring channels perpendicular to the corrugations. These rings are arranged in columns and connected in straight channels (5.4: 5.6 Å) and sinusoidal channels (5.1: 5.5 Å) of similar size. These two channels are orthogonal to each other and generate intersections with diameters of 8.9 Å. The characteristics of ZSM-5 that help it to reduce coke formation are unique channel structure, thermal stability, acidity, and shape-selective property. In addition, the pore system and the absence of large cages with small windows[18, 24, 73]are beneficial to catalyst efficiency.

1.3.2.6 Acidity

The tetrahedral structure of AlO_4 in the zeolite has a negative charge on the oxygen atoms surrounding the Al ion lattice. This negative charge is neutralized by exchangeable countercations such as Na^+, K^+, Mg^{2+}, etc. These cations are stabilized in the zeolite channels and can be easily removed by chemical treatments. One of the advantages of solid acids is that they possess specific acidic sites that differ markedly in their strength and nature[75, 76]. There are two types of zeolite acid sites, which are Brønsted (BAS) and Lewis acid (LAS) sites. A proton can be transported from the catalytic solid to the adsorbed molecule by means of Brønsted acid sites (BAS), while an electronic pair of an adsorbed molecule is accepted by Lewis acid sites (LAS) and thus a coordination bond with the surface is formed. These active sites are formed in the zeolite as shown in **Figure 1.10** by exchanging ammonium or multi-charge cations followed by a calcination process[77].

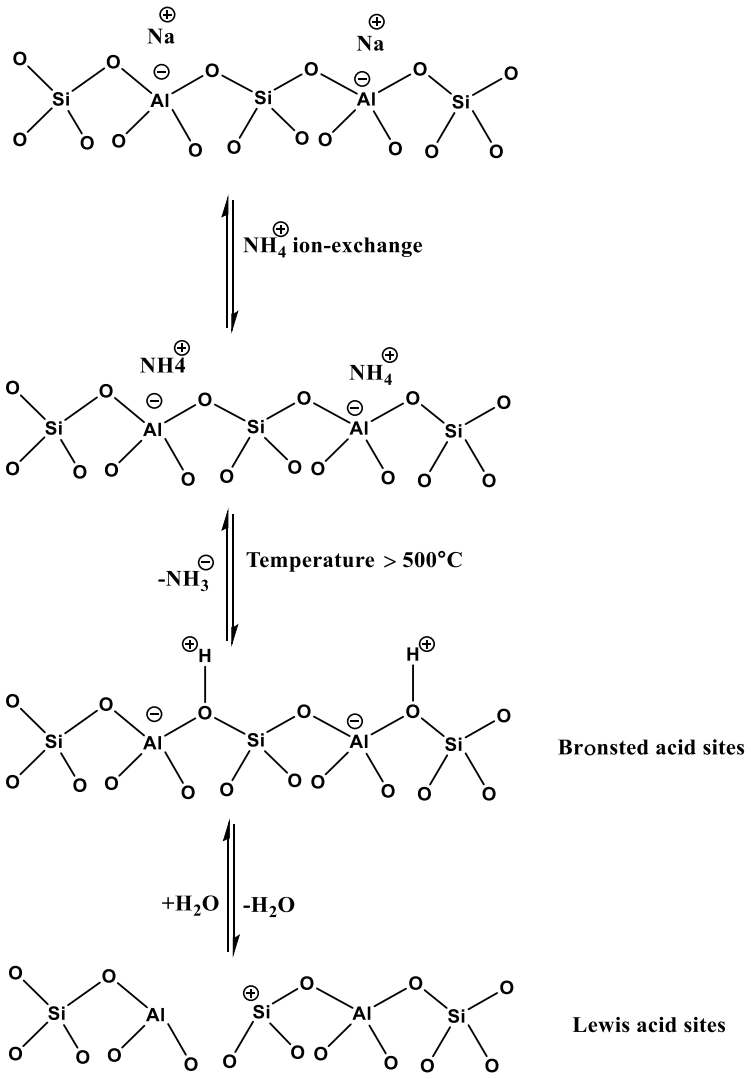


Figure 1.10. A schematic diagram of the formation of acidic sites in zeolite, Adapted from[78].

1.3.2.7 Conversion of hydrocarbons into olefins on ZSM-5

This section will highlight some of the results obtained in the catalytic cracking process of hydrocarbons using ZSM-5 zeolite focusing on the most important methods applied to improve the performance of ZSM-5 zeolite and increase the selectivity toward light olefins.

Afroukhteh-Langaroudi *et al.*[79] have investigated the catalytic cracking of *n*-hexane and *n*-heptane as model compounds for light naphtha over H-ZSM-5 with two SiO_2/Al_2O_3 ratios (i.e., 50 and 300) at different temperatures 500, 550 and 600°C. When the reaction temperature was increased, the conversion of *n*-hexane and *n*-heptane cracking was 83-93% over the H-

ZSM-5 (50) and markedly higher than the cracking over H-ZSM-5(300) which was between 32% and 64%. The production of total olefins from *n*-hexane on H-ZSM-5(50) was between 17% and 34.4%, while H-ZSM-5(300) produced about 47.7 to 51.6% - when increasing the reaction temperature. On the other hand, the production of total olefins from *n*-heptane was from 19.8% to 27.7% for H-ZSM-5(50) and from 47.9% to 55.8% for H-ZSM-5(300). Higher selectivity values for propylene (19.5 %) and ethylene (31.0 %) from *n*-hexane were obtained over H-ZSM-5 (300) at 600℃ compared to ZSM-5(50) (i.e., 14.3% for ethylene and 15.4% for propylene). Whereas the selectivity values for propylene and ethylene from *n*-heptane cracking over H-ZSM-5(300) (i.e., 20.4% for ethylene and 28% for propylene at 600℃) were markedly higher that those (i.e., 9.9% for ethylene and 13.7% for propylene) for H-ZSM-5 (50).

Kubo *et al.*[80] have studied the catalytic cracking of *n*-heptane over H-ZSM-5 with various Si/Al ratios using a fixed-bed reactor at 450-650℃ under atmospheric pressure. They noticed that a higher temperature enhances the yield for ethylene + propylene. They also found the higher yield for ethylene + propylene was 59.7% at 650℃ over H-ZSM-5 (Si/Al = 31) while the ratio of propylene to ethylene was 0.72 at 99.6% *n*-heptane conversion. They concluded the monomolecular reaction is dominant for catalytic cracking of heptane at a high temperature (i.e., 650℃).

Tarighi *et al.*[81] studied the catalytic cracking of *n*-heptane and the effect of the reaction temperature and the catalyst-to-feed (C/F) ratio on ZSM-5. The cracking tests were done at 500, 550, and 600℃ and atmospheric pressure in a fixed bed. **Table 1.2** below shows the results obtained from the effect of the reaction temperature on catalytic cracking of *n*-heptane over ZSM-5 zeolite at 500, 550 and 600°C and catalyst-to-feed = 3. The selectivity of ethylene and total olefins improved with rising temperature while propylene selectivity remained stable.

Table 1.2. The conversion and selectivity for catalytic cracking of *n*-heptane over ZSM-5 at different temperatures and C/F=3 (Reproduced from[81]).

				Selectivity (wt.%)				
Catalyst	*T (℃)*	*Conv. (wt.%)*	*Dry gas*	*Ethylene*	*Propylene*	*Butenes*	*Total olefins*	*Total alkanes*
ZSM-5	500	32.1	2.1	11.4	28.2	8.3	47.9	50.0
	550	53.9	3.7	18.5	28.3	6.3	53.1	43.4
	600	57.4	4.4	20.4	28.0	7.4	55.8	39.8

On the other hand, they also investigated the *n*-heptane cracking reaction over ZSM-5 at different catalyst-to-feed (C/F) ratios (i.e., 0.5, 1.5, and 3 by weight) at 550℃, the catalytic results are listed in **Table 1.3**. According to results in **Table 1.3**, the increase in the C/F ratio did not have a large effect on the total olefins and alkanes selectivity, although it did affect the *n*-heptane conversion.

Table 1.3. The conversion and selectivity of catalytic cracking of *n*-heptane over ZSM-5 at different catalytic-to-feed (C/F) ratio and 550℃ (Reproduced from[81]).

				Selectivity (wt.%)				
Catalyst	*C/F (g/g)*	*Conv. (wt.%)*	*Dry gas*	*Ethylene*	*Propylene*	*Butenes*	*Total olfins*	*Total alkanes*
ZSM-5	0.5	9.7	4.3	12.0	34.9	10.4	57.6	38.4
	1.5	36.3	2.7	12.4	31.7	9.2	53.3	43.4
	3	53.9	3.7	18.5	28.3	6.3	53.1	43.4

The catalytic cracking of liquefied petroleum gas (LPG), which consists of 46.8% propane, 30.3% *n*-butane and 21.6% iso-butane, over H-ZSM-5 catalyst with different framework aluminum (Al nitrate and Al hydroxide) at various reaction temperatures (500, 550, 600, and 650℃) and a weight hourly space velocity (WHSV) of 250 ml.(min g^{-1}) was

investigated by Abbasizadeh *et al.*[2] in a fixed bed reactor. They concluded that the LPG conversion enhanced from 55.8-56.4% to 90.4-92.7% over two types of H-ZSM-5 when the reaction temperature increased from 500℃ to 650℃. Moreover, the yield of light olefins increased from 10.7-12.8% to 24.1-26.0 for ethylene, 8.9-10.9% to 22.2-23.0% for propylene, and from 1.05-1.26% to 2.04-2.28% for butene with an increase in temperature.

At the same time, they also looked into the kinetic modeling of LPG over two types of H-ZSM-5 with different Al frameworks using Langmuir-Hinshelwood-Hougen-Watson theory (LHHW) at 500-650℃CAt the beginning of cracking reaction of LPG over H-ZSM-5, the monomolecular (protolytic) cracking of the C-C bond was dominant. The reaction of the active proton with the olefins resulting from the cracking process decreases when the Brønsted acid sites (BAS) of H-ZSM-5 are in single positions. In contrast, the undesired and heavy products are formed when the BAS are close (Al atoms are close), increasing the hydrogen transfer and isomerization reactions.

Konno *et al.*[82] investigated the catalytic cracking of *n*-hexane, cyclohexane, and methylcyclohexane, which represent part of the hydrocarbons in naphtha, over H-ZSM-5 with a Si/Al ratio of 150 using a fixed-bed reactor at reaction temperatures ranging from 550℃ to 650℃ under atmospheric pressure and the amount of catalyst to feed rate (W/F) 0.125 $g.h^{-1}$ for four hours and half. **Table 1.4** shows the results of catalytic cracking of different feedstock.

Table 1.4. The conversion, olefin selectivities, and olefin yields over H-ZSM-5 (Si/Al=150) for *n*-hexane, cyclohexane, and methylcyclohexane. (Reproduced from[82])

Reactant	*Conversion (mol.%)*	*Selectivity for olefins (mol.%)*	*Yield (mol.%)*		
			Propylene	*Ethylene*	*Butenes*
n-hexane	83-79	55	25	18-13	< 5
cyclohexane	73-30	55-63	22-13	16-3	< 5

methylcyclohexane	78-13	50	9-1	17-4	1

In another study, Konno *et al.*[83] scrutinized the catalytic cracking of *n*-hexane, cyclohexane, and methylcyclohexane over macro-H-ZSM-5 using a fixed-bed reactor at 650℃ and atmospheric pressure for 260 min and 0.25 h of catalyst to feed rate (W/F). At the beginning of the reaction, they obtained the highest conversion values for model naphtha, which were about 95% and decreased with a time-on-stream (TOS) to 70%. The olefin yield increased with TOS from 17 mol.% to 21 mol.% for propylene and from 2 mol.% to 5 mol.% for butene. By contrast, the ethylene yield decreased from 21 mol.% to 13 mol.% with TOS and the amount of coke was 17.0% after 260 min.

Under the same conditions, they studied the effect of nano-H-ZSM-5 (a zeolite with particle size below 100nm) on the catalytic cracking of cyclohexane and methylcyclohexane. The methylcyclohexane has the highest conversion of 100% during the whole time on stream, while *n*-hexane conversion lies at about 90%. The olefin yield was stable at 30 mol.% for propylene and 5 mol.% for butene, while the ethylene yield reduced slightly from 22 mol.% to 19 mol.% with time-on-steam (TOS). The total amount of coke over nano-H-ZSM-5 was reduced to 2.9% compared to 17% for macro-ZSM-5. By comparing the results between nano and macro H-ZSM-5, they concluded the nano-ZSM-5 was active and stable and produced a high yield of light olefins, which clearly indicates the pore size and hence the product diffusion plays an essential role in producing olefins.

The catalytic cracking of 1-hexene over ZSM-5 with different Si/Al ratios (i.e., 15 and 140) was examined by Blay *et al.*[29] in a fixed-bed reactor (made of quartz glass) at 500℃ and 1.06 bar. They did the study using several shorter contact times weight hourly space velocity (WHSV) as shown in **Table 1.5**. When growing the contact time over ZSM-5 (140), the conversion and olefin yields were improved.

Table 1.5. The conversion, and olefin yields over ZSM-5 (Si/Al=15 and 140) for 1-Hexene. (Reproduced from[29])

Catalyst	*WHSV^{-1}(s)*	*Conv. (%)*	*Yield (mol. %)*			
			C_2H_4	*C_3H_6*	*n-C_4H_8*	*i-C_4H_8*
ZSM-5(15)	0.7	32.9	5.7	28.6	6.8	3.6
	1.3	48.8	8.2	41.3	12.4	7.5
	2.5	73.2	17.1	66.8	18.5	10.7
	4.8	89.6	22.9	72.2	22.5	14.3
ZSM-5(140)	5.0	41.8	5.8	59.4	5.7	2.7
	10.0	63.1	7.7	69.6	12.1	6.6
	19.9	80.4	10.5	85.9	17.3	10.5
	39.8	92.1	13.7	91.8	23.9	14.9

Mohiuddin *et al.*[84] examined the catalytic cracking of naphtha over H-ZSM-5 with SiO_2–to-Al_2O_3 molar ratio of 30. They use a stainless steel fixed-bed reactor at 550℃, atmospheric pressure, and a weight hourly space velocity (WHSV) of approximately 16 h^{-1} for 7 hours. The H-ZSM-5 catalyst showed the greatest initial conversion of 56% during the third hour of reaction and declined to ~ 48% with time-on-stream (TOS). Moreover, the selectivity for ethylene lessened with TOS from 9.0% in the third hour to 2.0% for ethylene and 20.8% to 12.6% for propylene. In contrast, butene selectivity improved with TOS from 7.6% in the third hours to 11.7% in the last hours.

Hou *et al.*[85] recently analysed the catalytic cracking of *n*-pentane using H-ZSM-5 zeolites with a Si/Al ratio of 12.5. The feed was pumped into a stainless steel tube by a syringe pump at atmosphere pressure and weight hourly space velocity (WHSV) of 3.7h^{-1}. The reaction test was conducted first at different reaction temperatures from 400 to 550℃ to characterize the activity. They found the conversion improved from 6.3% to approximately 63%, and the yield of ethylene and propylene (E+P) grew from 3.3 wt.% to about 37 wt.% when the reaction

temperature was increased. The selectivity of light olefins at 450℃ was 16.1 wt.% for ethylene, 36.1 wt.% for propylene, and 10.6 wt.% for butene. Furthermore, they examined the lifetime of catalyst at 550℃ for 12 hours on stream. The rate of *n*-pentane conversion declined gradually over H-ZSM-5 with time-on-stream (TOS) from 62.5 to 45.4%. Also, the yield of ethylene and propylene (E+P) was gradually reduced from about 38 wt.% to about 28 wt.% with time-on-stream (TOS), and the coke amount was 14.9 mg after 12 hours on stream.

1.3.2.8 Conversion of hydrocarbon into olefins on modified ZSM-5

There are several methods to modify zeolites in order to improve olefin production. The methods to modify ZSM-5 are given below[4]:

1. Treatment with phosphorus,
2. Loading a rare-earth, alkali metals and/ or alkali earth metals into ZSM-5 in suitable amounts,
3. Loading of transition metals into ZSM-5,
4. Creating hierarchical pore structures in ZSM-5 by steaming, alkaline treatment, and acid leaching.

This section will be highlight some of the most relevant results in the catalytic cracking process of hydrocarbons on modified ZSM-5 zeolites.

The acidity of the modified catalyst must be considered when using a ZSM-5 additive to boost light olefin production. It was discovered that changing the Si/Al ratio in ZSM-5 significantly impacted light olefin production [86, 87]. The majority of hydrogen transfer reactions in ZSM-5 occur on the surfaces of the catalysts. These reactions are more evident at low Si/Al ratios with high acidity. The hydrogen transfer process produces fewer light olefins and lower molecular weight hydrocarbons such as ethane and methane. The zeolite's overall acidity and stability are also altered *via* the hydrothermal deactivation approach.

Several factors such as the loading of metals or phosphorus over ZSM-5, the temperature of catalyst calcination, and preparation method (e.g., Ion exchange, impregnation)[8, 33, 88] can influence the stability (or durability) and structure of the catalyst. For instance, according to Wattanapaphawong *et al.*[8] and to van der Bij *et al.*[89], the optimum phosphorus loading is 1% to get a robust catalyst and increase the yield of light olefins.

Phosphate modification is widely used technique for enhancing the stability and performance of ZSM-5 zeolite[90]. Phosphate stabilises Al^{3+} ions in the lattice, decreasing Al loss from the zeolite framework. Additionally, it inhibits structural changes, giving a high hydrothermal stability to ZSM-5 catalysts[91]. Moreover, phosphate modified ZSM-5 zeolite retains more significant acidity than ZSM-5 zeolite when subjected to intense hydrothermal conditions[89]. Phosphate treatment generally entails impregnation with less acidic ammonium phosphates as well as an additional phosphate source (usually a solution of H_3PO_4). This is followed by a calcination step between 450 and 650°C and drying process at 70-120°C for 1 to 6 hours. The interaction between the zeolite structure and phosphate species seems independent of the phosphate supply. On the other hand, the impact of treatment on activity is highly reliant on characteristics such as the Si/Al ratio, the Al/P ratio, the activation conditions, and the crystal size of the zeolite[92, 93].

Notably, excess phosphate utilised during treatment is deposited as polyphosphates on the exterior surface of ZSM-5 crystals. Any aluminium that is displaced during heat treatment may react with any accessible phosphate to generate amorphous aluminophosphate. In most of the cases, ZSM-5 additions will have an alumina binder. The binder and the excess phosphate will subsequently react, resulting in the production of an aluminophosphate species, which can help in stabilizing the system. The addition of phosphate to ZSM-5 zeolite reduces ZSM-5 Brønsted acidity, increasing the synthesis of light olefins[8, 91, 94].

When transition metal compounds are incorporated into ZSM-5 zeolite the resulting material presents bifunctional properties owing to the generation of additional Lewis acid sites. Combining Lewis sites for paraffinic feedstock dehydrogenation and Brønsted acid sites for olefin cracking can boost light olefin yield[95]. Lewis acid sites seem to primarily accelerate C-H dissociation and dehydrogenation by boosting recombination and desorption of hydrogen, while Brønsted acid sites appear to enhance C-C cracking events. The addition of trace amounts of Fe compounds to ZSM-5 improves both the activity and selectivity of the isobutane cracking reaction. Lu *et al.*[96] studied the effect of loading different small amount of Fe oxide over H-ZSM-5 to produce light olefins from catalytic cracking of isobutane. The catalytic cracking of isobutane was carried out in a fixed bed reactor at 625℃. They remark that the inclusion of a trace quantity of Fe (0.01 mmol. g^{-1}) results in a total yield of olefins, ethylene, and propylene of 65.6%, 24.6%, and 32.4%, respectively, when compared to unmodified H-ZSM-5 zeolites (i.e., 55.5% total olefins, 21.3% ethylene, and 25.1% propylene). This is due to the fact that a trace quantity of Fe will alter the acidity of the H-ZSM-5 catalyst. It also facilitates the dehydrogenation of isobutane.

Lu *et al.*[97] studied the catalytic cracking of isobutene in a fixed-bed reactor at 575℃ over H-ZSM-5 with different Si-to-Al ratios and modified with 0.010 mmol g^{-1} Fe^{3+} and 0.004 mmol g^{-1} Cr^{3+}. They found the conversion of isobutene over H-ZSM-5 and modified H-ZSM-5 was similar at ~ 99.5% when the ratio of SiO_2/Al_2O_3 was less than 50. However, the conversion slightly declined to ~ 98% when the SiO_2/Al_2O_3 ratio was 50. When increasing the SiO_2/Al_2O_3 ratio to 150 the conversion over H-ZSM-5 rapidly reduced to ~ 95.5% but improved to ~99% over Cr-Fe-modified HZSM-5. On the other hand, the yield of total olefins for H-ZSM-5 and modified HZSM-5 was ~ 47% and 49%, respectively when the ratio of SiO_2/Al_2O_3 was below 50. While the overall yield of olefins over modified H-ZSM-5 rapidly improved to ~ 58% when the ratio of SiO_2/Al_2O_3 was 50 and stayed stable at this value when

increasing the SiO_2/Al_2O_3 ratio to 150. On the contrary, the total yield of olefins rose to 56% over H-ZSM-5 (SiO_2/Al_2O_3 =50) and then it rapidly dropped off to 50% on increasing the SiO_2/Al_2O_3 ratio to 150. They concluded that a small amount of Fe and Cr played a prominent role in improving the total yield of olefins over H-ZSM-5 with a high Si to Al ratio.

In another study, Mohiuddin *et al.*[84] assessed the catalytic cracking of naphtha over H-ZSM-5 (SiO_2/Al_2O_3=30) modified with different loadings (0.5-5 wt%) of Fe and Cr at 550℃ using a fixed bed reactor. They obtained the highest propylene selectivity (i.e., 23.6%) and 61.3% total olefin selectivity over 2% Fe-HZSM-5 catalyst. Furthermore, neraly 65% selectivity to aromatics (BTX) over 2% Cr/HZSM-5 was obtained. This indicates that Fe and Cr are good promoters of the formation of propylene (Fe) and BTX compounds (Cr) and also enhance the ZSM-5 catalyst's stability.

The ZSM-5-type zeolite are convenient cracking catalysts for producing light olefins from a variety of feedstocks such as *n*-hexane, *n*-heptane, and light naphtha, among others. The modification of zeolite with phosphorous leads to an increase in the selectivity for light olefins and to high hydrothermal stability of the zeolite by stabilizing the of aluminium ions and thereby preventing structural ZSM-5 changes. Furthermore, the Brønsted acidity (BAS) of the ZSM-5 decreases when modification with phosphorus through reacting with the acid sites of zeolites[8, 88, 89, 94, 98-101].

Additionally, the incorporation of rare-earth, alkali metals and/or alkali earth metals and also the addition of some transition metals affects the acid properties of zeolites, reflected in the enhancement of the formation of olefins [36, 98, 102-105].

Metal oxides such as Co, Ni, Fe, Cu, V, and Cr enhance the ZSM-5 catalytic perfromance toward the production of light olefins, specifically the utilization of Cr, and Fe oxides[84, 106-110]. Small amounts of chromium and iron on zeolite enhances the reactivity of catalytic cracking of hydrocarbons, which produces high activity and high selectivity towards

light olefins.[97, 111]. These metals change the acidity distribution in zeolite by improving the active centres[112, 113]. Interestingly chromium oxide also reduces coke formation, improving catalyst life[114].

1.3.3 Industrial production of light olefins via catalytic cracking

Currently, approximately 30% of world propylene production is via fluid catalytic cracking (FCC). It is considered one of the oldest and largest industrial processes which started in 1939 and culminating in 1942 when refineries started to use it[115]. It is the second-largest source of light olefins in the world after steam cracking[4, 116]. The catalytic cracking features product control, unlike non-catalytic routes[38]. Heat and catalysts play a significant role in the FCC process as heavy crude oil components are broken down into lighter and more useful products such as diesel, gasoline, olefin, and alkane. **Figure 1.11** shown the feeds used for the FCC unit, such as vacuum gas oil (VGO), vacuum residue (VR), atmospheric residue (AR), and even deasphalted oil blended with VGO.

All the feedstock type is a fraction of crude oil with a heavy boiling point range of 330 to 550°C[4, 116].

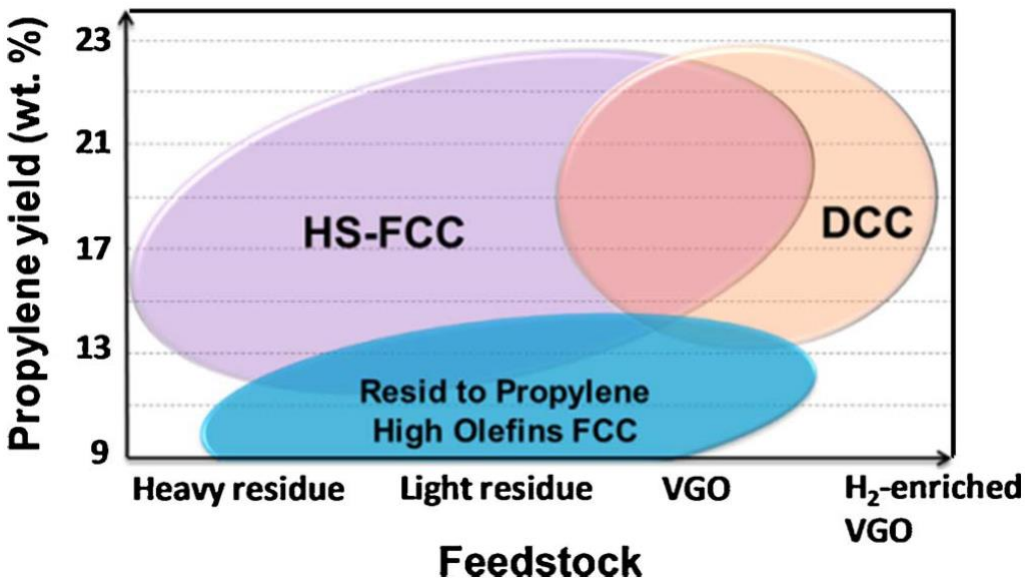


Figure 1.11. Propylene yield based on the type of feedstock in FCC unit. Adapted from[4].

Saudi Aramco and their partners developed Resid FCC and high-severity fluid catalytic cracking (HS-FCC) technology to deal with feeds with high contents of asphaltenes and metals. In contrast, deep catalytic cracking (DCC), which was developed based on a normal riser cracking process by a Chinese research institute, and the conventional FCC process are used for lighter feeds[4, 117].

Figure 1.12 shows the configuration of FCC technology including catalyst regenerator, reactor, and the distillation/separation sections. The cracking reaction is an endothermic process. The heat required to break down the products is produced by burning a small portion of the feedstock in a regenerator[46]. The catalyst is heated to a temperature between 480℃ and 570℃. In contrast, the feedstock is heated at a temperature between 260℃ and 425℃ before the feedstock is combined with the catalyst. The combination of hot catalyst and feedstock occurs in the lower part of the riser reactor. The ratio of the catalyst to oil is more than one during fusion in the riser, while the typical ratio is about 6, and the residence time is less than one second. The catalyst cracks the reactants after combination, and this process produces gases

and oil. The feedstock/catalyst mixture is transported at a time of less than a second to the riser reactor and rapidly achieves high temperatures to generate gaseous and liquid products. The catalyst and the residual/suspended oil are then separated from the product mixture by steam treatment at the top of the riser reactor where the temperature has dropped to 500℃. The products are transferred to the distillation column for separation, where the olefins are separated from the liquid fuel. The spent catalyst is continuously reused and generated through the regeneration device in which the carbon (or coke) deposited on the catalyst during the cracking process is removed. The catalyst is reactivated at a maximum temperature of 760℃ in the presence of an adequate amount of oxygen to burn off and remove the carbon as carbon dioxide[4, 46].

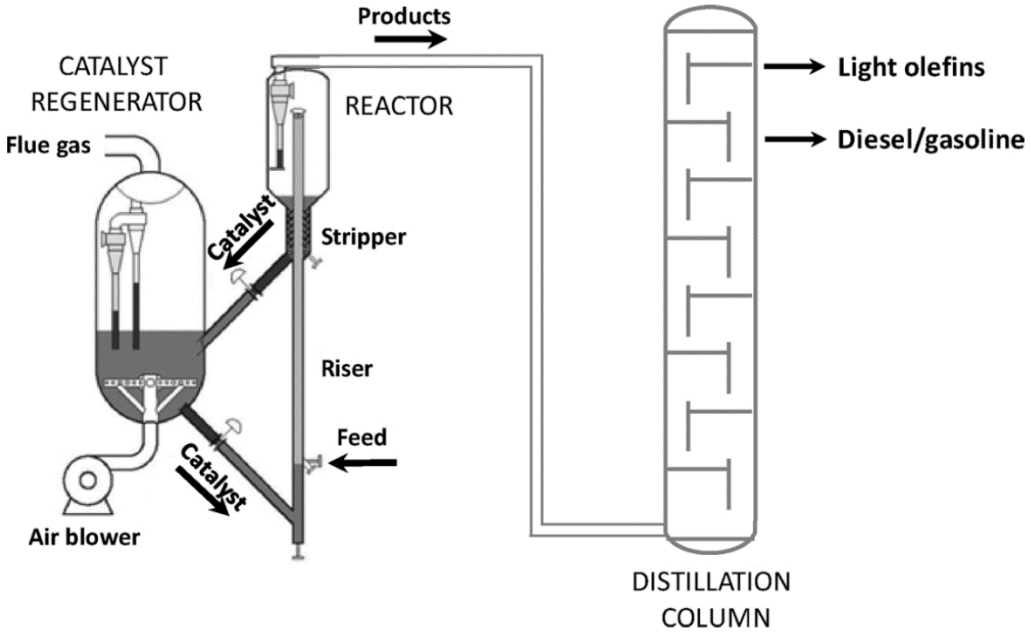


Figure 1.12. Diagrammatic representation of FCC reactor and regenerator. Adapted from[4].

1.3.3.1 Material and composition

As discussed below, a suitable catalyst for the FCC process must have various chemical and physical properties to enable the cracking of C-C bonds of hydrocarbon molecules to the required products, the catalyst must have acid characteristics[7, 46, 118]. The catalyst needs to be

stable at high temperatures and steam partial pressures. It must also have large pore diameters with acid sites able to break bigger molecules and get access to smaller pores during fluidization. Furthermore, the catalyst components must be available in a form that allows fluidization in the regenerator and form the least amount of coke at the high cracking activity of heavy feedstock so that the catalyst remains active during the reaction.

The first catalyst employed for the FCC process was made of clay. In the 1940s, catalysts based on SiO_2–Al_2O_3 or SiO_2–MgO were discovered and significantly improved compared to the performance of natural clay catalysts[34, 46]. The KVO_3-impregnated Al_2O_3 catalyst was also utilised to produce light olefins through naphtha cracking[119]. The KVO_3/Al_2O_3 catalyst increased ethylene yield and propylene output by 10 and 5%, respectively. The coke formation rose when the reactor's axial length and reaction temperature were raised. The deposition of coke on the catalyst surface was prevented by adding KVO_3. The decreased coke deposition caused by these catalysts is attributable to the coke gasification by KVO_3 and an increase in the CO_x content in the gas phase products. Lee *et al.*[120], employed KVO_3-B_2O_3 as the catalyst, which was supported on SA5203 comprising mostly Al_2O_3 and around 12% glassy silica as a binder. Mukhopadhyay and Kunzru[121] investigated the catalytic cracking of naphtha using calcium aluminate ($12CaO\text{-}7Al_2O_3$) catalysts in a fixed-bed reactor operation at 760-820℃ and atmospheric pressure. The addition of K_2CO_3 greatly reduced coke production and also lowered the selectivity for hydrocarbons (such as ethylene, propylene) relative to the potassium modified catalyst.

However, the most significant progress occurred in the early 1960s with the invention of zeolite Y, which outperformed all previous catalysts. This catalyst resulted in a significant increase in the production and quality of gasoline yield. Since then, Zeolite Y has been the primary component of FCC catalysts in different enhanced forms [34].

FCC catalysts comprise a combination of an active component (zeolite), a matrix (amorphous silica-alumina) and a binder (bentonite clay), and a filler catalyst as shown in **Figure 1.13**[5, 7, 34, 122-124]. The major active catalyst in this formulation is ultra-stabilized zeolite Y (USY), which is made up of spherical particles properly designed for a fluidized circulation reactor. The zeolite crystals alongside clay particles are dispersed into the matrix. Large voids and pores in the spherical particles are required for mass transport of the heavy feedstock. Physical and catalytic roles are combined in the catalyst matrix (amorphous SiO_2–Al_2O_3 or SiO_2–MgO)[7], providing particle integrity and attrition resistance which also plays the function of heat transfer medium and enables hydrocarbon diffusion into and out of the catalyst microspheres. The matrix also acts as a catalyst, affecting reaction pathways, catalyst activity and selectivity, product quality and poison resistance. The catalyst's physical strength is provided by the binder (bentonite clay) and filler. They also have high heat capacity, which is necessary for balancing matter in the catalyst and conducting enough heat from the regenerator to riser[7, 122]. Although the as-prepared zeolite is not particularly stable at hydrothermal conditions, the use of USY zeolite overcomes this issue. Another approach is the introduction of rare earth (RE) ions into the zeolite Y. Both above-described methods enhance the catalyst's activity and the hydrothermal stability [7, 46].

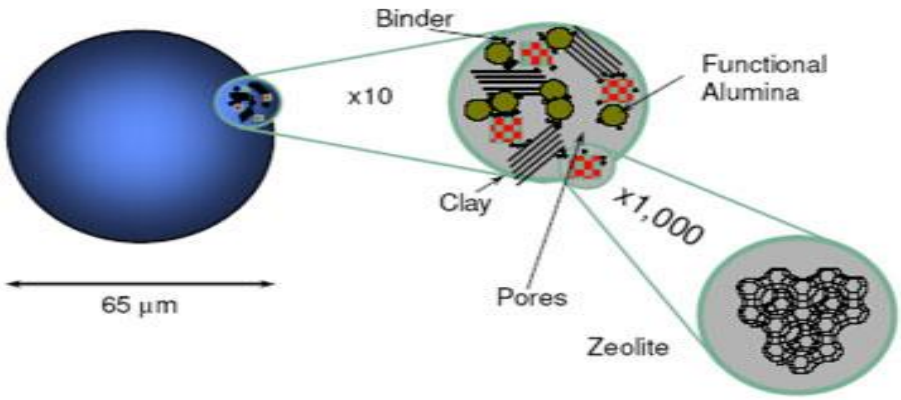


Figure 1.13. Schematic representation of FCC catalyst formulation, adapted from[34].

1.3.3.2 ZSM-5 as a propylene yield-increasing additive in FCC catalysts

ZSM-5-based additives have been utilised in the FCC process to improve the gasoline octane number since the 1980s. It is now commonly used as an FCC additive to increase the output of light olefins, particularly propylene[125]. The ability of the ZSM-5 based zeolite catalyst to increase gas octane number and light olefin selectivity has been well-documented in the literature[118, 126, 127].

ZSM-5 preferentially breaks the C-C bonds of FCC feedstock into light olefins (C2–C5), mostly propylene due to its unusual shape selectivity and medium pore size distribution. On the other hand, the octane number of gasoline increases since it contains more aromatics and less paraffin[5]. Initially, FCC feedstocks are converted over a HY zeolite-based catalyst to produce gasoline-range olefins. The large pore structure of HY zeolite promotes hydrogen transfer processes and bimolecular cracking, resulting low production of light olefins[128]. Consequently, ZSM-5 based catalysts are used as an additive to commercial Y zeolite FCC-base catalyst. The ZSM-5 zeolite content within the catalyst body is determined by the feedstock composition, desired products, and process operating conditions.

ZSM-5 is a shape-selective microporous material able to crack linear and low-octane gasoline pool compounds selectively into light olefins (C_2–C_5) and particularly propylene [5, 129]. ZSM-5 converts gasoline into light olefins through cracking because it inhibits hydrogen transfer reactions that typically result in undesirable gasoline-range paraffins cracking.

Nguyen *et al.* recently investigated the effect of the La/Al ratio (La/Al = 0.25, .05, and 1.0 molar ratios) over ZSM-5 in the cracking of vacuum gas oil (VGO) to propylene production at 520°C and catalyst-to-oil ratio 2 using a short contact time micro activity testing unit (SCT-MAT)[103]. They found the 1La-ZSM-5 and H-ZSM-5 exhibit similar propylene yields (i.e., 13.9 wt.%) due to the similar specific BET area and NH_3-TPD profiles, while the other samples produced lower propylene yields.

Fresh sample characterization data suggested that using a lower La concentration might result in improved La ion interaction with the ZSM-5 framework. The reduction in micropore surface area after adding La might be a key factor in the successful integration of La cations into the ZSM-5 framework.

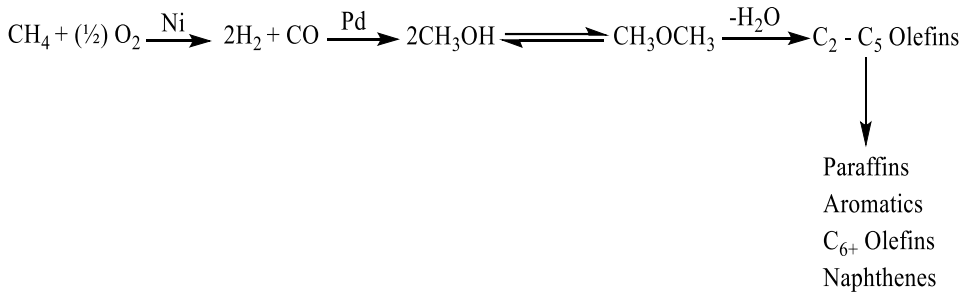
The addition of alkali and/or alkali earth metal oxo species into the ZSM-5 alters the acidic property not only by decreasing the population of acid sites but also by weakening the strength of those that remain. The acidity measurements through NH_3-TPD over alkaline earth modified HZSM-5 catalysts confirm the strong modification of acid sites to weak acid sites when alkaline earth cations are incorporated into ZSM-5. Furthermore, this can also hinder the hydrogen transfer reactions and thereby enhancing the light olefins production[130, 131]. Importantly, the zeolite crystal structure collapses when it is treated with strong alkali solutions and produces amorphous materials containing very small acid sites and macrospores[95, 132]. The use of weak alkali solutions leads to the dissolution of small quantities of alumina and silica thus creating mesoporous structures.

1.4 Other processes to produce light olefins

1.4.1 The Methanol to Olefins Process

Methanol is a significant chemical building block and is used in the manufacture of chemicals such as formaldehyde, methyl tert-butyl ether (MTBE), acetic acid and a wide range of other chemical products. Methanol is produced from natural gas and then converted into light olefins that can be employed subsequently as precursors for further chemistry. Methane is first incompletely converted to syngas in an endothermic process using steam to lessen coking during the reaction. The unreacted methane is then converted exothermally to syngas by using oxygen at high temperatures. The syngas from those two phases is converted to methanol through an exothermic synthesis process at around 200-280°C. A part of the methanol

is converted into dimethyl ether (DME) and water. The resulting DME can be converted into light olefins at a temperature of 600 °C and a pressure of 1-3 bar[62, 133-135].



(1-7)

The conversion of methane into syngas via steam reforming is an endothermic reaction that is usually accomplished on a Ni catalyst at high temperatures (800-1000ºC) and pressures (3-10 bar) with methane conversions close to 100%.

The synthesis of methanol from syngas is an exothermic reaction and the conversion is equilibrium limited with a maximum conversion of syngas to methanol of about 25 %. The reaction can be carried out at a temperature and pressure of 250–300°C and 50–150 bar, and the catalyst for the reaction is usually $Cu/ZnO/Al_2O_3$ [136].

Several catalysts such as zeolites and silica alumina-phosphate (SAPO) have also been used for producing olefins from methanol. ZSM-5 and SAPO-34 have showed high selectivity and excellent catalytic performance for the production of olefins. They have attracted a lot of interest from researchers to enhance their catalytic properties and hence the selectivities for light olefins [137-141].

1.4.2 Oxidative Coupling of Methane

Natural gas conversion to more valuable fuels and chemicals has grown in popularity as low-cost conventional and shale natural gas sources become more widely available. More than 90% of natural gas is methane and the remaining compounds correspond to light hydrocarbons and other components including some sulphur compounds. Exactly 40 years ago,

Keller and Bhasin[142] suggested the possibility of conjugating two molecules of methane by oxidation to produce ethane and ethylene.

$$2CH_4 + (1/2)\ O_2 \longrightarrow C_2H_6 + H_2O \qquad (1\text{-}8)$$

$$2CH_4 + O_2 \longrightarrow C_2H_4 + 2H_2O \qquad (1\text{-}9)$$

Methane is a very stable molecule because it lacks a functional group that would assist its chemical reactivity. It is preferable for the reaction to be conducted in a cyclic mode. In the first step of this reaction, methane is isolated from natural gas and cleaned of impurities before mixing with oxygen. The reaction between methane and oxygen is catalyzed by alkali metals (Group 1) and the alkaline earth metals (Group 2) of the Periodic Table and creates methyl radicals ($\cdot CH_3$) and water. Due to the high reactivity of methyl radicals, they combine to form alkanes, specifically ethane. Ethane is then converted to ethylene by dehydrogenation. On the other hand, it is possible to co-feed both methane and oxygen to the catalyst as studied by Ito *et al.*[143] using Li- doped MgO catalysts. These have the highest activity for converting methane to ethylene in the presence of O_2. It is worth remarking that the introduction of chlorine into the stream of reactants markedly enhances the ethylene yield[144].

Despite all the research that has attempted to develop the oxidative coupling process for methane (OCM), it suffers from major obstacles that prevent its industrial implementation. Two critical disadvantages are: (1) the high temperature required to break a strong C-H bond (about 439 kJ/mol)[145] to activate methane. [62, 145-147]. Catalysts may reduce reaction temperatures to about 800°C and below, even though they are still considered high-temperature processes and require a robust reactor design. (2) The limited selectivity for ethylene production. Furthermore, even a little increase in oxygen content may cause the exothermic process to shift toward CO and CO_2. Another issue to consider is the kind of oxygen supply (pure oxygen or

air). The creation of an industrially dependable and stable catalyst, as well as the operation of the reaction at low temperatures, are the major goals of OCM research[148].

1.4.3 Paraffin Dehydrogenation

As the demand for propylene has increased hydrogen removal technology has received considerable attention from researchers. Four technologies are commercially available for propane dehydrogenation. These are CATOFIN from ABB Lummus, Oleflex from UOP, Fluidized Bed Dehydrogenation (FBD) from Snamprogetti, and Steam Active Reforming (STAR) from Phillips Oil. Related technology can be utilized for ethane dehydrogenation, but an economically attractive commercial reactor has not yet been created[149-151].

Dehydrogenation technology requires high temperatures, which is the main drawback of this technique. This catalytic process needs many steps to separate the desired products when this technology is working at low temperatures. Therefore, it is necessary to recycle a large amount of unreacted paraffin to obtain the required final product in a large amount. Researchers are focusing on finding solutions to overcome these problems and have proposed using membrane systems to obtain desired products at low temperatures[152]. Others, have attempted to remove hydrogen by oxidation to achieve a balance during the reaction and allow reaction under more moderate temperatures[153]. However, there are no commercial factories currently operating with these solutions.

1.5 Scope of the thesis

The goal of my DPhil project is to explore novel catalytic systems based on combinations of ZSM-5 zeolite and metal oxides to produce light olefins through the catalytic cracking of the high molecular weight hydrocarbons present in naphtha.

The aim is to understand fully the fundamental processes occurring in the catalytic cracking of naphtha. Accordingly, zeolite catalysts with different SiO_2/Al_2O_3 ratios have been first evaluated in a fixed-bed unit at 550°C. The cracking performances of the zeolites to produce light alkenes are examined using *n*-heptane as a model compound as it constitutes the main component of light naphtha.

The growing need for increasing the production of light olefins, has created new opportunities to develop zeolite-based catalysts for cracking naphtha to high-value products, particularly propylene. The most active and common catalysts for hydrocarbon cracking are solid proton-donor acids, including zeolites, which are the key components of industrial cracking catalysts. In fact, H-ZSM-5 is the most efficient catalyst for naphtha cracking to light olefins. Several factors affecting the light olefin production include the activity of H-ZSM-5, such as the zeolite acidity, Si/Al ratio, and the temperature of the reaction system.

The need for light olefins on a worldwide scale, and worries about the sustainability of their production, led researchers to explore an alternative, environmentally friendly technology that may satisfy this need while protecting the environment. This study focuses on the production of high-quality light olefin by the catalytic cracking of light naphtha utilising a hybrid kaolin-zeolite (H-ZSM-5) catalyst in a fixed-bed reaction configuration. The objective is to develop a new technology with the potential to convert *n*-heptane (which will serve as a model compound) and naphtha (which will serve as the industrial feedstock) into light olefins (ethylene, propylene, and butylene) and aromatics in a single-step reaction. The primary aim of this work is to design, develop, and improve highly selective solid catalysts for converting the relatively high molecular weight hydrocarbons that are found in naphtha into the required chemicals. In order to accomplish this goal, it is necessary to get a fundamental understanding of the processes that take place during the catalytic cracking of naphtha in order to devise a technique for the production of advanced cracking catalysts.

My studies will encompass all of these important aspects in an attempt to understand- and thence to optimise- the catalyst performance.

In summary, Chapter 1 discusses the methods to produce light olefins. Following this introduction, Chapter 2 covers the experimental techniques alongside the catalyst preparation, catalyst characterisation, as well as the process for catalytic reaction. The effects of Si/Al ratios in H-ZSM-5 zeolite and the preparation method for a chromium oxide-HZSM-5 catalyst with different loadings were examined on the catalytic cracking of *n*-heptane as model compound for light naphtha in Chapter 3. The influence of various metal oxides such as MgO, ZrO_2, TiO_2, SiO_2, Al_2O_3 and kaolin combined with a specific amount of H-ZSM-5 zeolite (i.e., 20 wt.%) on the catalytic cracking of *n*-heptane to produce light olefins was extensively investigated and discussed in Chapter 4. Chapter 5 comprehensively discusses the results obtained from the effect of various loading of H-ZSM-5 on kaolin on the catalyst activity of *n*-heptane and naphtha into light olefin whilst Chapter 6 embodies the overall conclusions of this research work based on the evaluation if different catalytic systems and the parent zeolite. A section of proposed future work followed by an Appendix is also given.

1.6 References

1. Akah, A.; Williams, J.; Ghrami, M., An Overview of Light Olefins Production via Steam Enhanced Catalytic Cracking. *Catalysis Surveys from Asia,* **2019,** *23* (4), 265-276.
2. Abbasizadeh, S.; Asadi, S.; Karimzadeh, R., Kinetic modeling of LPG catalytic cracking using Langmuir–Hinshelwood–Hougen–Watson theory. *Research on Chemical Intermediates,* **2019,** *45* (11), 5681-5703.
3. Kubo, K.; Iida, H.; Namba, S.; Igarashi, A., Selective Formation of Light Olefins by Catalytic Cracking of Naphtha Components over ZSM-5 Zeolite Catalysts. *Journal of the Japan Petroleum Institute,* **2018,** *61* (1), 10-19.
4. Alotaibi, F. M.; González-Cortés, S.; Alotibi, M. F.; Xiao, T.; Al-Megren, H.; Yang, G.; Edwards, P. P., Enhancing the production of light olefins from heavy crude oils: Turning challenges into opportunities. *Catalysis Today,* **2018,** *317*, 86-98.
5. Corma, A.; Corresa, E.; Mathieu, Y.; Sauvanaud, L.; Al-Bogami, S.; Al-Ghrami, M. S.; Bourane, A., Crude oil to chemicals: light olefins from crude oil. *Catalysis Science & Technology,* **2017,** *7* (1), 12-46.
6. Sadrameli, S. M., Thermal/catalytic cracking of liquid hydrocarbons for the production of olefins: A state-of-the-art review II: Catalytic cracking review. *Fuel,* **2016,** *173*, 285-297.
7. Akah, A.; Al-Ghrami, M., Maximizing propylene production via FCC technology. *Applied Petrochemical Research,* **2015,** *5* (4), 377-392.
8. Wattanapaphawong, P.; Reubroycharoen, P.; Mimura, N.; Sato, O.; Yamaguchi, A., Effect of carbon number on the production of propylene and ethylene by catalytic cracking of straight-chain alkanes over phosphorus-modified ZSM-5. *Fuel Processing Technology*, **2020,** *202*, 106367.
9. Ra, E. C.; Kim, K. Y.; Kim, E. H.; Lee, H.; An, K.; Lee, J. S., Recycling Carbon Dioxide through Catalytic Hydrogenation: Recent Key Developments and Perspectives. *ACS Catalysis,* **2020,** *10* (19), 11318-11345.
10. Wang, G.; Xu, C.; Gao, J., Study of cracking FCC naphtha in a secondary riser of the FCC unit for maximum propylene production. *Fuel Processing Technology,* **2008,** *89* (9), 864-873.
11. Yee, C.; Prasetiawan, H.; Hisyam, A.; Azahari, A.; Maharon, I., Sensitivity study of the propane dehydrogenation process in an industrial radial moving bed reactor. *Journal of Engineering Science and Technology,* **2015,** *10*, 62-74.
12. Al-Absi, A. A.; Aitani, A. M.; Al-Khattaf, S. S., Thermal and catalytic cracking of whole crude oils at high severity. *Journal of Analytical and Applied Pyrolysis,* **2020,** *145*, 104705.
13. Mao, R.; Yan, H.; Muntasar, A.; Al-Yassir, N., Blending of Non-Petroleum Compounds with Current Hydrocarbon Feeds to Use in the Thermo-Catalytic Steam-Cracking Process for the

Selective Production of Light Olefins. In *New and Future Developments in Catalysis*, Elsevier Inc., **2013**; pp 143-173.

14. Matar, S.; Hatch, L. F., Chemicals Based on Ethylene. In *Chemistry of petrochemical processes*, Second ed.; Gulf professional publishing: Elsevier, **2001**; pp 188-212.
15. Torres Galvis, H. M.; de Jong, K. P., Catalysts for production of lower olefins from synthesis gas: a review. *ACS catalysis*, **2013,** *3* (9), 2130-2149.
16. Ghashghaee, M.; Shirvani, S.; Kegnæs, S., Steam catalytic cracking of fuel oil over a novel composite nanocatalyst: Characterization, kinetics and comparative perspective. *Journal of Analytical and Applied Pyrolysis*, **2019,** *138*, 281-293.
17. Bereciartua, P. J.; Cantín, Á.; Corma, A.; Jordá, J. L.; Palomino, M.; Rey, F.; Valencia, S.; Corcoran, E. W.; Kortunov, P.; Ravikovitch, P. I., Control of zeolite framework flexibility and pore topology for separation of ethane and ethylene. *Science*, **2017,** *358* (6366), 1068-1071.
18. Alotibi, M. F.; Alshammari, B. A.; Alotaibi, M. H.; Alotaibi, F. M.; Alshihri, S.; Navarro, R. M.; Fierro, J. L. G., ZSM-5 Zeolite Based Additive in FCC Process: A Review on Modifications for Improving Propylene Production. *Catalysis Surveys from Asia*, **2020,** *24* (1), 1-10.
19. Hussain, A. I.; Aitani, A. M.; Kubů, M.; Čejka, J.; Al-Khattaf, S., Catalytic cracking of Arabian Light VGO over novel zeolites as FCC catalyst additives for maximizing propylene yield. *Fuel*, **2016,** *167*, 226-239.
20. Al-Khattaf, S.; Saeed, M. R.; Aitani, A.; Klein, M. T., Catalytic cracking of light crude oil to light olefins and naphtha over E-Cat and MFI: microactivity test versus advanced cracking evaluation and the effect of high reaction temperature. *Energy & fuels*, **2018,** *32* (5), 6189-6199.
21. Galadima, A.; Muraza, O., Recent Developments on Silicoaluminates and Silicoaluminophosphates in the Methanol-to-Propylene Reaction: A Mini Review. *Industrial & Engineering Chemistry Research*, **2015,** *54* (18), 4891-4905.
22. Blay, V.; Epelde, E.; Miravalles, R.; Perea, L. A., Converting olefins to propene: Ethene to propene and olefin cracking. *Catalysis Reviews*, **2018,** *60* (2), 278-335.
23. Matar, S.; Hatch, L. F., Chemicals Based on Propylene In *Chemistry of petrochemical processes*, Secand ed.; Gulf professional publishing: Elsevier, **2001**; pp 213-237.
24. Suganuma, S.; Katada, N., Innovation of catalytic technology for upgrading of crude oil in petroleum refinery. *Fuel Processing Technology*, **2020,** *208*, 106518.
25. Sholl, D. S.; Lively, R. P., Seven chemical separations to change the world. *Nature*, **2016,** *532* (7600), 435-437.
26. del Campo, P.; Navarro, M. T.; Shaikh, S. K.; Khokhar, M. D.; Aljumah, F.; Martínez, C.; Corma, A., Propene Production by Butene Cracking. Descriptors for Zeolite Catalysts. *ACS Catalysis*, **2020,** *10* (20), 11878-11891.

27. Sattler, J. J. H. B.; Ruiz-Martinez, J.; Santillan-Jimenez, E.; Weckhuysen, B. M., Catalytic Dehydrogenation of Light Alkanes on Metals and Metal Oxides. *Chemical Reviews,* **2014,** *114* (20), 10613-10653.
28. Gutiérrez-Sevillano, J. J.; Dubbeldam, D.; Rey, F.; Valencia, S.; Palomino, M.; Martín-Calvo, A.; Calero, S., Analysis of the ITQ-12 zeolite performance in propane− propylene separations using a combination of experiments and molecular simulations. *The Journal of Physical Chemistry C,* **2010,** *114* (35), 14907-14914.
29. Blay, V.; Miguel, P. J.; Corma, A., Theta-1 zeolite catalyst for increasing the yield of propene when cracking olefins and its potential integration with an olefin metathesis unit. *Catalysis Science & Technology,* **2017,** *7* (24), 5847-5859.
30. *On-Purpose Propylene in an Era of Uncertainty*; Nexant ECA.: www.nexanteca.com, **2016**.
31. Wang, S.; Zhu, Z. H., Catalytic Conversion of Alkanes to Olefins by Carbon Dioxide Oxidative Dehydrogenation-A Review. *Energy & Fuels,* **2004,** *18* (4), 1126-1139.
32. Carlotta, P.; Régis, P.; Alban, C.; Pascal, F.; Alain, B., Power-to-Liquid catalytic CO_2 valorization into fuels and chemicals: focus on the Fischer-Tropsch route. *Journal of CO_2 Utilization,* **2020,** *38*, 314-347.
33. Rahimi, N.; Karimzadeh, R., Catalytic cracking of hydrocarbons over modified ZSM-5 zeolites to produce light olefins: A review. *Applied Catalysis A: General,* **2011,** *398* (1-2), 1-17.
34. Park, Y.-K.; Lee, C. W.; Kang, N. Y.; Choi, W. C.; Choi, S.; Oh, S. H.; Park, D. S., Catalytic Cracking of Lower-Valued Hydrocarbons for Producing Light Olefins. *Catalysis Surveys from Asia,* **2010,** *14* (2), 75-84.
35. Ren, T.; Patel, M.; Blok, K., Olefins from conventional and heavy feedstocks: Energy use in steam cracking and alternative processes. *Energy,* **2006,** *31* (4), 425-451.
36. Xu, H.; Yuan, Q.; Yajie, T.; Zhenheng, D.; Xiangwen, Z.; Guozhu, L., Reaction pathways of n-pentane cracking on the fresh and regenerated Sr, Zr and La-loaded ZSM-5 zeolites. *Chemical Engineering Journal,* **2018,** *349*, 297-308.
37. Brandon, R.; Ashley, C.; Xinwei, B.; Victor, A.; Dushyant, S.; Jianli, H., Catalytic direct conversion of ethane to value-added chemicals under microwave irradiation. *Catalysis Today,* **2020,** *356*, 3-10.
38. Al Abdullah, M.; Rodriguez Gomez, A.; Vittenet, J.; Bendjeriou-Sedjerari, A.; Xu, W.; Abba, I. A.; Gascon, J., A Viewpoint on the Refinery of the Future: Catalyst and Process Challenges. *ACS Catalysis,* **2020,** *10*, 8131-8140.
39. Amghizar, I.; Vandewalle, L. A.; Van Geem, K. M.; Marin, G. B., New Trends in Olefin Production. *Engineering,* **2017,** *3* (2), 171-178.
40. Kossiakoff, A.; Rice, F. O., Thermal decomposition of hydrocarbons, resonance stabilization and isomerization of free radicals1. *Journal of the American Chemical Society,* **1943,** *65* (4), 590-595.

41. Matar, S.; Hatch, L. F., Crude Oil Processing and Production of Hydrocarbon Intermediates. In *Chemistry of Petrochemical Processes* Second ed.; *Gulf professional publishing: Elsevier*, **2001**; pp 49-110.
42. Greensfelder, B. S.; Voge, H. H.; Good, G. M., Catalytic and thermal cracking of pure hydrocarbons: Mechanisms of Reaction. *Industrial & Engineering Chemistry,* **1949,** *41* (11), 2573-2584.
43. Froment, G. P.; Van de Steene, B. O.; Van Damme, P. S.; Narayanan, S.; Goossens, A. G., Thermal cracking of ethane and ethane-propane mixtures. *Industrial & Engineering Chemistry Process Design and Development,* **1976,** *15* (4), 495-504.
44. Zdenek, B.; Petr, Z.; Tomas, H., The kinetic model of thermal cracking for olefins production. *Chemical Engineering and Processing: Process Intensification,* **2003,** *42* (6), 461-473.
45. Sedighi, M.; Keyvanloo, K.; Towfighi, J., Modeling of thermal cracking of heavy liquid hydrocarbon: application of kinetic modeling, artificial neural network, and neuro-fuzzy models. *Industrial & Engineering Chemistry Research,* **2011,** *50* (3), 1536-1547.
46. Vogt, E. T. C.; Weckhuysen, B. M., Fluid catalytic cracking: recent developments on the grand old lady of zeolite catalysis. *Chemical Society Reviews,* **2015,** *44* (20), 7342-70.
47. Speight, J. G., Fouling During Catalytic Cracking. In Fouling in Refineries, *Gulf Professional Publishing*, **2015**; pp 271-302.
48. Speight, J. G., Catalytic Cracking. In Heavy and extra-heavy oil upgrading technologies, *Gulf Professional Publishing*, **2013**; pp 39-67.
49. Speight, J. G., Catalytic Cracking Processes. In Heavy Oil Recovery and Upgrading, *Gulf Professional Publishing*, **2019**; pp 357-421.
50. Speight, J. G., Catalytic Cracking. In The Refinery of the Future, *William Andrew*, **2010**; pp 181-208.
51. Corma, A.; Orchillés, A. V., Current views on the mechanism of catalytic cracking. *Microporous and Mesoporous Materials,* **2000,** *35-36*, 21-30.
52. Kotrel, S.; Knözinger, H.; Gates, B. C., The Haag–Dessau mechanism of protolytic cracking of alkanes. *Microporous and Mesoporous Materials,* **2000,** *35-36*, 11-20.
53. W.O. Haag; R.M. Dessau, 8th International Congress on Catalysis Berlin, Dechema, Frankfurt am Main, **1984**; Vol. 2, p 305.
54. Abrevaya, H., Cracking of naphtha range alkanes and naphthenes over zeolites. In Studies in Surface Science and Catalysis, *Elsevier*, **2007**; Vol. 170, pp 1244-1251.
55. Caeiro, G.; Carvalho, R. H.; Wang, X.; Lemos, M. A. N. D. A.; Lemos, F.; Guisnet, M.; Ramôa Ribeiro, F., Activation of C_2–C_4 alkanes over acid and bifunctional zeolite catalysts. *Journal of Molecular Catalysis A: Chemical,* **2006,** *255* (1-2), 131-158.

56. To, A. T.; Resasco, D. E., Hydride transfer between a phenolic surface pool and reactant paraffins in the catalytic cracking of m-cresol/hexanes mixtures over an HY zeolite. *Journal of Catalysis,* **2015,** *329*, 57-68.
57. Sadeghbeigi, R., Fluid catalytic cracking handbook: An expert guide to the practical operation, design, and optimization of FCC units. Fourth ed.; *Butterworth-Heinemann*: **2020**.
58. Fahim, M. A.; Al-Sahhaf, T. A.; Elkilani, A., Fundamentals of Petroleum Refining. *Elsevier*: **2009**.
59. Venuto, P. B.; Habib Jr, E. T., Fluid catalytic cracking with zeolite catalysts. Marcel Dekker, Inc.,New York, NY: United States, **1979**.
60. Ball, M. C.; Norbury, A. H., Physical data for inorganic chemists. *Addison-Wesley Longman Limited*: **1974**.
61. Harrison, R., Chemistry, Physical Science, Physics—Book of Data. *Nuffield Advanced Science* **1972**.
62. Yoshimura, Y.; Kijima, N.; Hayakawa, T.; Murata, K.; Suzuki, K.; Mizukami, F.; Matano, K.; Konishi, T.; Oikawa, T.; Saito, M., Catalytic cracking of naphtha to light olefins. *Catalysis Surveys from Japan,* **2001,** *4* (2), 157-167.
63. Shafei, E. N.; Masudi, A.; Yamani, Z. H.; Muraza, O., Acidity modifications of nanozeolite-Y for enhanced selectivity to olefins from the steam catalytic cracking of dodecane. *RSC Advances,* **2022,** *12* (28), 18274-18281.
64. Al-hazmi, M.; Odedairo, T. A.; Al-zenaidi, A.; Al-khattaf, S.; Al-yassir, N.; Aitani, A.; Siddiqui, A. M., Catalytic methods for converting naphtha into olefins. U.S. Patent No.10,099,210: **2018**.
65. Pandey, S. C.; Ralli, D. K.; Saxena, A. K.; Alamkhan, W. K., Physicochemical characterization and applications of naphtha. *Journal of Scintific & Industrial Research,* **2004,** *63*, 276-282.
66. Antos, G. J.; Aitani, A. M., *Catalytic naphtha reforming, revised and expanded*. *CRC Press*: **2004**.
67. Kulprathipanja, S., Zeolites in industrial separation and catalysis. *John Wiley & Sons*: **2010**.
68. Fang, Q.-R.; Yuan, D.-Q.; Sculley, J.; Lu, W.-G.; Zhou, H.-C., A novel MOF with mesoporous cages for kinetic trapping of hydrogen. *Chemical Communications,* **2012,** *48* (2), 254-256.
69. Ewing, M. B.; Lilley, T. H.; Olofsson, G. M.; Ratzsch, M. T.; Somsen, G., Standard quantities in chemical thermodynamics. Fugacities, activities and equilibrium constants for pure and mixed phases (IUPAC Recommendations 1994). *Pure and Applied Chemistry*, **1994,** *66* (3), 533-552.
70. Baerlocher, C.; McCusker, L. B.; Olson, D. H., Atlas of Zeolite Framework Types. *Elsevier*: **2007**.
71. Bellussi, G.; Pollesel, P., Industrial applications of zeolite catalysis: production and uses of light olefins. In Studies in Surface Science and Catalysis, *Elsevier*, **2005**; Vol. 158, pp 1201-1212.

72. Flanigen, E. M.; Broach, R. W.; Wilson, S. T., Introduction. In Zeolites in industrial separation and catalysis, Kulprathipanja, S., Ed. *John Wiley & Sons*: **2010**; pp 1-26.
73. Kokotailo, G.; Lawton, S.; Olson, D.; Meier, W., Structure of synthetic zeolite ZSM-5. *Nature,* **1978,** *272* (5652), 437-438.
74. Broach, R. W., Zeolite Types and Structures. In Zeolites in industrial separation and catalysis, Kulprathipanja, S., Ed. *John Wiley & Sons*: **2010**; pp 27-59.
75. Corma, A., Inorganic solid acids and their use in acid-catalyzed hydrocarbon reactions. *Chemical Reviews,* **1995,** *95* (3), 559-614.
76. Corma, A.; Garcia, H., Organic reactions catalyzed over solid acids. *Catalysis Today,* **1997,** *38* (3), 257-308.
77. Bradley, S. A.; Broach, R. W.; Mezza, T. M.; Prabhakar, S.; Sinkler, W., Zeolite Characterization. In Zeolites in Industrial Separation and Catalysis, Kulprathipanja, S., Ed. *John Wiley & Sons*: **2010**; pp 85-171.
78. Gates, B. C., Catalytic chemistry. *Wiley*, **1991**.
79. Afroukhteh-Langaroudi, N.; Tarighi, S.; Khonakdara, H., Catalytic Cracking of *n*-Hexane and *n*-Heptane over ZSM-5 Zeolite: Influence of SiO_2/Al_2O_3 Ratio. *Petroleum Chemistry,* **2018,** *58* (5), 457-463.
80. Kubo, K.; Iida, H.; Namba, S.; Igarashi, A., Selective formation of light olefin by *n*-heptane cracking over HZSM-5 at high temperatures. *Microporous and Mesoporous Materials,* **2012,** *149* (1), 126-133.
81. Tarighi, S.; Afroukhteh-Langaroudi, N.; Khonakdar, H. A., Conversion of *n*-heptane over different catalysts: Effect of catalyst-to-oil ratio and temperature. *Petroleum Science and Technology,* **2017,** *35* (23), 2201-2207.
82. Konno, H.; Tago, T.; Nakasaka, Y.; Ohnaka, R.; Nishimura, J.-i.; Masuda, T., Effectiveness of nano-scale ZSM-5 zeolite and its deactivation mechanism on catalytic cracking of representative hydrocarbons of naphtha. *Microporous and Mesoporous Materials,* **2013,** *175*, 25-33.
83. Konno, H.; Ohnaka, R.; Nishimura, J.-i.; Tago, T.; Nakasaka, Y.; Masuda, T., Kinetics of the catalytic cracking of naphtha over ZSM-5 zeolite: effect of reduced crystal size on the reaction of naphthenes. *Catalysis Science & Technology,* **2014,** *4* (12), 4265-4273.
84. Mohiuddin, E.; Mdleleni, M. M.; Key, D., Catalytic cracking of naphtha: The effect of Fe and Cr impregnated ZSM-5 on olefin selectivity. *Applied Petrochemical Research,* **2018,** *8* (2), 119-129.
85. Hou, X.; Zhu, W.; Tian, Y.; Qiu, Y.; Diao, Z.; Feng, F.; Zhang, X.; Liu, G., Superiority of ZrO_2 surface enrichment on ZSM-5 zeolites in *n*-pentane catalytic cracking to produce light olefins. *Microporous and Mesoporous Materials*, **2019,** *276*, 41-51.

86. Buchanan, J. S., The chemistry of olefins production by ZSM-5 addition to catalytic cracking units. *Catalysis Today,* **2000,** *55* (3), 207-212.
87. Siddiqui, M. B.; Aitani, A.; Saeed, M.; Al-Khattaf, S., Enhancing the production of light olefins by catalytic cracking of FCC naphtha over mesoporous ZSM-5 catalyst. *Topics in Catalysis,* **2010,** *53* (19-20), 1387-1393.
88. Yamaguchi, A.; Jin, D.; Ikeda, T.; Sato, K.; Hiyoshi, N.; Hanaoka, T.; Mizukami, F.; Shirai, M., P-ZSM-5 Pretreated by High-Temperature Calcination as Durable Catalysts for Steam Cracking of *n*-Hexane. *Catalysis Letters,* **2014,** *144* (1), 44-49.
89. van der Bij, H. E.; Weckhuysen, B. M., Phosphorus promotion and poisoning in zeolite-based materials: synthesis, characterisation and catalysis. *Chemical Society Reviews,* **2015,** *44* (20), 7406-28.
90. Blasco, T.; Corma, A.; Martínez-Triguero, J., Hydrothermal stabilization of ZSM-5 catalytic-cracking additives by phosphorus addition. *Journal of Catalysis,* **2006,** *237* (2), 267-277.
91. Xue, N.; Olindo, R.; Lercher, J. A., Impact of forming and modification with phosphoric acid on the acid sites of HZSM-5. *The Journal of Physical Chemistry C,* **2010,** *114* (37), 15763-15770.
92. van der Bij, H. Phosphatation of zeolites: a combined spectroscopy, microscopy and catalysis study. Utrecht University, **2014**.
93. Nianhua, X.; Xiangke, C.; Lei, N.; Xuefeng, G.; Weiping, D.; Yi, C.; Min, G.; Zaiku, X., Understanding the enhancement of catalytic performance for olefin cracking: Hydrothermally stable acids in P/HZSM-5. *Journal of Catalysis,* **2007,** *248* (1), 20-28.
94. Dan, L.; Won Choon, C.; Chul Wee, L.; Na Young, K.; You Jin, L.; Chae-Ho, S.; Yong Ki, P., Steaming and washing effect of P/HZSM-5 in catalytic cracking of naphtha. *Catalysis Today,* **2011,** *164* (1), 154-157.
95. Rane, N.; Kersbulck, M.; R.A; Hensen, E. J. M., Cracking of *n*-heptane over Brønsted acid sites and Lewis acid Ga sites in ZSM-5 zeolite. *Microporous and Mesoporous Materials,* **2008,** *110* (2), 279-291.
96. Jiangyin, L.; Zhen, Z.; Chunming, X.; Pu, Z.; Aijun, D., FeHZSM-5 molecular sieves – Highly active catalysts for catalytic cracking of isobutane to produce ethylene and propylene. *Catalysis Communications,* **2006,** *7* (4), 199-203.
97. Lu, J.; Zhao, Z.; Xu, C.; Duan, A.; Wang, X.; Zhang, P., Catalytic cracking of isobutane over HZSM-5, FeHZSM-5 and CrHZSM-5 catalysts with different SiO_2/Al_2O_3 ratios. *Journal of Porous Materials,* **2008,** *15* (2), 213-220.
98. Rahimi, N.; Moradi, D.; Sheibak, M.; Moosavi, E.; Karimzadeh, R., The influence of modification methods on the catalytic cracking of LPG over lanthanum and phosphorus modified HZSM-5 catalysts. *Microporous and Mesoporous Materials,* **2016,** *234*, 215-223.

99. Kubo, K.; Iida, H.; Namba, S.; Igarashi, A., Effect of steaming on acidity and catalytic performance of H-ZSM-5 and P/H-ZSM-5 as naphtha to olefin catalysts. *Microporous and Mesoporous Materials,* **2014,** *188*, 23-29.
100. Lin, L.; Qiu, C.; Zhuo, Z.; Zhang, D.; Zhao, S.; Wu, H.; Liu, Y.; He, M., Acid strength controlled reaction pathways for the catalytic cracking of 1-butene to propene over ZSM-5. *Journal of Catalysis,* **2014,** *309*, 136-145.
101. Corma, A.; Mengual, J.; Miguel, P. J., Stabilization of ZSM-5 zeolite catalysts for steam catalytic cracking of naphtha for production of propene and ethene. *Applied Catalysis A: General,* **2012,** *421-422*, 121-134.
102. Al-Yassir, N.; Siddiqui, M. A.; Saeed, M. R.; Aitani, A. M.; Al-Khattaf, S. S.; Alzenaidi, A. S.; Guggilla, V. S., Methods for producing ethylene and propylene from naphtha. U.S. Patent No.10,550,333, **2020**.
103. Nguyen, L.-P.; Van Tran, T.; Ngo, P. T.; Ngoc Luong, T.; Vo, P. N. X.; Thanh Dang, T., Modification of a ZSM-5 catalyst by La for use in fluid catalytic cracking. *Petroleum Science and Technology,* **2019,** *37* (14), 1713-1721.
104. Pouria, R.; Vafi, L.; Karimzadeh, R., Propane catalytic cracking on pretreated La-ZSM-5 zeolite during calcination for light olefins production. *Journal of Rare Earths*, **2017,** *35* (6), 542-550.
105. Han, D.; Sun, N.; Liu, J.; Li, C.; Shan, H.; Yang, C., Synergistic effect of W and P on ZSM-5 and its catalytic performance in the cracking of heavy oil. *Journal of Energy Chemistry*, **2014,** *23* (4), 519-526.
106. Yang, M.; Shao, J.; Yang, Z.; Yang, H.; Wang, X.; Wu, Z.; Chen, H., Conversion of lignin into light olefins and aromatics over Fe/ZSM-5 catalytic fast pyrolysis: Significance of Fe contents and temperature. *Journal of Analytical and Applied Pyrolysis*, **2019,** *137*, 259-265.
107. Jun, J.-W.; Kim, T.-W.; Choi, W. C.; Kim, C.-U., Propane to light olefins by one-pot cascade and series reactions. *Chemical Engineering Journal*, **2019,** *377*, 120114.
108. Cheng, Y.; Miao, C.; Hua, W.; Yue, Y.; Gao, Z., Cr/ZSM-5 for ethane dehydrogenation: enhanced catalytic activity through surface silanol. *Applied Catalysis A: General,* **2017,** *532*, 111-119.
109. Gusev, A. A.; Psarras, A. C.; Triantafyllidis, K. S.; Lappas, A. A.; Diddams, P. A.; Vasalos, I. A., ZSM-5 Additive Deactivation with Nickel and Vanadium Metals in the Fluid Catalytic Cracking (FCC) Process. *Industrial & Engineering Chemistry Research,* **2020,** *59* (6), 2631-2641.
110. Abbasizadeh, S.; Karimzadeh, R., Influence of various aluminum distributions on modification of ZSM-5 zeolite framework with cobalt ions in alkane catalytic cracking. *Research on Chemical Intermediates,* **2019,** *45* (3), 955-972.

111. Lu, J.; Zhao, Z.; Xu, C.; Duan, A.; Zhang, P., CrHZSM-5 zeolites–highly efficient catalysts for catalytic cracking of isobutane to produce light olefins. *Catalysis Letters,* **2006,** *109* (1-2), 65-70.
112. Amin, N. A. S.; Anggoro, D. D., Characterization and activity of Cr, Cu and Ga modified ZSM-5 for direct conversion of methane to liquid hydrocarbons. *Journal of Natural Gas Chemistry,* **2003,** *12* (2), 123-134.
113. Wang, K.; Fan, S.; Zhang, J.; Ma, Q.; Zhang, W.; Zhao, T.-S., Effects of synergy between Cr_2O_3 and hierarchical HZSM-5 on transformation of LPG toward propylene and ethylene. *Fuel Processing Technology,* **2018,** *179*, 53-59.
114. Fan, S.-B.; Wang, D.; Li, H.-B.; Tuo, J.; Zhang, X.-L.; Gao, X.-H.; Zhao, T.-S., Enhancing stability and coaromatization of *n*-hexane and methanol over [Zn,Cr]/HZSM-5. *Applied Catalysis A: General,* **2020**, 117602.
115. Letzsch, W., Fluid catalytic cracking (FCC). In Handbook of Petroleum Processing, *Springer,* **2008**; pp 239-286.
116. Chiranjeevi, T.; Ravichander, N.; Gokak, D. T.; Ravikumar, V.; Choudary, N. V., The Selection of Fluid Catalytic Cracking Catalysts and Additives: The Significance of Attrition Studies. *Petroleum Science and Technology,* **2013,** *32* (4), 470-478.
117. Parthasarathi, R. S.; Alabduljabbar, S. S., HS-FCC High-severity fluidized catalytic cracking: a newcomer to the FCC family. *Applied Petrochemical Research,* **2014,** *4* (4), 441-444.
118. Biswas, J.; Maxwell, I. E., Recent process- and catalyst-related developments in fluid catalytic cracking. *Applied Catalysis,* **1990,** *63* (1), 197-258.
119. Jeong, S. M.; Chae, J. H.; Lee, W.-H., Study on the catalytic pyrolysis of naphtha over a KVO_3/α-Al_2O_3 catalyst for production of light olefins. *Industrial & Engineering Chemistry Research,* **2001,** *40* (26), 6081-6086.
120. Lee, W.-H.; Jeong, S. M.; Chae, J. H.; Kang, J.-H.; Lee, W.-J., Coke Formation on KVO_3−B_2O_3/SA5203 Catalysts in the Catalytic Pyrolysis of Naphtha. *Industrial & Engineering Chemistry Research,* **2004,** *43* (8), 1820-1826.
121. Mukhopadhyay, R.; Kunzru, D., Catalytic pyrolysis of naphtha on calcium aluminate catalysts. Effect of potassium carbonate impregnation. *Industrial & Engineering Chemistry Research,* **1993,** *32* (9), 1914-1920.
122. Al-Khattaf, S., The influence of alumina on the performance of FCC catalysts during hydrotreated VGO catalytic cracking. *Energy & Fuels,* **2003,** *17* (1), 62-68.
123. Yan, H. T.; Mao, R. L. V., Hybrid catalysts used in the Catalytic Steam Cracking process (CSC): Influence of the pore characteristics and the surface acidity properties of the ZSM-5 zeolite-based component on the overall catalytic performance. *Applied Catalysis A: General,* **2010,** *375* (1), 63-69.

124. Perego, C.; Millini, R., Porous materials in catalysis: challenges for mesoporous materials. *Chemical Society Reviews*, **2013,** *42* (9), 3956-3976.
125. Yarulina, I.; De Wispelaere, K.; Bailleul, S.; Goetze, J.; Radersma, M.; Abou-Hamad, E.; Vollmer, I.; Goesten, M.; Mezari, B.; Hensen, E. J., Structure–performance descriptors and the role of Lewis acidity in the methanol-to-propylene process. *Nature Chemistry*, **2018,** *10* (8), 804-812.
126. Degnan, T. F.; Chitnis, G. K.; Schipper, P. H., History of ZSM-5 fluid catalytic cracking additive development at Mobil. *Microporous and Mesoporous Materials*, **2000,** *35-36*, 245-252.
127. Harding, R. H.; Peters, A. W.; Nee, J. R. D., New developments in FCC catalyst technology. *Applied Catalysis A: General*, **2001,** *221* (1), 389-396.
128. Buchanan, J. S., Reactions of model compounds over steamed ZSM-5 at simulated FCC reaction conditions. *Applied Catalysis*, **1991,** *74* (1), 83-94.
129. Roberto, P.; Alazne, G.; María, L. F.; David, T.; Javier, B.; José, M. A., Upgrading of heavy coker naphtha by means of catalytic cracking in refinery FCC unit. *Fuel Processing Technology*, **2020,** *205*, 106454.
130. Pekka, T.; Tuula, T. P., Acidic properties of ZSM-5 zeolite modified with Ba^{2+}, Al^{3+} and La^{3+} ion-exchange. *Journal of Molecular Catalysis A: Chemical*, **1996,** *110* (2), 153-161.
131. Jung, J. S.; Park, J. W.; Seo, G., Catalytic cracking of *n*-octane over alkali-treated MFI zeolites. *Applied Catalysis A: General*, **2005,** *288* (1-2), 149-157.
132. Masaru, O.; Shin-ya, S.; Junko, T.; Yasuto, N.; Mikihiro, N.; Eiichi, K.; Masahiko, M., Alkali-treatment technique — new method for modification of structural and acid-catalytic properties of ZSM-5 zeolites. *Applied Catalysis A: General*, **2001,** *219* (1), 33-43.
133. Froment, G.; Dehertog, W.; Marchi, A., Zeolite catalysis in the conversion of methanol into olefins. *Catalysis*, **1992,** *9* (1), 1-64.
134. Gogate, M. R., Methanol-to-olefins process technology: current status and future prospects. *Petroleum Science and Technology*, **2019,** *37* (5), 559-565.
135. Magomedova, M.; Galanova, E.; Davidov, I.; Afokin, M.; Maximov, A., Dimethyl Ether to Olefins over Modified ZSM-5 Based Catalysts Stabilized by Hydrothermal Treatment. *Catalysts*, **2019,** *9* (5), 485.
136. Ma, Y.; Ge, Q.; Li, W.; Xu, H., Methanol synthesis from sulfur-containing syngas over Pd/CeO_2 catalyst. *Applied Catalysis B: Environmental*, **2009,** *90* (1-2), 99-104.
137. Liu, B.; France, L.; Wu, C.; Jiang, Z.; Kuznetsov, V. L.; Al-Megren, H. A.; Al-Kinany, M.; Aldrees, S. A.; Xiao, T.; Edwards, P. P., Methanol-to-hydrocarbons conversion over MoO_3/H-ZSM-5 catalysts prepared via lower temperature calcination: a route to tailor the distribution and evolution of promoter Mo species, and their corresponding catalytic properties. *Chemical Science*, **2015,** *6* (9), 5152-5163.

138. Guisnet, M.; Gilson, J.-P., Zeolites for cleaner technologies. *Imperial College Press London*, **2002**; Vol. 3.
139. Ali, M. A.; Ahmed, S.; Al-Baghli, N.; Malaibari, Z.; Abutaleb, A.; Yousef, A., A Comprehensive Review Covering Conventional and Structured Catalysis for Methanol to Propylene Conversion. *Catalysis Letters*, **2019,** *149* (12), 3395-3424.
140. Kianfar, E., Comparison and assessment of zeolite catalysts performance dimethyl ether and light olefins production through methanol: a review. *Reviews in Inorganic Chemistry*, **2019,** *39* (3), 157-177.
141. Sano, T., Production of Light Olefins from Methanol and Ethanol Using ZSM-5 Type Zeolite Catalysts. *Journal of the Japan Petroleum Institute*, **2017,** *60* (6), 263-276.
142. Keller, G.; Bhasin, M., Synthesis of ethylene via oxidative coupling of methane: I. Determination of active catalysts. *Journal of Catalysis*, **1982,** *73* (1), 9-19.
143. Ito, T.; Wang, J.; Lin, C. H.; Lunsford, J. H., Oxidative dimerization of methane over a lithium-promoted magnesium oxide catalyst. *Journal of the American Chemical Society*, **1985,** *107* (18), 5062-5068.
144. Burch, R.; Squire, G.; Tsang, S., Role of chlorine in improving selectivity in the oxidative coupling of methane to ethylene. *Applied Catalysis*, **1989,** *46* (1), 69-87.
145. Reyniers, G. C.; Froment, G. F.; Kopinke, F.-D.; Zimmermann, G., Coke Formation in the Thermal Cracking of Hydrocarbons. 4. Modeling of Coke Formation in Naphtha Cracking. *Industrial & Engineering Chemistry Research*, **1994,** *33* (11), 2584-2590.
146. Ngan, D. Y.-k.; Chan, P.-y. J.; Baumgartner, A. J. Thermal cracking of crude oil and crude oil fractions containing pitch in an ethylene furnace. U.S. Patent 6632351, **2003**.
147. Yamaguchi, A.; Jin, D.; Ikeda, T.; Sato, K.; Hiyoshi, N.; Hanaoka, T.; Mizukami, F.; Shirai, M., Deactivation of ZSM-5 zeolite during catalytic steam cracking of *n*-hexane. *Fuel Processing Technology*, **2014,** *126*, 343-349.
148. Lunsford, J. H., Catalytic conversion of methane to more useful chemicals and fuels: a challenge for the 21st century. *Catalysis Today*, **2000,** *63* (2-4), 165-174.
149. Sanfilippo, D., Dehydrogenation of paraffins; key technology for petrochemicals and fuels. *Cattech*, **2000,** *4* (1), 56-73.
150. Zhang, Y.; Yao, W.; Fang, H.; Hu, A.; Huang, Z., Catalytic alkane dehydrogenations. *Science Bulletin*, **2015,** *60* (15), 1316-1331.
151. Takht Ravanchi, M.; Kaghazchi, T.; Kargari, A., Application of membrane separation processes in petrochemical industry: a review. *Desalination*, **2009,** *235* (1-3), 199-244.
152. Weyten, H.; Luyten, J.; Keizer, K.; Willems, L.; Leysen, R., Membrane performance: the key issues for dehydrogenation reactions in a catalytic membrane reactor. *Catalysis Today*, **2000,** *56* (1-3), 3-11.

153. Wolf, D.; Dropka, N.; Smejkal, Q.; Buyevskaya, O., Oxidative dehydrogenation of propane for propylene production—comparison of catalytic processes. *Chemical Engineering Science*, **2001,** *56* (2), 713-719.

Chapter 2

Experimental methods, instrumentation, and fundamentals

2.1 Introduction

Zeolites are crystalline aluminosilicates with well-organised micropore networks and active acid sites. Because their catalytic characteristics are inextricably linked to their porosity structure, crystallinity, and acid site concentration/composition, characterising these aspects is critical for understanding and controlling catalytic activity. X-ray powder diffraction (XRD), N_2 physisorption, Transmission electron microscopy (TEM), Scanning electron microscopy (SEM), Thermogravimetric analysis (TGA), and ammonia temperature-programmed desorption (TPD) are the most regularly utilised analytical methods to analyse zeolites. The XRD technique is frequently used to validate the zeolite's phase and crystallinity degree. The TEM and SEM electron microscopy techniques aid in analysing its porous structure and surface texture, and the N_2 physisorption can estimate its surface area pore size and volume. Thermogravimetric analysis (TGA) can help to characterise the carbon deposited in spent samples. Another helpful approach is the TPD of ammonia (or propylamine), which can provide valuable information about the strength and the concentration of acid sites whilst analysis of pyridine adsorption by IR spectroscopy can distinguish Lewis and Brønsted acid sites. Altogether these methods were employed to characterise zeolites used in the conversion of high hydrocarbon molecular in light naphtha to light olefins in this study.

This chapter aims to provide and explain the analytical techniques most often employed in this study not only for the characterisation of zeolites but also for analysing the different gaseous and liquid products obtained upon the catalytic cracking reaction of *n*-heptane and light naphtha as described in the following chapters. Details on specific instrument types, operating settings, fundamentals, and instances of data produced are also described.

2.2 Catalyst Preparation

There are different methods to prepared solid catalysts such as the impregnation method, wet-impregnation, precipitation, and mixing. The synthesis methods and procedures used in this thesis are described in this chapter.

Conventional synthesis of catalysts is done by the impregnation method. The zeolites were initially calcined in a static air atmosphere at 550°C for 5h using a heating rate of 3°C.min^{-1}. This treatment is carried out to convert the NH_4-Zeolite to the H-zeolite form by releasing NH_3. Zeolite samples are hereafter referred as HZ23, HZ30, HZ50, HZ80 and HZ280 that correspond to SiO_2/Al_2O_3 ratios of 23, 30, 50, 80 and 280, respectively. The metal-containing catalyst was synthesised using the impregnation method. In a typical procedure, the appropriate amount of the nitrate salts was dissolved in excess deionized water and stirred until the salt was completely dissolved. Zeolite was then slowly added to the aqueous solution to give a suspension that was stirred at room temperature for 3-4h in a magnetic stirrer hotplate and then heated at 80-100°C until all the water was evaporated. Subsequently, the paste was dried at 80-100°C overnight in an oven under static air atmosphere. The catalyst was then calcined at 350°C for 5h using a heating rate of 3°C.min^{-1} to convert the metal nitrate to the oxide form.

On the other hand, the kaolin-zeolite catalyst was prepared using the suspension method. Kaolin was first calcined at 550°C to get the free proton form. The appropriate amount of zeolite was added in excess deionized water and stirred at room temperature to give a suspension. Kaolin was then added to the suspension slowly and stirred at room temperature for 3-4h. The catalyst was then placed into an oven to dry at 80°C overnight in static air atmosphere. The catalyst was then calcined at 550°C for 2h. A similar procedure was applied when metal oxides such as Al_2O_3, SiO_2, TiO_2, ZrO_2 and MgO were used to synthesise metal oxide-zeolite catalyst formulations.

2.3 Evaluation of Catalyst Performance

2.3.1 Feedstock

The cracking performances of the zeolites to produce light alkenes are examined using *n*-heptane as a model compound as it constitutes one of the main components of light naphtha.

Samples of real naphtha provided from SABIC. Light naphtha was analysised by GC-MS and GC-Sulphur Chemiluminescence Detector (SCD) using the standard method ASTM D5623 at Intertek and its composition is given in **Table 2.1.** The quantification of hydrocarbon types is shown in **Table 2.2**. Note that the overall sulfur content resulted 0.0174 wt.% whilst the main hydrocarbon components are C_5, C_6, and C_7 compounds.

Table 2.1. Summary of light naphtha composition.

Test	Result
Density at 15°C	0.688 $g.ml^{-1}$
Sulphur Content	0.017 wt.%
Mercaptan Sulphur	54 ppm
IBP	23°C
FBP	173°C

Table 2.2. The quantification of hydrocarbon types (wt.%) in light naphtha.

Carbon Number	Cycloalkane	isomer-Paraffin	*n*-paraffin	Cyclo-Olefin	isomer-Olefin	*n*-Olefin	Aromatic	Total
4	-	0.32	2.05	-	-	0.02	-	2.4
5	3.32	12.77	16.23	0.28	1.60	0.71	-	34.92
6	10.57	10.82	8.87	0.01	0.01	-	2.02	32.29
7	5.57	5.51	3.60	-	0.01	-	1.01	15.70
8	2.97	2.79	2.04	-	-	-	1.00	8.80
9	1.64	1.36	1.37	-	-	-	0.37	4.74
10	0.21	0.17	0.75	-	-	-	-	1.13
11	-	-	0.03	-	-	-	-	0.03
12+	-	-	-	-	-	-	-	-
Poly	-	-	-	-	-	-	-	-
Total	24.29	33.75	34.94	0.29	1.62	0.73	4.39	100.0

2.3.2 Catalyst performance test

A fixed bed reactor is the preferred option for most heterogeneous catalyst experiments, and it is often used by academic researchers for small scale testing[1, 2]. The powder catalyst body is put in a fixed bed that is held between two supporting layers, forming a type of sandwich-like structure in such reactors as given in **Figure 2.1**.

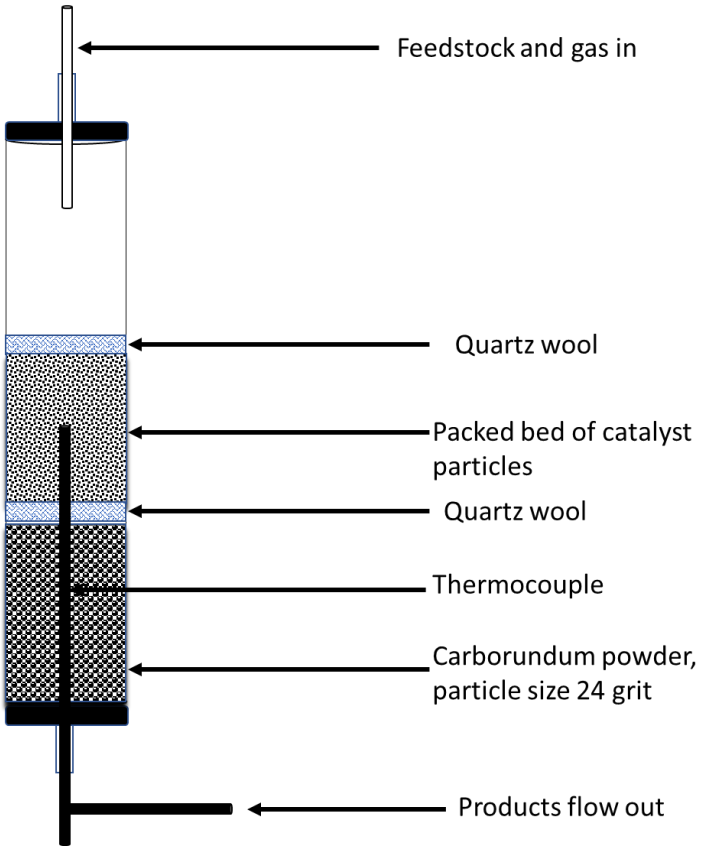


Figure 2.1. Schematic representation of a fixed-bed tubular reactor used in the present investigations, which is routinely used for conducting small scale catalyst tests.

The bed structure loading is intended to aid in ensuring consistent contact between the reactants and the settling catalyst. To support the loaded catalysts and prevent the powders from escaping, which might cause downstream channel obstruction, a supporting pad (in some instances quartz wool) and/or frits (e.g., sand, or carborundum powder) are placed slightly under the catalyst bed bottom. In many situations, the top of the catalyst bed is additionally

coated with a porous pad or quartz wool to prevent disruption of the catalyst packing. One common feature of such reactors is their tubular design. The reactor is forged into a tube shape using high-quality stainless steels or other materials, which is typically mounted vertically to ensure that the catalyst bed is packed as uniformly as possible and that the gas flow passing through can be directed smoothly from top to bottom to avoid disturbing the catalyst bed packing due to flow turbulence.

The integrated catalyst test system used in our investigations is schematically shown in **Figure 2.2**, with a tubular fixed bed reactor serving as the central component.

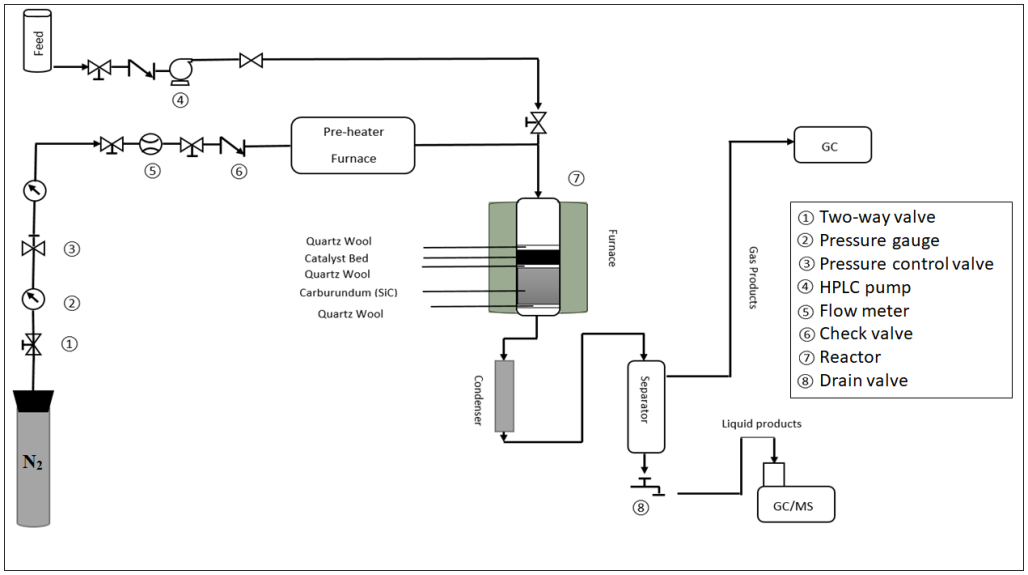


Figure 2.2. Schematic diagram of the reaction system.

The catalytic cracking of *n*-heptane was conducted in a custom-designed micro-reactor (Micro Reactor 10A, Beijing Brightly Instrument Co., LTD), **Figure 2.3.** It is equipped with a stainless-steel fixed bed reactor, an oven, several flowmeters, an ice trap, a condenser, and several temperature controllers.

Typically, 0.5 g of catalyst is mixed with 0.5 g of silicon carbide (SiC), which enhances the thermal conductivity of the catalyst bed minimizing the formation of hot spots, was loaded into the centre of the reactor tube (8 mm I.D). The catalyst bed is located in the centre of the

heating zone of the furnace over a quartz wool and silicon carbide (SiC) bed. Normally, before the reaction, the catalyst bed was initially heated up to 500℃ at 10℃.min^{-1} and then heated up to 550℃ at 5℃. min^{-1} under atmospheric pressure of nitrogen flow (20 ml.min^{-1}). The catalyst was left for 1h at 550℃ under N_2 flow to ensure that it is fully dehydrated and activated. Subsequently, *n*-heptane (Sigma-Aldrich, for HPLC, ≥99%) as feedstock was pumped into the reactor using a HPLC (High Performance Liquid Chromatography) pump with a flowrate of 0.1 ml.min^{-1} for all experiments, and the flowrate of reactant injection was carefully pre-calibrated periodically. The flowrate of reactant injection is critical for managing the feedstock Wight Hourly Space Velocity (WHSV), which has a direct impact on reaction rate, accurate catalytic performances, and the amount of coke buildup. In our studies, a catalyst loading of 0.5 g and a mild LHSV of 8.2h^{-1} were suitable to measure the intrinsic catalytic performance of samples.

All the products in the gas phase and N_2 as carrier gas pass across a condenser to condense the liquid product and hence separating liquid and gaseous products. The light hydrocarbon products (C1-C4) were analysed by an online gas chromatograph (PerkinElmer, Claurs 580 GC) every 30 minutes during 4 hours of time on stream. Before the gas products pass to GC analysis, an ice trap was set up to ensure that no vapor of the liquid products is present in the gas stream. Liquid products were collected in the separator through condenser and analysed by gas chromatograph-mass spectrometer (Shimadzu GC/MS-QP 2010 SE). After the reaction, the catalyst was cooled down overnight under 10 ml.min^{-1} of N_2 flow and then collected to be characterised after reaction.

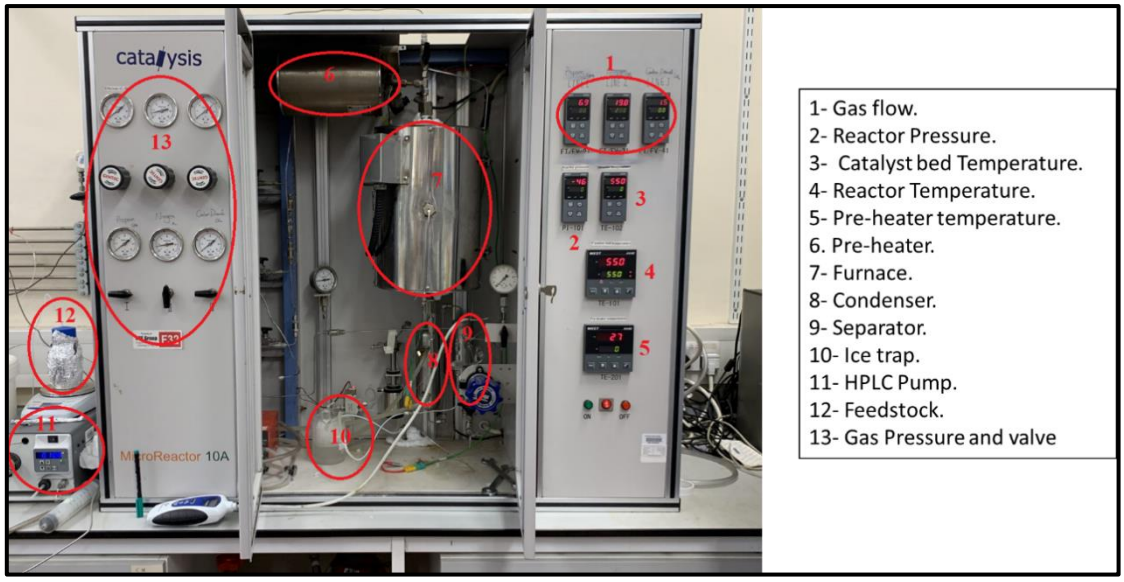


Figure 2.3. MicroReactor 10A benchtop pilot plants used in this investigation.

2.3.3 Calibration of reactants flowrates

Calibration of the pump flow rate is necessary to get proper feed ratios while preparing the catalyst testing unit for the reaction. The High-Performance Liquid Chromatography (HPLC) pump was calibrated using *n*-heptane (Sigma-Aldrich, HPLC, ≥99%) as shown in **Figure 2.4**. Note that the actual flowrate resulted nearly 90 % of the set value.

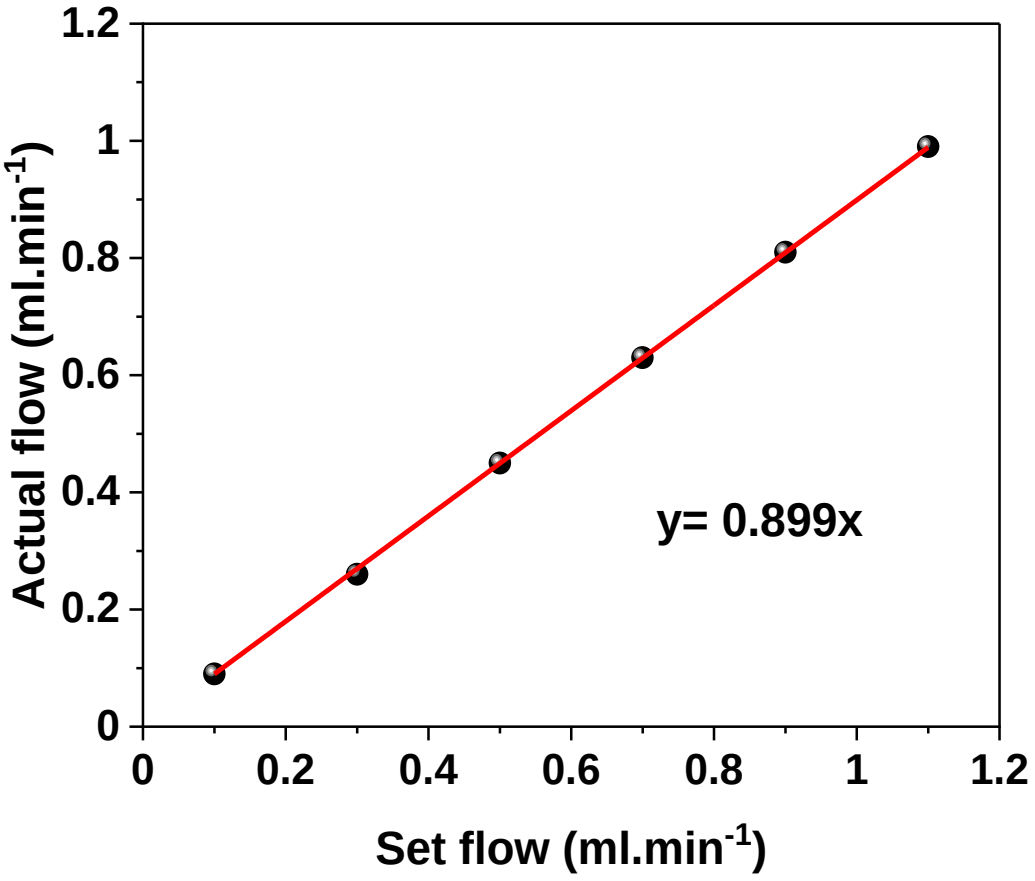


Figure 2.4. Calibration of HPLC pump for liquid feedstock.

2.4 Products analysis

2.4.1 Gas Chromatography (GC)

Gas chromatography is an analytical technique commonly used in hydrocarbon cracking research to identify and quantify the gaseous products by separating gas mixture into its constituents through the GC column[3]. Solutes are carried through the column in a separation process with a gaseous mobile phase and they are identified with a specific or universal detector when eluted. As seen in **Figure 2.5**, a sample is injected from the sample injector and promptly heated to a predetermined temperature in a heating chamber to guarantee complete vaporisation of all components. The carrier gas or mobile phase is often an inert gas such as helium or an unreactive gas such as nitrogen. Although helium is the most utilised carrier gas in around 90% of devices, nitrogen is favoured for superior separation[4]. The carrier gas moves the sample via

a column covered with a conductive material. For effective separation of analytes, the column property is crucial. GC columns might be long, thin capillary tubes with the stationary phase coated on the interior wall, or tubes with materials packed inside[5, 6]. The various components move at different speeds depending on the interaction with the column stationary phase. As a consequence, the individual components come out at different retention times. Because the operations are temperature-dependent, the column is usually put in a thermally controlled oven[7].

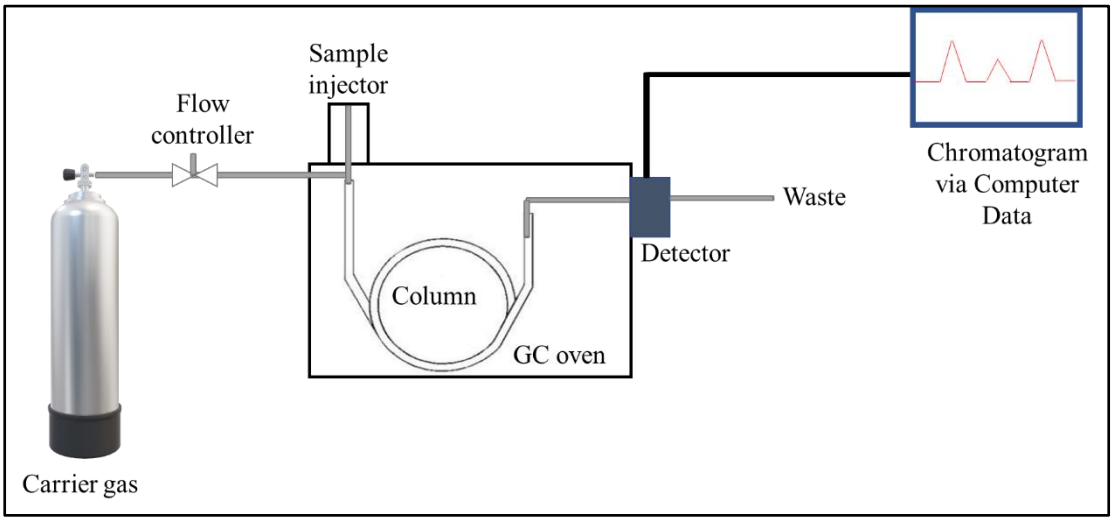


Figure 2.5. Schematic illustration of the Gas Chromatography (GC) apparatus used in this study.

In GC, different detectors are used, and their effectiveness is determined on the kind of component being examined. One of these common detectors are flame ionization detectors (FID), and thermal conductivity detectors (TCD). Thermal conductivity detectors identify changes in the column effluent's thermal conductivity and transfer them to the reference gas. The discharge thermal conductivity decreases as the sample is removed from the gas chromatography column. As a consequence, a discernible signal emerges. This gauges the gas mixture's thermal conductivity as it flows through a filament. A Wheatstone Bridge circuit is used in most TCDs to measure the resistance of a platinum filament that is heated at a constant temperature. As the gas flows through the filament, the temperature drops by an amount

proportional to the thermal conductivity of the gas and the velocity of gas flow. The resistance of the filament changes as the temperature rises. At a constant flow rate, gases of differing compositions and thermal conductivities cool the filament based on the concentrations of the gases. The thermal conductivity detector (TCD) is capable of detecting hydrogen, carbon monoxide, carbon dioxide, nitrogen, air, and other inorganic gases[8].

A flame ionization detector (FID) is often used to detect hydrocarbons including methane, ethane, and ethylene, as well as other carbon-based chemicals. Low noise, linear response over a broad range, high sensitivity, and minimal effect from operational conditions such as detector temperature, gas flow rates, and other parameters make FID the most extensively and effectively used gas chromatographic detector. The FID operates by burning carbon compounds to create ions by passing sample and carrier gas from the column through a hydrogen-air flame. These ions are collected as they travel between electrodes positioned near the flame, and a current is generated that is proportionate to the quantity of chemical being burnt. An electrometer detects the current and produces a digital signal that can be recorded[8].

Experimental conditions

In this thesis, a Perkin-Elmer Clarus 580 GC was used to analysis the gas products. The calibration process is carried out using the optimal conditions for separating substances under the direction of experts from Perkin-Elmer UK. The GC has a 30m long FID column with 0.53 mm diameter and Elite Alumina BOND phase. The GC oven was held at 80℃ for 10 min and then increased up to 200℃ with a heating rate of 25℃. min^{-1}, the temperature was hold for 5 min. The total analysis time resulted 30 min, including the instrument cooling time. The H_2 and air flow rates are set to 45 and 450 $mL.min^{-1}$, respectively, for FID. Helium is employed as the carrier gas for TCD at a flow rate of 40 $mL.min^{-1}$ and an operating temperature of 200°C. The GC was meticulously calibrated using reference gases, with an error range of ±0.01–0.1.

2.4.2 Gas Chromatography-Mass Spectrometry (GC-MS)

Gas chromatography mass spectrometry (GC/MS) is a technique for determining the composition of substances based on their mass spectra. Using mass spectral databases, each compound's unique mass spectrum may be compared and identified based on its mass spectrum[9]. Quantitation may likewise be conceivable using norms. GC/MS examination can similarly be utilized to inspect solids, fluids, and gases. For fluids, the sample to be investigated is infused straightforwardly. For gases, tight needles are utilized to move parts straightforwardly into the GC. For solids, the analytical procedure involves outgassing, pyrolysis, or solvent extraction[10].

In GC/MS (**Figure 2.6**), gas chromatography separates sample components, while mass spectrometry identifies them separately. The material being analysed is dissolved and then introduced into the device. The gas chromatograph is the instrument's first component. It is an oven with polymer-coated, long, thin glass tubes. The sample is carried through the column by a stream of helium gas. The sample's chemical components interact with the polymer covering. As a result, these components reach the end of the column at various times. Each component exits the column and enters the detector, where it is detected and recorded. The magnitude of the peak is proportional to the component's concentration in the sample[11]. The sample in a GC/MS instrument is always a chemically homogenous gas. This is produced by the GC component and may be delivered straight to the ioniser. After being ionised, the fragmented chemical is transferred to the mass analyzer, where the ions are conveyed via an electrical or magnetic field that classifies them based on their m/z ratios. The m/z ratio, commonly known as mass-to-charge, is the fragment's mass divided by its charge. At the end of the analysis, the detector detects the beam of freshly separated ions. The detector also generates the mass spectrum based on the variations in their intensities. A data system then displays, catalogues, and compares the mass spectrum of a sample to a library of mass spectra[12].

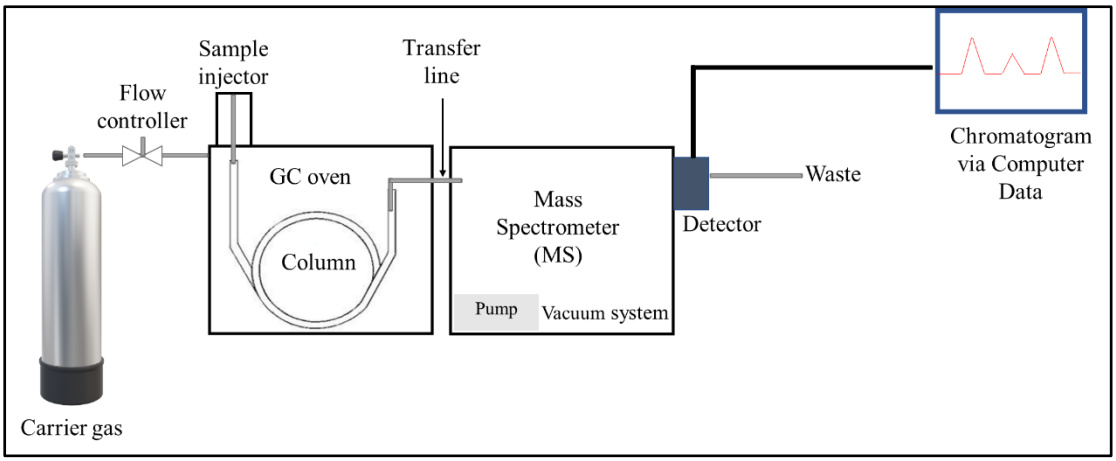


Figure 2.6. Schematic representation of the GC-MS instrumentation used in this investigation.

The mass spectrometer (MS) is the most frequently used detector in GC/MS. Mass Spectrometry detects the gas chromatography-separated components in addition to classifying them. The chemical components are broken into ions during mass spectrometry. Because the method in which each chemical fragments differs, the range of fragmented ions and their relative abundance may be recorded as a mass spectrum that allows individual components to be separated. In addition to NPD (Nitrogen-phosphorus) and ECD (Electron capture) detectors, GC/MS uses TCD, FID, and ECD (Electron capture).

Calibration of GC-MS

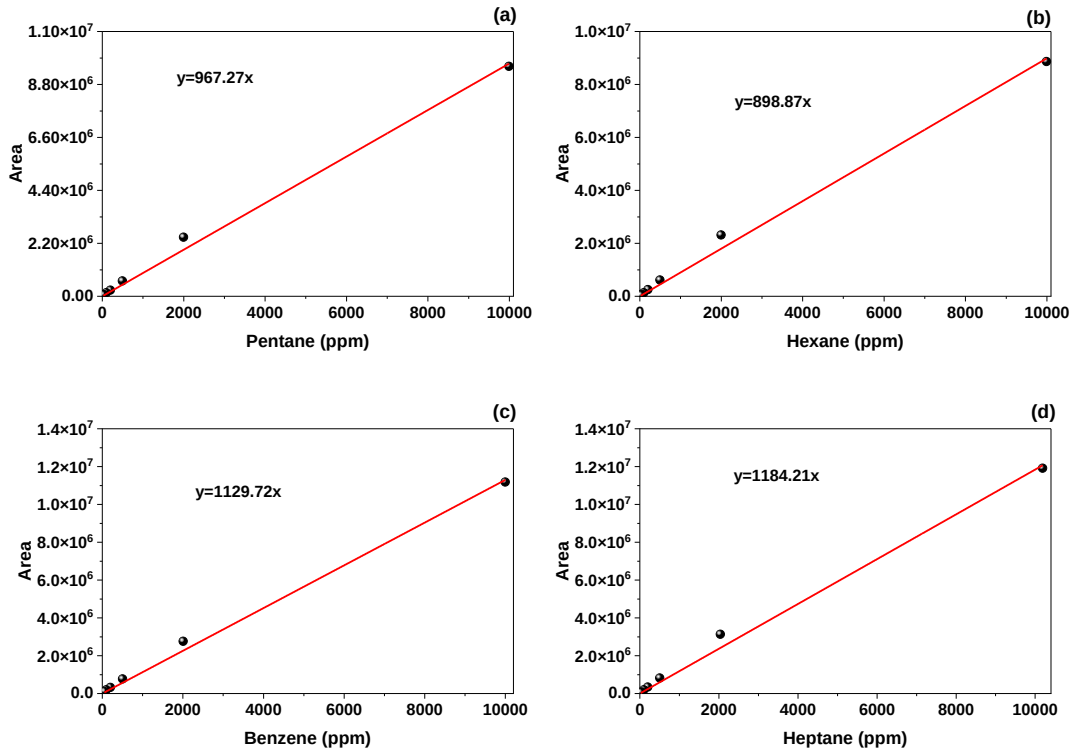
To prepare the GC-MS for the analysis of liquid products, it is important to calibrate the liquid product such as BTX (benzene, toluene, and xylene) and feedstock (*n*-heptane) instruments to get accurate results.

The objective of the calibration study was to create a method for detecting the amount of a certain product using the GC-MS response (normally, integrated chromatography peak area).

During our calibration, known concentrations of the main-product substances were prepared in dichloromethane solvent and subsequently analyzed with a GC instrument, with all

chromatography peaks integrated. Then, the calibration curves are produced to calculate the unknown quantity of a detected product as shown in **Figure 2.7.**

When working within the linear range of the detector, which is considered to be the most reliable, the fundamental principle is that the integrated peak area, which is a kind of GC detector response, is directly proportional to the amount of a substance that is being chromatographed. This is the most reliable method[10, 13-15].



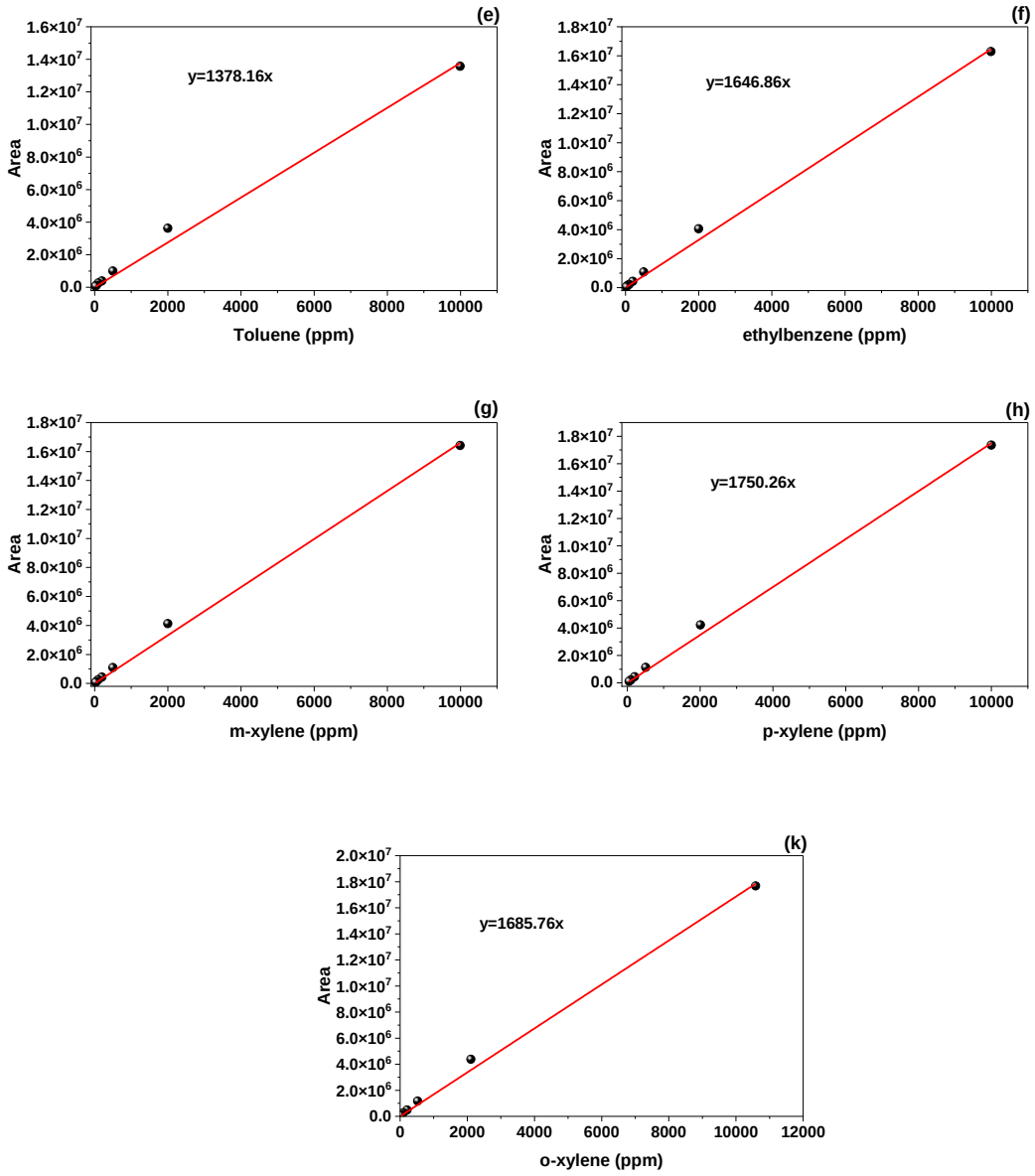


Figure 2.7. GC-MS calibration for a range of liquid products.

Experimental conditions

A Shimadzu GC/MS-QP 2010 SE gas chromatograph-mass spectrometer was utilised to analyse the liquid product. The GC-MS is fitted with a 30m x 0.25 mm ID capillary column (SHIM-5MS). The temperature of the oven was increased up to 50 °C and hold for 1 min before rising to 100℃ at a rate of 5℃. min^{-1} and holding for 1 min. Finally, the temperature is rose to 200℃ at a rate of 20℃.min^{-1} to culminate the heating program. The temperature of the ion

source is 250℃, the temperature of the interface is 250℃, and the voltage of the detector is 0.7 kV.

2.5 Calculating methods

The equation used throughout to calculate the conversion, selectivity, and yield of olefin through catalytic cracking of *n*-heptane and naphtha are given below[16-18]:

$$Yield\ (wt.\%) = \frac{Mass\ of\ \ product}{Mass\ of\ feed\ (inlet)}\ X100 \quad (2\text{-}1)$$

$$Conversion\ (wt.\%) = \frac{M\ input - M\ output\ (\ unconverted)}{M\ input} X\ 100, \quad (2\text{-}2)$$

$$Selectivity(mol.\%) = \frac{Moles\ of\ specific\ gas\ product\ X\ Number\ of\ C\ atoms}{\sum(\ Total\ moles\ of\ gas\ product\ X\ Number\ of\ C\ atoms)}\ X100, \quad (2\text{-}3)$$

$$Carbon\ Balance\ (\%) = B_c = \frac{C_{outlet}^{p} + C_{outlet}^{Feed} + C_{coke}}{C_{inlet}^{Feed}} \times 100 \quad (2\text{-}4)$$

Where:

C_{inlet}^{Feed}= Moles of carbon of inlet feed.

C_{outlet}^{Feed}= Moles of carbon of outlet feed.

C_{outlet}^{p}= Moles of carbon of outlet product (gas and liquid compounds).

C_{coke}= Moles of Carbon of Coke.

Due to the complexity of the feedstock (naphtha), the yield of hydrocarbon was Calculated by one method for all the experiments as reported in the literature[18-20].

The weight hourly space velocity (WHSV) was calculated by using this method below:

$$WHSV\ (h^{-1}) = \frac{Total\ mass\ feed\ flow\ rate\ to\ the\ reactor\ (g.h^{-1})}{Total\ catalyst\ weight\ (g)} \quad (2\text{-}5)$$

Where can use the feed density to calculate the mass flow feed as shown below:

$$Mass\ of\ feed\ (g.min^{-1}) = density\ (\ g.ml^{-1}) \times volume\ (ml.min^{-1}) \quad (2\text{-}6)$$

$$Mass\ of\ feed\ (g.h^{-1}) = Mass\ \ feed\ (g.min^{-1}) \times time\ (60min.h^{-1}) \quad (2\text{-}7)$$

In this thesis, the catalytic experiments are performed between 2 and 4 times. Moreover, the experimental results, such as conversion, selectivity, and yield have an error between 3 and 6%. The error percentage was computed using equation (A-4) in the appendix section.

2.6 Catalyst characterization methods

2.6.1 X-Ray Diffraction (XRD)

One of the scientific techniques most used in materials science and catalysis is X-ray powder diffraction (XRD). It is applied to study the crystalline structure of the catalysts, which is considered as a fingerprint of each sample. X-ray diffraction is a strong and diverse analytical tool to investigate the characteristics and structure of materials. This method reveals the locations of atoms and ions in a crystal lattice, resulting in a structural description in terms of bond lengths, bond angles, and the associated positions of ions and molecules in a framework's unit cell[21, 22]. The phase composition and crystallite size of crystalline materials may also be determined using this approach[22-24].

Scientist Wilhelm Conrad Röntgen discovered X-ray technology in 1895. The X-ray crystallography was discovery by Max von Laue in 1912[22, 25]. This technique can show us essential information for the sample, such as determining the crystalline phase, the crystal structure, unit cell dimensions, and crystalline materials' atomic spacing[26, 27].

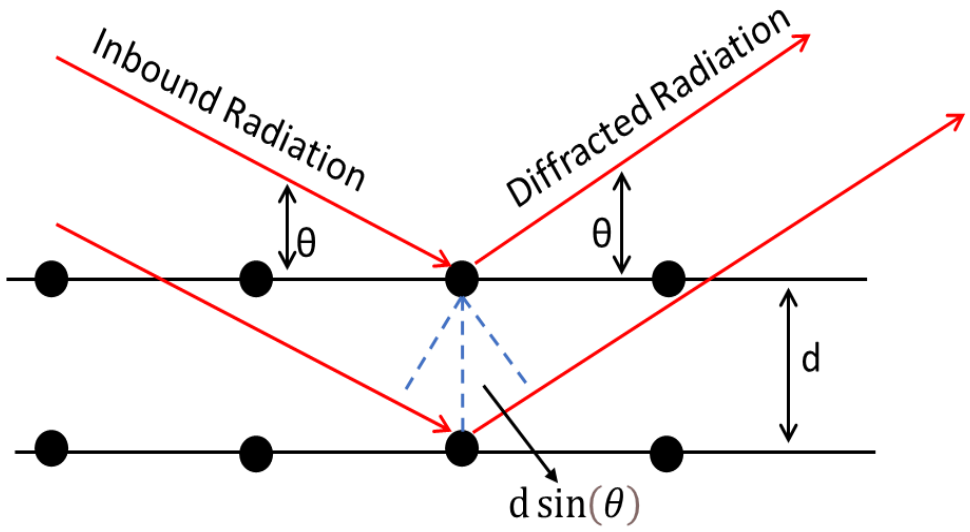


Figure 2.8. Illustration of Bragg's Law derived by treating layers of atom as reflecting planes.

Figure 2.8 shows a simplified representation of the diffraction phenomena, with X-rays impinging on the crystallite's surface. Some X-rays will scatter from an atom's electron cloud in the top layers, which are only surface sensitive, while others will pass through and scatter from the second layer. XRD relied on constructive interference of X-rays dispersed from atom planes separated by a distance comparable to the wavelength of the radiation (100 pm). Bragg's equation describes the connection between the lattice point separated by *d*, the scattering angle θ, and the X-ray wavelength λ in which constructive interference will be detected. The route difference is indicated by $2\,d sin$, while the refected beam deviation is denoted by 2θ[22, 28]. The equation that describes Bragg's law is as follows:

$$n\lambda = 2\,d\,sin\,\theta \qquad (2\text{-}8)$$

Where:

n is an integer,

λ = wavelength of the incident X-rays.

d = the spacing between diffracting planes.

θ = The angle formed by the incident X-ray and the diffraction plane.

The diffraction pattern is created by recording the intensity of diffracted X-rays as a function of scattering angle. The peak locations and full width half maximum (FWHM) of a given peak may be determined from the diffraction pattern using not only the crystal lattice but also the crystallite size; parameters used to compute the lattice[29]. The XRD patterns most significant contribution is that it indicates the degree of crystallinity of the catalysts or a doped component on/in it. On the other side, it predicts the size of any extant crystallites and more importantly offers information on the unit cell atomic constituents, since *d*-spacings and cell diameters may be derived[30].

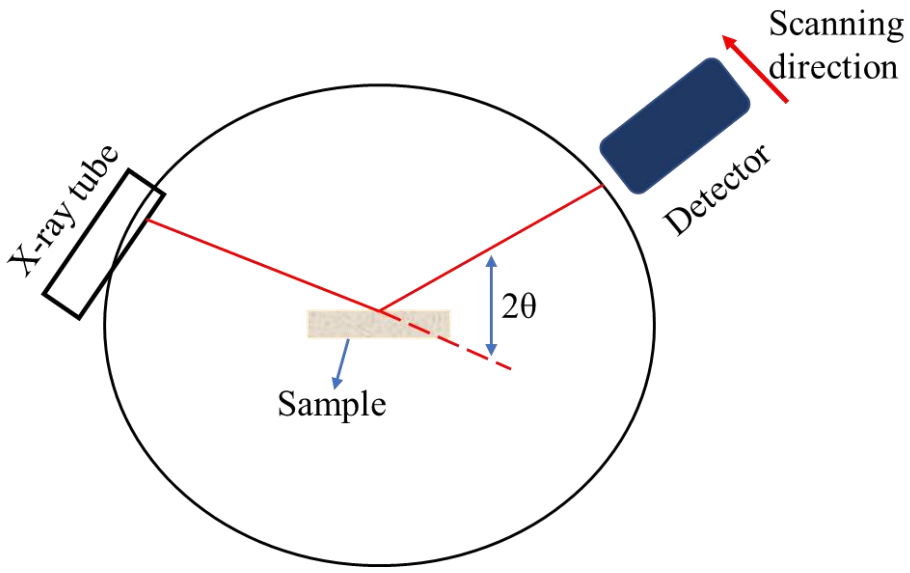


Figure 2.9. A typical XRD experiment on a thin film sample is shown in this diagram, where θ denotes the diffraction angle (Bragg angle).

In general, the X-ray measuring instrument consists of three main parts: the sample holder, the X-ray source and the X-ray detector as shown in **Figure 2.9** above[31, 32]. Electrons are produced at the cathode of the X-ray source and accelerated, by applying a voltage, towards the target anode. On starting the anode, the electrons reserve K-shell electrons from the atoms in the target (typically Cu). Higher shell electrons then drop into the K-shell holes, emitting X-ray photos[29, 31]. When the sample begins to rotate through the sample holder, the X-ray detector

rotates with it to measure the returned X-rays. There are many different components to X-rays, with K_β and K_α being the most popular types. K_α consists of $K_{\alpha1}$ and $K_{\alpha2}$ with a slight difference in wavelength[29, 31].

In 1918, Scherrer developed an equation that can be estimated the nano crystallite size by X-ray radiation by measuring the full width at half maximum of peaks (FWHM) at any 2θ in the pattern as follows[33]:

$$L = \frac{K\lambda}{\beta . \cos\theta} \qquad (2\text{-}9)$$

Where (L) is the nano crystallite size, (K) is a constant related to crystallite shape, normally taken as 0.9, (λ) is the X-ray wavelength in nanometre (nm), (β) is the peak width of the diffraction peak profile at half maximum height resulting from small average crystallite size in radians, and (θ) is the Bragg's angle of the diffraction.

Experimental conditions

In this work, powder X-ray diffraction (XRD) for samples were recorded on a Bruker-Eco D8 ADVANCE using Cu Kα radiation λ= 1.5418Å[29] at 40kV, 25 mA with a scanning range of 2θ from 5º to 90º. The sample does not need any extra preparation; it just is crushed into a fine powder and then placed on a sample holder. After that, the sample holder should be positioned on the revolving stage.

2.6.2 Thermogravimetric Analysis (TGA)

In catalyst research, thermal techniques have been extensively employed to determine the thermal properties of materials and to estimate the composition of materials. In a particular atmosphere, the thermal process can measure weight change and rate of weight change as a function of temperature. These data are then used to determine the material's composition, thermal stability and the coke amount in catalyst[34]. Moreover, thermogravimetric analysis can

provide physical and chemical-physical information such as vaporization, sublimation, desorption, chemisorption, decomposition, oxidation, reduction, and decomposition reactions[35].

The carbon materials and precursors in catalysts can be quantified through derivative Thermogravimetry (DTG) by heating or cooling the sample in a defined atmosphere and determined heating/cooling rate. The DTG profile is presented in a temperature-dependent curve and shows the temperature that the highest rate of mass change tends to take place[35] as given in **Figure 2.10**.

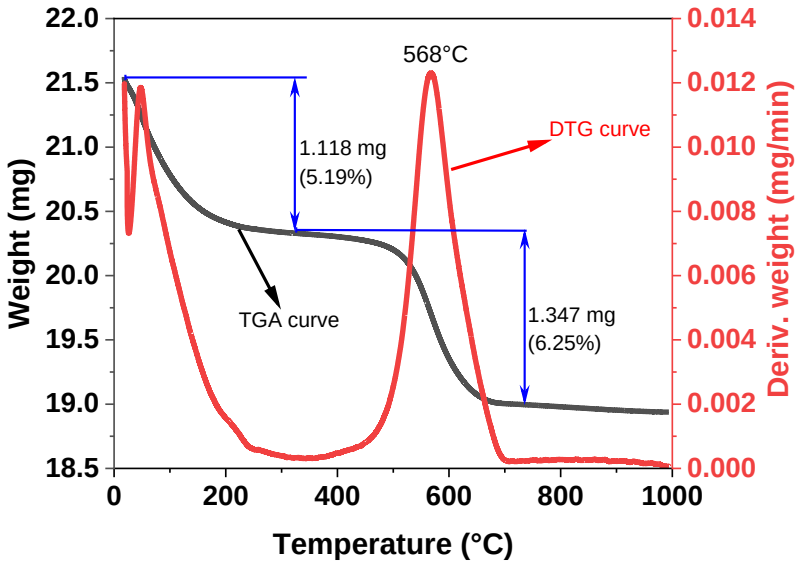


Figure 2.10. TGA and DTG curves of ZSM-5 with rate of 10ºC.min^{-1} in air atmosphere.

Experimental conditions

In this work, the thermogravimetric analysis (TGA) for the samples was carried out using SDT Q-600 measurement. The technique is mainly used to characterise the carbon deposited in spent samples when the sample is analysed in dry air flow atmosphere. The TGA equipment consists of a crucible attached to a very sensitive analytical balance. The crucible is kept in a furnace during the temperature program. Therefore, approximately 15-25 mg of spend samples was loading in an alumina crucible. The sample was heated from room temperature to

1000°C at a heating rate of 10°C.min^{-1} under a dry compressed air with a 100 mL.min^{-1} flow rate to burn off all so-called coke precursors.

2.6.3 NH_3-temperature-Programmed Desorption (TPD)

One of the important factors for zeolite activity is acidity alongside zeolite topology. The acid sites in zeolite often determine catalyst performance and hence reaction output. Consequently, temperature-programmed desorption (TPD) is a popular and versatile approach for identifying acid sites in the field of catalysis. It can count the amount of acid sites based on their capacity to collect probe base molecules[36-38]. Because the ammonia molecule is extremely basic, it forms strong bonds with the Brønsted acid sites[39]. It may also attach less firmly to Lewis acid sites; however, in certain situations, distinguishing between Brønsted and Lewis acid sites may be problematic[40]. This problem may be overcome by doing a TPD of amines instead of ammonia, with propylamine frequently used instead of ammonia.

Before measuring the zeolite acidity by TPD (**Figure 2.11**), several steps must be taken. The most important step is pretreatment of the catalyst; this step is done by passing a low-pressure flow of inert gas at room temperature, raising the temperature to a high temperature, and cleaning the catalyst surface. Afterwards, at a suitable temperature, ammonia molecules are introduced to a dehydrated catalyst, where saturation of NH_3 on the catalyst acidic sites be accomplished. Then a temperature-programmed heating procedure is used to have the ammonia molecules desorbed as the temperatures increase. A thermal conductive detector (TCD) can detect and quantify the emitted ammonia, and the data is often displayed in the form of a temperature dependent concentration (signal intensity) curve. The area below the desorbed peak is related to the number of particles desorbed and increase proportionally[22].



Figure 2.11. The NH_3-temperature programed desorption instrument used in this investigation.

Experimental conditions

NH_3-TPD determines the total acidity of the catalyst samples. The analyses were carried out in a Micromeritics AutoChem II equipped with a TCD detector. Prior to the analysis, impurities were removed from the sample by heating it up to 550℃ under a He flow (50 ml. min^{-1}) and maintaining this temperature for 45 min. Afterwards, the sample was cooled down to 150℃ and, once the TCD signal stabilized, the NH_3 was injected (150 µl.min^{-1}) until saturation. Finally, the desorption of the chemisorbed NH_3 was conducted by heating the sample up to 550℃ using a heating ramp rate of 5℃. min^{-1}.

2.6.4 Brunauer, Emmett and Teller (BET) analysis

In the realm of heterogeneous catalysis, the surface area plays a crucial role in catalytic activity. BET is the foundation of a significant analytical approach for measuring the specific surface area of a substance. There are several techniques for measuring surface area, and each approach may provide distinct results. The majority of approaches are based on the physisorption of nitrogen (N_2), and either a single point method or a multipoint method is used

to compute the surface area. The BET method, invented in 1938 and named after Brunauer, Emmet, and Teller, is a popular and commonly used approach for estimating surface area[41-44].

In surface science, the BET technique is commonly used to calculate the surface areas of materials through physical adsorption of gas molecules. The following formulae are used to calculate total surface area S_{total} and specific surface area S:

$$S_{BET} = \frac{(v_m N_S)}{\mathrm{V}} \quad (2\text{-}10)$$

$$v_m = v_a \left(1 - \frac{P}{P_0}\right) \quad (2\text{-}11)$$

where:

N is the Avogadro's number (6.022×10^{23} mol^{-1}),

S: cross section of the adsorbing species,

v_a : volume of gas adsorbed at normal pressure and temperature, in ml;

v_m : amount of gas adsorbed at standard temperature and pressure, in ml, to sustain a monolayer absorption on the surface of the sample;

P: partial vapour pressure of adsorbate in equilibrium with the surface at -196℃ (liquid nitrogen controlled), in Pa;

P_0 = the saturation pressure of the adsorbate gas, in Pa;

α: mass of sample (g).

Experimental conditions

In the present study the surface areas of the samples were determined by the BET method using a Micrometrics ASAP2000 (Gemini) instrument as shown in **Figure 2.12**. Measurement of the surface area was achieved by N_2 physisorption at -196℃, the temperature of liquid nitrogen. Before each measurement, the sample was degassed for 1 h at 100℃ under flowing N_2. The sample tube (with sample) was first evacuated, and the void volume of the

apparatus measured using helium. Afterwards the sample tube was again evacuated after immersed into liquid nitrogen, followed by adsorption of the nitrogen gas. The pressure drops versus volume of nitrogen adsorbed was then recorded, which could be used to calculate the surface area according to the method described above.

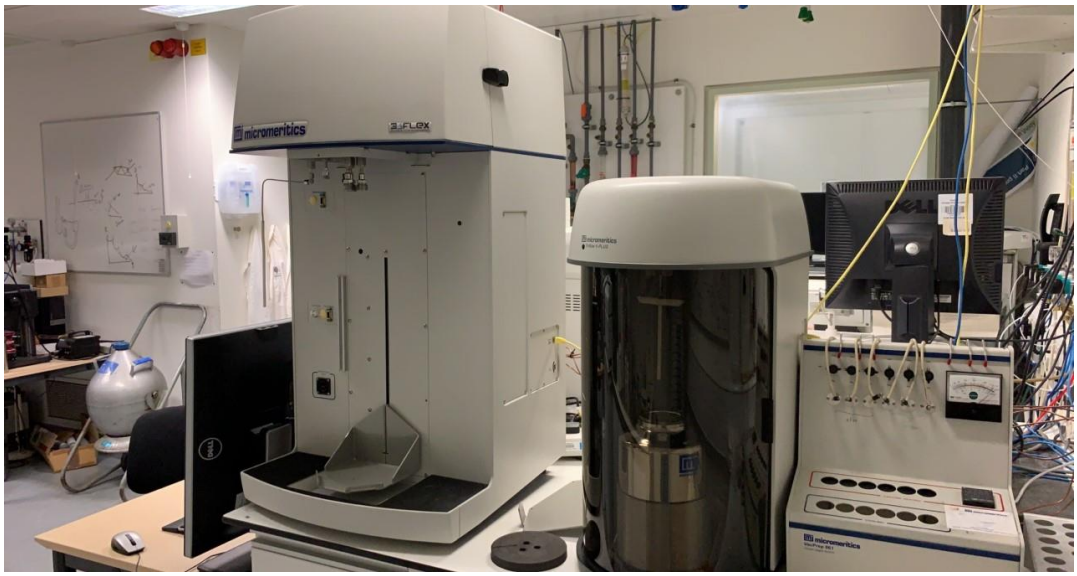


Figure 2.12. The Brunauer, Emmentt and Teller (BET) instrument used in this investigation.

2.6.5 Scanning Electron Microscopy (SEM)

Scanning electron microscopy (SEM) is a robust and well-established method that has been extensively used in a variety of scientific applications to examine materials. As shown in **Figure 2.13** the components of a standard scanning electron microscope include the electron gun, condenser lenses, apertures, scanning mechanism, and specimen chamber[45, 46]. The electron cannon creates the electron beam in a high vacuum and is placed at the top of the electron column. Normally, a tungsten filament is used to produce free electrons by thermionic emission at around 2700 K. The electron beam is then accelerated toward an anode by a high voltage ranging from 200 V to 30 kV, before going *via* condenser lenses and a set of apertures to generate a convergent electron beam that is focused to a size one thousand times smaller than its initial size. Accordingly, condenser lenses are principally responsible for controlling

the strength of the electron beam, whilst apertures operate to minimise and eliminate extraneous electrons from the lenses[46]. Finally, the pictures are created by scanning the beam over the surface of the specimen, causing electrons to be released from the specimen and captured by a properly positioned detector[45]. The specimen chamber is positioned in the lowest section of the column, above the specimen stage and controls, where the secondary electron detector is installed. A goniometer may be used to regulate the stage's x-y-z movement, 360º rotation, and 90º tilt.

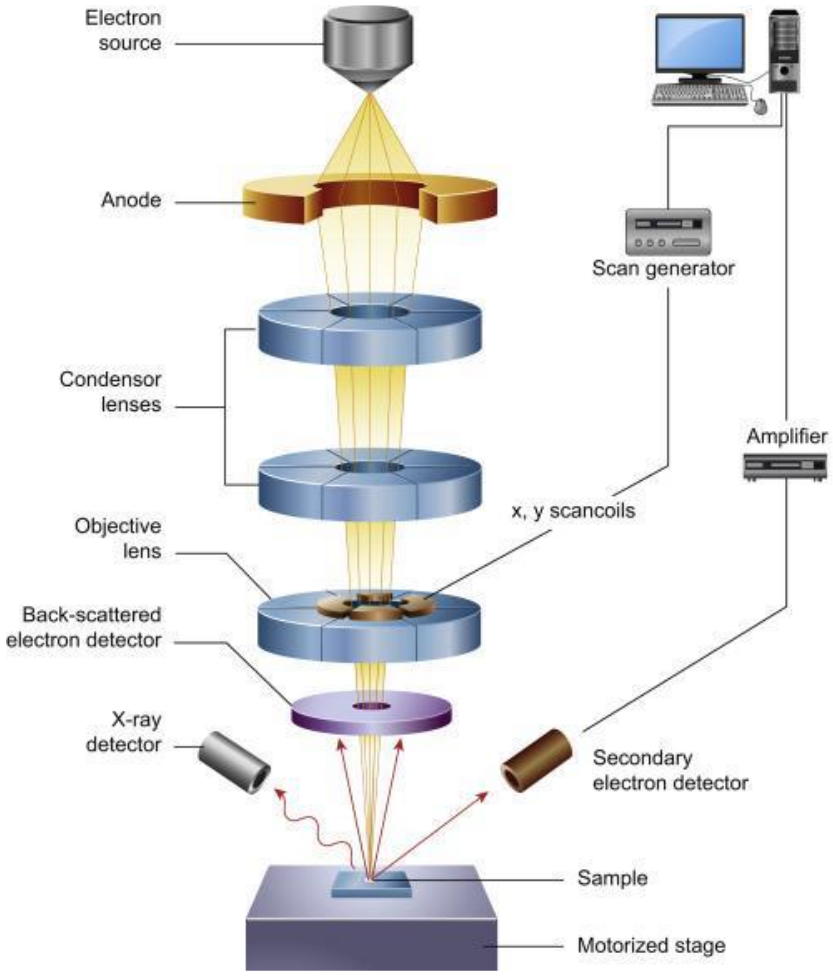


Figure 2.13. A schematic illustration of a scanning electron microscope (SEM). Adapted from[45].

SEM uses two distinct forms of signals, known as secondary and backscattered electrons, to visually examine the surface of a specimen. These electrons are dispersed in

different directions. There are two distinct ways in which the specimen and the electron beam interact with one another, and both of these ways may result in the generation of secondary and backscattered electrons. The production of secondary electrons results from the inelastic collision and scattering of incoming electrons with electrons that are already present in the material. With a precision of around 10 nm or better[46], the surface structure of a material may be deduced by using this signal as a probe. It is possible to resolve topographical contrast and atomic number contrast further from the surface of the material with a resolution of >1 micrometer by using backscattered electrons, which are the result of an elastic collision and scattering event between incident electrons and specimen nuclei or electrons[46]. Backscattered electrons are a result of an elastic collision and scattering event between incident electrons and specimen nuclei or electrons.

Experimental conditions

A scanning electron microscope (ZEISS sigma 300) was used to characterize the surface morphology of the samples before and after the catalytic cracking process. Images were taken using the Inlens detector of the Zeiss Sigma 300 Scanning Electron Microscope. The samples were coating with a carbon in a mini sputter for 300 seconds. Images were taken at 5 KV at different magnifications.

2.6.6 Energy dispersive X-ray analysis (EDX)

An X-ray method known as EDX is used in the process of determining the elemental make-up of a sample. Inside of the scanning electron microscope, the sample is subjected to a barrage of electron beams in order to perform an EDX Analysis. An electron in the inner shell is excited by the incoming beam, which then causes the electron to expel itself, which ultimately leads to the development of an electron hole inside the atom's electronic structure.

An electron from an outer shell with a higher energy level will ultimately move into a place that was previously held by an inner shell electron that was expelled. However, in order to be possible, the outer electron that is being transferred has to let part of its energy go in the form of X-ray[45, 47].

The amount of energy that is given off by the transferring electron is dependent not only on which shell it is moving from, but also on which shell it is moving to. In addition, the process of transfer results in the emission of X-rays by the atoms of each element, each of which have a distinct amount of energy. In this way, the identification of the atom from which the X-ray was produced may be determined by measuring the quantities of energy that are present in the X-rays that are being released by a specimen while it is being bombarded by an electron beam[45, 48].

The EDX detector is used to determine the ratio of the total number of emitted X-rays to their total energy. The element that the X-rays were released from has an effect on the energy level of the X-rays that they emit. The energy of each individual X-ray is converted into a voltage signal of a size proportionate to its magnitude by the EDX detector. This is accomplished by a method that consists of three stages. Ionization of the atoms is the first step in the process of converting the X-ray into a charge. Second, the field effect transmitter amplifier changed this voltage signal into a charge so it could be sent. In the last step, the voltage signal is sent into the pulse processor so that it may be measured. The amplifier produces a voltage ramp as its output, with each X-ray manifesting as a step along the ramp in terms of its voltage value[45, 48].

Experimental conditions

The surface element concentrations were analyzed by energy-dispersive X-ray spectroscopy (EDX; ZEISS EVO). EDX analysis was performed from a wide-angle general surface at 15 KV.

2.6.7 Transmission Electron Microscopy (TEM)

In the same way as scanning electron microscopy (SEM) transmission electron microscopy (TEM) is an electron microscopy, is also a kind of electron microscopy that may be used for chemical analysis, the study of the development of layers, as well as the composition and flaws in materials. Transmission electron microscopy, often known as TEM, is a technique that may be used for the purpose of better comprehending the interior microstructure of materials on the nanoscale scale. Real-space pictures of materials may be produced, depending on the imaging settings, with resolutions on the scale of a few tenths to a few nanometers, and diffraction information can be collected concurrently from particular locations in the images. Under certain imaging conditions, variations in the intensity of electron scattering across a thin specimen can be used to image strain fields, defects such as dislocations and second-phase particles, and even atomic columns in materials[47, 49]. This is possible because of the fact that the intensity of electron scattering varies across the specimen. A transmission electron microscope (TEM) may be subdivided into numerous distinct subtypes, including an analytical electron microscope, a high-resolution transmission electron microscope (HRTEM), and a scanning transmission electron microscope (STEM) (AEM). Quantum wells, quires, and dots may all be analysed using a HRTEM to determine their quality as well as their form, size, and density. The transmission electron microscopy (TEM) method can only be used to study thin materials, in contrast to the scanning electron microscopy (SEM) approach, which can study any sample[47, 49, 50]. The electron column of the transmission electron microscope (TEM) is seen in **Figure 2.14**. This column is comprised of the illuminating system, the objective lens/stage, and the imaging system, all of which function in a vacuum.

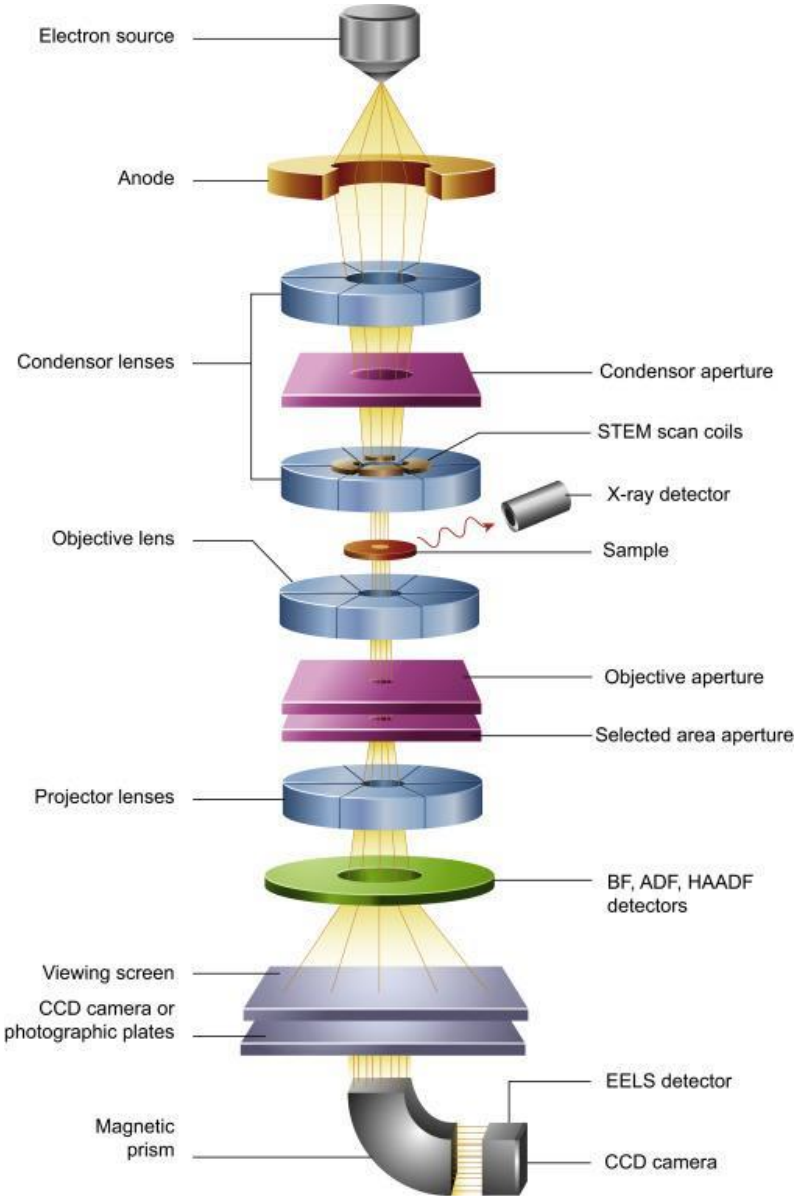


Figure 2.14. A schematic illustration of a Transmission electron microscope (TEM). Adapted from[45].

The electrons that are released from the electron cannon are going to be accelerated by the lighting system, and then they will be transferred to the specimen. An electron beam of accelerated electrons (with an energy in the range of 20 – 1000 keV) is formed by passing the electrons through a series of condenser lenses, which results in the beam having the appropriate diameter. After that, the electron beams collide with the specimen that is situated on the stage, which is subsequently moved in front of the objective lens. Based on the principles of electron optics, the objective lens creates a picture of the electron density distribution at the exit surface

of the specimen[50]. The diffraction, projection, and intermediate lenses that are located below the objective lens in the imaging system are responsible for the following formation and magnification of the numerous pictures that are created, as well as the diffraction pattern. These lenses magnify either the diffraction pattern or the picture onto a fluorescent screen, which then turns the electrons into a visible light signal that can be seen and recorded using a detector such as a CCD or a television camera.

Experimental conditions

While the powdered samples are in eppendorf tubes with ethanol. The amount of solid sample in the suspension should be between 0.1% and 1%. The solid sample in the suspension is kept in an ultrasonic water bath until it is completely homogeneously dispersed. Care should be taken to avoid any visible lumps. The resulting suspension is dripped 3-5 µl onto the carbon-coated grid fixed with the help of a micropipette. The substance placed on the carbon-coated grill is waited until it dries completely. The dried sample is put into the Hitachi HT-7700 brand device with Lanthanum hexaboride (LaB6) electron gun, operating under accelerating voltage in the range of 40-120 kV. As the device can switch from search mode (viewing the on-screen camera) to high-quality, full-size picture capture mode (main camera mode) with the push of a button, it enables quick image capture of the selected area.

2.6.8 X-ray photoelectron spectroscopy (XPS)

In the middle of the 1960s, Siegbahn and his research group were responsible for the development of X-ray photoelectron spectroscopy[51]. When metals oxide is loaded onto zeolite catalyst, it is essential to evaluate the oxidation states of the metal species before and after synthesis. The X-ray photoelectron spectroscopy (XPS) technique is used to characterise the surface region of materials because it provides information on the elemental composition, the oxidation state of elements, and the dispersion of one phase over another. This information is obtained by analysing the energy distribution of electrons ejected from the material when it is

exposed to X-rays of a well-defined energy. XPS is used to characterise the surface region of materials because it provides information on X-ray photoelectron spectroscopy (XPS) identifies the specific chemical elements that are located at the surface as well as the type of the chemical bond that exists between these atoms. It is unable to identify hydrogen or helium, but it can detect the other elements[51-53].

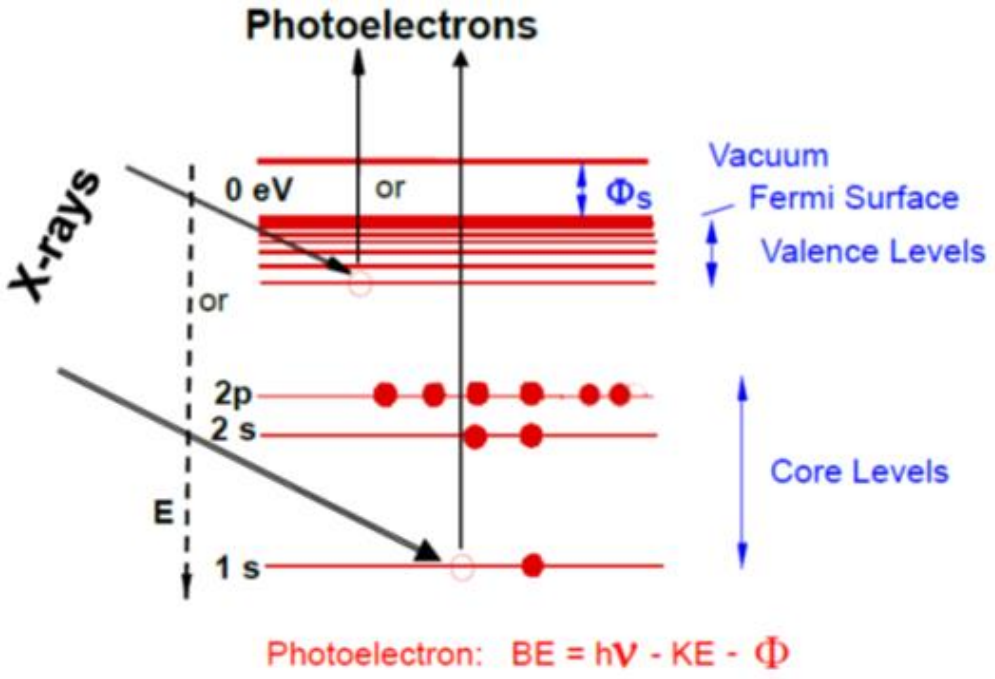


Figure 2.15. The energy distribution of the photoelectrons released in XPS. Adapted from [54].

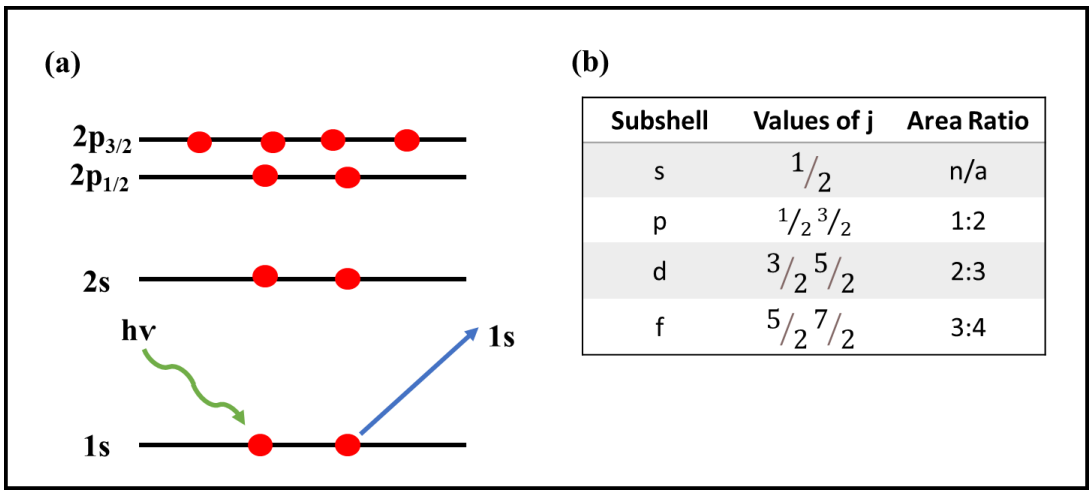
As shown in **Figure 2.15**, the photoelectron emission principle is the foundation of XPS. In a typical XPS spectrum, some of the photo-ejected electrons inelastically scatter through the sample to the surface, while others undergo prompt emission and suffer no energy loss in escaping the surface and entering the surrounding vacuum. This is because prompt emission occurs before the photo-ejected electrons inelastically scatter through the sample. After being photo-ejected into the vacuum, these electrons are captured by an electron analyzer, which then determines the amount of kinetic energy that they possess. An electron energy analyzer will create an energy spectrum that demonstrates the relationship between the

intensity (number of photo-ejected electrons vs time) and the binding energy (the energy the electrons had before they left the atom). There is a one-to-one correspondence between a significant energy peak in the spectrum and a particular element[52].

Irradiating the sample with X-rays of energy $h\nu$ causes it to be exposed. The kinetic energy, or KE, of the photoelectrons that have been released is measured. After that, the work function (ϕ) of the instrument is used in order to compute the binding energy (BE) of the photoelectrons that have been emitted. This connection may be explained as given in eq. (2-12). In addition, the chemical environment of the atom may cause a change in the binding energy of up to several eVs in either direction. Therefore, XPS has the potential to provide information on the elements that are present on the surface, the oxidation state of those elements, surface functional groups, and surface adsorbates that are present.

$$BE = h\nu - KE - \phi \quad (2\text{-}13)$$

XPS emission of a photoelectron and notation (i.e., nl_j) for its core level are shown in **Figure 2.16,** where n is the main quantum number, l denotes the quantum number of angular momentum, and j denotes the equation (l + s), where s denotes the spin angular momentum number and may take on the values ±1/2. With the exception to the s levels (l = 0), all orbital levels result in a doublet, with the binding energies of the two potential states varying. This phenomenon is called spin-orbit splitting (or j-j coupling) [51, 55]. Additionally, the peaks will have certain area ratios dependent on the degeneracy of each spin state. This refers to the amount of distinct spin combinations that may give rise to the total j value as illustrated in **Figure 2.16b**[52]. For instance, when n = 2 and l = 1, the value of j for the 2p spectrum will be 1/2 and 3/2. It is expected that the area ratio for the two spin orbit peaks, $2p_{1/2}$ and $2p_{3/2}$, will be equal to one another, or 1:2. This will indicate that there are two electrons in the $2p_{1/2}$ level and four electrons in the $2p_{3/2}$ level. When an analysis of the spectra of the p, d, and f core levels is conducted, these ratios should be taken into consideration.



(b)

Subshell	Values of j	Area Ratio
s	$^1/_2$	n/a
p	$^1/_2$ $^3/_2$	1:2
d	$^3/_2$ $^5/_2$	2:3
f	$^5/_2$ $^7/_2$	3:4

Figure 2.16. (a) Emission of a photoelectron in XPS, (b) Spin-orbit splitting j values and peak area ratios. Adapted from[56].

Experimental conditions

XPS measurements were obtained using a Specs Flex-Mod system. Monochromatized AlKα x-rays were used in non-focusing mode at 15 kV and 400 W with an excitation energy of 1486.6 eV is used for the analysis. Pass energy of 100 eV step size 1 eV and 40 eV step size 0.1 eV was used for the survey spectra and high-resolution elemental spectra, respectively. The photoelectrons were detected by the 150 mm radius hemispherical analyzer PHOBIOS 150 with a 2D CCD detector. A low energy flood gun is used for the charge neutralization during the measurements. Analyzer lens and scan mode are chosen for the medium are 1.5 kV and fixed analyzer transmission, respectively. To avoid charging effects, data were processed using CasaXPS peak fitting software and binding energies were referred to the C 1s peak with a 284.00 eV correction.

2.7 References

1. Judit, A.; Eleni, A.; Angelos, L.; Michael, S.; Merete, H. N.; Aud, B.; Johan, E. H.; Gisle, Ø., In situ catalytic upgrading of biomass derived fast pyrolysis vapours in a fixed bed reactor using mesoporous materials. *Microporous and Mesoporous Materials*, **2006,** *96* (1), 93-101.
2. Stefanidis, S. D.; Kalogiannis, K. G.; Iliopoulou, E. F.; Lappas, A. A.; Pilavachi, P. A., In-situ upgrading of biomass pyrolysis vapors: Catalyst screening on a fixed bed reactor. *Bioresource Technology*, **2011,** *102* (17), 8261-8267.
3. Steehler, J. K., Instant Notes: Analytical Chemistry (Kealey, D.; Haines, P. J.). *Journal o f Chemical Education*, **2003,** *80* (3), 267.
4. Mut Günzler, I. I.; Williams, A., Handbook of analytical techniques,. *Evolution*, **2001,** *1*.
5. Imadeddine, A.; Anouar, E.; Joachim, F.; Raphael, H.; Didier, T.; Jerome, V., Feasibility of the preparation of silica monoliths for gas chromatography: Fast separation of light hydrocarbons. *Journal of Chromatography A*, **2015,** *1383*, 127-133.
6. Sun, J. H.; Guan, F. Y.; Zhu, X. F.; Ning, Z. W.; Ma, T. J.; Liu, J. H.; Deng, T., Micro-fabricated packed gas chromatography column based on laser etching technology. *Journal of Chromatography A*, **2016,** *1429*, 311-316.
7. Grob, R. L.; Barry, E. F., Modern practice of gas chromatography. *John Wiley & Sons*, **2004**.
8. Sevcik, J. G., Detectors in gas chromatography. *Elsevier*, **2011**.
9. Pavia, D. L.; Lampman, G. M.; Kriz, G. S.; Vyvyan, J. A., Introduction to Spectroscopy. *Cengage Learning*, **2014**.
10. Hübschmann, H.-J., Handbook of GC-MS: fundamentals and applications. J*ohn Wiley & Sons*, **2015**.
11. De Hoffmann, E.; Stroobant, V., Mass spectrometry: principles and applications. *John Wiley & Sons*, **2007**.
12. Sparkman, O. D.; Penton, Z.; Kitson, F. G., Gas chromatography and mass spectrometry: a practical guide. *Academic press*, **2011**.
13. Leonid, M. B., Theory of gas chromatography. In Gas Chromatography, Second ed.; Poole, C. F., Ed. *Elsevier*, **2021**; pp 19-97.
14. Poole, C., Gas chromatography. *Elsevier*, **2012**.
15. Ki-Hyun, K., The properties of calibration errors in the analysis of reduced sulfur compounds by the combination of a loop injection system and gas chromatography with pulsed flame photometric detection. *Analytica Chimica Acta*, **2006,** *566* (1), 75-80.
16. Shao, Q.; Wang, P.; Tian, H.; Yao, R.; Sun, Y.; Long, J., Study of the application of structural catalyst in naphtha cracking process for propylene production. *Catalysis Today*, **2009,** *147*, S347-S351.

17. Liu, B.; France, L.; Wu, C.; Jiang, Z.; Kuznetsov, V. L.; Al-Megren, H. A.; Al-Kinany, M.; Aldrees, S. A.; Xiao, T.; Edwards, P. P., Methanol-to-hydrocarbons conversion over MoO_3/H-ZSM-5 catalysts prepared via lower temperature calcination: a route to tailor the distribution and evolution of promoter Mo species, and their corresponding catalytic properties. *Chemical Science,* **2015,** *6* (9), 5152-5163.
18. Alabdullah, M.; Shoinkhorova, T.; Rodriguez-Gomez, A.; Dikhtiarenko, A.; Vittenet, J.; Ali, O. S.; Morales-Osorio, I.; Xu, W.; Gascon, J., Composition-performance Relationships in Catalysts Formulation for the Direct Conversion of Crude Oil to Chemicals. *ChemCatChem,* **2021,** *13* (7), 1806-1813.
19. Richard, D.; Mikhail, A. V.; Ameen, A. A.-M.; Chengdong, Y.; Dmitriy, A. F.; Muneer, A. S.; Alexey, J. K.; Rustam, R. D.; Almaz, L. Z.; Saar, D. F.; Ranel, I. G.; Ilfat, Z. R.; Michael, K.; Vladimir, V. K.; Konstantin Yu, P., Oil dispersed nickel-based catalyst for catalytic upgrading of heavy oil using supercritical water. *Fuel,* **2022,** *313,* 122702.
20. Božena, V.; Elena, H.; Pavol, H.; Jana, Č.; Michal, H.; Michal, K.; Vladimír, J., Two-stage thermal and catalytic cracking of polypropylene using natural clinoptilolite in a catalytic step to petrochemicals and fuels. *Journal of Analytical and Applied Pyrolysis,* **2022**, 105679.
21. Duckett, S.; Gilbert, B.; Cockett, M., *Foundations of molecular structure determination*. *Oxford University Press*, **2015**.
22. Che, M.; Védrine, J. C., Characterization of solid materials and heterogeneous catalysts: From structure to surface reactivity. *John Wiley & Sons*, **2012**.
23. Eley, C. W. The rational design of photocatalytic semiconductor nanoparticles. *Oxford University, UK*, **2014**.
24. Jia, T. Photocatalytic hydrogen production over layered materials. *University of Oxford,* **2014**.
25. Farmelo, G., The discovery of X-rays. *Scientific American,* **1995,** *273* (5), 86-91.
26. Frank H. Chung; Smith, D. K., Industrial applications of X-ray diffraction. *Taylor & Francis*, **1999**.
27. Steven A. Bradley; Robert W. Broach; Thomas M. Mezza; Sesh Prabhakar; Sinkler, W., Zeolite Characterization. In Zeolites in Industrial Separation and Catalysis, Kulprathipanja, S., Ed. *John Wiley & Sons*, **2010**.
28. Leng, Y., *Materials characterization:* introduction to microscopic and spectroscopic methods. *John Wiley & Sons*, **2013**.
29. Iwashita, N., X-ray Powder Diffraction. In Materials science and engineering of carbon: characterization, Inagaki, M.; Kang, F., Eds. Butterworth-Heinemann: *Elsevier,* **2016**.
30. Thomas, J. M.; Thomas, W. J., Principles and practice of heterogeneous catalysis. *John Wiley & Sons*, **2014**.
31. Waseda, Y.; Matsubara, E.; Shinoda, K., X-ray diffraction crystallography: introduction, examples and solved problems. *Springer Science & Business Media,* **2011**.

32. Brundle, C. R.; Evans, C. A.; Wilson, L.; Wilson, S.; Wilson, G., Encyclopedia of materials characterization: surfaces, interfaces, thin films. *Butterworth-Heinemann,* **1992**.
33. Monshi, A.; Foroughi, M. R.; Monshi, M. R., Modified Scherrer equation to estimate more accurately nano-crystallite size using XRD. *World Journal of Nano Science and Engineering,* **2012,** *160* (2), 154-160.
34. Gabbott, P., Principles and applications of thermal analysis. *John Wiley & Sons*, **2008**.
35. Ming-ming, C., Thermal Analysis. In Materials Science and Engineering of Carbon: Characterization, Michio Inagaki; Feiyu Kang, Eds. *Elsevier*, **2016**; pp 249-272.
36. Cvetanović, R. J.; Amenomiya, Y., Application of a Temperature-Programmed Desorption Technique to Catalyst Studies. *Advances in Catalysis*, **1967,** *17*, 103-149.
37. Katada, N.; Igi, H.; Kim, J.-H.; Niwa, M., Determination of the acidic properties of zeolite by theoretical analysis of temperature-programmed desorption of ammonia based on adsorption equilibrium. *The Journal of Physical Chemistry B,* **1997,** *101* (31), 5969-5977.
38. Miller, J.; Hopkins, P.; Meyers, B.; Ray, G.; Roginski, R.; Zajac, G.; Rosenbaum, N., The effect of nonframework aluminum on acidity in dealuminated mordenite. *Journal of Catalysis,* **1992,** *138* (1), 115-128.
39. Niwa, M.; Katada, N., Measurements of acidic property of zeolites by temperature programmed desorption of ammonia. *Catalysis Surveys from Asia,* **1997,** *1* (2), 215-226.
40. Juskelis, M.; Slanga, J.; Roberie, T.; Peters, A., A comparison of CaO, beta, and a dealuminated Y by ammonia TPD and by temperature programmed 2-propylamine cracking. *Journal of Catalysis*, **1992,** *138*, 391–394.
41. Brunauer, S.; Emmett, P. H.; Teller, E., Adsorption of gases in multimolecular layers. *Journal of the American Chemical Society,* **1938,** *60* (2), 309-319.
42. Dollimore, D.; Spooner, P.; Turner, A., The BET method of analysis of gas adsorption data and its relevance to the calculation of surface areas. *Surface Technology,* **1976,** *4* (2), 121-160.
43. Fagerlund, G., Determination of specific surface by the BET method. *Matériaux et Construction,* **1973,** *6* (3), 239-245.
44. Bhambhani, M.; Cutting, P.; Sing, K.; Turk, D., Analysis of nitrogen adsorption isotherms on porous and nonporous silicas by the BET and αs methods. *Journal of Colloid and Interface Science,* **1972,** *38* (1), 109-117.
45. Hübschen, G.; Altpeter, I.; Tschuncky, R.; Herrmann, H.-G., Materials characterization using nondestructive evaluation (NDE) methods. *Woodhead publishing,* **2016**.
46. Cheney, B., Introduction to scanning electron microscopy. *Materials Engineering department San Jose State University,* **2007**.
47. Sigle, W., Analytical transmission electron microscopy. *Annual Review of Materials Research,* **2005,** *35* (1), 239-314.

48. M. Abd Mutalib; M. A. Rahman; M. H. D. Othman; A. F. Ismail; J .Jaafar, Scanning Electron Microscopy (SEM) and Energy-Dispersive X-Ray (EDX) Spectroscopy. In Membrane Characterization, *Elsevier*, **2017**; pp 161-179.
49. Tang, C. Y.; Yang, Z., Transmission Electron Microscopy (TEM). In Membrane Characterization, *Elsevier*, **2017**; pp 145-159.
50. Williams, D. B.; Carter, C. B., The transmission electron microscope. In Transmission electron microscopy, *Springer*, **1996**; pp 3-17.
51. Aziz, M.; Ismail, A. F., X-Ray Photoelectron Spectroscopy (XPS). In Membrane Characterization, Hilal, N.; Ismail, A. F.; Matsuura, T.; Oatley-Radcliffe, D., Eds. *Elsevier*, **2017**; pp 81-93.
52. John F. Moulder; William F. Stickle; Peter E. Sobol; Bomben, K. D., Handbook of X-ray Photoelectron Spectroscopy. *Perkin-Elmer Corporation*, **1992**.
53. Oswald, S., X-ray photoelectron spectroscopy in analysis of surfaces. In Encyclopedia of Analytical Chemistry: Applications, Theory and Instrumentation, *John Wiley & Sons*, **2006**.
54. Adongo, J. Modification of Surfaces with Carboxymethylthio and Piperazinyl Chelating Ligands for Heavy Metal Trapping Applications. MSc Thesis, *Humboldt-Universität zu Berlin*, **2019**.
55. Briggs, D., XPS: basic principles, spectral features and qualitative analysis. In Surface Analysis by Auger and X-ray Photoelectron Spectroscopy, D. Briggs; Grant, J. T., Eds. *IM Publications*: **2003**; p 38.
56. Stevie, F. A.; Donley, C. L., Introduction to x-ray photoelectron spectroscopy. *Journal of Vacuum Science & Technology A*, **2020,** *38* (6), 063204.

Chapter 3

Effect of H-ZSM-5 with different Si/Al ratios and preparation methods for various CrO_x-H-ZSM-5 formulations on the catalytic cracking of *n*-heptane as a model compound for light naphtha

Overview

This chapter describes the effect of the SiO_2/Al_2O_3 ratio of H-ZSM-5 (MFI-type) zeolite catalysts on the catalytic cracking of naphtha. The cracking properties of zeolites for the production of light alkenes are investigated using *n*-heptane as a model compound since it is the primary constituent of light naphtha. A series of H-ZSM-5 catalysts with SiO_2/Al_2O_3 ratios = 23, 30, 50, 80, and 280 are examined in a fixed-bed unit at 550℃. Additionally, the H-ZSM-5 catalyst with SiO_2/Al_2O_3 ratio = 80 has been modified with Cr compounds in an attempt to increase the catalyst stability and light olefins selectivity under cracking conditions. It was found that higher SiO_2/Al_2O_3 values alongside the modification of H-ZMS-5 (SiO_2/Al_2O_3 = 80) with Cr oxide enhanced the yield of light olefins.

3.1 Introduction

Several research groups have explored the catalytic cracking of light alkanes (C5–C8) over different zeolites in order to understand the processes related to naphtha cracking and explain catalyst performance and reaction mechanisms[1-3]. Zeolites have been utilised extensively to break up hydrocarbons to lower molecular weight compounds, such as light olefins[4], because of their strong acidity, high thermal and hydrothermal stability, and significant resistance to deactivation by coking during the cracking process. Thus ZSM-5 -MFI (Mobil type five)-zeolite has been identified as a prime candidate for catalytic cracking[3, 5-7]. ZSM-5 is a high-silica-content synthetic zeolite[8] with a SiO_2/Al_2O_3 ratio that ranges from around 20 to almost infinite (pure Si)[9]. The catalytic activity of zeolites is attributed to the high Brønsted acidity of the bridging Si– (OH)– Al sites, which are produced when aluminium is incorporated into the silicate framework[10]. Modifying the acidity of zeolites has been shown to increase the output of light olefins. Variations in the Si/Al ratio in zeolites may alter the acidity of the catalysts. Hydrogen transfer reactions in ZSM-5 mostly occur on the catalyst's surface,

and the reactions are more visible at low Si/Al ratios and under high acidity (low pH). Higher hydrogen, BTX (benzene, toluene, and xylene) and lower light olefins are produced as a consequence of the hydrogen transfer process[11].

When transition metal compounds are incorporated into ZSM-5 zeolite, intriguing bifunctional catalysis is achieved. This is related to the production of additional Lewis acid sites in the ZSM-5 framework. Combining Brønsted acid sites for greater olefin cracking with Lewis sites for paraffinic feedstock dehydrogenation may boost light olefin yield[12]. Lewis acid sites seem to primarily accelerate C-H dissociation and dehydrogenation by boosting recombination and desorption of hydrogen, while Brønsted acid sites appear to enhance C-C cracking events. The addition of trace amounts of a Cr compound to ZSM-5 improves both the activity and selectivity of the isobutane cracking reaction[13, 14].

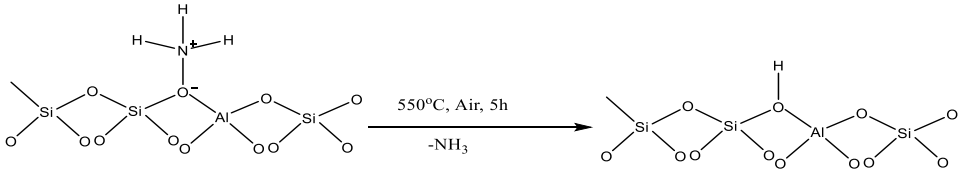
Since Frey and Huppke first reported in 1933 the dehydrogenation activity of Cr_2O_3, chromium oxide-based catalysts have been one of the most intensively researched formulations[15]. Leuna in Germany was the first to develop and market the dehydrogenation of butanes over a chromia-alumina catalyst, followed by Universal Oil Products (UOP) in United States together with Imperial Chemical Industries (ICI) in England[16]. UOP used chromia-supported alumina catalysts in the 1940s to industrially dehydrogenate butane to make butene, which was then dimerized and hydrogenated to produce high-octane aviation fuels. Since then, these catalysts have been used in several methods for the dehydrogenation of light olefins. Metal oxides such as Cr and Fe oxide enhance the ZSM-5 catalyst performance toward the production of light olefins[13, 17, 18]. A small amount of chromium and iron mixed with the zeolite enhances the reactivity of catalytic cracking of hydrocarbons, which produces high activity and high selectivity towards light olefins[14, 19]. These metals change the acidity distribution in ZSM-5 zeolite improving the catalytic performance[20, 21]. Zeolite modification using chromium oxide (Cr_2O_3) had a very positive effect on the selectivity for light olefin (between 8-17%)[13, 14, 19].

The aim of this Chapter is to study the influence of the SiO_2/Al_2O_3 ratio (i.e., 23, 30, 50, 80, and 280) of H-ZSM-5 on the selective cracking of *n*-heptane to light olefins. A zeolite with a large yield of light olefins was selected and then modified with Cr oxide to enhance the catalytic performance and gain understating about the role played by Cr_2O_3 entities on the production of light olefins.

3.2 Experimental

3.2.1 Preparation of catalysts

All the zeolites used in this thesis are commercial samples provided by Zeolyst. The zeolites were initially calcined in a static air atmosphere at 550°C for 5 h using a heating rate of 3°C.min^{-1} in order to remove the ammonium (NH_4^+) and activate the Brønsted acid sites to the H-zeolite form (**Figure 3.1**). Then, the sample was cooled and stored in dry air for further use. H-ZSM-5 samples are hereafter referred as HZ23, HZ30, HZ50, HZ80, and HZ280 that correspond to SiO_2/Al_2O_3 ratios of 23, 30, 50, 80, and 280, respectively, as listed in **Table 3.1**. The composition of each zeolite is given in **Figure 3.1A,** according to the supplier (Zeolyst International).



(3.1)

Figure 3.1. Schematic representation of the Brønsted acid site formation via ammonium cation decomposition.

Table 3.1. Si/Al ratios and surface areas for ZSM-5 zeolites from Zeolyst International.

Zeolite Products	Supplier code	SiO_2/Al_2O_3 mole ratio	Nominal cation form	Na_2O (wt.%)	Surface Area(m^2/g)
HZ23	CBV2314	22	Ammonium	0.05	439
HZ30	CBV3024E	33.1	Ammonium	0.05	443
HZ50	CBV5524G	57	Ammonium	0.05	450
HZ80	CBV8014	85.2	Ammonium	0.05	480
HZ280	CBV28014	322	Ammonium	0.05	437

Solid catalysts may be made using a number of processes; however, below only the procedures used in our studies are shown.

3.2.1.1 Impregnation method (IMP)

Transition metal-containing catalysts were synthesised using an impregnation method. In a typical procedure, the appropriate amount of the chromium (III) nitrate nonahydrate ($Cr(NO_3)_3.9H_2O$, 99%, Sigma Aldrich) was dissolved in excess deionized water and stirred on a magnetic hot plate until the salt completely dissolved. A zeolite sample (HZ80, SiO_2/Al_2O_3= 80) was then added to the solution slowly, and stirred for 3-4h at room temperature, and then at 80-100°C until all the water had evaporated. This was followed by drying at 80-100°C overnight. The catalysts were then calcined at 350°C for 5h using a heating rate of $3°C.min^{-1}$ to convert the transition metals to the oxide form. The catalysts were labelled and stored as xCr_2O_3/HZ80-IMP, where x is the chromium loading assuming the formation of Cr_2O_3 in the catalyst (5-20 wt.%).

3.2.1.2 Mechanical mixture method (MM)

The mechanical catalyst preparation method used the following procedure: in an excess of deionized water, the necessary quantity (10 wt.%) of chromium (III) oxide (Cr_2O_3, 98+%, Alfa Aesar) was dispersed through stirring on a magnetic hot plate at room temperature. After that, zeolite (HZ80, SiO_2/Al_2O_3= 80) was slowly added to the solution and stirred at room temperature for 3-4 hours before being heated to 80-100°C until all of the water had evaporated.

After that, it was dried overnight at 80-100°C. To convert the transition metals to the oxide form, the catalysts were calcined at 350°C for 5 hours at a heating rate of 3°C.min^{-1}. The catalysts were denoted and stored as 10 wt.% Cr_2O_3/HZ80-MM.

3.2.2 Characterisation of catalysts

The fresh and spent catalysts were carefully characterised by a range of techniques such as X-ray Powder diffraction (XRD), scanning electron microscopy (SEM), Energy dispersive X-ray spectroscopy (EDX), Thermogravimetric analysis (TGA), Brunauer-Emmett-Teller (BET), and X-ray Photoelectron Spectroscopy (XPS).

Below, are brief details of the characterisation techniques and the experimental conditions are described, further details are outlined in Chapter 2.

The X-ray powder diffraction patterns were collected by means of a Bruker-Eco D8 ADVANCE diffractometer (Cu-Kα radiation, λ = 1.5406 Å) working at 40 kV–25 mA and equipped with a Lynxeye detector. Samples were scanned range of 2θ from 5° to 90°.

Thermogravimetric analysis (TGA) in flowing air enables the determination of the type of carbon deposited in the spent samples. The catalyst sample was heated from room temperature to 1000°C at a heating rate of 10°C min^{-1} under ambient atmosphere with a 100 mL min^{-1} flow rate of dry compressed air to burn off all so-called "coke" deposits. Between 10 and 20 mg of spent sample was loaded into a small alumina crucible for the test.

N_2 physisorption measurements were carried out at a liquid nitrogen temperature using Micromeritics Micro Active (TriStar II Plus). Before the analysis, samples were weighed and placed in quartz tubes. Then, degassed under vacuum at 50°C for 24 hours to remove impurities on the sample surface. The BET surface area was determined by nitrogen gas adsorption at -196°C with a Micromeritics brand 3flex model device. Adsorption and desorption points were calculated between 0 and 1 relative pressure (p/p0).

A scanning electron microscope (ZEISS EVO) was used to characterize the surface morphology of the samples before and after the catalytic cracking process. Images were taken using the Inlens detector of the Zeiss Sigma 300 Scanning Electron Microscope. Samples were coated with carbon in a mini sputter for 300 seconds. Images were taken at 5 KV at different magnifications. The surface element concentrations were analyzed by energy-dispersive X-ray spectroscopy (EDX; ZEISS EVO). EDX analysis was performed from a wide-angle general surface at 15 KV.

X-ray photo-electron spectroscopy (XPS) measurements were carried out in a Specs Flex-Mod system. Monochromatized Al K_α x-rays were used in non-focusing mode at 15 kV and 400 W with an excitation energy of 1486.6 eV for the analysis. Pass energy of 100 eV (step size 1 eV) and 40 eV (step size 0.1 eV) was used for the survey spectra and high-resolution elemental spectra, respectively. The photoelectrons were detected by the 150 mm radius hemispherical analyzer PHOBIOS 150 with a 2D CCD detector. A low energy flood gun is used for the charge neutralization during the measurements. Analyzer lens and scan modes chosen for the medium are 1.5 kV and fixed analyzer transmission, respectively. To avoid charging effects, data were processed using CasaXPS peak fitting software and binding energies were referred to the C 1s peak with a 284.00 eV correction.

3.2.3 Experimental conditions

The catalytic cracking of *n*-heptane as a model compound in light naphtha was carried out in a fixed-bed reactor. The catalyst bed was heated up to 500°C at 5°C. min^{-1} under an atmospheric pressure flow of nitrogen (20 $ml.min^{-1}$) as an inert carrier gas. The catalyst was left for 1h at 550°C under N_2 flow to ensure that it was fully dehydrated. Subsequently, *n*-heptane (≥99%) as feedstock was pumped into the reactor with a 0.1 $ml.min^{-1}$ flow rate for all experiments.

The light hydrocarbon products (C_1-C_4) were analyzed by an online gas chromatograph (PerkinElmer, Claurs 580 GC) every 30 minutes during 4 hours of time-on-stream (TOS) using a thermal conductivity detector (TCD) to analyze the non-hydrocarbons (i.e., CO, CO_2, N_2, O_2) and an ionized flame detector (FID) for light hydrocarbon products (C_1-C_4). Liquid products were collected every 1h in the separator through the condenser and analyzed by gas chromatograph-mass spectrometer using MS detector (Shimadzu GC/MS-QP 2010 SE).

3.3 Results and Discussion

3.3.1 Effect of H-ZSM-5 with different Si/Al ratios on the cracking of *n*-heptane

3.3.1.1 Pre-reaction analysis of catalysts

3.3.1.1.1 X-ray diffraction (XRD) analysis

Figure 3.2 shows the X-ray diffraction patterns between $5^o < 2\theta < 90^o$ of the H-ZSM-5 with diverse SiO_2/Al_2O_3 ratios for the fresh samples. According to the literature[22-24], the peaks belonging to an MFI-type zeolite were seen in the X-ray diffraction patterns of samples with various SiO_2/Al_2O_3 ratios in **Figure 3.3**. This suggests that the SiO_2/Al_2O_3 ratio has little effect on the MFI structure. It has been noted that the H-ZSM-5 zeolite inherent lattice structure is unaltered, with no new phases formed. However, the intensity of the H-ZSM-5 peaks were enhanced as the SiO_2/Al_2O_3 ratio increased.

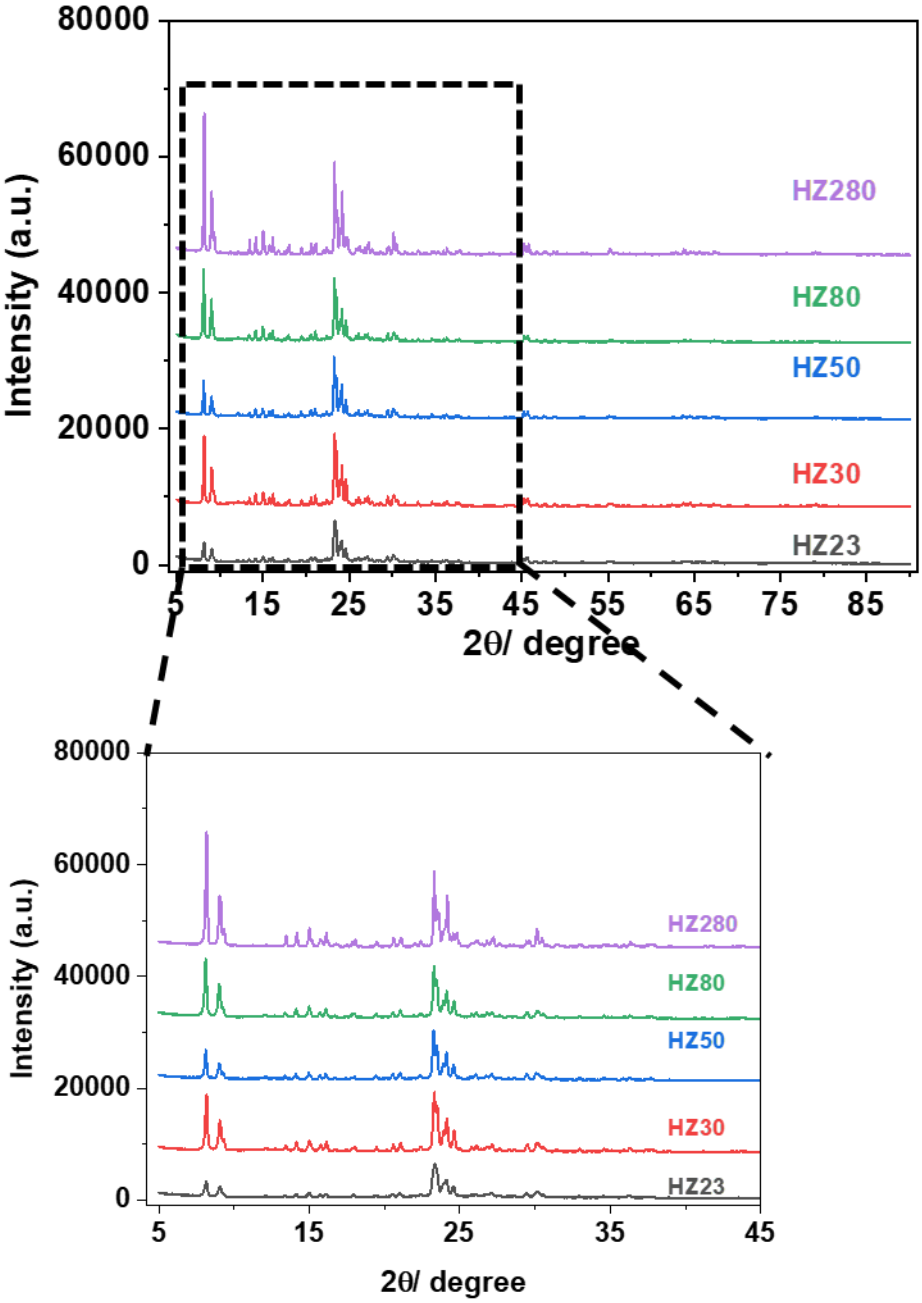


Figure 3.2. Comparison of powder X-ray diffraction patterns of the H-ZSM-5 zeolite for fresh samples with SiO_2/Al_2O_3 (23, 30, 50, 80, and 280) molar ratios.

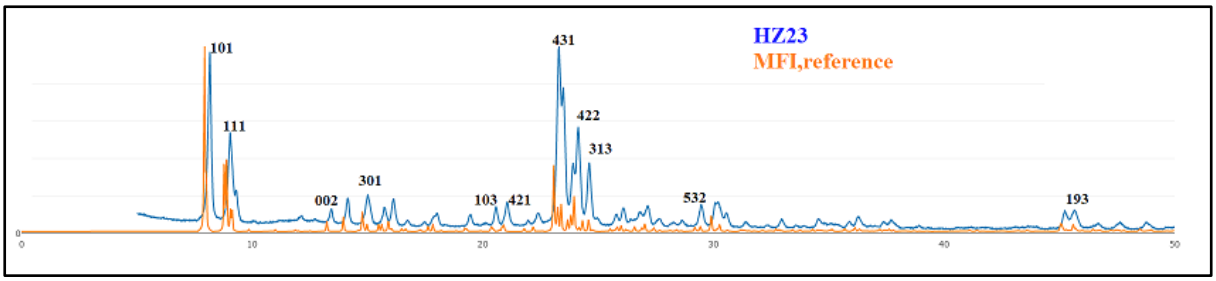


Figure 3.3. Comparison of X-ray powder diffraction patterns for fresh HZ23 catalyst and ZSM-5 reference (MFI type).

3.3.1.1.2 Thermogravimetric analysis (TGA)

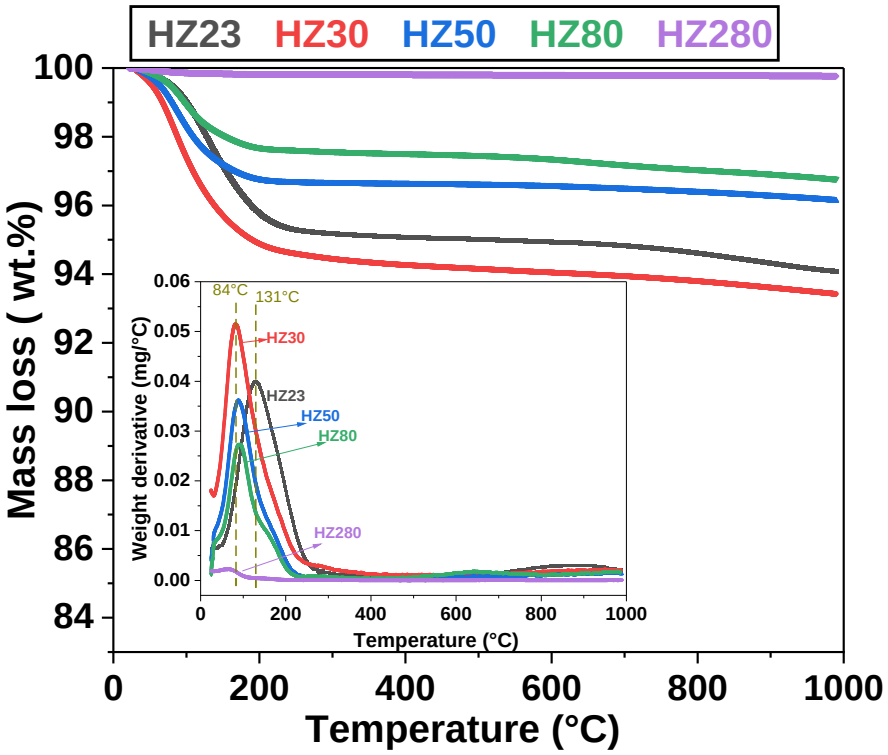


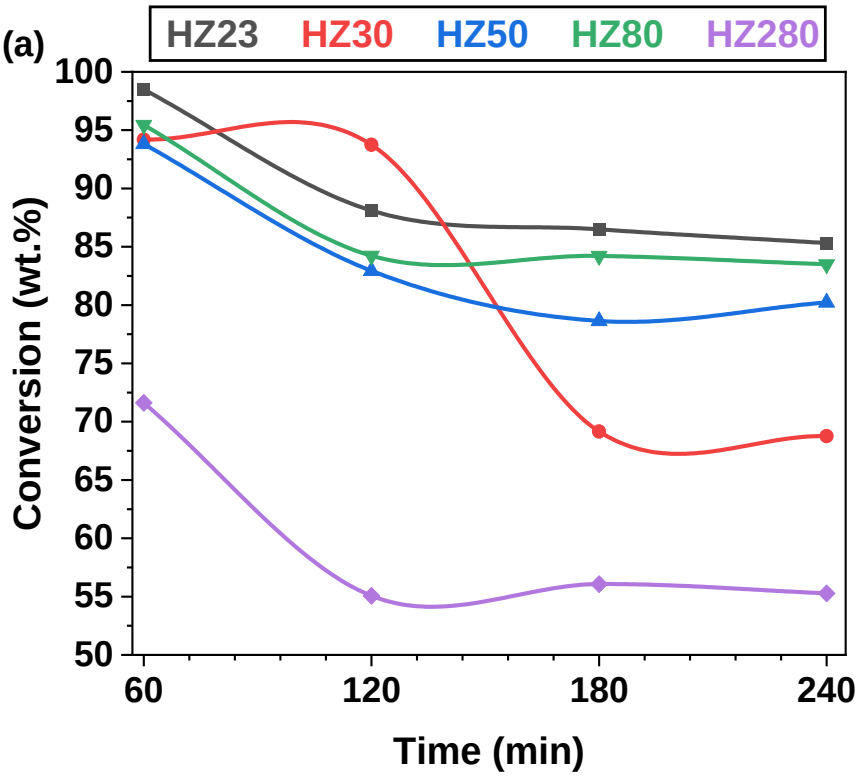
Figure 3.4. Thermogravimetric analysis (TGA) samples under air flow for zeolite with different SiO_2/Al_2O_3 ratios. Inset plot shown the weight derivative thermogravimetry (DTG) curves (b) of the fresh H-ZSM-5 zeolite for fresh samples with SiO_2/Al_2O_3 (23, 30, 50, 80, and 280) molar ratios.

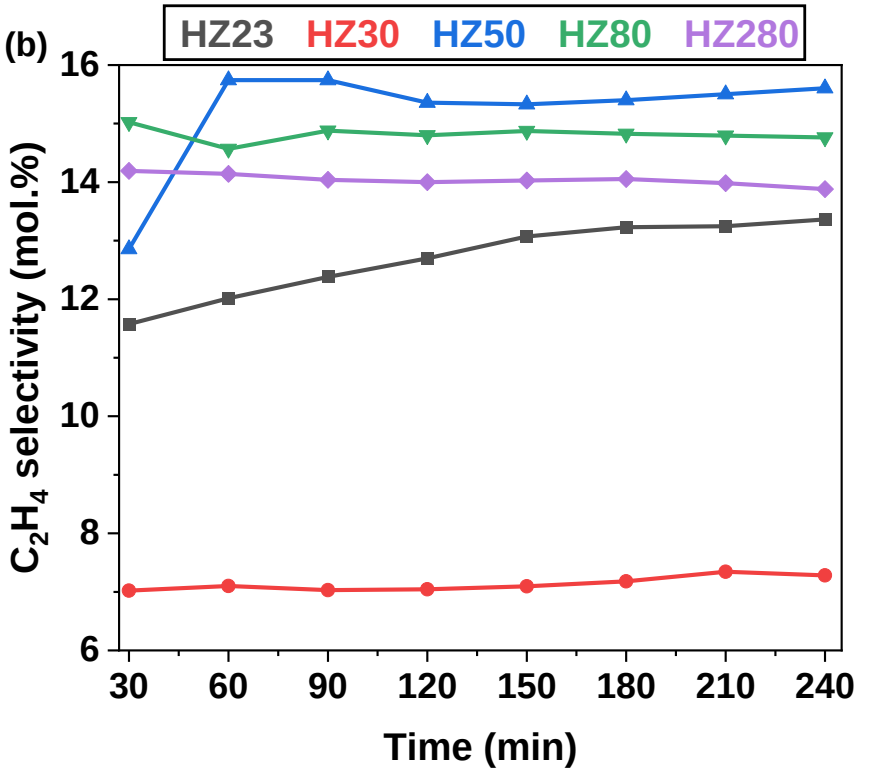
The Thermogravimetric (TGA) profiles for the fresh H-ZSM-5 with different ratios of SiO_2/Al_2O_3 is shown in **Figure 3.4**. The data show one primary weight loss step, which is about 4.8% for samples with lower SiO_2/Al_2O_3 ratio and about 1.4% for samples with higher

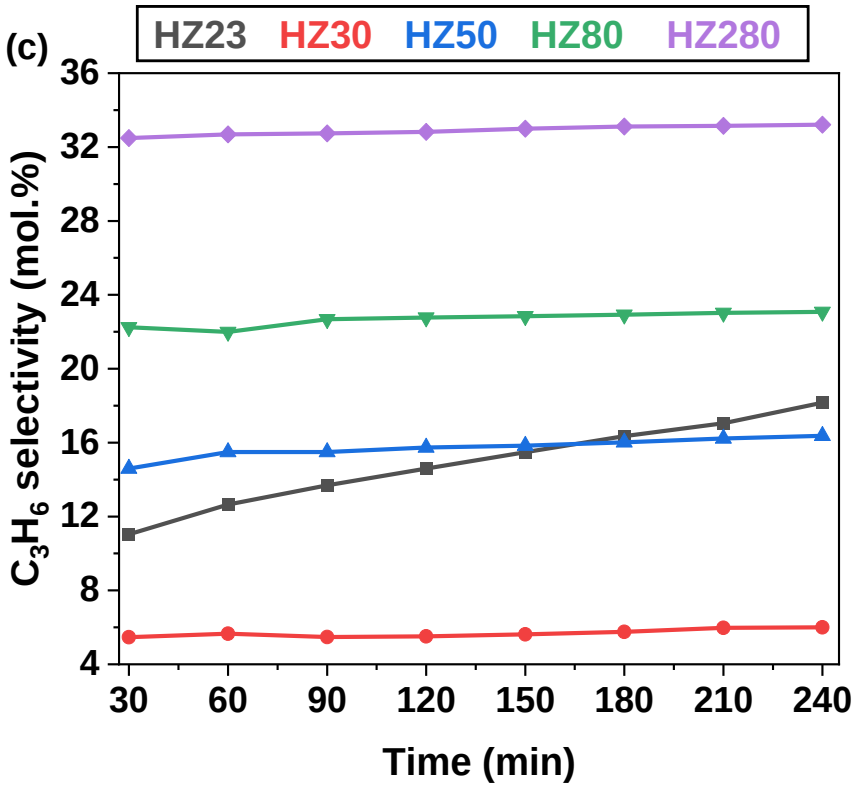
SiO_2/Al_2O_3 ratio. The process starts when the physically-adsorbed water from the ZSM-5 is released at a temperature below 200°C.

3.3.1.2 Evaluation of catalyst performance

The catalytic cracking of *n*-heptane was evaluated over a fixed bed reactor at 550°C and atmospheric pressure for 4h. Initially, the catalytic performances of a series of H-ZSM-5 zeolites with different SiO_2/Al_2O_3 ratios were evaluated to select the zeolite with the highest (optimum) yield of light olefins. The overall carbon balance for these tests was between 94 and 97 % including residual carbon; these values were calculated according to equation (2-4) as given in Chapter 2 (experimental methods). These numbers are within the expected range for cracking reactions.




(b)
HZ23
HZ30
HZ50
HZ80
HZ280
C_2H_4 selectivity (mol.%)
16
14
12
10
8
6
30
60
90
120
150
180
210
240
Time (min)


(c)
HZ23
HZ30
HZ50
HZ80
HZ280
C_3H_6 selectivity (mol.%)
36
32
28
24
20
16
12
8
4
30
60
90
120
150
180
210
240
Time (min)

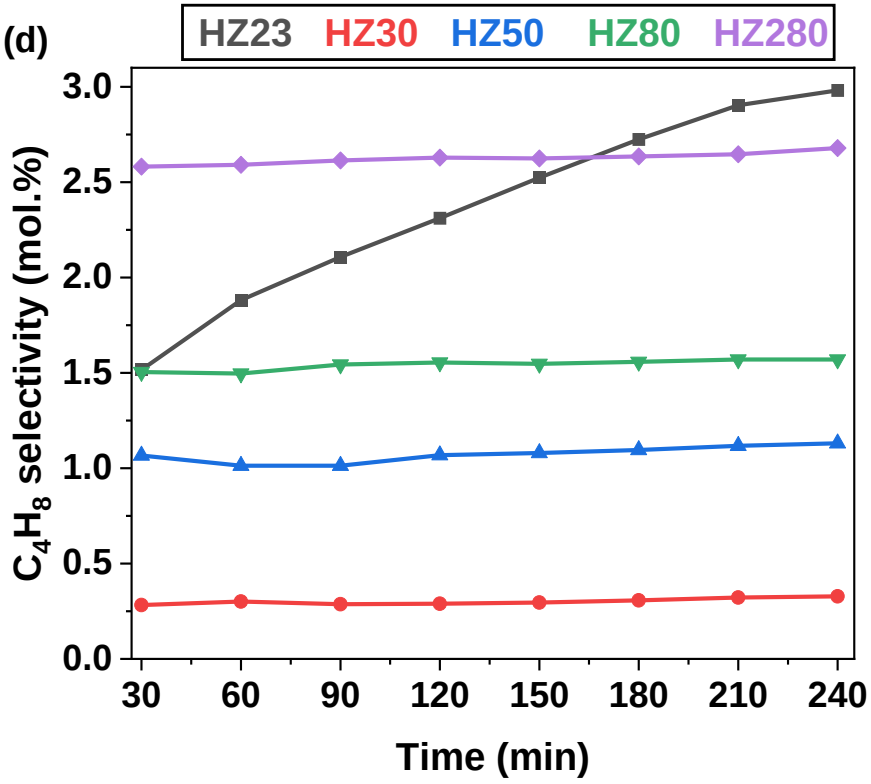


Figure 3.5. Effect of time-on-stream on *n*-heptane conversion (a), C_2H_4 selectivity (b), C_3H_6 selectivity (c) and C_4H_8 selectivity (d) over HZ23, HZ30, HZ50, HZ80 and HZ280 zeolite catalysts. The reactions were conducted at 550°C, atmospheric pressure (0.1 MPa), wight hour space velocity (WHSV) 8.2 h^{-1}, and 20 $ml.min^{-1}$ N_2 flowrate. The estimated errors were between 3 and 6%.

Figure 3.5, illustrates the conversion to, and selectivity for, light hydrocarbons during the cracking reaction of *n*-heptane over HZ23, HZ30, HZ50, HZ80, and HZ280 zeolite catalysts. The dependency of the conversion with time on stream for catalysts operating at 550°C is shown in **Figure 3.5a.** Between the catalysts tested, the highest conversion values were about 86, 84, and 78 wt.% over HZ23, HZ80, and HZ50 zeolite catalysts, respectively, at a time on stream between 180 and 240 min. The HZ280 catalyst achieved the lowest conversion (approximately 60 wt.%) from the series of tested zeolites. The HZ30 zeolite catalyst exhibits intermediate values of conversions of about 70 wt.% at a time on stream between 180 and 240min.

The effect of time-on-stream (TOS) on *n*-heptane conversion and selectivity for light olefin (ethylene, propylene, and butylene) over different SiO_2/Al_2O_3 ratios of zeolite are displayed in **Figure 3.5b-d**. The HZ50 zeolite catalyst shows slightly higher selectivity for ethylene (about 16 mol.%) than HZ80 and HZ280 catalysts (i.e., ca. 15 mol.%). The selectivity for ethylene for HZ23 catalysts increased with time-on-stream from 11 up to 14 mol.% at the end of the catalytic test while the HZ30 catalyst showed stability all the time on stream at 7 mol.%.

The catalysts with higher SiO_2/Al_2O_3 ratios (i.e., HZ280 and HZ80) showed higher selectivity for propylene (i.e., about 35 and 23 mol.% from HZ280 and HZ80, respectively) and butylene (2.8-1.6 mol.%) than the other zeolites as given in **Figure 3.5 c-d**. The selectivity for propene (ca. 11 mol.%) and butene (about 1.5 mol.%) for the HZ30 catalyst increased with time on stream. The opposite behaviour was exhibited by the HZ30 catalyst with the stable value for propene (ca. 5 mol.%) and butene (0.2 mol.%) selectivity.

On the other hand, the selectivity for propene and butene for HZ23 increased with time on stream from 11 to 18 mol.% and 1.5 to 3.0 mol.%, respectively. When the yields of light alkenes (ethene, propene, and butene) are considered, see **Table 3.2**, we can conclude that HZ280 followed by HZ80 produced the highest yield of light alkenes, the minimum yield of BTX and alkanes.

Therefore, as discussed in the next sections, HZ80 zeolite was selected as the primary catalyst to be modified with different promoters, owing to its higher *n*-heptane conversion than HZ280. ZSM-5 (SiO_2/Al_2O_3 ratio 50) was previously investigated in the catalytic cracking of *n*-heptane at 550°C using a MAT (micro-activity test) unit by Afroukhteh-Langaroudi *et al.*[25] The selectivity of ethene, propene, and butene reached 7.7, 11.2, and 4.1% respectively. Taright *et al.*[26] also investigated the catalytic cracking of *n*-heptane over ZSM-5 at 550°C using a MAT

unit. The selectivity for ethene, propene, and butene reached 18.5, 28.3, and 6.3%, respectively. This study produced higher alkene selectivity than most of the reports in the literature, likely due to different reaction systems (MAT unit versus our fixed-bed reactor unit) and zeolite supplier.

Table 3.2. Yield of hydrocarbon products from the catalytic cracking of *n*-heptane over HZ23, HZ30, HZ50, HZ80 and HZ280 zeolite catalysts. The reactions were conducted at 550°C, atmospheric pressure (0.1 MPa), wight hour space velocity (WHSV) 8.2 h^{-1} and 20 $ml.min^{-1}$ N_2 flowrate. The estimated errors were between 3 and 6%.

Samples	Time (min)	Products Yield (wt.%)				
		C_2H_4	C_3H_6	C_4H_8	Alkane*	BTX
HZ23	60	10.7	11.3	1.6	76.3	0.0
	240	13.0	16.3	1.7	65.4	3.6
HZ30	60	6.6	5.2	0.3	86.1	1.9
	240	6.1	4.9	0.3	75.7	13.1
HZ50	60	13.9	14.7	1.0	69.9	0.5
	240	14.8	15.5	1.1	65.4	3.1
HZ80	60	15.1	22.6	1.5	60.5	0.2
	240	14.9	23.2	1.6	58.5	1.8
HZ280	60	14.7	33.8	2.7	47.2	1.6
	240	14.6	34.7	2.8	46.9	1.1

*Total alkane (CH_4+C_2H_6+C_3H_8+C_4H_{10})

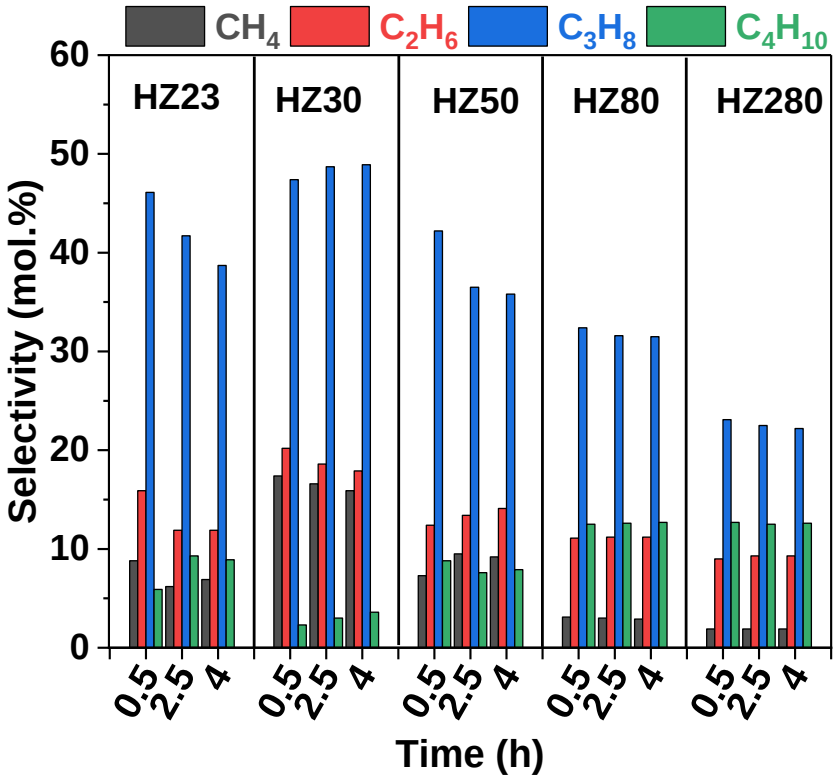


Figure 3.6. Selectivity of produced alkanes from the *n*-heptane catalytic cracking over HZ23, HZ30, HZ50, HZ80 and HZ280 zeolite catalysts. The reactions were conducted at 550°C, atmospheric pressure (0.1 MPa), wight hour space velocity (WHSV) 8.2 h^{-1} and 20 $ml.min^{-1}$ N_2 flowrate. The estimated errors were between 3 and 6%.

The selectivity for alkane (i.e., methane, ethane, propane, and butane) for the cracking of *n*-heptane over zeolite catalysts with different SiO_2/Al_2O_3 ratios at the beginning, middle, and end of the reaction are shown in **Figure 3.6**. The CH_4 selectivity decreased with time on stream from about 8.8 to 6.9 mol. % and 17.4 to 15.9 mol.% over the HZ23 and HZ30 zeolite sample while it was preserved over HZ80 and HZ280 at 3.0 mol. %, 1.9 mol. % respectively.

In the first 30 minutes, the selectivity of CH_4 over HZ50 was stable at 7.3 mol. % and then increased to 9.2 mol. %. The selectivity for C_2H_6 is in the range of 20–9 mol. %, while C_3H_8 and C_4H_{10} are in the range of 48.7-22.5 mol. % and 2.3-12.7 mol. % for all zeolite catalysts, respectively. The C_3H_8 and C_4H_{10} selectivity for HZ80 and HZ280 catalysts resulted

fairly stable at about 32-23 mol. % and 12.7-12.5 mol. % respectively. It is worth remarking that the main alkane produced was propane whatever the SiO_2/Al_2O_3 ratio.

The modification of the zeolite with an appropriate promoter could enhance the propene selectivity from the selective dehydrogenation of propane[13, 14, 19], which is described in the next section.

3.3.1.3 Post-reaction analysis of catalysts

3.3.1.3.1 X-ray diffraction (XRD) analysis

The XRD diffractograms for the spent zeolite samples are shown in **Figure 3.7**. The peak at 2θ= 12º corresponds to SiC and grease (used to disperse the solid in the sample holder) as given in **Figure 3.2A**. The crystallite size at 23.3º in 2θ from XRD patterns of the fresh and spent samples are shown in **Table 3.3**. There was no change in the crystallite sizes of zeolites with SiO_2/Al_2O_3 ratios 30, 50, and 80, which means the zeolite crystal structures were well maintained during the catalytic cracking reaction. In contrast, the spent zeolites with high and low SiO_2/Al_2O_3 (i.e., 23 and 280) show higher crystallite size compared with the fresh samples. A previous report showed that reducing the size of zeolite particles decreases the concentration of the strong acidic sites[27].

Table 3.3. The crystallite size of fresh and spent zeolite catalysts with different SiO_2/Al_2O_3 ratios determined from the X-ray peak at 2θ = 23.3º.

Sample	Crystallite size of fresh catalyst (nm)	Crystallite size of spent catalyst (nm)
HZ23	32.2	43.4
HZ30	81.1	73.1
HZ50	81.1	81.1
HZ80	81.1	81.1
HZ280	102.7	139.9

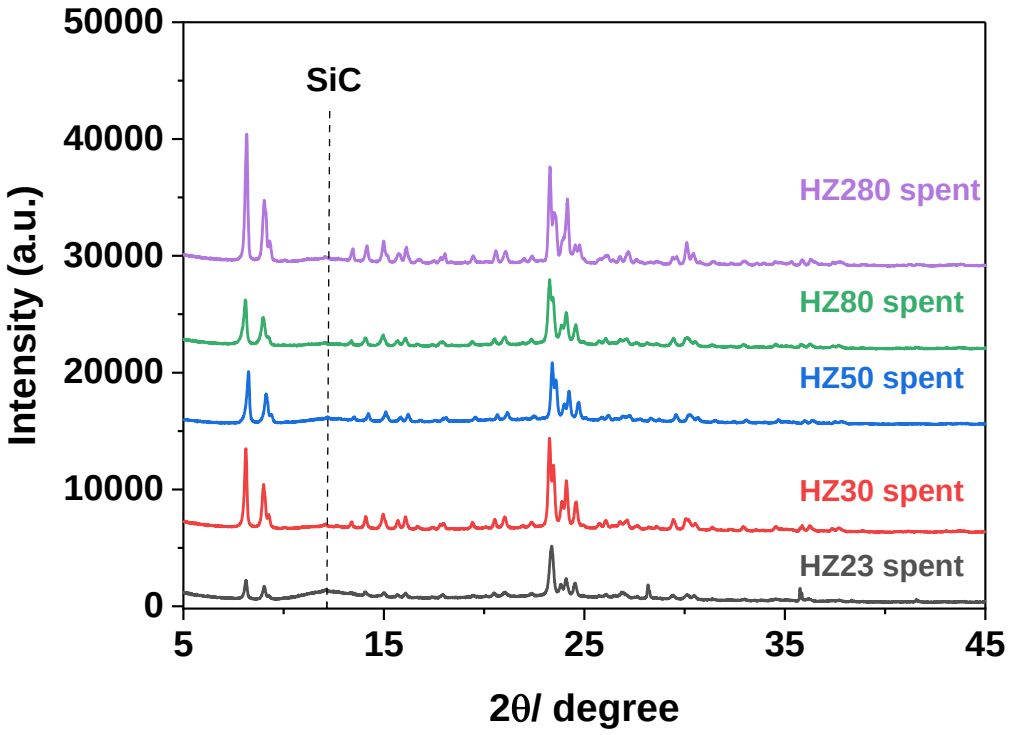


Figure 3.7. Comparison of powder X-ray diffraction patterns of the H-ZSM-5 zeolite for spent samples with SiO_2/Al_2O_3 (23, 30, 50, 80, and 280) molar ratios.

3.3.1.3.2 Thermogravimetric analysis (TGA)

TGA analysis gives critical information on the hydrophobicity, dehydration, and quantity of coke deposition on the HZ23, HZ30, HZ50, HZ80, and HZ280 samples utilised in this study. TGA studies were conducted in air (at a rate of 100 $mL.min^{-1}$) at temperatures ranging from 20 to 1000℃. As shown in **Figure 3.8**, samples exhibit two distinct weight loss steps. The weight loss step between 25-300℃ is attributed to dehydration (87℃) and possible desorption of aromatic products (246℃), whilst the weight loss step at temperatures above 300°C corresponds to the combustion of hard coke formed[28], this is particularly noticeable in HZ23 and HZ80 zeolites. This coke formation has been proposed as the primary cause of catalyst deactivation.

Based on the superior catalytic performance of HZ80 in *n*-heptane catalytic cracking, this zeolite was modified with different loadings of chromium oxide using two preparation methods to improve the olefin production as discussed in the next section.

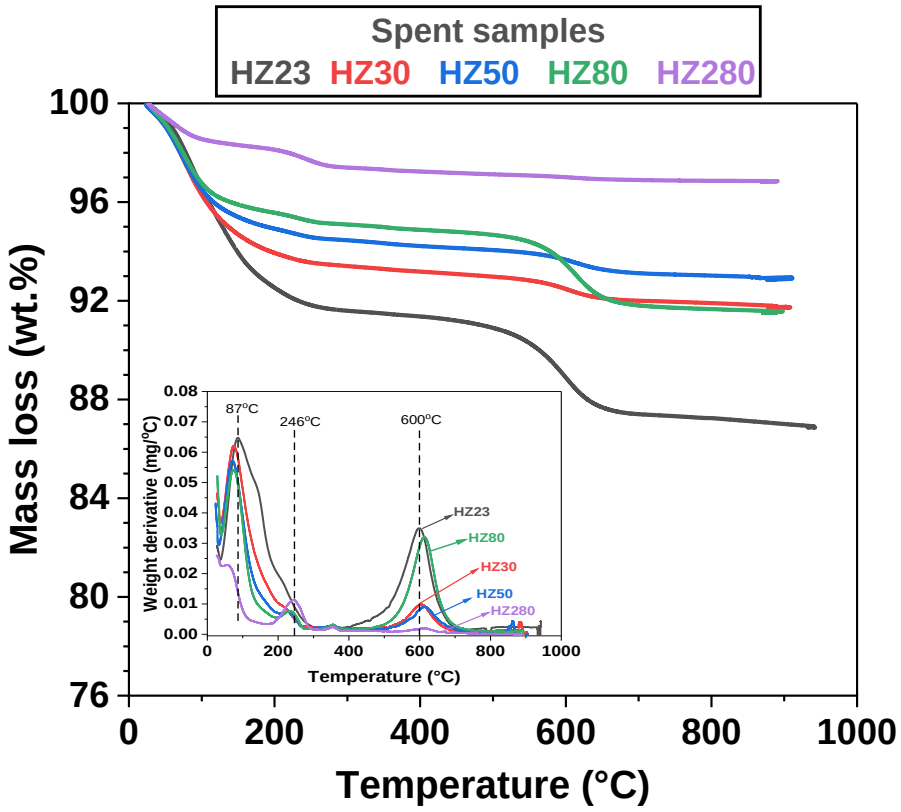


Figure 3.8. Thermogravimetric analysis (TGA) of spent samples under air for zeolites with different SiO_2/Al_2O_3 ratios. Inset plot shows the weight derivative thermogravimetry (DTG) curves of the fresh H-ZSM-5 zeolite for spent samples with SiO_2/Al_2O_3 (23, 30, 50, 80, and 280) molar ratios.

3.3.2 Influence of metal oxide loading and preparation method for HZ80 zeolite on the cracking reaction of *n*-heptane

3.3.2.1 Pre-reaction analysis of catalysts

3.3.2.1.1 X-ray diffraction (XRD)

The unmodified Cr_2O_3, HZ80, and Cr_2O_3-modified catalysts containing 5, 10, and 20 wt.% and prepared by different methods were examined by X-ray diffraction (XRD) before the catalytic reaction as shown in **Figure 3.9**.

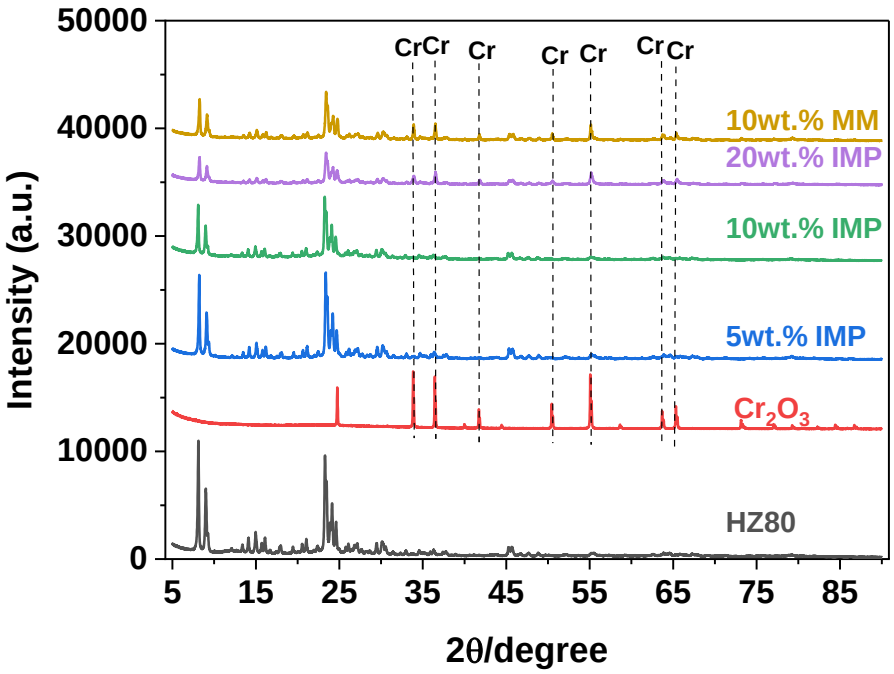


Figure 3.9. Comparison of powder X-ray diffraction patterns of the HZ80, pure Cr_2O_3, and Cr oxide loading by different method for fresh samples. (MM = mechanical mixture, IMP = impregnation method).

The peaks at 5º < 2θ < 30º in all the samples correspond to H-ZSM-5 (MFI type). Moreover, the diffraction peaks of a pure Cr_2O_3 sample were detected at 2θ= 24.7º, 33.8º, 36.4º, 41.6º, 50.4º, 55.1º, 63.6º, and 65.5º. These peaks correspond to the [012], [104], [110], [113], [024], [116], [214], and [300] lattice planes of Cr_2O_3[29]. Compared to the catalyst prepared *via* impregnation (IMP) and mechanical (MM) method the peak of Cr_2O_3 at 2θ= 24.7º overlapped with a HZ80 peak. However, the diffraction peaks of Cr_2O_3 at 33.8º, 36.4º, 41.6º, 50.4º, 55.1º, 63.6º, and 65.5º in 2θ can be clearly observed on MM-synthesised catalysts and 20 wt.% impregnation-prepared Cr_2O_3/HZ80 catalysts. Meanwhile, these peaks can hardly be observed on both 5 and 10 wt.% Cr_2O_3/HZ80 (IMP) owing to either the high dispersion or low crystallinity of the CrO_x species present. In theory, the XRD could readily detect Cr_2O_3, and Cr metal with high concentration and strong crystallinity. According to X-ray diffractograms for the fresh samples (**Figure 3.9**), no Cr_2O_3 phase was detected in the sample prepared by impregnation with a Cr oxide loading between 5 and 10 wt.%. However, when the average

crystallite size of Cr_2O_3 as shown in **Table 3.4**. A slight diminution in particle size was observed whilst increasing Cr loading from 5 to 10 wt.% using the impregnation method (IMP). On the other hand, an increase in particle size was observed when loading 20 wt.% Cr_2O_3 in HZ80 while the 10 wt.% Cr_2O_3/HZ80 catalyst prepared by mechanical mixer (MM) showed the largest crystallite size of Cr_2O_3.

Table 3.4. The average of particle size and loading amount for Cr_2O_3 from X-ray patterns for catalysts.

Catalyst	Particle size (nm)	Cr_2O_3 amount (wt.%)
5 wt.% Cr_2O_3/HZ80- IMP	16 ± 3	1.5 ±0.5
10 wt.% Cr_2O_3/HZ80- IMP	12 ±1	2.4 ±0.5
20 wt.% Cr_2O_3/HZ80- IMP	27.5 ±0.8	11.6 ±0.5
10 wt.% Cr_2O_3/HZ80- MM	39 ±1	9.9 ±0.4

The change in particle size depends on the Cr oxide loading and the preparation method. It is well known that X-ray diffraction enables the determination the phase composition and crystallite size of materials. Moreover, it also can help to identify the amount of Cr_2O_3 through XRD pattern refinement by knowing the amount of crystalline Cr_2O_3 detected by diffraction[30]. The Cr_2O_3 amount (wt.%) was calculated for all the samples using the X-ray results and are listed in **Table 3.4**. It is noticeable that the determined Cr_2O_3 content is markedly lower than the nominal composition, excepting the value for the catalyst prepared by MM that gave results similar to the nominal composition. This finding is attributed to the possible presence of Cr_2O_3 species within the zeolite nanochannels and the presence of very small crystallites as a consequence of use of the impregnation method. It is also expected the impregnation method did not put as much Cr on the catalyst surface.

3.3.2.1.2 Brunauer-Emmett-Teller (BET) analysis

The surface areas of fresh zeolite (HZ80) and the zeolite modified with different loading of Cr_2O_3 using different synthesis methods are summarised in **Table 3.5**. The parent zeolite (HZ80) and zeolite modified by 10 wt.% Cr_2O_3 using the impregnation method have the highest surface area compared to the other catalyst formulations. The parent zeolite (HZ80) has nearly a 420 $m^2.g^{-1}$ surface area and the 10 wt.% Cr_2O_3/HZ80- IMP has a surface area of about 426 $m^2.g^{-1}$. Other catalysts, however, have less surface area than parent zeolite. Measured surface areas of 5 and 20 wt.% Cr_2O_3/HZ80 synthesised by impregnation method (IMP) are 302 and 292 $m^2.g^{-1}$, respectively. This suggests that the loaded Cr_2O_3 significantly affected the zeolite surface area possibly as Cr_2O_3 species have blocked the zeolite pores, resulting in an apparent decrease in zeolite surface area.

Table 3.5. The surface area (BET) analysis of the fresh Cr_2O_3-HZ80 catalyst series for the selective cracking reaction of *n*-heptane toward light olefins.

Catalyst	BET ($m^2.g^{-1}$)	t-plot micropore ($m^2.g^{-1}$)	t-plot External ($m^2.g^{-1}$)
HZ80	430	245	184
5 wt.% Cr_2O_3/HZ80- IMP	302	200	102
10 wt.% Cr_2O_3/HZ80- IMP	426	287	139
20 wt.% Cr_2O_3/HZ80- IMP	292	193	99
10 wt.% Cr_2O_3/HZ80- MM	409	239	171

Importantly, the micropore area slightly increased relative to the external area in the IMP-prepared catalysts whilst the MM formulation showed comparable values to the pristine zeolite (**Table 3.5**). This trend clearly indicates that Cr_2O_3 species generated during the

impregnation process blocked both the nanochannel of the zeolite and affected the external surface area.

3.3.2.1.3 Thermogravimetric analysis (TGA)

All Cr_2O_3 containing HZ80 samples were studied by thermogravimetric analysis (TGA), in order to measure surface moisture and thermostability for the catalysts. The results in **Figure 3.10** showed that with increasing temperature from 25℃ to 1000℃, all samples exhibited one weight loss domain.

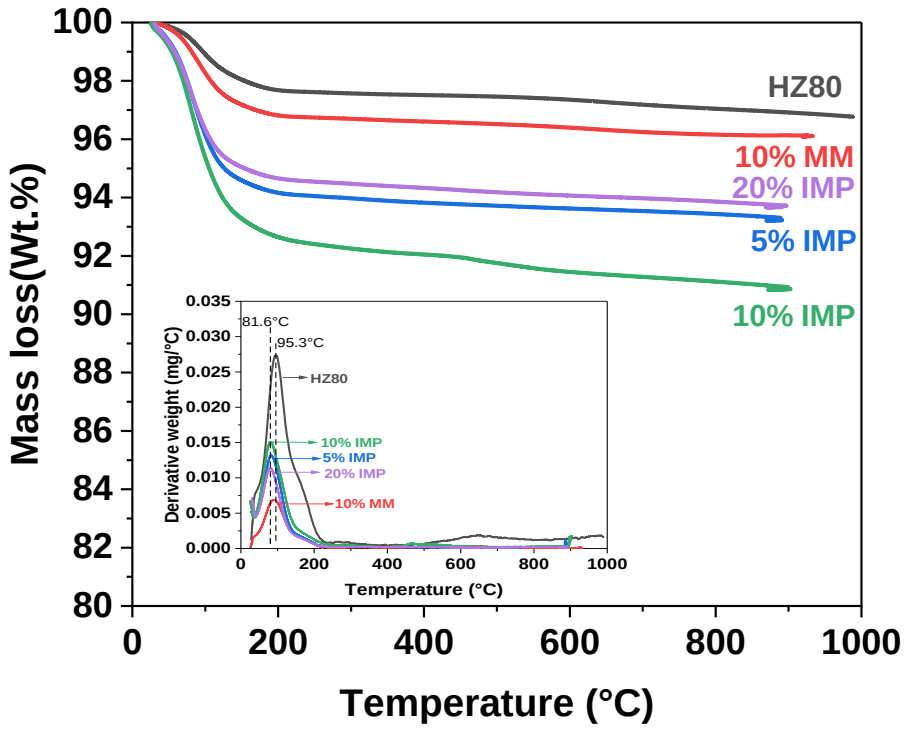


Figure 3.10. TGA for fresh samples under air flow for different Cr oxide over HZ80 catalyst. Inset plot shown the weight derivative thermogravimetry (DTG) curves of the five catalysts under air flow.

The weight loss domain was attributable to water removal between 25°C and 200°C. The total weight loss of the samples containing 5 wt.%, 10 wt.%, and 20 wt.% Cr_2O_3 prepared by IMP resulted 6.1%, 7.7%, and 5.6%, respectively. However, the 10 wt.% Cr_2O_3-HZ80 catalyst formulation prepared *via* MM exhibited a weight loss of only 3.5%, which was ca.1%

higher than the parent HZ80 zeolite and lower than the catalyst synthesis by IMP, about 2-4%. Nevertheless, all the samples were thermally stable at temperatures between 400 and 600℃, which is the range of the catalytic cracking reaction temperature. The derivative thermogravimetry (DTG) curves were compared in the range of 25–1000℃ as illustrated in **Figure 3.10**. It was found that the peaks of water desorption for the catalysts with different Cr oxide loadings over HZ80 zeolite occur at 80-100℃ with slight differences in the maximum temperature, which is presented in an ascending order of 10 wt.% ≈ 20 wt.% IMP < 5 wt.% IMP < 10 wt.% MM ≈ HZ80.

3.3.2.1.4 Scanning electron microscopy (SEM)

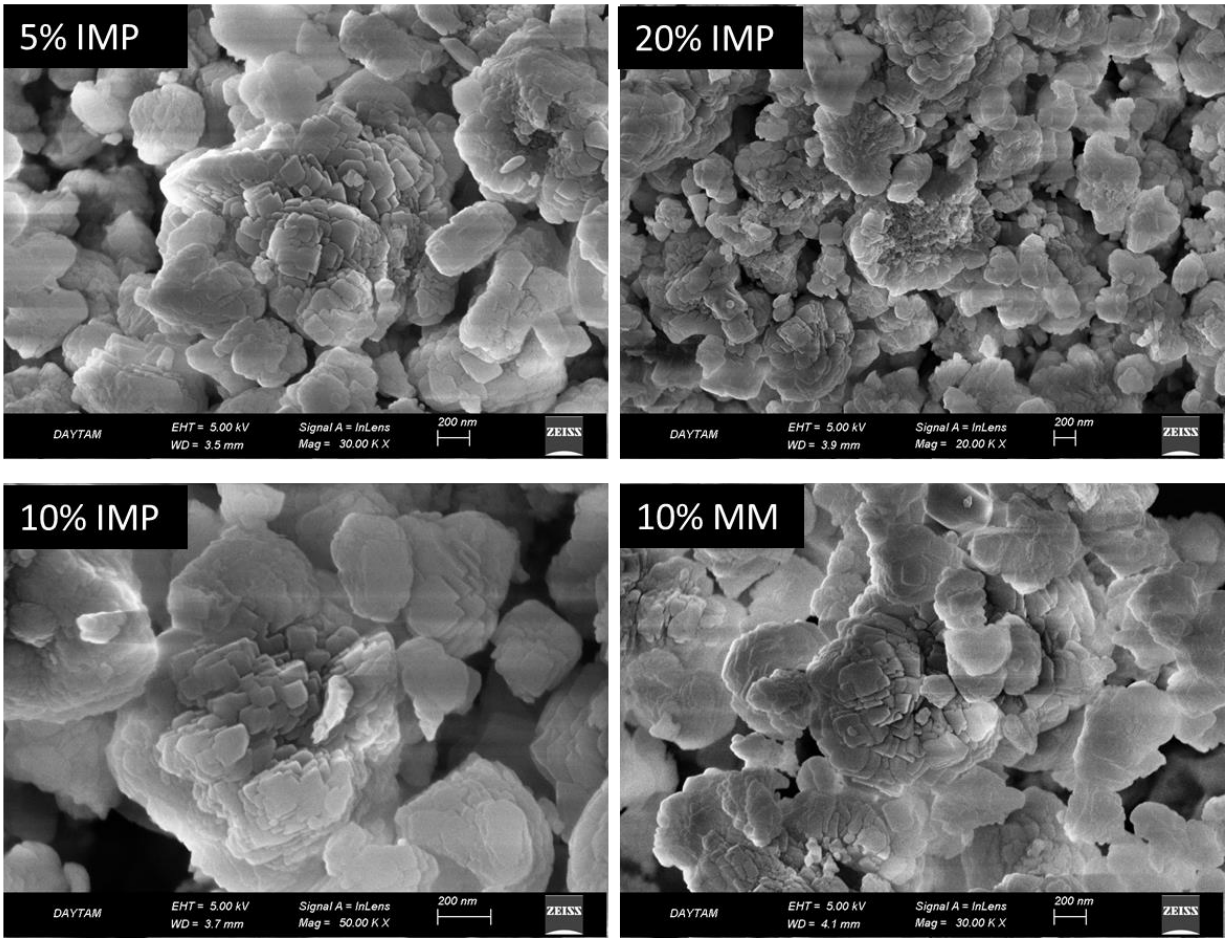
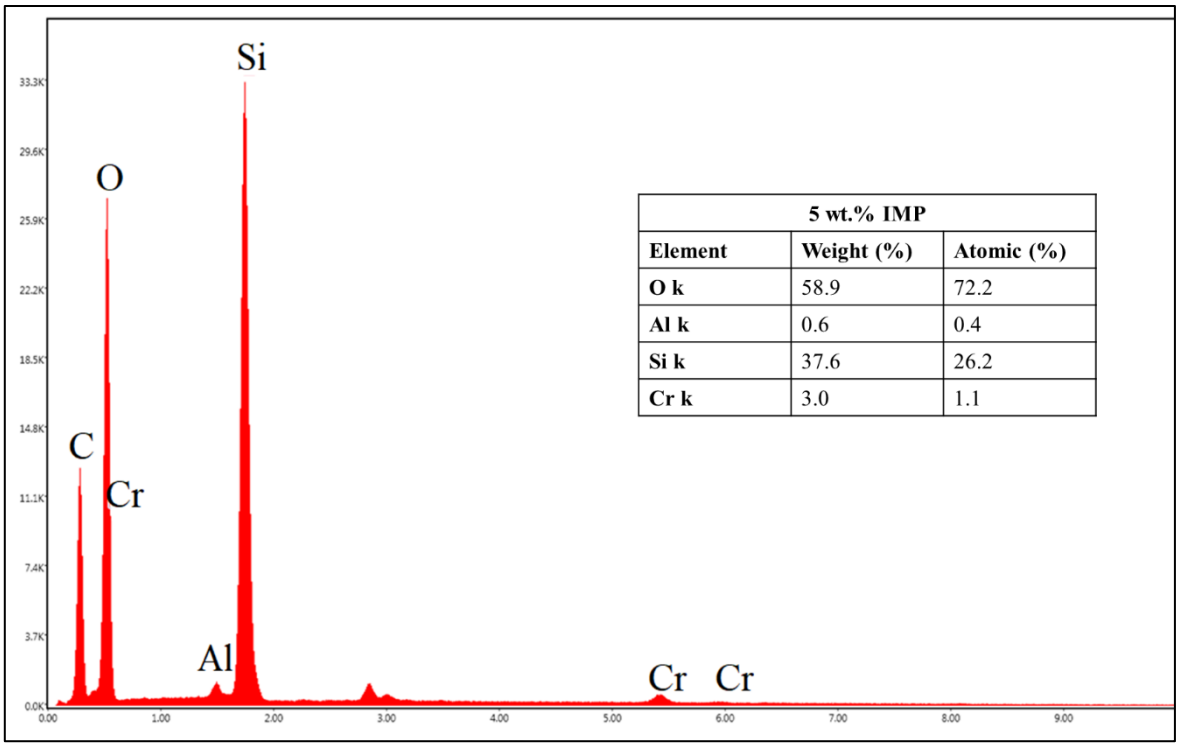


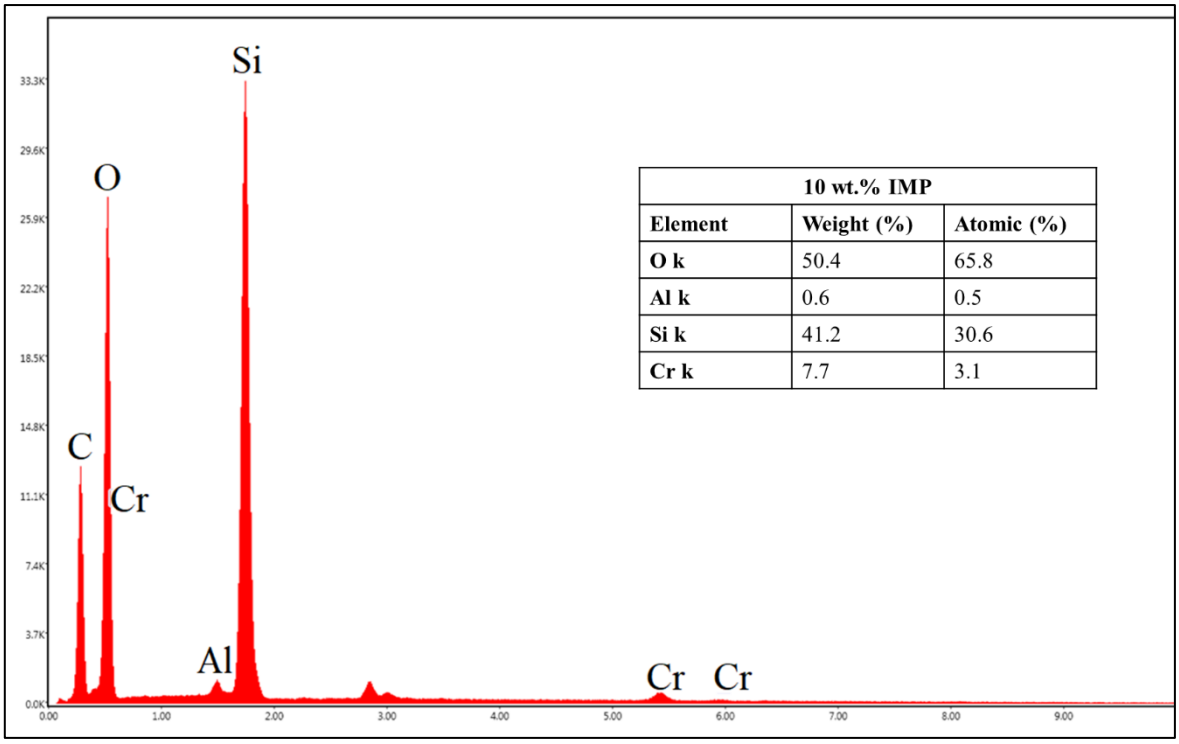
Figure 3.11. Scanning electron microscopy (SEM) images of Cr loading over HZ80 synthesis by different methods.

The images of SEM for the HZ80 modified by Cr oxide using two methods and different loading are depicted in **Figure 3.11**. The morphology of the catalysts did not change markedly when varying amounts of Cr oxide were loaded probably due to the similarity in the morphology of Cr_2O_3[31] and zeolite[32]. Furthermore, after treatment of the HZ80 by Cr oxide, the MFI-typical hexagonal structure of HZ80 was conserved. A relatively wide distribution of particle size is expected since nanocrystallites, presumably, chromium oxide, are dispersed on large aggregated particles of zeolite.

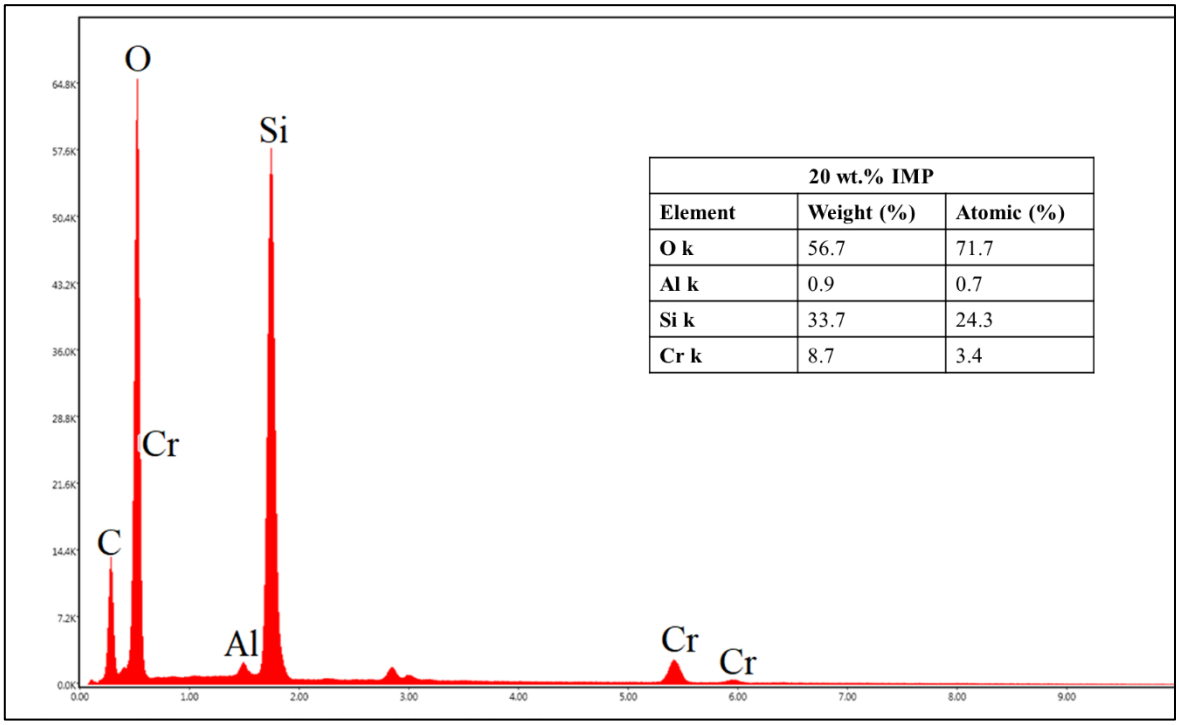
3.3.2.1.5 SEM-EDX elemental analysis



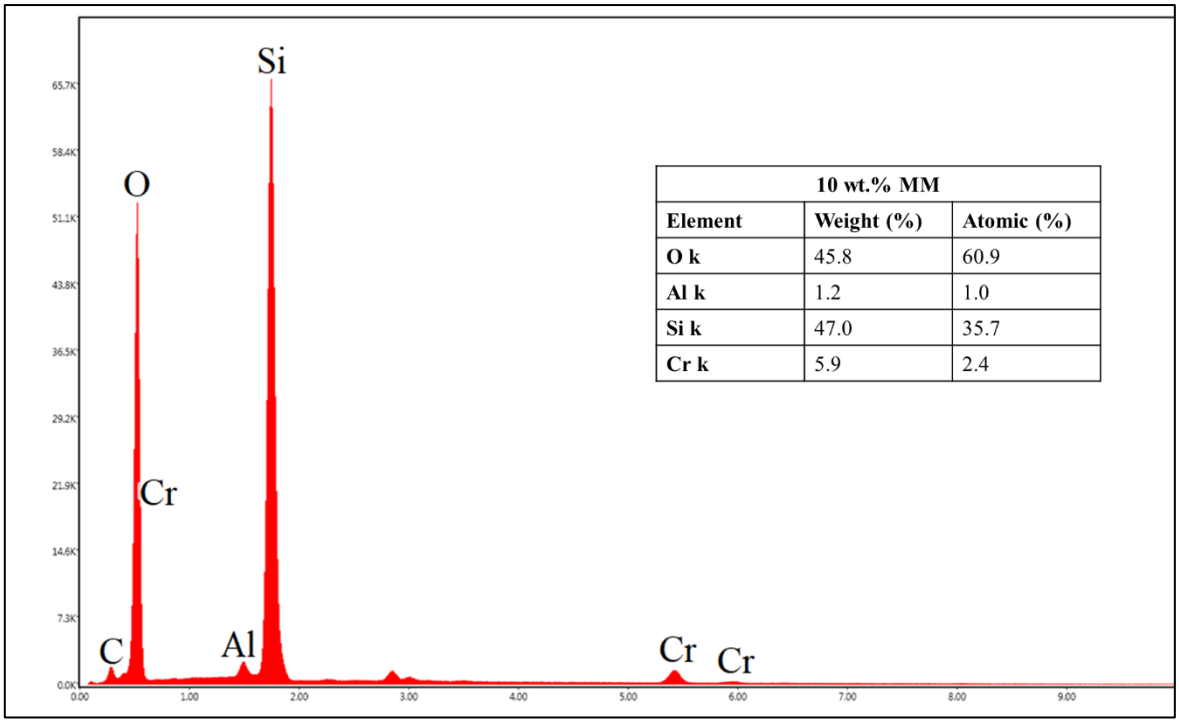
5 wt.% IMP		
Element	**Weight (%)**	**Atomic (%)**
O k	58.9	72.2
Al k	0.6	0.4
Si k	37.6	26.2
Cr k	3.0	1.1



10 wt.% IMP		
Element	**Weight (%)**	**Atomic (%)**
O k	50.4	65.8
Al k	0.6	0.5
Si k	41.2	30.6
Cr k	7.7	3.1



20 wt.% IMP		
Element	**Weight (%)**	**Atomic (%)**
O k	56.7	71.7
Al k	0.9	0.7
Si k	33.7	24.3
Cr k	8.7	3.4



10 wt.% MM		
Element	**Weight (%)**	**Atomic (%)**
O k	45.8	60.9
Al k	1.2	1.0
Si k	47.0	35.7
Cr k	5.9	2.4

Figure 3.12. SEM-EDX analysis of different loadings of Cr oxide on HZ80.

SEM-EDX elemental analysis was used to determine the final metal loading of the catalysts on the external surface. The SEM-EDX data are displayed quantitatively in **Figure 3.12**, where metals are recognized by characteristic peaks, which enable the quantification of the metal loading on the HZ80 catalyst. According to the SEM-EDX results, the amount of Cr loading of the 10 wt.% Cr_2O_3-HZ80 catalyst prepared by mechanical mixture (MM) was 5.9 %, and O was 45.8%. On the other hand, the EDX elemental analysis of 10 wt.% Cr_2O_3-HZ80 sample prepared via impregnation method (IMP) was shown the Cr content about 7.7%, and O about 50.4%. The difference of Cr_2O_3 loading between the nominal composition and the experimental results is due to incorporation of Cr_2O_3 inside the zeolite channel.

Moreover, the EDX elemental analysis of both catalysts revealed that for samples prepared by the impregnation method, as given in **Figure 3.12**, the 5 wt.% and 20 wt.% Cr_2O_3-HZ80 catalyst had a Cr content of 2.9% and 8.7%, and O content of 58.9%, and 56.7%, respectively. As mentioned before, the EDX measures the element loading on the external

surface of the catalysis, which means some amounts of the metals will be inside the zeolite channels[33], and the stoichiometric value used in preparation will not be close to the EDX results. It is noticeable that the atomic ratio of Si/Al is close to 60 for 5 and 10 wt.% Cr oxide-containing catalyst whilst about 37 (close to the expected value - of 40) for 20 % and 10 % Cr oxide/zeolite prepared by MM.

3.3.2.1.6 X-ray photoelectron spectroscopy (XPS)

The XPS analysis can provide insight into the various electronic effects induced on nanoparticles when different supports or promoters are used. For this reason, the XPS technique was applied to determine the oxidation state of Cr oxide species and relative concentration on the catalyst's top surface layers.

Figure 3.3A shows the obtained XPS spectra of Cr for the samples prepared by different methods. The Cr 2p orbitals are the most important XPS feature for characterisation. According to the literature[34, 35], Cr has three main oxidation states Cr (0), Cr (III), and Cr (VI). The binding energies for Cr, Cr^{3+}, and Cr^{6+} oxides are 574.3, ~576, and ~580 eV, respectively. In the case of XPS, the data were collected and corrected after the calibration conducted by the lowest carbon 1s binding energy for sp2 at 284.0 eV as given in **Figure 3.3A.** However, it is clear that charging is taking place during the scans which may explain the odd oxygen 1s spectra (**Figure 3.4A**) and the shifts in the Cr 2p spectra. Experiments showed the binding energies for the Cr 2p for all the cases is ~ 574eV which is in the range expected for Cr^{3+} as shown in **Figure 3.3A**. The peaks are too high in binding energy to be Cr metal (~571 eV) and also too broad. The peaks are certainly not high enough for there to be any Cr^{6+} present (>579 eV). Although there looks to be more than one state of Cr present, it is probable that the charging of the samples noted in the carbon 1s and oxygen 1s is causing that. **Figure 3.5A** shows the wide survey XPS spectrum for the HZ80 zeolite catalysts modified with Cr using

different method and loading before the catalytic cracking test. Interestingly, the type of anchored Cr oxide species is strongly dependent upon the Cr oxide loading and the preparation method[36, 37]. The Cr oxide-HZ80 catalysts, made by impregnation method, had the most intense spectrum when increased the Cr loading which might suggest highly dispersed Cr on the HZ23 zeolite. The quantification of Cr on the surface (**Table 3.6**) shows that the MM method results in much higher amounts, which could be due to reduced penetration into the surface or simply that the impregnation method did not put as much Cr on the surface as expected or the possible presence of isolated species of Cr oxide into the zeolite cavity[38]. Due to the variations in cluster size and oxidation state of the metal center in various reaction conditions, chromium oxide-based catalysts for dehydrogenation of alkanes are very complicated systems[37].

The oxidation state of the reduced Cr form is also noticeably affected by the support. For example, when loading at 4 wt.%, Cr^{2+} is mainly formed as a reduced form on silica, whereas both a mixed $Cr^{2+/}Cr^{3+}$ and Cr^{3+} species are obtained on mixed alumina/silica and alumina supports respectively[37]. According to a recently published work, the inclusion of silica may enhance reducibility compared to alumina, resulting in a higher contact of the active site with the support[39]. Obviously, these Cr species were not observed in the present study, instead only Cr^{3+} was clearly identified regardless of the Cr loading and synthesis method.

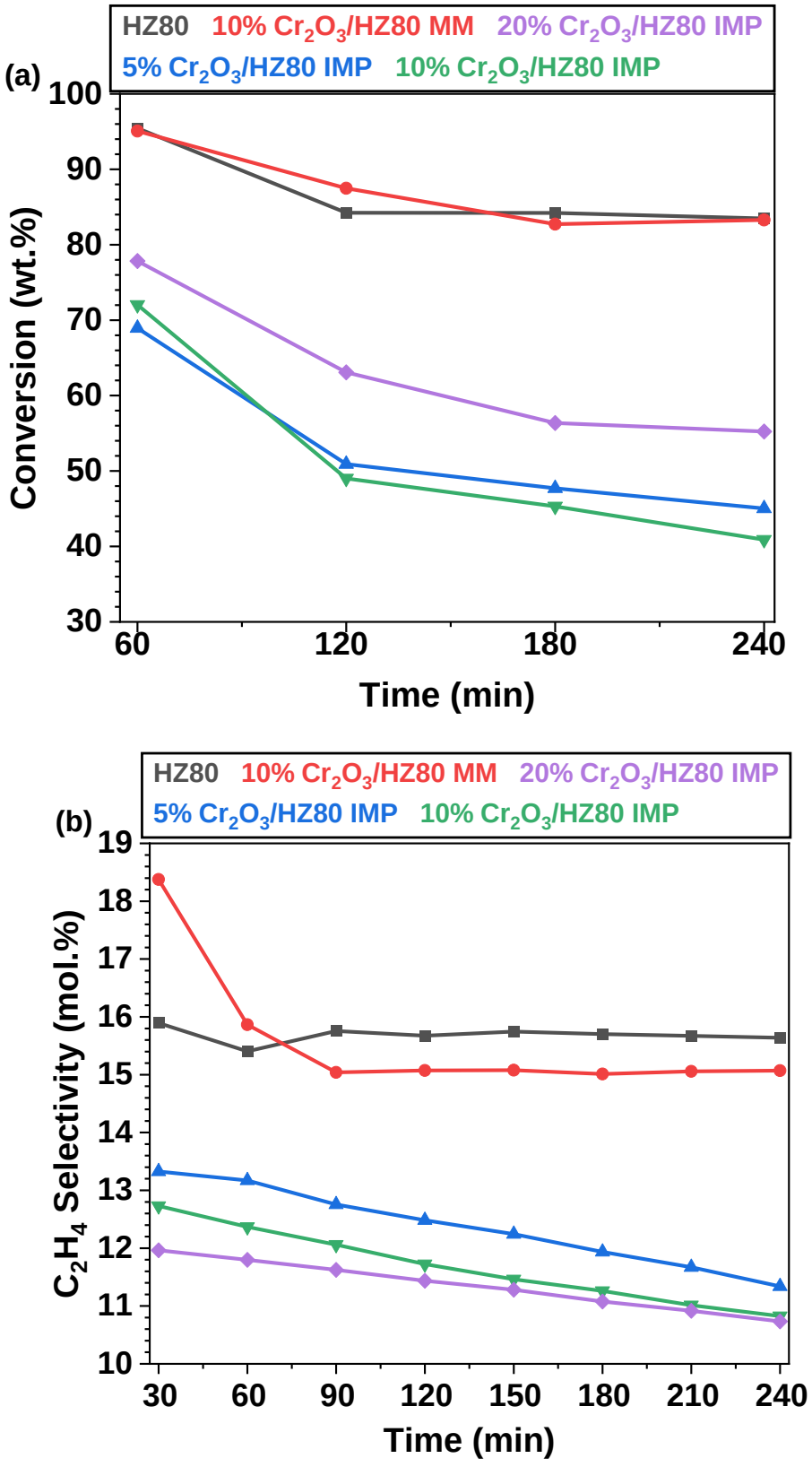
Table 3.6. The binding energies, FWHM and surface compositions (%) of HZ80 zeolite modified with Cr_2O_3 *via* impregnation and mechanical methods.

Catalyst	Name	Binding Energies (eV)	FWHM (eV)	Atomic (%)
5 wt.% IMP	O 1s	530.06	3.10	55.46
	C 1s	248.06	4.27	12.73
	Cr 2p	577.06	12.95	0.89
	Si 2p	104.06	2.95	30.92
10 wt.% IMP	O 1s	530.21	3.50	56.20
	C 1s	284.21	3.70	10.41
	Cr 2p	576.21	7.94	1.40
	Si 2p	103.21	3.04	32.00
20 wt.% IMP	O 1s	530.89	3.05	57.33
	C 1s	285.89	4.51	10.42
	Cr 2p	574.89	5.94	2.37
	Si 2p	105.89	3.07	29.88
10 wt.% MM	O 1s	531.26	2.65	91.47
	C 1s	288.26	4.97	3.63
	Cr 2p	574.26	5.67	1.97
	Si 2p	108.26	2.27	2.93

3.3.2.2 Catalytic performance tests

Figure 3.13 shows the conversion and selectivity of the HZ80 zeolite modified by Cr_2O_3 and the unmodified zeolite. The overall carbon balance for these tests were between 93 and 97 % including residual carbon, this value is within the expected range of cracking reactions. The parent HZ80 catalyst has the highest initial conversion of 95 wt.% during the first hour of reaction and decreases to ~ 85 wt.% with time-on-stream. The *n*-heptane conversions are lower for Cr_2O_3–promoted HZ80 catalysts compared with the parent ZSM-5, except, importantly, for the 10 wt.% Cr_2O_3-HZ80 catalyst formulation prepared by mechanical mixture (MM), which showed similar results to the parent HZ80 for *n*-heptane conversion during the whole time on stream. This finding suggests that the impregnation and mechanical mixture methods to modify HZ80 with Cr_2O_3 strongly affect the catalytic performance of the parent zeolite. Generally, Cr_2O_3 modification didn't improve conversion when the samples

were prepared by the impregnation method but does have a big impact on selectivity as discussed below.



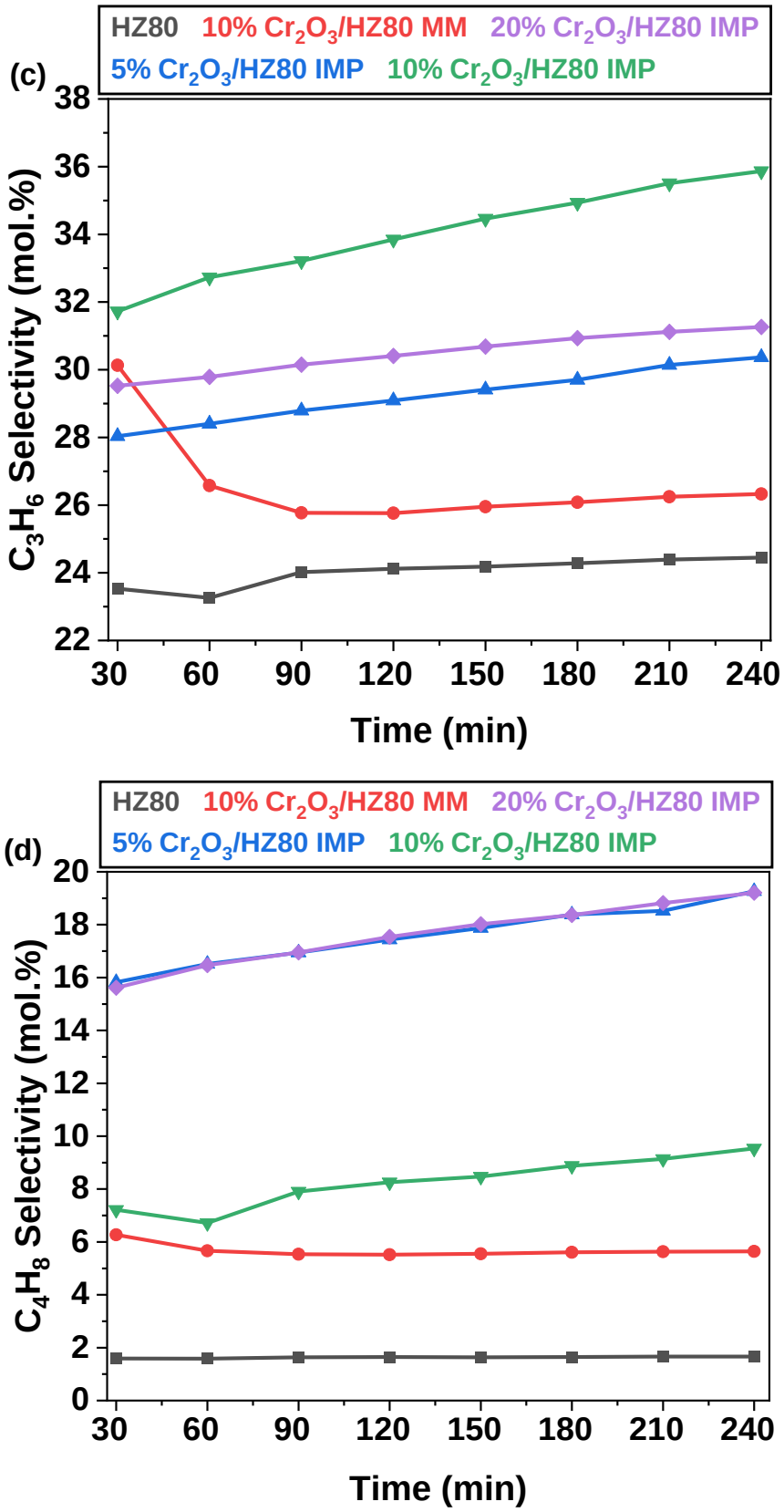


Figure 3.13. Effect of Cr_2O_3 loading and preparation method over HZ80 zeolite catalyst on *n*-heptane conversion (a), C_2H_4 selectivity (b), C_3H_6 selectivity (c) and C_4H_8 selectivity (d). The reactions were conducted at 550°C, atmospheric pressure (0.1 MPa), wight hour space velocity (WHSV) 8.2 h^{-1} and 20 $ml.min^{-1}$ N_2 flow rate. The estimated error was between 3 and 6%.

The Cr_2O_3-modified catalysts containing 5, 10, and 20 wt.% prepared *via* impregnation method show lower *n*-heptane conversions than the parent HZ80. This may be due to diminution of the catalyst acidity with the loading of chromium oxide, which would block stronger Brønsted acid sites responsible for cracking reaction[13, 14]. Obviously, the type of Cr oxide species and location (inside or outside of zeolite porous) might also affect the zeolite catalytic performance. The effect of modification with Cr oxide on the selectivity of light olefins (ethene, propene, and butene) over the HZ80 zeolite catalyst is shown in **Figure 3.13 b-d**. All the catalysts exhibit C_2H_4 selectivity lower than the parent HZ80 zeolite, particularly the catalyst series prepared by impregnation. An opposite trend was obtained for the selectivity of C_3H_6 and C_4H_8, which are indeed markedly superior, especially for the catalysts prepared *via* impregnation, then the unmodified HZ80 zeolite interestingly, there are negligible changes in selectivity to propylene and butylene whatever the chromium oxide loading.

Lu *et al.*[19] investigated the cracking of isobutene at 550℃ and the selectivity of ethene, propene, and butene reached 25.3%, 28% , and 7.2% respectively when 0.004 mmol. g^{-1} Cr was loaded on H-ZSM-5 (SiO_2/Al_2O_3 ratio 80) by the impregnation method. Mohiuddin *et al.*[13] investigated the catalytic cracking of naphtha at 550℃ and the selectivity for ethene, propene, and butene reached 3.4%, 11.4%, and 9.9% respectively when using 5% Cr oxide over HZSM-5 (SiO_2/Al_2O_3 ratio 30). Note that in both these cited investigations different feedstocks and zeolites with different SiO_2/Al_2O_3 ratios were used compared to our work.

Table 3.7. Yield of hydrocarbon products for *n*-heptane cracking over Cr_2O_3-HZ80. The reactions were conducted at 550°C, atmospheric pressure (0.1 MPa), wight hour space velocity (WHSV) 8.2 h^{-1} and 20 ml min^{-1} N_2 flowrate. The estimated error was between 3 and 6%.

Samples	***Time (min)***	***Products Yield (wt.%)***				
		C_2H_4	**C_3H_6**	**C_4H_8**	**Alkane***	**BTX**
HZ80	60	15.1	22.6	1.5	60.5	0.2
	240	14.9	23.2	1.6	58.5	1.8
10% Cr_2O_3/HZ80 (MM)	60	16.5	27.4	5.8	50.2	0.1
	240	14.4	25.1	5.4	53.4	1.8
10% Cr_2O_3/HZ80 (IMP)	60	12.3	30.0	6.5	46.9	4.3

20% Cr_2O_3/HZ80 (IMP)	240	10.6	32.9	8.6	42.5	5.4
	60	12.2	28.2	14.9	48.4	2.0
5% Cr_2O_3/HZ80 (IMP)	240	10.1	28.6	17.3	46.6	5.9
	60	11.2	26.2	14.8	49.1	3.7
	240	9.6	26.4	16.2	47.2	10.1

*Total alkane (CH_4+C_2H_6+C_3H_8+C_4H_{10})

The product yields of light olefin (ethene, propene, and butene) and BTX in the catalytic cracking of *n*-heptane over Cr_2O_3/HZ80 catalyst are shown in **Table 3.7**. Note that the total yield of alkenes (C_2H_4+C_3H_6+C_4H_8) from HZ80 zeolite is stable with time on stream. Whilst the total alkenes yield for the IMP-synthesised (IMP = impregnation) catalysts increase with time on stream. However, the BTX yield for this catalyst was higher than that for the catalysts prepared by the MM method and HZ80 zeolite. Moreover, the total alkenes yield from MM-prepared catalyst (MM = mechanical mixing) (ca. 50 wt.%) is fairly constant and clearly superior to that from the parent HZ80 zeolite (ca. 39 wt.%) and impregnation-prepared Cr_2O_3/HZ80 catalysts (between 48 and 56 wt.%).

This trend clearly reveals that the catalyst synthesis method and the degree of interaction of the chromium oxide with HZ80 zeolite does have an important impact over the generation of alkenes and the stability of the catalyst under operating conditions.

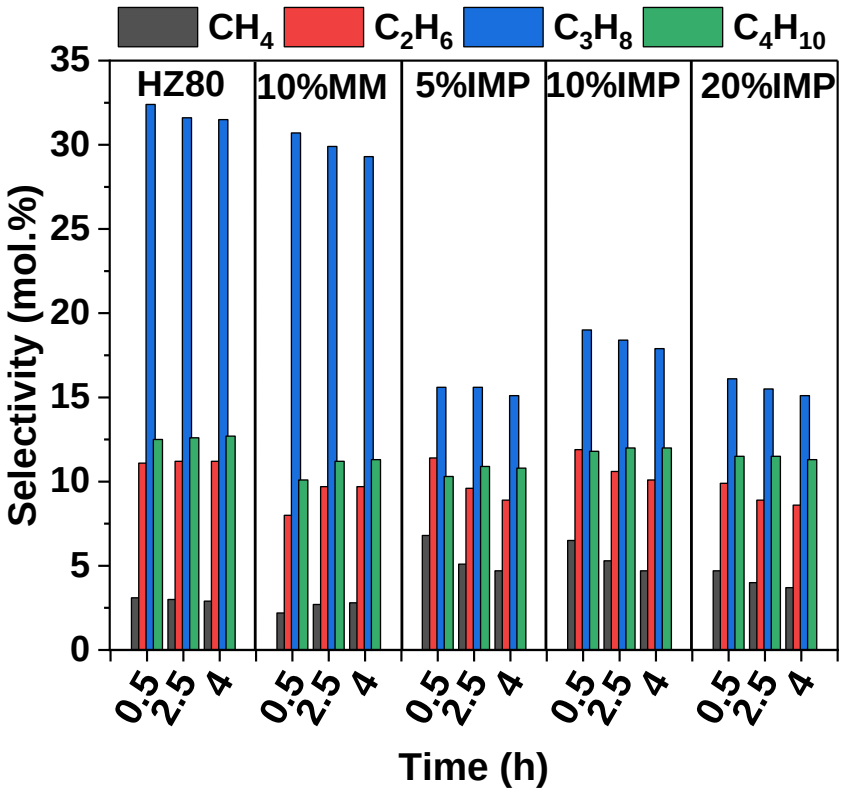


Figure 3.14. Selectivity for alkanes for *n*-heptane catalytic cracking over Cr_2O_3/HZ80. The reactions were conducted at 550°C, atmospheric pressure (0.1 MPa), wight hour space velocity (WHSV) 8.2 h^{-1} and 20 $ml.min^{-1}$ N_2 flowrate. The estimated error was between 3 and 6%.

Figure 3.14 shows the selectivity for alkane from the catalytic cracking of *n*-heptane over the Cr oxide-modified catalysts. The selectivity of CH_4 for 10 % Cr_2O_3/HZ80 (MM) and parent HZ80 zeolite catalysts stayed reasonably stable at about 3 mol.% with time on stream. On the contrary, the catalysts synthesized by the impregnation method exhibited higher methane selectivity (between 3.7 and 6.8 mol.%) than parent HZ80 zeolite (ca. 3 mol.%). On the other hand, the C_2 and C_4 selectivity from the MM-prepared catalyst and the parent HZ80 zeolite were fairly comparable whilst the propane selectivity was slightly low for the former catalyst (i.e., MM) in agreement with its high selectivity to propene (see **Figure 3.13c**).

On the other hand, the ethylene selectivity from the catalysts synthesized by impregnation did not vary markedly with Cr_2O_3 loading (ca. 13-11 mol.%) and was significantly lower than that from parent ZSM-5 (i.e., 16 mol.%) likely due to the similarity of

n-heptane conversion. However, this catalyst series showed total olefins selectivity significantly higher than that from parent HZ80 zeolite (i.e., 55-60 mol.%).

Table 3.8. Catalytic cracking of *n*-heptane and distribution of olefins over HZ80 modified by 10 wt.% Cr oxide loading using different preparation methods at a several weight hourly space velocities (WHSV). The conversion of *n*-heptane and alkene selectivity correspond to a TOS of 3h at 550℃, atmospheric pressure (0.1 MPa), 20 ml min^{-1} N_2 flow rate and *n*-heptane flow rate between 0.05 and 0.7 mL. min^{-1} to have WHSV between 4.1 and 57.5 h^{-1}.

	10 wt.% Cr_2O_3/HZ80 (IMP)			***10 wt.% Cr_2O_3/HZ80 (MM)***		
Weight hourly space velocity (WHSV, h^{-1})	8.2	6.2	4.1	57.5	49.3	8.2
Conversion (wt.%)	45.3	61.5	56.8	47.8	49.6	82.7
Olefin selectivity (mol.%)	55.7	54.4	60.0	46.6	46.7	46.7
Olefin yield (wt.%)	49.1	53.7	58.4	43.3	43.5	44.4
BTX yield (mol.%)	9.1	5.8	5.8	4.1	3.1	2.0

It is well-established that pre-treated Cr oxide can be used to improve the yield of aromatics such as BTX, and olefins[13, 21, 36, 40]. It's noteworthy to remark that adding Cr oxide to the zeolite will change the acidity distribution strength[40, 41]. Moreover, Cr oxide species have been found to aid in reducing coking[41]. In this section, we will look at how the preparation methods affect the catalytic performance and maximizing the olefins production of Cr oxide-containing HZ80 catalysts.

Table 3.8 summarize the effect of the weight hourly space velocities (WHSV) on *n*-heptane conversion in the 10 wt.% Cr_2O_3 over HZ80 zeolite by different synthesized methods. The WHSV values were calculated according to equation (2-5) as given in Chapter 2 (experimental methods). As can see in **Table 3.8** the feed contact time is inversely related to the space velocity and the *n*-heptane conversion reduces as the WHSV increases. Furthermore, catalyst synthesized by the mechanical method (MM) shows good olefin selectivity and the yields remain fairly constant (i.e., 43 and 47%) with an increase in the WHSV. However, in

contrast, for the Cr_2O_3-containing catalyst prepared by the impregnation method, the olefin production decreased when increasing the WHSV. On the other hand, the yield of aromatics (BTX) was significantly higher for IMP-prepared catalyst regardless of the WHSV. In fact, the catalyst synthesised by the impregnation method shows a higher olefin yield and selectivity than the catalyst prepared by the mechanical method. This trend reveals the marked effect of the catalyst synthesis method on its activity. It can be seen in XRD results (**Figure 3.9** and **Table 3.4**), the Cr_2O_3 in samples prepared by the impregnation method (IMP) is much less than the nominal composition of those formulations. This would be consistent with species of Cr oxide accessing pores/channels in the zeolite during sample preparation, these not being detectable by XRD. Whereas the amount of Cr_2O_3 for the sample prepared by mechanical mixture (MM) coincided with the nominal composition (i.e., 10 wt.%) suggesting that the oxide resides primarily on the exterior of the zeolite.

3.3.2.3 Post-reaction analysis of catalysts

3.3.2.3.1 X-ray diffraction analysis

The catalysts with Cr_2O_3 loading of HZ80 prepared by the two methods were examined by X-ray diffraction after the catalytic cracking of *n*-heptane and the results are shown in **Figure 3.15**. Comparing the X-ray results of the solid catalysts in pre-reaction (**Figure 3.9**) and post-reaction stages (i.e. after catalytic cracking of *n*-heptane at 550°C for 4h) can be noted that the characteristic peaks of HZ80 zeolite were observed whilst the formation of coke was not evident in the used catalysts. Importantly, no changes in the MFI-type structure indicates that the zeolite structure is well maintained during the catalytic cracking reaction. According to **Figure 3.2A**, the peak at $2\theta=12^{o}$ corresponds to SiC and grease (which were employed to disperse the solids in the sample holder).

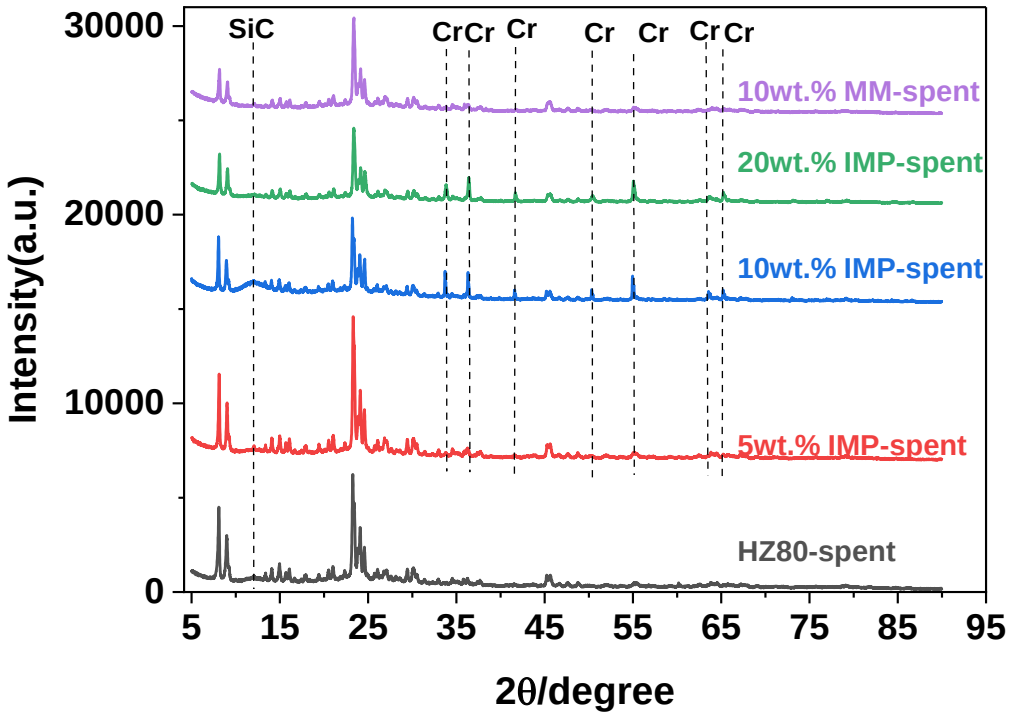


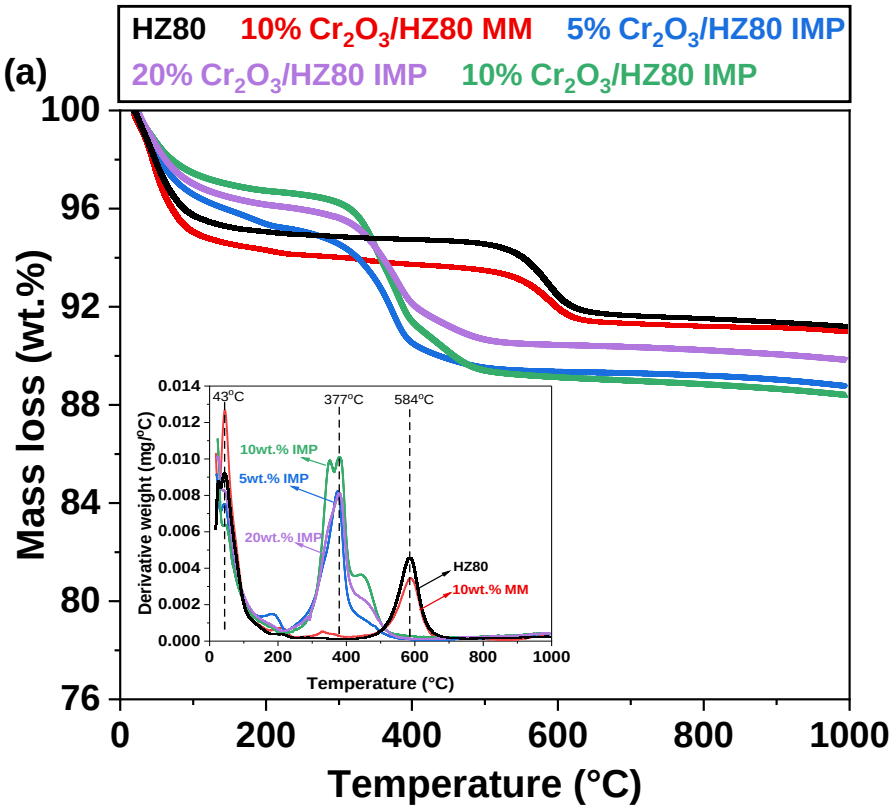
Figure 3.15. Comparison of powder X-ray diffraction patterns of the spent HZ80 zeolite, and Cr oxide-modified HZ80 catalysts prepared by impregnation and mechanical mixture.

Interestingly, in the X-ray patterns (**Figure 3.15**), the diffraction peak intensity for Cr_2O_3 at the angle 2θ = 33.8º, 36.4º, 41.6º, 50.4º, 55.1º, 63.6º, and 65.5º decreased or disappeared for the 10 wt.%Cr_2O_3-HZ80 prepared by mechanical mixing (MM). The opposite trend was obtained for the 10 wt.%Cr_2O_3-HZ80 synthesised by the impregnation method. However, no clear changes were observed for the diffraction peaks for 20 and 5 wt.%Cr_2O_3-HZ80 prepared by impregnation method, which suggest that it was largely stable under the reaction conditions.

3.3.2.3.2 Thermogravimetric measurement (TGA)

Although no unambiguous diffraction peaks for coke were seen in the X-ray for the spent samples, thermogravimetric measurement (TGA) showed the existence of coke residues.

After the activity tests, the catalysts turned to black colour due to coke formation. According to the literature, thermogravimetric measurement (TGA) curve may be classified into many areas based on temperature range[42, 43]. As illustrated in **Figure 3.16a,** the loss of water and volatile species, products, or chemical intermediates happens in the first weight loss (WL) step between 25-200°C. The second WL at 200-400°C corresponds to oxidation of coke of mobile carbonaceous residues or physisorbed products (or side products), sometimes known as "soft coke". The WL related to more bulky and highly unsaturated carbonaceous molecules correspond to "hard coke" at temperatures between 400 and 700 °C[42, 43]. The catalyst deactivation has been attributed to the deposition of these 2 types of cokes[41, 44].



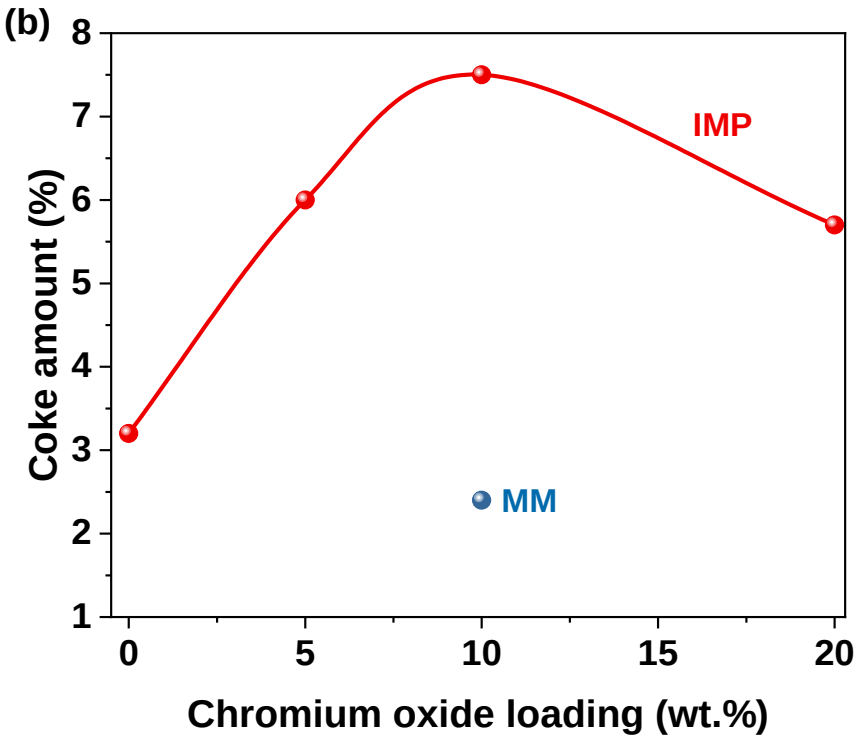


Figure 3.16. (a)TGA for spent samples under Air flow. Inset plot shown the weight derivative thermogravimetry (DTG) curves of the five catalysts under air flow, (b) Coke content versus Cr oxide loading for the spent Cr_2O_3-HZ80 catalysts.

The derivative thermogravimetry (DTG) curves were compared in the range 25-1000℃, as proved in the inset **Figure 3.16a**. The results showed that all catalysts had peaks at temperatures below 200℃ due to loss of water and adsorbed *n*-heptane. The catalysts synthesised by the impregnation method show an obvious exothermic signal (soft coke) at 377℃. On the other hand, the catalyst prepared by the mechanical mixture method (MM) presented a soft coke peak at 340℃. Additionally, it shows a hard coke peak at 584℃ as seen for the parent zeolite (HZ80).

Figure 3.16b shows the relationship between the coke content and the Cr oxide loading. The coke content for spent Cr_2O_3-HZ80 catalysts was calculated from the weight loss above 250℃. The coke content in spent samples was in ascending order as follows: 10 wt.% Cr_2O_3/HZ80-MM < HZ80 < 20 wt.% Cr_2O_3/HZ80-IMP < 5 wt.% Cr_2O_3/HZ80-IMP < 10 wt.%

Cr_2O_3/HZ80-IMP. Interestingly, the minimum coke content was obtained in the MM-prepared catalyst whilst the maximum coke content was for the equivalent catalyst prepared by impregnation, likely due to the different distribution of chromium oxides species. Generally, the Cr addition causes an increase in coke formation for the catalysts prepared *via* impregnation. Carbon deposition was probably influenced by different distribution of chromium oxides species. There is a significant decrease in *n*-heptane conversion after 180 min on TOS as the amounts of coke in the spent catalysts as goes up in **Figure 3.17**.

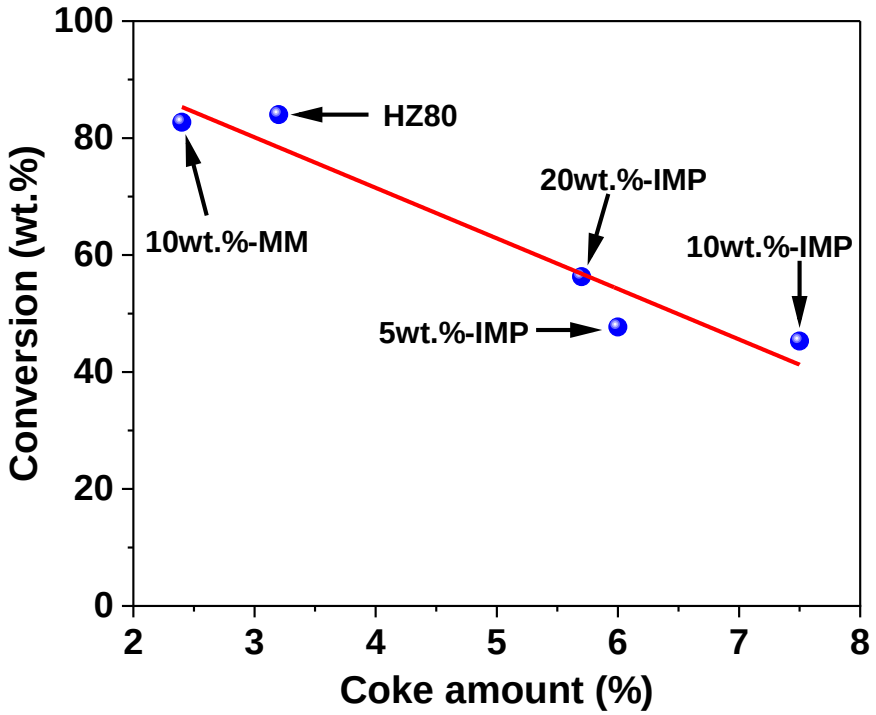


Figure 3.17. The relationship between the amount of coke and conversion in spent Cr_2O_3/HZ80 catalysts at 180 min of TOS.

3.3.2.3.3 Brunauer-Emmentt-Teller (BET) analysis

The BET surface areas of spent Cr_2O_3/HZ80 samples are summarised in **Table 3.9**. By comparing the surface area of Cr_2O_3/HZ80 catalysts before (**Table 3.5**) and after catalytic cracking of *n*-heptane (**Table 3.9**), it can be noted that there is a significant decrease in the surface area in the spent catalysts. The 'coking' effect is common in zeolite catalysed processes

and has long been thought to be the primary cause of catalyst deactivation[28, 45, 46]. The linear relationship between the surface area and the deposited coke content is depicted in **Figure 3.18**.

The massive influence of the impregnated Cr_2O_3 species over the coke deposition is noticeable with the IMP-prepared catalyst. While the Cr_2O_3 sites generated upon the impregnation method favour coke formation upon the cracking reaction, pore-blocking by Cr_2O_3 entities may also contribute to the accumulation of coke on the zeolite surface, most notably at the locations where Cr_2O_3 species migrate into the channels. According to the XPS results in **Table 3.6**, the sample prepared by mechanical mixture and impregnation method contained mainly Cr^{3+} as Cr_2O_3. However, the distribution of chromium oxides may be effected by the preparation method.

Table 3.9. The surface area (BET) analysis of the spent Cr_2O_3-HZ80 catalyst series for the selective cracking reaction of *n*-heptane toward light olefins.

Catalyst	**BET** ($m^2.g^{-1}$)	**t-plot micropore** ($m^2.g^{-1}$)	**t-plot External** ($m^2.g^{-1}$)
spent HZ80	319	255	65
Spent 5 wt.% Cr_2O_3/HZ80- IMP	253	188	65
Spent 10 wt.% Cr_2O_3/HZ80- IMP	230	176	55
Spent 20 wt.% Cr_2O_3/HZ80- IMP	229	168	61
Spent 10 wt.% Cr_2O_3/HZ80- MM	322	198	125

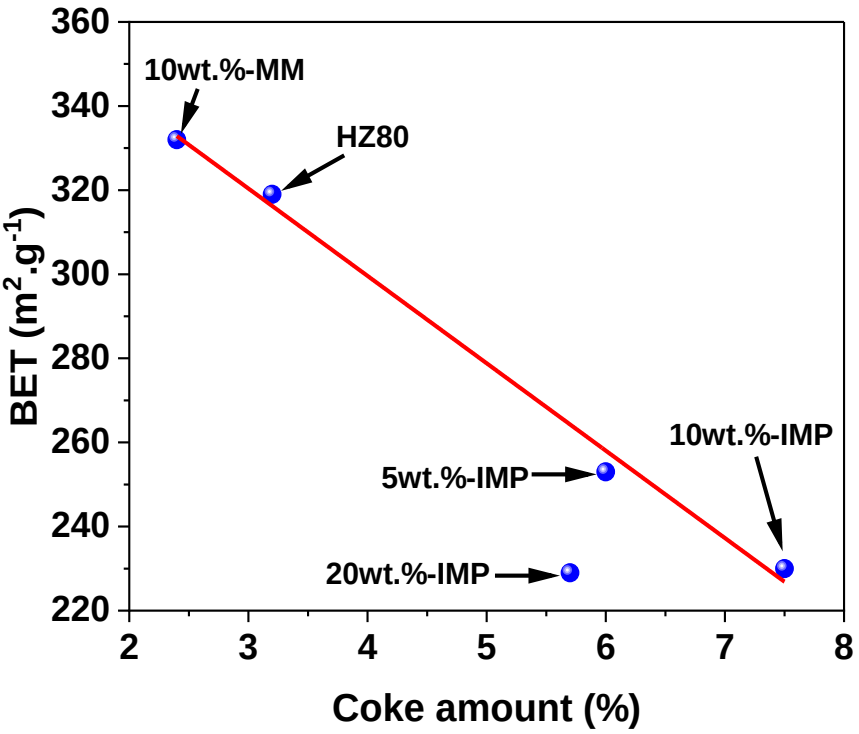


Figure 3.18. The relationship between the amount of coke and surface area in spent Cr_2O_3/HZ80 catalysts.

3.3.2.3.4 X-ray photoelectron spectroscopy (XPS)

To further rationalize the Cr synthesis effect, the surfaces of 10 wt.% Cr_2O_3-HZ80 spent sample synthesized by two methods were characterized using X-ray photoelectron spectroscopy (XPS). The obtained XPS spectra for Cr are shown in **Figure 3.3A**, while **Table 3.10** illustrates the binding energies and surface atomic (%) of the various Cr species. The spectrum for 10 wt.% Cr_2O_3-HZ80 catalyst prepared by impregnation method and mechanical mixture (**Figure 3.3A)** indicates the existence of one surface species: Cr^{3+} at 574.00 eV. Compared the fresh sample prepared by impregnation method, the Cr 2p peak is progressively shifted to lower binding energies from 574.0 eV to the highest value of 573.0 eV of spent sample. However, in 10 wt.% Cr_2O_3-HZ80 spent sample, the decrease of the Cr signals occurred owing to the carbon depositions on catalyst surface after catalytic cracking reaction[47].

On the other hand, coke structure existed in the spent catalysts, as evidenced by C 1s of XPS spectra shown in **Figure 3.3A**. A peak at 284.0 eV corresponds to carbon on the fresh catalysts. After the catalytic cracking reaction, the same C 1s peak position is observed at 284.0 eV for the spent catalysts with peak intensity growth indicating the formation of coke without significant shifting in the peak signal which is more clear on catalyst prepared by IMP method[48]. Also, there is a noticeable increase in Cr^{3+} species after *n*-heptane catalytic cracking for the MM-prepared catalysts (**Table 3.10**) compared with the fresh formulations (**Table 3.6**). All 10 wt.% Cr_2O_3/HZ80 catalysts prepared by different method did not show any change in the oxidation state of Cr.

Table 3.10. The binding energies, FWHM and surface compositions of various Cr oxide species for the spent 10 wt.% Cr_2O_3-HZ80 catalysts prepared by impregnation and mechanical methods.

Catalyst	**Name**	**Binding Energies (eV)**	**FWHM (eV)**	**Atomic (%)**
10 wt.% IMP-spent	O 1s	532.09	3.88	57.33
	C 1s	284.09	4.69	17.05
	Cr 2p	576.09	8.76	1.15
	Si 2p	103.09	3.39	30.60
10 wt.% MM- spent	O 1s	532.16	2.16	43.63
	C 1s	288.16	6.37	28.67
	Cr 2p	575.16	15.29	2.00
	Si 2p	108.16	2.98	25.70

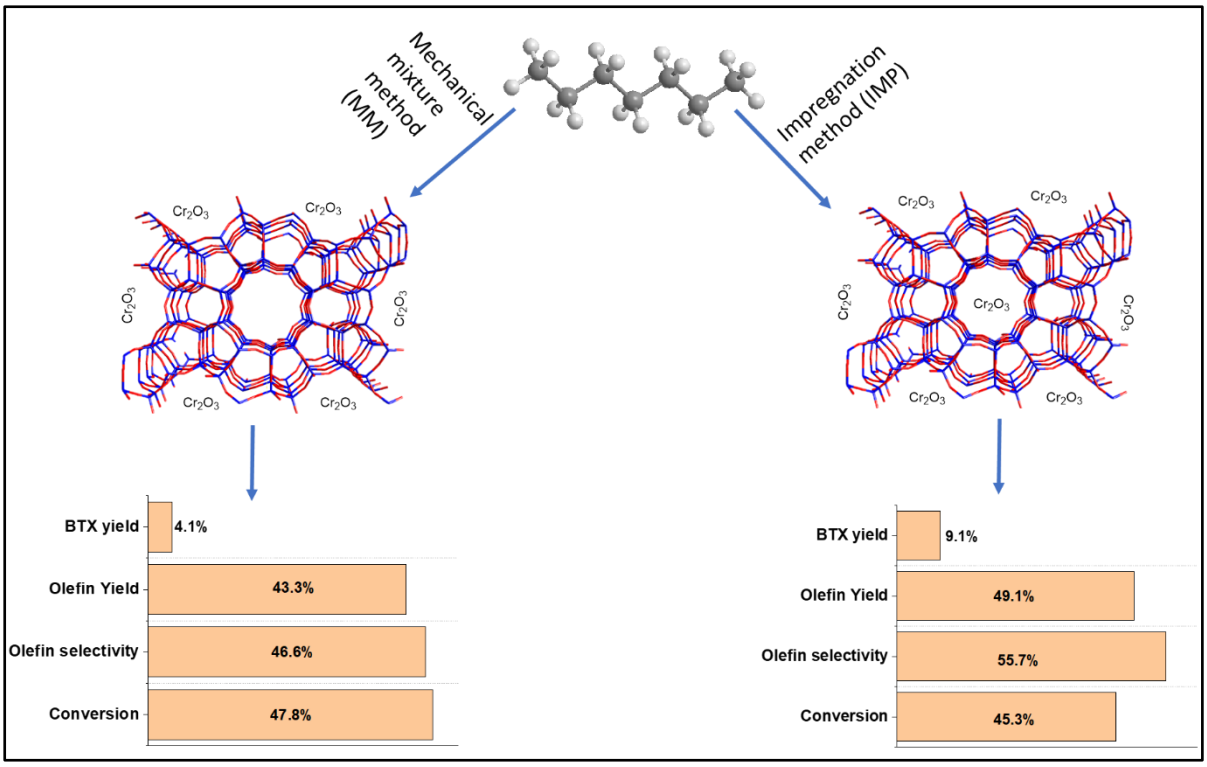


Figure 3.19. Schematic representation of the influence of the synthesis methods of Cr_2O_3-HZ80 catalyst over the production of light alkenes and BTX through the catalytic cracking of *n*-heptane at fairly similar conversion.

As described in **Figure 3.19** above, the synthesis of Cr_2O_3 over zeolite (HZ80) demonstrates a high synergy in the production of light olefins by the catalytic cracking of *n*-heptane. The catalysts prepared by impregnation method produce light olefins selectively and enhance their yield. By contrast, the catalysts prepared by mechanical mixture showed slightly less olefin selectivity and yield compared with the impregnation method. This is due to the presence of Cr_2O_3 crystallite in the catalyst. It is interesting to note that the Cr_2O_3 dispersed onto the zeolite using mechanical combination, generated the least quantity of coke, which is anticipated to be reflected in an extension of the catalyst's lifetime.

3.4 Conclusion

The first part of this chapter revealed that the SiO_2/Al_2O_3 ratio for H-ZSM-5 zeolite is not perhaps the primary determinant of the performance of the zeolite catalyst. Other properties such as the specific surface, sample acidity, and zeolite topology (or zeolite framework type) are critical for zeolite catalytic performance. We have found that HZ80 and HZ280 were more selective toward light olefins (ethene, propene, and butene) formation than H-ZSM-5 zeolite with a lower SiO_2/Al_2O_3 ratio.

As previously stated, our aim is to modify further the zeolites to improve their catalytic performance toward light olefin formation from the catalytic cracking reaction of *n*-heptane as model feedstock and light naphtha as targeted raw material. This chapter also highlights the importance of zeolite modification by Cr_2O_3 using two synthesis methods.

Cr_2O_3 loading on HZ80 zeolite through the mechanical mixture (MM) method further improves the *n*-heptane conversion (i.e., 95 wt.%) compared to catalyst formulation prepared by impregnation method (IMP). The catalyst's physicochemical characteristics, as well as their catalytic activity and selectivity, were all affected by Cr addition. Chromium modified zeolite prepared by the impregnation method produced a drop in the surface area, which reduced further with increased chromium loading. The optimal Cr loading (i.e., 10 wt.%) increased selectivity to olefins, particularly ethylene. Interestingly the Cr_2O_3 loaded over zeolite by mechanical mixture produced the lowest coke amount which is expected to be reflected in a longer catalyst lifetime.

The catalyst synthesised by the mechanical method revealed a higher particle size than the impregnation method, suggesting that Cr_2O_3 is on the surface rather than inside the zeolite channels.

A novel contribution of this chapter is the significant enhancement of the yield of olefins and catalyst stability when the zeolite is modified with Cr_2O_3 made by the impregnation

route (IMP). We have shown that the impregnation method (IMP) method was superior to the mechanical mixture (MM) approach.

3.5 References

1. Yong, W.; Toshiyuki, Y.; Seitaro, N.; Junko, N. K.; Takashi, T., Catalytic cracking of *n*-hexane for producing propylene on MCM-22 zeolites. *Applied Catalysis A: General*, 2015, *504*, 192-202.
2. Yuta, N.; Jun-ichi, N.; Teruoki, T.; Takao, M., Deactivation mechanism of MFI-type zeolites by coke formation during *n*-hexane cracking. *Chemical Engineering Journal*, **2015,** *278*, 159-165.
3. Ziyauddin, S. Q.; Palani, A.; M.A; Abdullah, M. A.; Gazali, T.; Hassan, A., Enhanced light olefins production via *n*-pentane cracking using modified MFI catalysts. *Heliyon*, **2022,** *8* (3), e09181.
4. Janda, A.; Bell, A. T., Effects of Si/Al Ratio on the Distribution of Framework Al and on the Rates of Alkane Monomolecular Cracking and Dehydrogenation in H-MFI. *Journal of the American Chemical Society*, **2013,** *135* (51), 19193-19207.
5. Fengqiu, C.; Liyong, M.; Dang-guo, C.; Xiaoli, Z., Synthesis of hierarchical porous zeolite and its performance in n-heptane cracking. *Catalysis Communications*, **2012,** *18*, 110-114.
6. Wang, Y.; Yokoi, T.; Namba, S.; Kondo, J. N.; Tatsumi, T., Improvement of catalytic performance of MCM-22 in the cracking of *n*-hexane by controlling the acidic property. *Journal of Catalysis*, **2016,** *333*, 17-28.
7. Li, S.-C.; Lin, Y.-C.; Li, Y.-P., Understanding the Catalytic Activity of Microporous and Mesoporous Zeolites in Cracking by Experiments and Simulations. *Catalysts*, **2021,** *11* (9), 1114.
8. Sadeghbeigi, R., Fluid Catalytic Cracking Handbook: An Expert Guide to the Practical Operation, Design, and Optimization of FCC Units. Fourth ed.; *Elsevier*, **2020**.
9. Chester, A. W.; Derouane, E. G., Zeolite characterization and catalysis. *Springer*, **2009**; Vol. 360.
10. Armaroli, T.; Simon, L. J.; Digne, M.; Montanari, T.; Bevilacqua, M.; Valtchev, V.; Patarin, J.; Busca, G., Effects of crystal size and Si/Al ratio on the surface properties of H-ZSM-5 zeolites. *Applied Catalysis A: General*, **2006,** *306*, 78-84.
11. Alotibi, M. F.; Alshammari, B. A.; Alotaibi, M. H.; Alotaibi, F. M.; Alshihri, S.; Navarro, R. M.; Fierro, J. L. G., ZSM-5 Zeolite Based Additive in FCC Process: A Review on Modifications for Improving Propylene Production. *Catalysis Surveys from Asia*, **2020,** *24* (1), 1-10.
12. Rane, N.; Kersbulck, M.; Van Santen, R.; Hensen, E., Cracking of *n*-heptane over Brønsted acid sites and Lewis acid Ga sites in ZSM-5 zeolite. *Microporous and Mesoporous Materials*, **2008,** *110* (2-3), 279-291.
13. Mohiuddin, E.; Mdleleni, M. M.; Key, D., Catalytic cracking of naphtha: The effect of Fe and Cr impregnated ZSM-5 on olefin selectivity. *Applied Petrochemical Research*, **2018,** *8* (2), 119-129.

14. Lu, J.; Zhao, Z.; Xu, C.; Duan, A.; Zhang, P., CrHZSM-5 Zeolites – Highly Efficient Catalysts for Catalytic Cracking of Isobutane to Produce Light Olefins. *Catalysis Letters,* **2006,** *109* (1), 65-70.
15. Frey, F.; Huppke, W., Equilibrium dehydrogenation of ethane, propane, and the butanes. *Industrial & Engineering Chemistry,* **1933,** *25* (1), 54-59.
16. Bhasin, M. M.; McCain, J. H.; Vora, B. V.; Imai, T.; Pujadó, P. R., Dehydrogenation and oxydehydrogenation of paraffins to olefins. *Applied Catalysis A: General,* **2001,** *221* (1), 397-419.
17. Mingfa, Y.; Jingai, S.; Zixu, Y.; Haiping, Y.; Xianhua, W.; Zhengshun, W.; Hanping, C., Conversion of lignin into light olefins and aromatics over Fe/ZSM-5 catalytic fast pyrolysis: Significance of Fe contents and temperature. *Journal of Analytical and Applied Pyrolysis,* **2019,** *137*, 259-265.
18. Abbasizadeh, S.; Karimzadeh, R., Influence of various aluminum distributions on modification of ZSM-5 zeolite framework with cobalt ions in alkane catalytic cracking. *Research on Chemical Intermediates,* **2019,** *45* (3), 955-972.
19. Lu, J.; Zhao, Z.; Xu, C.; Duan, A.; Wang, X.; Zhang, P., Catalytic cracking of isobutane over HZSM-5, FeHZSM-5 and CrHZSM-5 catalysts with different SiO_2/Al_2O_3 ratios. *Journal of Porous Materials,* **2008,** *15* (2), 213-220.
20. Amin, N. A. S.; Anggoro, D. D., Characterization and activity of Cr, Cu and Ga modified ZSM-5 for direct conversion of methane to liquid hydrocarbons. *Journal of Natural Gas Chemistry,* **2003,** *12* (2), 123-134.
21. Wang, K.; Fan, S.; Zhang, J.; Ma, Q.; Zhang, W.; Zhao, T.-S., Effects of synergy between Cr_2O_3 and hierarchical HZSM-5 on transformation of LPG toward propylene and ethylene. *Fuel Processing Technology*, **2018,** *179*, 53-59.
22. Treacy, M. M.; Higgins, J. B., Collection of simulated XRD powder patterns for zeolites fifth (5^{th}) revised edition. *Elsevier,* **2007**.
23. Konno, H.; Tago, T.; Nakasaka, Y.; Ohnaka, R.; Nishimura, J.-i.; Masuda, T., Effectiveness of nano-scale ZSM-5 zeolite and its deactivation mechanism on catalytic cracking of representative hydrocarbons of naphtha. *Microporous and Mesoporous Materials,* **2013,** *175*, 25-33.
24. Xu, H.; Weijun, Z.; Yajie, T.; Yuan, Q.; Zhenheng, D.; Fuxiang, F.; Xiangwen, Z.; Guozhu, L., Superiority of ZrO_2 surface enrichment on ZSM-5 zeolites in *n*-pentane catalytic cracking to produce light olefins. *Microporous and Mesoporous Materials,* **2019,** *276*, 41-51.
25. Afroukhteh-Langaroudi, N.; Tarighi, S.; Khonakdara, H. A., Catalytic Cracking of *n*-Hexane and *n*-Heptane over ZSM-5 Zeolite: Influence of SiO_2/Al_2O_3 Ratio. *Petroleum Chemistry*, **2018,** *58*, 457-463.

26. Tarighi, S.; Afroukhteh-Langaroudi, N.; Khonakdar, H. A., Conversion of *n*-heptane over different catalysts: Effect of catalyst-to-oil ratio and temperature. *Petroleum Science and Technology*, **2017,** *35*, 1-7.
27. Juan, S.; Ting-jun, F. U.; Jiang-wei, C.; Wei-li, W. A. N.; Rui-yue, Q. I.; Zhong, L. I., Effect of ZSM-5 crystal size on its catalytic properties for conversion of methanol to gasoline. *Journal of Fuel Chemistry and Technology*, **2017,** *45* (1), 75-83.
28. Mores, D.; Kornatowski, J.; Olsbye, U.; Weckhuysen, B. M., Coke formation during the methanol-to-olefin conversion: in situ microspectroscopy on individual H-ZSM-5 crystals with different Brønsted acidity. *Chemistry–A European Journal*, **2011,** *17* (10), 2874-2884.
29. Gibot, P., Centimetric-sized chromium (III) oxide object synthesized by means of the carbon template replication. *Ceramics*, **2020,** *3* (1), 92-100.
30. Waseda, Y.; Matsubara, E.; Shinoda, K., X-ray diffraction crystallography: introduction, examples and solved problems. S*pringer Science & Business Media*, **2011**.
31. Bagabas, A. A.; Alsawalha, M.; Taha, K. K.; Albaid, A.; Sohail, M.; Alqahtani, M.; Alrasheed, R.; Alqarn, A.; Ashamari, B.; Parkin, I. P., High Surface Area of Polyhedral Chromia and Hexagonal Chromium Sulfide by the Thermolysis of Cyclohexylammonium Hexaisothiocyanatochromate(III) Sesquihydrate. *Chemistry Select*, **2021,** *6* (17), 4298-4311.
32. Losch, P.; Hoff, T. C.; Kolb, J. F.; Bernardon, C.; Tessonnier, J.-P.; Louis, B., Mesoporous ZSM-5 Zeolites in Acid Catalysis: Top-Down vs. Bottom-Up Approach. *Catalysts*, **2017,** *7* (8), 225.
33. Brune, D.; Hellborg, R.; Whitlow, H. J.; Hunderi, O., Surface characterization: A user's sourcebook. *John Wiley & Sons*, **2008**.
34. Thermo Scientific. https://www.jp.xpssimplified.com/periodictable.php.
35. Chastain, J.; King Jr, R. C., Handbook of X-ray photoelectron spectroscopy. *Perkin-Elmer Corporation*, **1992,** *40*, 221.
36. Sattler, J. J.; Ruiz-Martinez, J.; Santillan-Jimenez, E.; Weckhuysen, B. M., Catalytic dehydrogenation of light alkanes on metals and metal oxides. *Chemical Reviews*, **2014,** *114* (20), 10613-10653.
37. Monai, M.; Gambino, M.; Wannakao, S.; Weckhuysen, B. M., Propane to olefins tandem catalysis: a selective route towards light olefins production. *Chemical Society Reviews*, **2021**.
38. Kiani, D.; Sourav, S.; Tang, Y.; Baltrusaitis, J.; Wachs, I. E., Methane activation by ZSM-5-supported transition metal centers. *Chemical Society Reviews*, **2021,** *50* (2), 1251-1268.
39. Han, S.; Zhao, Y.; Otroshchenko, T.; Zhang, Y.; Zhao, D.; Lund, H.; Vuong, T. H.; Rabeah, J.; Bentrup, U.; Kondratenko, V. A.; Rodemerck, U.; Linke, D.; Gao, M.; Jiao, H.; Jiang, G.; Kondratenko, E. V., Unraveling the Origins of the Synergy Effect between ZrO_2 and CrO_x in Supported $CrZrO_x$ for Propene Formation in Nonoxidative Propane Dehydrogenation. *ACS Catalysis*, **2020,** *10* (2), 1575-1590.

40. Corma, A.; Corresa, E.; Mathieu, Y.; Sauvanaud, L.; Al-Bogami, S.; Al-Ghrami, M. S.; Bourane, A., Crude oil to chemicals: light olefins from crude oil. *Catalysis Science & Technology*, **2017,** *7* (1), 12-46.
41. Su-Bing, F.; Dan, W.; Hai-Bo, L.; Jie, T.; Xiao-Lan, Z.; Xin-Hua, G.; Tian-Sheng, Z., Enhancing stability and coaromatization of *n*-hexane and methanol over Zn,Cr /HZSM-5. *Applied Catalysis A: General*, **2020,** *599*, 117602.
42. Pradhan, A. R.; Wu, J. F.; Jong, S. J.; Tsai, T. C.; Liu, S. B., An ex situ methodology for characterization of coke by TGA and ^{13}C CP-MAS NMR spectroscopy. *Applied Catalysis A: General*, **1997,** *165* (1), 489-497.
43. Sangrama, K. S.; Siddharth, S. R.; Singh, I. D., Structural characterization of coke on spent hydroprocessing catalysts used for processing of vacuum gas oils. *Applied Catalysis A: General*, **2004,** *278* (1), 83-91.
44. Collett, C. H.; McGregor, J., Things go better with coke: the beneficial role of carbonaceous deposits in heterogeneous catalysis. *Catalysis Science & Technology*, **2016,** *6* (2), 363-378.
45. Guisnet, M.; Magnoux, P., Coking and deactivation of zeolites: Influence of the Pore Structure. *Applied Catalysis*, **1989,** *54* (1), 1-27.
46. Guisnet, M.; Ribeiro, F. R., Deactivation and regeneration of zeolite catalysts. *Imperial College Press*, **2011**.
47. Ruelas-Leyva, J. P.; Maldonado-Garcia, L. F.; Talavera-Lopez, A.; Santos-López, I. A.; Picos-Corrales, L. A.; Santolalla-Vargas, C. E.; Torres, S. A. G.; Fuentes, G. A., A Comprehensive Study of Coke Deposits on a Pt-Sn/SBA-16 Catalyst during the Dehydrogenation of Propane. *Catalysts*, **2021,** *11* (1), 128.
48. Mu, H.; Muhammad-Faryad, A.; Yue-Qin, S.; Xiao-Long, Z.; Jin An, W.; Xin-Yao, N.; Zheng, W., Study on the deactivation mechanism of HZSM-5 in the process of catalytic cracking of *n*-hexane. *Chemical Engineering Journal*, **2023,** *451*, 138793.

Chapter 4

Cracking of *n*-heptane on HZ23-support formulations: Effect of different supports

Overview

This chapter describes the effects of different supports on HZ23 zeolite catalyst in the catalytic cracking of naphtha. The cracking properties of zeolites for the production of light alkenes were investigated using *n*-heptane as a model compound since it is one of the primary constituents of light naphtha. Different supports such as SiO_2, Al_2O_3, kaolin, TiO_2, ZrO_2, and MgO were combined with 20 wt.% HZ23 zeolite to assess their influence over the formation of light alkenes. As before, the catalysts were tested in a fixed-bed unit at 550°C for 4 hours using a flow system and characterised by various techniques.

4.1 Introduction

This chapter describes the utilisation of metal-based catalysts in various formulations for the production of light olefins. The high stability of the catalyst, long lifetime performance and improved selectivity towards the desired products are the crucial factors when selecting optimal catalytic materials. Several other factors can influence the catalyst performance, such as the metal-support interaction, the dispersion of the active sites, appropriate porosity, and the surface area. Deciding on a suitable catalyst - in combination with the optimum conditions - will enhance olefin production[1]. According to the literature, the utilisation of heterogeneous catalysts supported by metal oxides is still a fertile research field, and which remains to be explored.

Metal oxides are one of the most significant constituents in global petrochemical processes[2]. The catalytic cracking of hydrocarbons using acidic catalysts has been extensively examined in the critically important area of olefin production. It was found that zeolites particularly have tremendous advantages for propylene production in a fixed-bed reactor under optimum operating conditions compared to other methods such as conventional steam cracking. It was also found that the use of appropriately dispersed metals could accelerate the

dehydrogenation process. Hodoshima *et al.* investigated the catalytic cracking of *n*-hexane or 1-hexene using two different catalysts, one a zeolite-based composite and the other an aluminium-oxide composite. It was found that the presence of Fe in Fe-Ga-Al-containing Al-ZSM-5 (MFI-type) catalyst reduces the acid site strength whilst Ga promotes the dehydrogenation of the hydrocarbons, enhancing the production of propylene under mild conditions. Furthermore, the propylene yield and the *n*-hexane conversion were improved over a H–Fe–Ga–Al-MFI/Al_2O_3 composite owing to the high dispersion of the zeolite on the metal oxide binder with high acid density[3, 4].

Rodaum *et al.* investigated the dispersion of rare earth elements on zeolite supports to generate basic sites which reduce the side reactions and improve light olefin production. Interestingly, compared to the pristine zeolite, the presence of highly dispersed MgO and Al_2O_3 enhances the yield of light olefins. Moreover, the ZSM-5/MgAlOx(y) formulation produced a higher yield of light olefins with the metal oxide content was increased. However, the preparation method of the catalysts must be considered a key step in the overall process since the traditional impregnation method can cause some drawbacks, such as pore blocking by oxide clusters or metal aggregation[5, 6]. Consequently, it is crucial to target the optimisation of both the amount and the strength of the zeolite acid sites is compared for achieving enhanced selectivity towards light olefins[7].

Zeng and co-workers studied the catalytic activities of different materials for 6h time on stream (TOS), which were compared to the pristine zeolite for the methanol to olefin reaction. They examined the performance of γ-Al_2O_3/HZSM-5 prepared by solid-state physical mixing and HZSM-5/γ-Al_2O_3 prepared by the liquid-phase precipitation coating. It was found that simply mixed approach the selectivity towards ethylene, propylene, and the yield of light olefins of 46.8%, 22.1%, and 65.7%, respectively. Whereas the selectivity of ethylene, propylene and the yield of light olefins using HZSM-5/γ-Al_2O_3 was 52.3%, 34.4%, and 81.9%,

respectively indicating a remarkable change with method of synthesis. In addition, the variation of the γ-Al_2O_3 loading also affected the catalyst activity, for instance 40% HZSM-5/γ-Al_2O_3 exhibited an enhanced catalytic performance and catalytic stability with a lifetime of 50h. Finally, the comparison of the spent catalyst of HZSM-5/γ-Al_2O_3 with zeolite itself indicated more carbon deposition in the latter compared to the small amount observed in the composite spent catalysts. This can be attributed to the formation of mesopores in the HZSM-5/γ-Al_2O_3 compared to the micropore structure of the zeolite catalyst[8].

Liu *et al.* reported that the choice of adequate metal oxide support can significantly influence the olefin production activity from syngas[9]. They developed an iron catalyst that exhibited an enhanced selectivity towards olefins and lower selectivity towards methane. The production of light olefins from syngas was also studied by Wang *et al.*[10]; they reported the enhanced conversion of CO towards light olefins over a catalyst of iron-carbon nanotubes. Longya *et al.*[11] also examined the catalytic conversion of syngas into light olefins over Fe catalysts, they found that a Fe-MnO/MgO catalyst was particularly effective for producing light olefin[12].

Nano-sized iron/cobalt-doped ceria-zirconia nanocomposites were assessed in the catalytic cracking of *n*-hexane as model compound for naphtha at a reaction temperature of 650℃. High conversion and stability were obtained over co- doped ceria-zirconia supports with iron and cobalt catalysts. The optimal loading of Fe and Co over ceria-zirconia was 10 wt.% each metal (10 wt.%Fe-10 wt.% Co/60 wt.% CeO_2- 20 wt.% ZrO_2). The catalyst showed high conversion (33.3 mol.%) and selectivity to ethylene and propylene (67.5 mol.%) after 10h TOS. In addition, the catalysts produced an olefin yield (ethylene and propylene) of about 22.5 mol.%. It was also found that the *n*-hexane interacts with metal ions and oxygen species in the lattice and the presence of Lewis acid sites on the surface of the catalysts assists the catalytic reaction. Moreover, they described the cracking mechanism as proceeding *via* the β-splitting

of the formed intermediate radical (carbenium-ion) from the FeCo/CeZr catalyst surfaces to form ethylene and propylene[13].

A series of bimetallic Pt-Sn/θ-Al_2O_3 catalysts were prepared and utilised in propane and butane dehydrogenation reactions. Lee *et al.* used 0.5 wt.% of Pt with different amounts of Sn (0.5, 0.75, 1.0 and 1.5wt%). They found that the increasing order of catalytic activities for propylene yield was as follows: $Pt_{0.5}\ Sn_{0.75} > (PtSn)_{0.5} > Pt_{0.5}\ Sn_{1.0} > Pt_{0.5}\ Sn_{1.5}$. On the other hand, the catalytic activity for butene production followed the order of $Pt_{0.5}\ Sn_{1.0} > Pt_{0.5}\ Sn_{0.75} > (PtSn)_{0.5} > Pt_{0.5}\ Sn_{1.5}$. The decrease in the olefin yields was attributed to the geometric effect resulting in the low surface area of the Pt metal. The incorporation of Sn into Pt catalyst promotes cracking to produce light olefins owing to the increase of the catalyst surface area[14].

Overall, the catalyst support plays a key role in reaction performance. It is essential to decide upon this catalyst component as it influences the mechanical properties of the catalysts. It controls the interaction of the substrate with the active sites on the catalyst which is then reflected in the yield and selectivity of the desired products. A survey of the literature shows that the use of metal oxides as catalytic supports in the cracking reaction has not been fully explored.

This chapter aims to move towards a fundamental understanding of the competing interaction mechanisms of the catalyst components together with the role of the support in the catalytic cracking of *n*-heptane over zeolite-metal oxide catalysts. Different metal oxides such as Al_2O_3, TiO_2, ZrO_2, MgO, SiO_2 and kaolin were combined with zeolite (HZ23, SiO_2/Al_2O_3= 23) *via* the suspension method and calcined at 550℃. These catalysts were then examined in the catalytic cracking of *n*-heptane into light olefins at the same temperature (550℃) for 4 hours in flow systems. For comparison, the pristine zeolite was also tested at 550℃ under similar operational conditions.

4.2 Experimental

4.2.1 Preparation of catalysts

The catalysts used in this study were based on H-ZSM-5 (HZ23) with different metal oxide or kaolin. The catalysts were prepared by mixing H-ZSM-5 (SiO_2 to Al_2O_3 ratio 23 and MFI-type zeolyst) with the different materials. The materials used as supports were silica oxide (amorphous SiO_2, anhydride, Sigma-Aldrich), aluminium oxide (γ-Al_2O_3, catalyst support, high surface area, and bimodal, Alfa Aesar), kaolin (anhydrous, Sigma Aldrich), titanium (IV) oxide (TiO_2, Alfa Aesar), zirconium oxide (ZrO_2, Alfa Aesar), and magnesium oxide (MgO, 98%, Sigma Aldrich). In a typical synthesis process, NH_4-ZSM-5 was initially pre-calcined at 550℃ for 5h in a static air atmosphere to get the hydrogen form. Samples containing this zeolite will hereafter be referred to as HZ23. The oxides or kaolin were mixed with an aqueous solution of HZ23 using deionized water. The zeolite was dispersed in deionized water and stirred for 10 minutes at room temperature. The supports were mixed slowly in the H-ZSM-5-containing suspension, the concentration of which was calculated 80 wt.% (ca. 10-15ml H_2O/g-support). The catalysts were stirred for 3-4 hours at room temperature on a magnetic hot plate. Then an overnight drying step at 80-100°C (ca. 15 h) was conducted. The catalysts were finally calcined at 550°C for 2 hours in a static air atmosphere at a heating rate of 3°C.min^{-1}.

4.2.2 Characterisation of catalysts

The fresh and spent catalysts were carefully characterised by a range of techniques such as X-ray powder diffraction (XRD), scanning electron microscopy (SEM), energy dispersive X-ray spectroscopy (EDX), thermogravimetric analysis (TGA), and N_2-physisorption measurements to determine surface area through Brunauer-Emmett-Teller (BET) method.

The powder X-ray diffraction pattern was collected by means of a Bruker-Eco D8 ADVANCE diffractometer (Cu-Kα radiation, λ = 1.5406 Å) working at 40 kV–25 mA and equipped with a Lynxeye detector. The sample was scanned in a range of 2θ from 5° to 90°.

Thermogravimetric analysis (TGA) in flowing air characterised the content and type of carbon deposited in the spent samples. The sample was heated from room temperature to 1000℃ at a heating rate of 10℃ min^{-1} in air with a 100 mL min^{-1} flow rate to remove all so-called coke precursors. Between 10 and 20 mg of spent sample were loaded into a small alumina crucible for the test.

The surface morphology of the sample was analysed using a scanning electron microscope (JEOL 840F). The N_2 physisorption measurements were carried out at a liquid nitrogen temperature using Micromeritics Micro Active (TriStar II Plus). Before the analysis, the samples were weighed and placed in quartz tubes. Afterwards, they were degassed under vacuum at 50ºC for 24 hours to remove impurities on the sample surface. The BET surface area was determined by nitrogen gas adsorption at -196℃ with a micromeritics brand 3flex model device. Adsorption and desorption points were calculated between 0 and 1 relative pressure (p/p0).

A scanning electron microscope (ZEISS EVO) was used to characterize the surface morphology of the samples before and after the catalytic cracking process. Images were taken using the Inlens detector of the Zeiss Sigma 300 Scanning Electron Microscope. The samples were poured on carbon tape and coated with a mini sputter for 300 seconds. Images were taken at 5 KV at different magnifications. The surface element concentrations were analyzed by energy-dispersive Xray spectroscopy (EDX; ZEISS EVO). EDX analysis was performed from a wide-angle general surface at 15 KV.

4.2.3 Experimental condition

The catalytic cracking tests were carried out in a fixed-bed reactor system coupled to a gas chromatography system (online GC, offline GC/MS). Typically, 0.5 g of each catalyst was loaded into the centre of the tube-shaped reactor, which was supported with carborundum (Fisher, 24 grit). By help of an HPLC pump, *n*-heptane (Sigma, 99%) was injected. Flowing N_2 as carrier gas into the reactor (20 $mL.min^{-1}$) was used. The temperature of the catalyst bed was raised to 550°C at a rate of 5°$C.min^{-1}$ under atmospheric pressure. In order to ensure that the catalyst was completely dehydrated for all experiments, it was left for 1 hour at 550°C under N_2 flow.

The gas and liquid products were separated at the system's termination (a cool water condenser was used). Gaseous products were examined in a PerkinElmer, Claurs 580 GC. The analysis was conducted through a thermal conductivity detector (TCD) for non-hydrocarbon and a flame ionisation detector (FID) for hydrocarbons every 30 minutes for four hours of time on stream (TOS) after the initial *n*-heptane injection into the catalyst bed. During the reaction, liquid products were collected every 1h in the separator and diluted in dichloromethane for analysis in the gas chromatograph-mass spectrometer instrument. Each component of liquid phase was quantified (Shimadzu GC/MS-QP 2010 SE). Chapter 2 depicts the catalyst testing system and tubular design.

4.3 Results and Discussion

4.3.1 Pre-reaction analysis of catalysts

4.3.1.1 X-ray diffraction (XRD)

The 20wt.% H-ZSM-5 (SiO_2/Al_2O_3 = 23, HZ23)-containing catalysts alongside the supports and the parent HZ23 were examined by X-ray diffraction (XRD) before the catalytic cracking of *n*-heptane as shown in **Figure 4.1**. Notably, the peaks positioned between 5º and 25º 2θ correspond to the MFI-type zeolite structure[15], which is well preserved for all catalyst formulations. In the 20 wt.% HZ23/MgO catalysts, characteristic XRD diffraction peaks at 43º and 62.4º in 2θ[16, 17]from crystalline MgO are also detected. According to the literature[18, 19], the XRD peaks at 45.9º and 67.2º in 2θ are associated with γ-Al_2O_3 for the 20 wt.% HZ23/Al_2O_3 sample and they correspond to the [400] and [440] lattice planes of γ-Al_2O_3 structure. In general, kaolin has a chemical formula of $Al_2Si_2O_5(OH)_4$ when it is calcined at 550°C the phase changes into metakaolin ($Al_2O_3Si_2O_4$) due to dehydroxylation as shown in 20 wt.% HZ23/kaolin[20]. The peaks of kaolin between 5º to 24.8º in 2θ agrees with previous research[20, 21], these peaks overlap with zeolite peaks in the 20 wt.% HZ23/kaolin samples. For the 20 wt.% HZ23/ZrO_2 catalysts, the characteristic peaks for the ZrO_2 were observed at the 2θ angles 28.3º, 31.6º, 50.4º, and 60.1º, which are associated with the lattice planes [-111], [111], [220], and [311], respectively[22-24]. The diffraction peaks at 25.6º [101], 38.0º [004], 48.2º [200], 54.1º [105], 55.3º [211], and 63.0º [112] in the X-ray pattern of the 20 wt.%HZ23/TiO_2 catalyst correspond to the phase of TiO_2[25, 26] whilst the strongest diffraction peak at 22.2º (2θ) for 20 wt.% HZ23/SiO_2 catalyst corresponds to SiO_2 , which may be attributed to the microspheres of SiO_2[27]. In general, the relatively small content of HZ23 produces weak XRD diffraction peaks whilst the strongest peaks correspond to the supports phase, whose crystallinity is markedly superior to that of the zeolite phase.

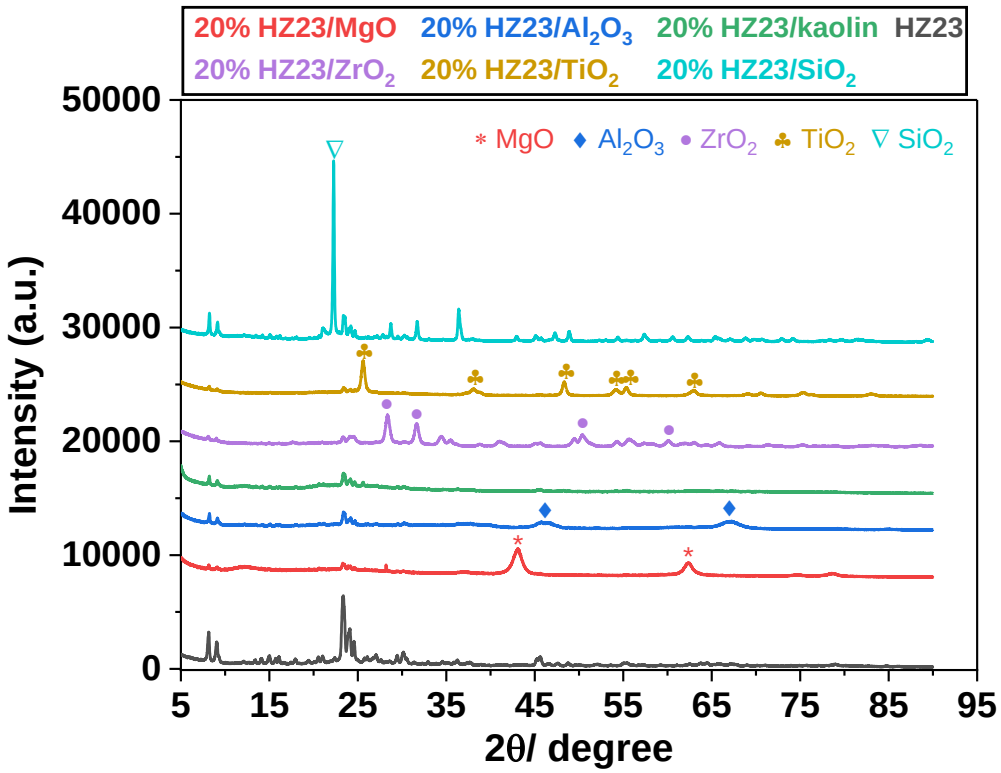


Figure 4.1. Comparison of powder X-ray diffraction patterns of the H-ZSM-5 zeolite (HZ23), and 20 wt.% HZ23 on different supports for fresh samples.

4.3.1.2 Brunauer-Emmentt-Teller (BET) analysis

The physical properties of surface areas of H-ZSM-5 (HZ23) with different supports are presented in **Figure 4.2**. As indicated in the figure, the parent zeolite has a very high surface area (ca. 355 $m^2.g^{-1}$) compared to the zeolite modified with different supports. Moreover, the surface area of H-ZSM-5 decreased when this was modified with different supports, following the descending order H-ZSM-5 (HZ23) > HZ23/Al_2O_3 > HZ23/TiO_2 > HZ23/MgO > HZ23/ZrO_2 > HZ23/kaolin > HZ23/SiO_2. According to the literature, the γ-Al_2O_3 has a surface area of about 250 $m^2.g^{-1}$ [28]. However, there is apparently a loss of surface area on both zeolite and γ-Al_2O_3 when they are mixed together, resulting an area of about 229 $m^2.g^{-1}$. Biris *et al.*[29] have determined that the surface area of MgO is about 130 $m^2.g^{-1}$, where here the combination of MgO and 20 wt.% H-ZSM-5 produced a surface area of 124 $m^2.g^{-1}$. An opposite trend was

obtained for the kaolin catalysts. Kaolin has a low surface area[20, 30] which increases remarkably to 94$m^2.g^{-1}$ when mixed with zeolite. The TiO_2 and SiO_2 supports have a higher surface areas[31, 32], and the combination with HZ23 decreased the surface area to 133, and 59 $m^2.g^{-1}$, respectively. However, the zeolite modified with ZrO_2 exhibits a surface area of about 99 $m^2.g^{-1}$, an increase in the surface area compared to the surface area of the ZrO_2 itself (ca. 75 $m^2.g^{-1}$)[33] was observed. An overall analysis of the surface areas for the supports-zeolite hybrid catalysts reveals a drastic decrease compared to the HZ23 owing to the relatively low surface area of oxides or kaolin.

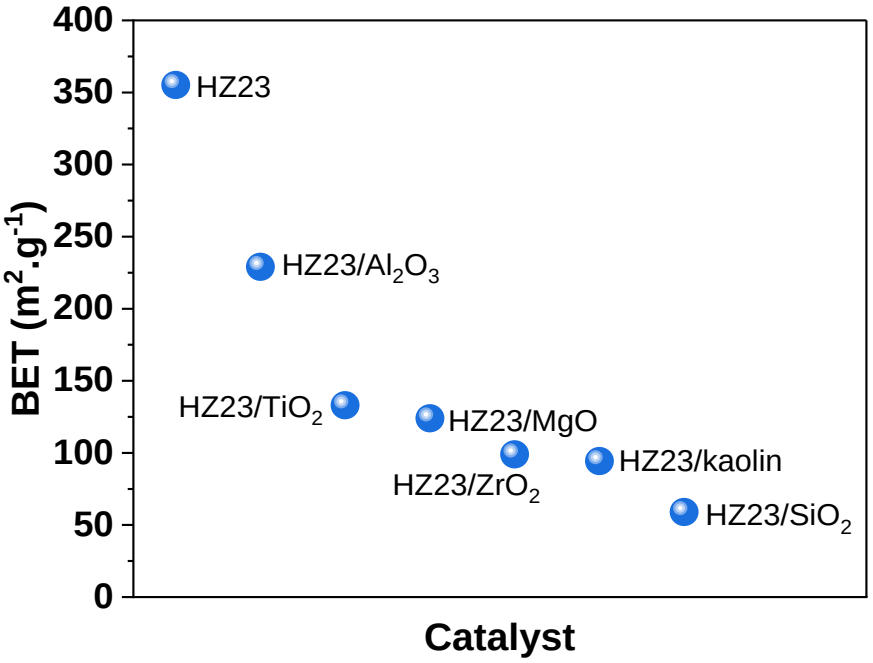


Figure 4.2. The surface area (BET) analysis of the fresh 20 wt.% H-ZSM-5 (HZ23) over different supports for the selective cracking reaction of *n*-heptane toward light olefins.

4.3.1.3 Thermogravimetric analysis (TGA)

The weight changes, during thermal decomposition in air, when samples were heated at 10°C.min^{-1} from room temperature to 1000°C, were determined using thermogravimetric analysis (TGA) for the fresh catalysts. The results are shown in **Figure 4.3a**. The TGA curve displays a steady weight reduction up to 200°C due to dehydration reaction, the weight loss

was about 2-4% during the thermal treatment of the catalysts. However, Al_2O_3 showed a greater weight loss (ca. 9%) at a temperature below 200℃. Also, the 20 wt.% HZ23/MgO catalyst showed a second step weight loss of 7 wt.% between 200 and 500℃ due to dehydroxylation and decarbonisation reactions of adsorbed water and CO_2 from the atmosphere. The other catalysts showed similar weight losses to the parent zeolite between 200℃ and 1000℃ as a consequence of the zeolite water loss until the final activation temperature is reached.

The above-described profiles clearly agree with the derivative thermogravimetry (DTG) curves as displayed in **Figure 4.3b**. They also show the peaks of water desorption within 40-200℃ with slight differences in the maximum temperature due to different chemical properties of the metal oxides. The DTG profile of the MgO-containing catalyst (**Figure 4.1A**) shows a major peak between 280 and 335℃ owing to CO_2 desorption[34]. The DTG profile of the 20 wt.% HZ23/kaolin catalyst shows a peak at a temperature above 600℃ associated with the complete dehydroxylation of kaolin to produce metakaolin[35].

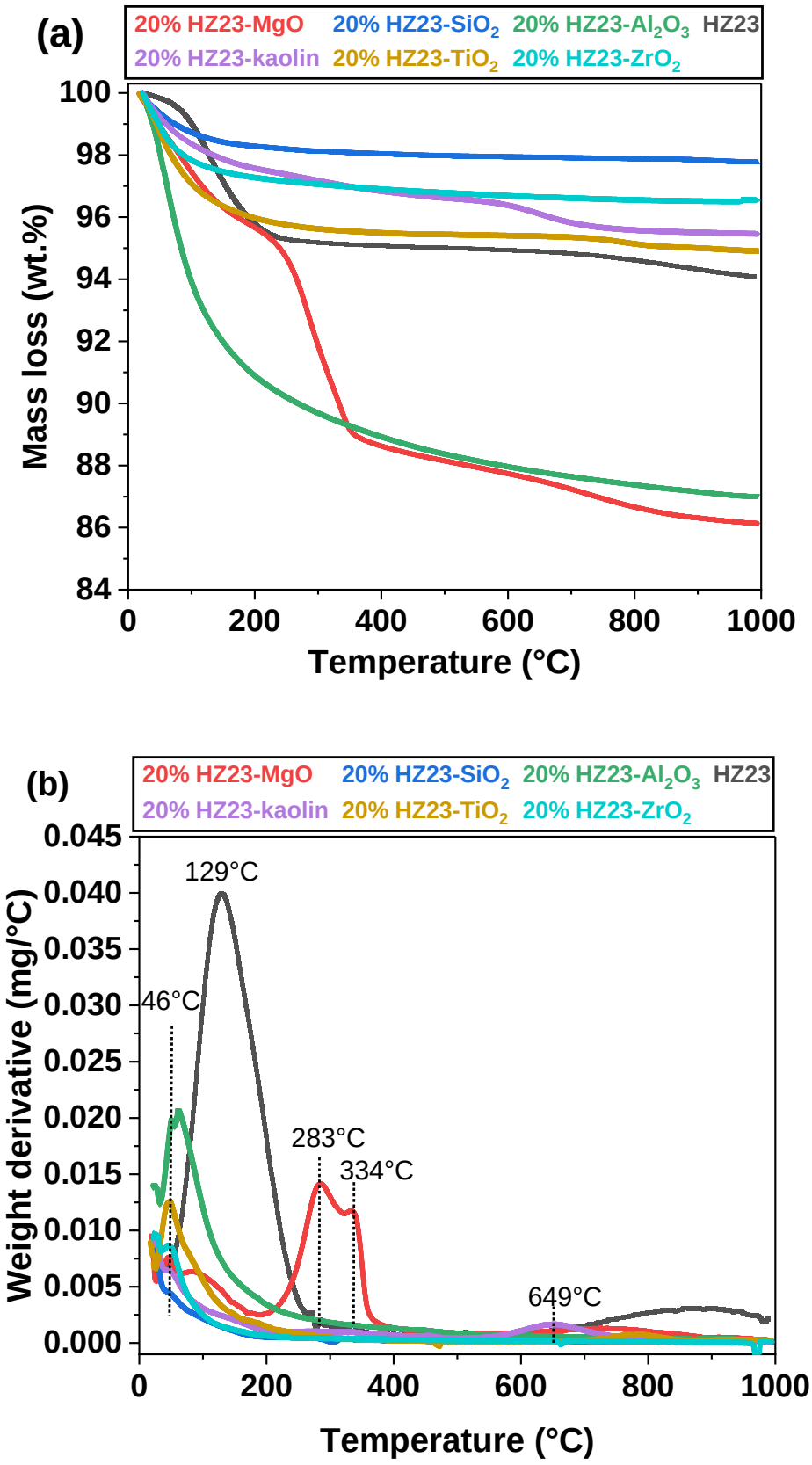


Figure 4.3. (a) TGA for fresh samples under air flow for 20 wt.% HZ23 with different supports catalyst. (b) weight derivative thermogravimetric (DTG) curves of the five catalysts under air.

4.3.1.4 Scanning Electron Microscopy (SEM)

Scanning electron microscopy (SEM) was used to interrogate the surface morphology of the catalysts. **Figure 4.4** and **Figure 4.2A** display the SEM images for the fresh catalysts with different oxides or kaolin. As shown in the SEM images, the catalyst surfaces revealed a uniform dispersion of zeolite over the different surfaces. This is encouraging in that it facilitates the selective cracking reactions by reducing the time required for hydrocarbons to diffuse into the zeolite channels. Likewise, these images reveal a certain homogeneity in the composition of the catalysts based on the visibly different shapes of supports and zeolite. Furthermore, the scanning electron micrograph of HZ23 revealed that it had a particle size distribution that was uniform, a shape that was more -or -less regular, and a crystallinity that was pronounced, together with a narrow particle size distribution.

The SEM images of the 20 wt.% HZ23/MgO catalyst are shown in **Figure 4.4** and **Figure 4.2A**. These show that, the catalyst particles have a large surface area. As can be seen in the SEM image, the morphology of the HZ23 zeolite with MgO resembles that of a flower or a star[36, 37]. The SEM image for the 20 wt.% HZ23/kaolin catalyst clearly reveals the lamellar or flat plate-like structure of kaolin with small sized crystals of HZ23. Kaolin is a layered aluminium silicate clay composed of double layers of stacked AlO_6 octahedra and SiO_4 tetrahedra[20, 38-40]. In general, the zeolite made up of groups of hexagonal particles and the external of a commercial zeolite particle is rough[8, 41]. However, the 20 wt.% HZ23/SiO_2 catalyst has a smooth external surface as shown in **Figure 4.4** and **Figure 4.2A**, and can readily be distinguished from the small crystals of HZ23. On the other hand, the 20 wt.% HZ23 catalysts with ZrO_2 and TiO_2 were entirely covered in HZ23 zeolite nanocrystals and show aggregates of small sized particles the surface of the zeolite HZ23 structure. The surface of the catalysts with ZrO_2 and TiO_2 seems to be coated with a large number of spherical nanoparticles, and the HZ23 zeolite is masked. However, the XRD analysis results (**Figure 4.1**) showed clear

evidence for the presence of the HZ23 structure but not it is base structure. Undoubtedly, the Al_2O_3 has altered the shape and porosity of the HZ23. In the SEM images (**Figure 4.4** and **Figure 4.2A**), the zeolite particles of the 20 wt.% HZ23/Al_2O_3 are still discernible, but their profiles are blurred. The zeolite particles are noticeably linked with a large number of inter crystalline gaps occupied by Al_2O_3; this effect is particularly evident in the SEM image.

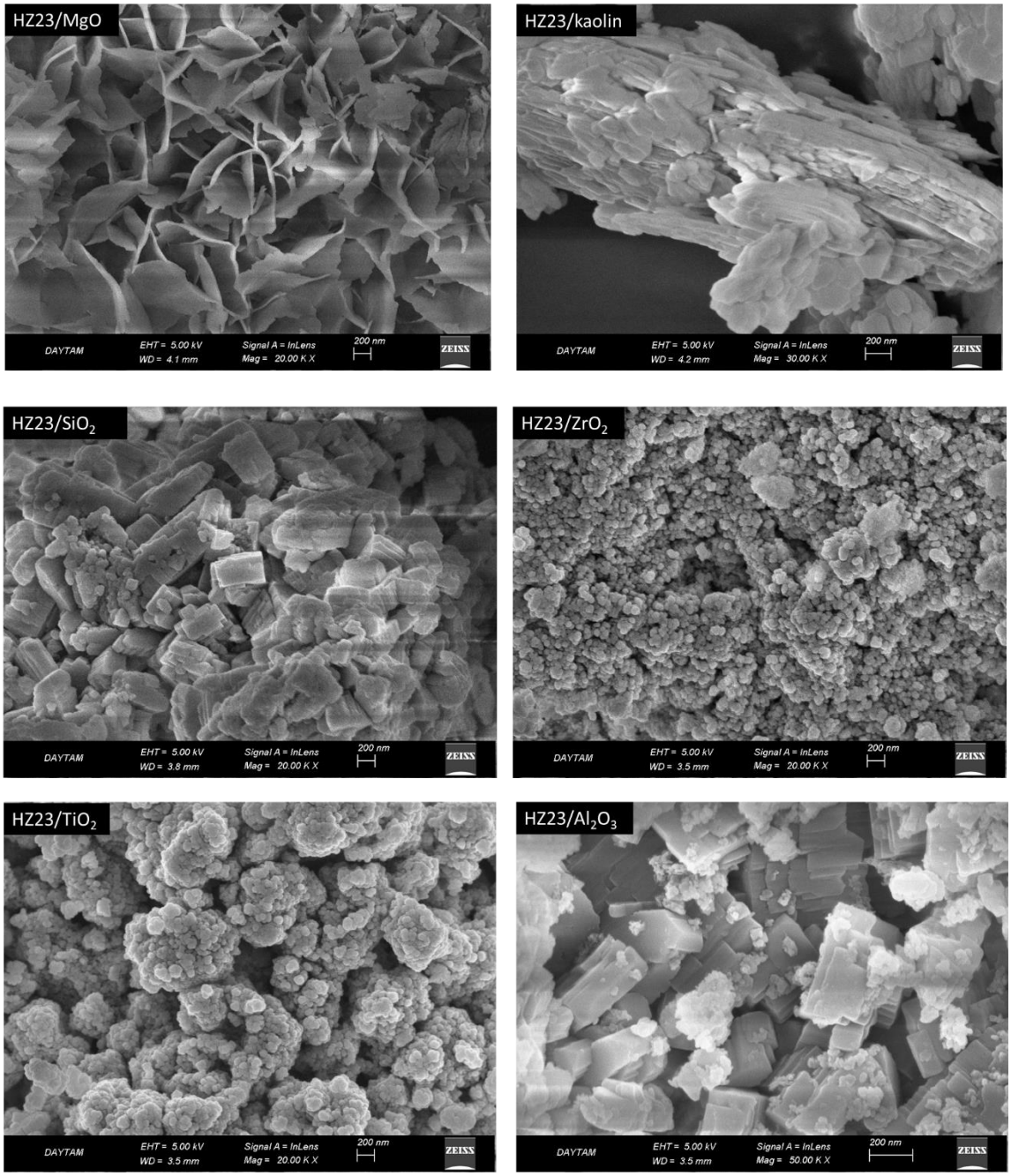


Figure 4.4. Scanning electron microscopy (SEM) images of 20 wt.% H-ZSM-5(HZ23) over different supports catalysis.

4.3.1.5 Transmission Electron Microscopy (TEM)

The transmission electron microscopy (TEM) technique provides information about the morphology, composition, and crystallography of samples. **Figure 4.5** and **Figure 4.3A** present the TEM images of HZ23/MgO, HZ23/kaolin, HZ23/SiO_2, HZ23/ZrO_2, HZ23/TiO_2, and

HZ23/Al_2O_3 before catalytic cracking of *n*-heptane. The TEM image for 20 wt.% HZ23/MgO catalyst calcined at 550℃ for 2h shows clearly the nanostructures of MgO, whose step edges have been observed in TEM images[34]. Furthermore, the electron micrograph clearly displays the nanostructure of zeolite on the MgO surfaces. This finding is consistent with the XRD results given in **Figure 4.1**. Interestingly, the TEM image for 20 wt.%HZ23/kaolin shows greater agglomeration and lower dispersion of the zeolite. In addition, this image shows how the kaolin morphology (dark areas) is a lamellar flat, parallel plates, while zeolite is present as particles. Interestingly, this image shown a good agreement with the structure of zeolite with kaolin described in the literature[20, 42, 43].

Normal scale and amplified TEM images for the 20 wt.% HZ23/SiO_2 catalyst are also shown in **Figure 4.5**. Zeolite distribution is significant on this catalyst. As can be seen in **Figure 4.1**, this catalyst also contains distinct XRD peaks due to crystalline HZ23. The typical cubic hexagonal morphology of HZ23 is evident in the TEM image of both pure HZ23 and the SiO_2-containing catalyst. As noted in the TEM result, zeolite particles appear to be connected to SiO_2, which is responsible for the large patches of diffuse black or grey colour in the image.

In addition, TEM analysis was also conducted on hybrid catalysts containing zeolite (HZ23) and ZrO_2, TiO_2, and Al_2O_3. As shown **Figure 4.5**, the dark areas correspond to the oxide component of the catalysts whilst the grey particles are associated with nanocrystals of zeolite, covering most of the surfaces of TiO_2, ZrO_2, and Al_2O_3 as can be seen in **Figure 4.5** and **Figure 4.3A**. The mild acidity of the supports rather than their relatively high surface area might play an important role in the high dispersion of the zeolite on the surface of the metal oxides. The X-ray diffraction (XRD) measurements confirmed to the presence of HZ23 (MFI-type) phase as given in **Figure 4.1**. Interestingly, the supports with acidic (i.e. Al_2O_3, TiO_2, ZrO_2) and basic (MgO) properties markedly affected the particle size of HZ23 whilst those with poor acid and base character (kaolin and SiO_2)[44] showed large crystals of zeolite. It is also

expected that the difference in the isoelectric points of the oxides or kaolin will affect the solution pH upon the catalyst synthesis and thereby influencing the zeolite dispersion[45].

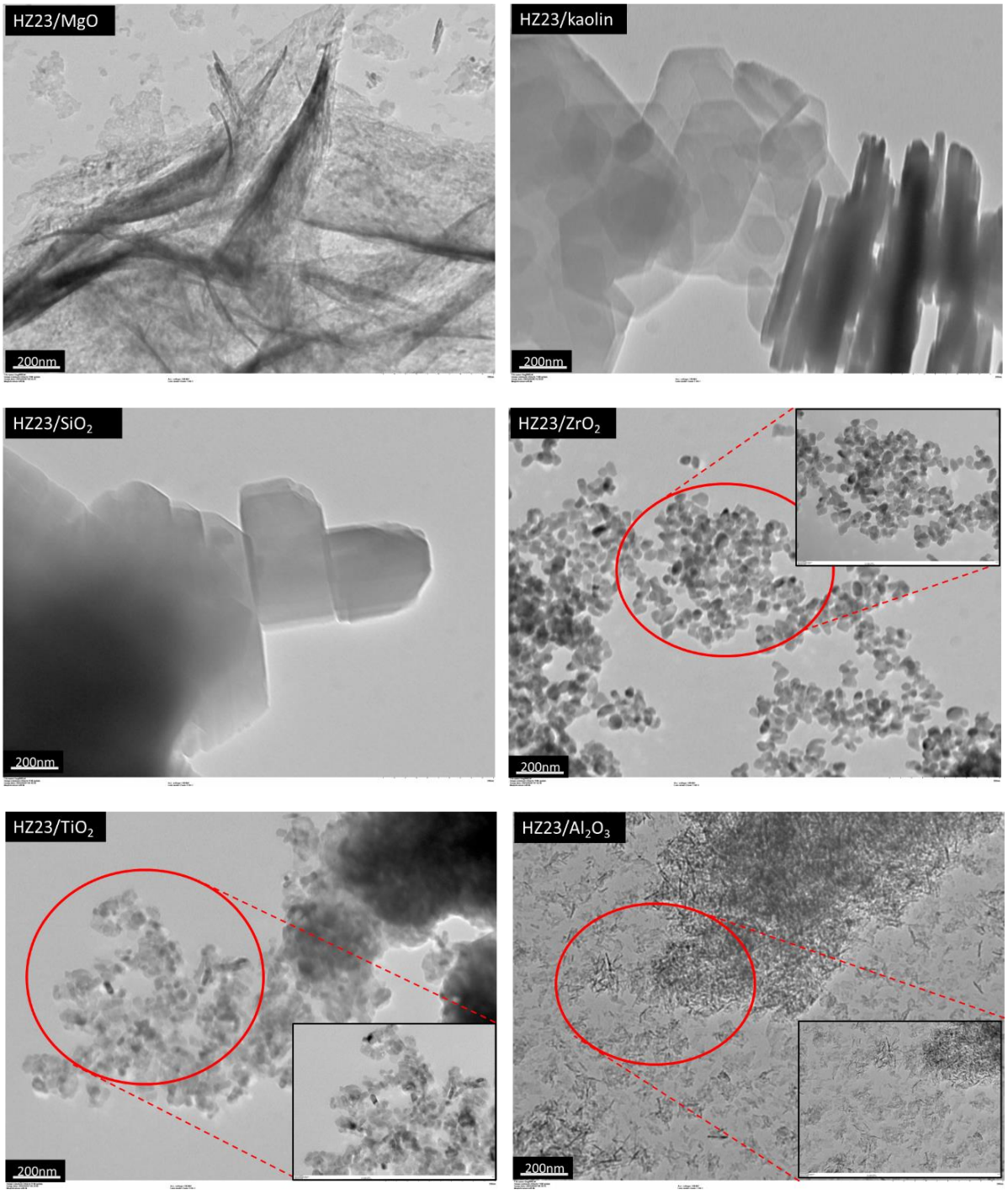
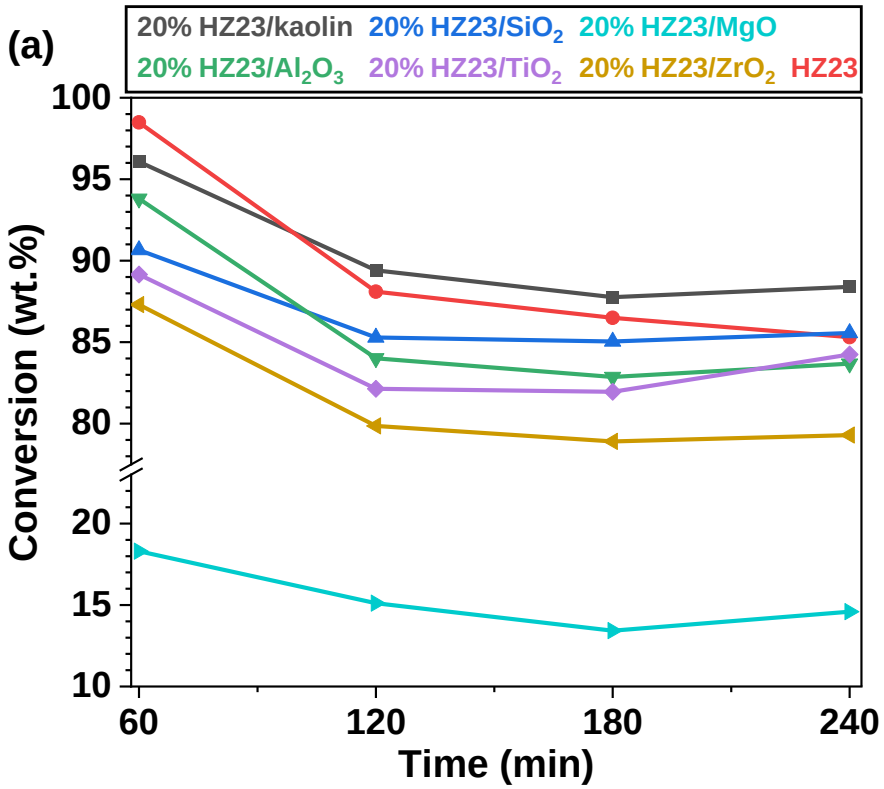
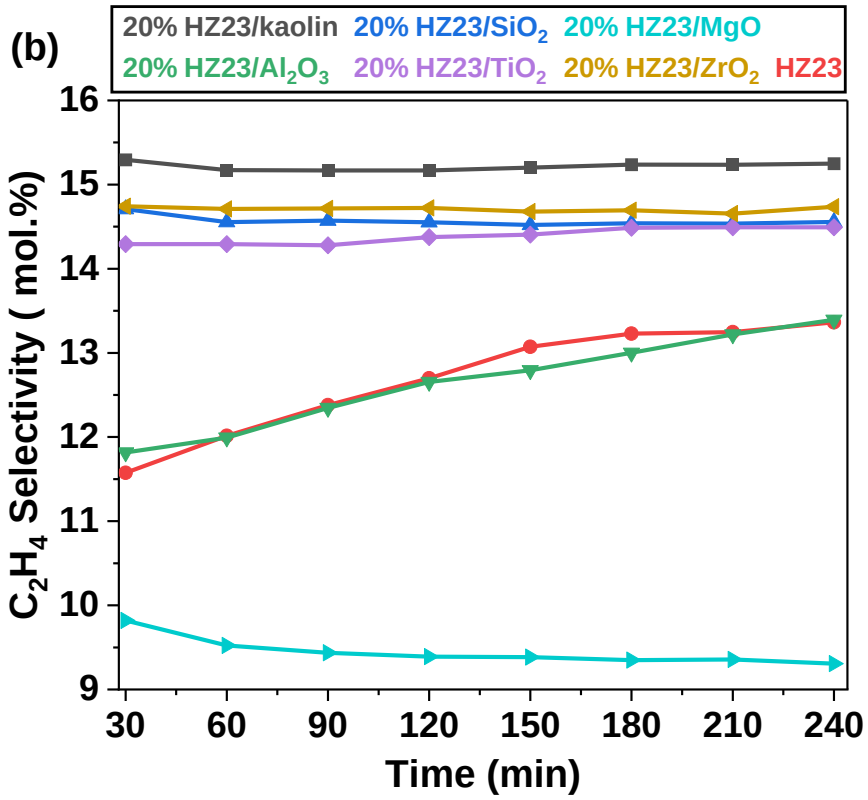


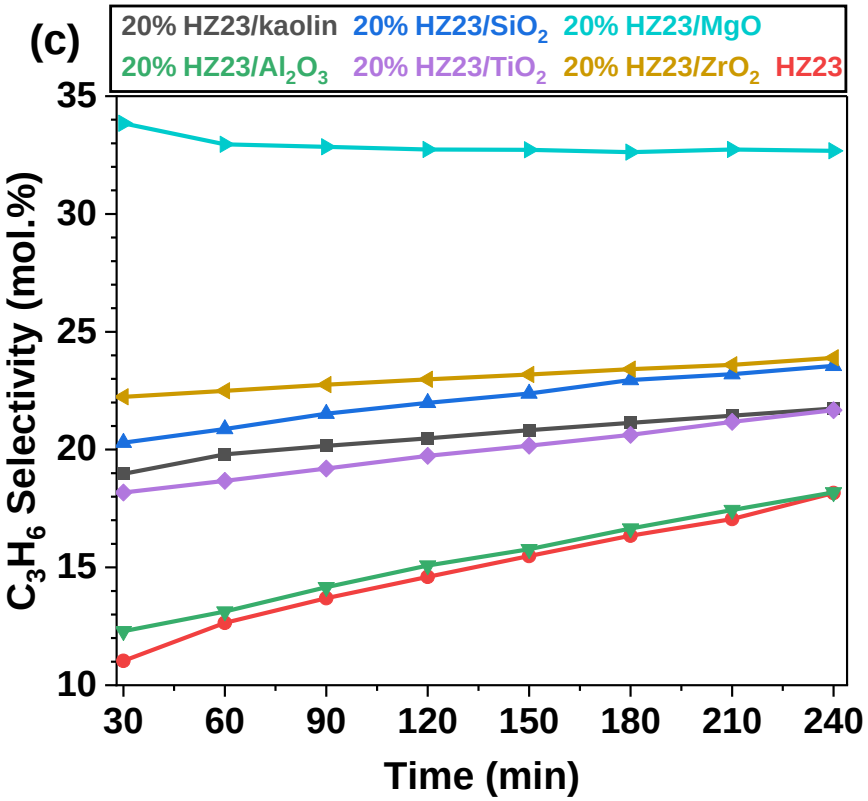
Figure 4.5. Transmission Electron Microscopy (TEM) image of 20 wt.% HZ23 over different supports.

4.3.2 Catalytic performance tests

In order to establish the reliability of the reaction set-up, the catalytic cracking of *n*-heptane was evaluated over fixed bed reactor at 550°C and atmospheric pressure for 4h. Initially, the catalytic performances of 20 wt.% HZ23 zeolites with different supports were evaluated to select the combination with HZ23 going the highest yield of light olefins. The overall carbon balance for these tests was above 90%, including residual carbon; this value is within the expected range of cracking reactions.




(b)
20% HZ23/kaolin
20% HZ23/SiO2
20% HZ23/MgO
20% HZ23/Al2O3
20% HZ23/TiO2
20% HZ23/ZrO2
HZ23
C2H4 Selectivity (mol.%)
Time (min)


(c)
20% HZ23/kaolin
20% HZ23/SiO2
20% HZ23/MgO
20% HZ23/Al2O3
20% HZ23/TiO2
20% HZ23/ZrO2
HZ23
C3H6 Selectivity (mol.%)
Time (min)

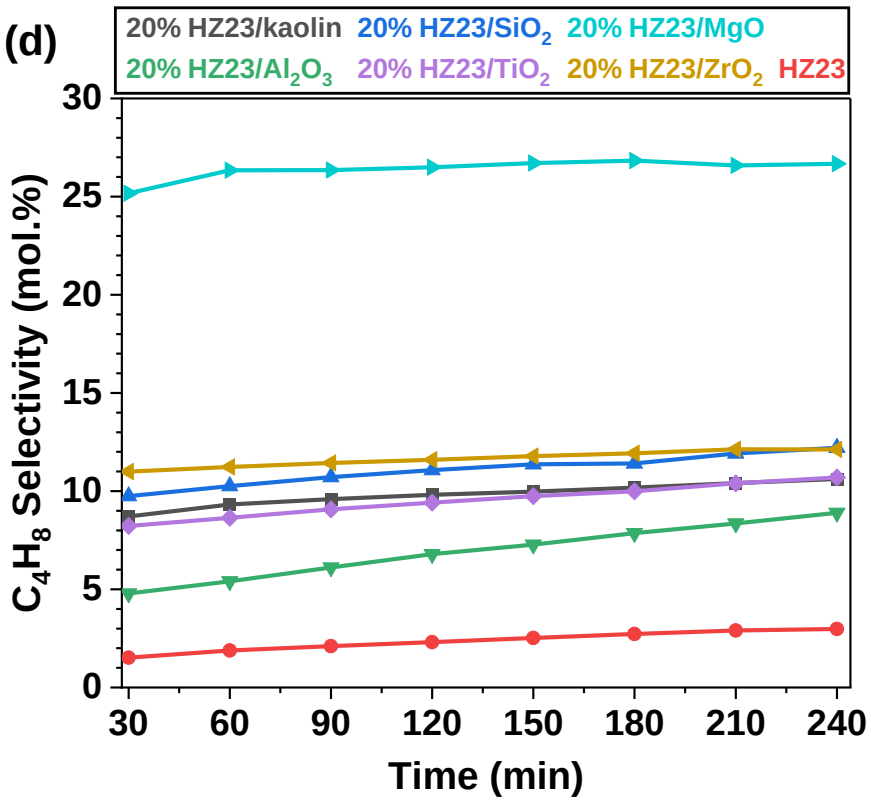


Figure 4.6. Effect of HZ23-oxide/kaolin formulations on *n*-heptane conversion (a), C_2H_4 selectivity (b), C_3H_6 selectivity (c) and C_4H_8 selectivity (d). The reactions were conducted at 550°C, atmospheric pressure (0.1 MPa), wight hour space velocity (WHSV) 8.2 h^{-1} and 20 $ml.min^{-1}$ N_2 flow rate. The estimated error was between 3 and 6%.

Zeolite (HZ23) combined with oxides or kaolin exhibited various levels of performance for *n*-heptane catalytic cracking with somewhat different selectivities for light olefin products as illustrated in **Figure 4.6**. Also included is the catalytic performance of unmodified HZ23 catalyst to illustrate clearly the strong influence of the support effect on the selectivity for olefins. After 4h of *n*-heptane catalytic cracking reaction at the selected 550°C temperature, the conversion for the catalysts tested is shown in **Figure 4.6a**.

The HZ23/MgO showed the lowest *n*-heptane conversion at about 18 wt.% during the first hour of reaction and decreased ca., to 15 wt.% with time-on-stream (TOS). However, the other catalysts showed higher conversions between 98-87 wt.% (included the parent HZ23) in the first hour and decreases about 2-12% with time-on-stream. This trend clearly indicates that a basic metal oxide (i.e., MgO) does not improve catalyst activity and stability.

Figure 4.6b-d illustrates the influence of time-on-stream (TOS) on *n*-heptane conversion and selectivity for light olefin (ethylene, propylene, and butylene) across various supports combined with zeolite (HZ23). The ethylene selectivity values for the *n*-heptane catalytic cracking over HZ23 are shown in **Figure 4.6b**. It can be observed that HZ23 with kaolin has the highest ethylene selectivity at about 15 mol.% and stability with time-on-stream. The zeolite (HZ23) with ZrO_2, TiO_2, and SiO_2 supports showed similar ethylene selectivity (ca. 14 mol.%), slightly lower than for kaolin. It is noticeable that the 20 wt.% HZ23-Al_2O_3 catalyst and the zeolite (HZ23) alone showed the lowest ethylene selectivity despite the slight increase from ~11.5 mol.% to 13.4 mol.% with TOS. This suggests that high acidity has a detrimental effect on the formation of ethylene.

The selectivity for propylene and butene are given in **Figure 4.6c-d**. It should be noted the zeolite (HZ23) modified by basic oxide (MgO) shows higher propylene and butene selectivity (values of about 33 mol.%, and 26 mol.%, respectively) than the other catalysts. The pure HZ23 and HZ23-Al_2O_3 displayed the lowest propylene and butene selectivity with the time-on-stream (TOS). However, propylene and butene selectivity for the zeolite (HZ23) modified by ZrO_2, SiO_2, kaolin, and TiO_2 have a similar range between 18-22 mol.% for propylene, and 8-11 mol.% for butene and increased slowly with time-on-steam (TOS). The propylene selectivity for zeolite (HZ23) over Al_2O_3 catalysts showed a similar trend to unmodified zeolite (HZ23).

Table 4.1 summarises the product yields of light olefin (ethene, propene, and butene) and BTX from the catalytic cracking of *n*-heptane on 20 wt.% HZ23 with different supports. The total olefins using the parent HZ23 zeolite increased with time on stream from 23.6 to 31 wt.%. Note that parent zeolite (HZ23) has a lower SiO_2/Al_2O_3 ratio (i.e., 23) and higher acidity[46], reflecting in a higher BTX yield (benzene, toluene, and xylene) (i.e., 3.6 wt.%) with time on stream.

On the other hand, the total olefin yields for 20 wt.% HZ23-metal oxide catalysts are higher than parent zeolite (HZ23) by 80-180%. The catalysts containing SiO_2, Al_2O_3, TiO_2, and ZrO_2 show total olefin yields in the range 29 to 47 wt.%. Whilst the total olefin yield for 20 wt.% HZ23-MgO catalyst was lower (below 6 wt.%) this is due to the relatively low *n*-heptane conversion (below 20 wt.%) as depicted in **Figure 4.6** and the possible contribution of thermal cracking reactions. It is noticeable that Al_2O_3-, TiO_2-, and ZrO_2-containing catalysts show comparable yields of BTX (between 3.1 and 3.3 wt.%) and higher than kaolin- and SiO_2-containg formulations (between 1.5 and 1.7 wt.%). No BTX was produced by the 20 wt.% HZ23/MgO catalyst.

This trend strongly implicates the acid-base properties of the catalyst playing a major role in the formation of alkenes and aromatic compounds[42].

Table 4.1. Yields of hydrocarbon products from *n*-heptane cracking over HZ23-oxide/kaolin formulations. The reactions were conducted at 550°C, atmospheric pressure (0.1 MPa), wight hour space velocity (WHSV) 8.2 h^{-1} and 20 $ml.min^{-1}$ N_2 flowrate. The estimated error was between 3 and 6%.

Samples	***Time (min)***	***Products Yield (wt.%)***				
		C_2H_4	**C_3H_6**	**C_4H_8**	**Alkane***	**BTX**
HZ23	60	10.7	11.3	1.6	76.3	0.0
	240	13.0	16.3	1.7	65.4	3.6
20 wt.% HZ23/kaolin	60	14.8	18.8	8.7	57.7	0.0
	240	14.6	20.7	10.1	53.1	1.5
20 wt.% HZ23/SiO_2	60	14.1	20.2	9.9	55.2	0.0
	240	14.0	22.6	11.7	50.1	1.7
20 wt.% HZ23/Al_2O_3	60	11.5	12.6	5.2	70.3	0.5
	240	12.6	17.1	8.4	58.9	3.1
20 wt.% HZ23/TiO_2	60	13.6	17.8	8.3	58.9	1.4
	240	13.6	19.4	9.4	54.4	3.3
20 wt.% HZ23/ZrO_2	60	14.1	21.6	10.8	52.1	1.5
	240	13.9	22.5	11.4	49.0	3.2

*Total alkane (CH_4+C_2H_6+C_3H_8+C_4H_{10}), 20 wt.%HZ23/MgO showed products yield less to 6 wt.%.

Figure 4.7 displays the selectivity for alkane (i.e., methane, ethane, propane, and butane) for the cracking of *n*-heptane over zeolite catalysts with various additives at different times on stream. The selectivity for CH_4 for the parent zeolite (HZ23) was in the range of 6-9 mol.%, which is higher than the metal oxide-containing 20 wt.% HZ23 formulations. It is noticeable that the selectivity for C_2H_6 for all the catalysts decreases with time on stream (TOS) by 7-10 mol.%, which is lower than that for the parent HZ23 (8.8-6.9 mol.%). On the other hand, the 20 wt.% HZ23/Al_2O_3 catalyst exhibited the highest C_3H_8 selectivity (about 42.1 mol.%) in the first hour of reaction than the other metal oxide-containing catalysts. However, the parent zeolite (HZ23) showed the highest C_3H_8 selectivity achieving, about 46.1 mol.%, at the beginning of the reaction but then decreased by 7-10% to 38.7 mol.% with TOS. The 20 wt.% HZ23 with TiO_2, SiO_2, ZrO_2, and kaolin showed stable propane selectivity TOS varying between 25.5-32.5 mol.%. Interestingly, the 20 wt.% HZ23/MgO catalyst exhibited the lowest selectivity for propane.

The selectivity for butane showed an opposite trend to that for propane. All the catalysts showed higher C_4H_{10} selectivity (i.e., 12-15 mol.%) than the parent zeolite (HZ23) (i.e., ca. 6-9 mol.%). In contrast, the butane selectivity from the 20 wt.% HZ23/MgO catalyst did not vary markedly with time on stream (ca. 9.2-9.7 mol.%) and was slightly higher than that from parent the HZ23 zeolite (i.e., 6-8.9 mol.%).

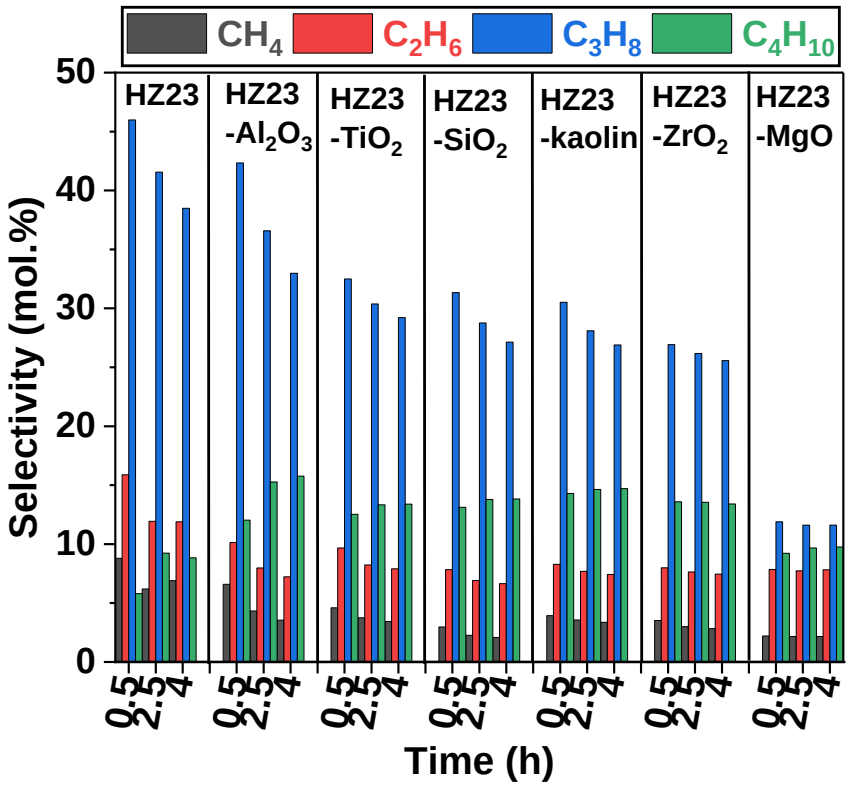


Figure 4.7. Selectivity of alkane on *n*-heptane catalytic cracking over HZ23-supports formulations. The reactions were conducted at 550°C, atmospheric pressure (0.1 MPa), wight hour space velocity (WHSV) 8.2 h^{-1} and 20 ml min^{-1} N_2 flowrate. The estimated error was between 3 and 6%.

4.3.3 Post- reaction analysis of catalysts

4.3.3.1 X-ray diffraction analysis

After the catalytic cracking of *n*-heptane, the catalysts consisting of 20 wt.% HZ23 on a variety of supports were subjected to X-ray diffraction analysis, as displayed in **Figure 4.8**. The spent zeolite (HZ23) is also presented with typical HZ23 XRD peaks at $5^o < 2\theta < 45^o$. The X-ray pattern of the used catalysts indicates no change or loss in the crystal structures of the catalyst components compared with the fresh samples (**Figure 4.1**).

Interestingly, although there was not a single carbon/coke signal identified in the diffraction patterns in the spent catalysts, as shown in **Figure 4.8**, the peak at $2\theta=12^o$ in the X-ray patterns corresponds to silicone grease used to load the catalyst on the sample holder, as shown in **Figure 4.4A**.

Moreover, the spent HZ23 exhibited several peaks at 2θ= 28º, 35º, and 41º belonging to the SiC used as the diluter in the catalyst bed. The fact that carbon is not clearly detected by X-ray diffraction is surely an indication of its low crystallinity or highly amorphous character.

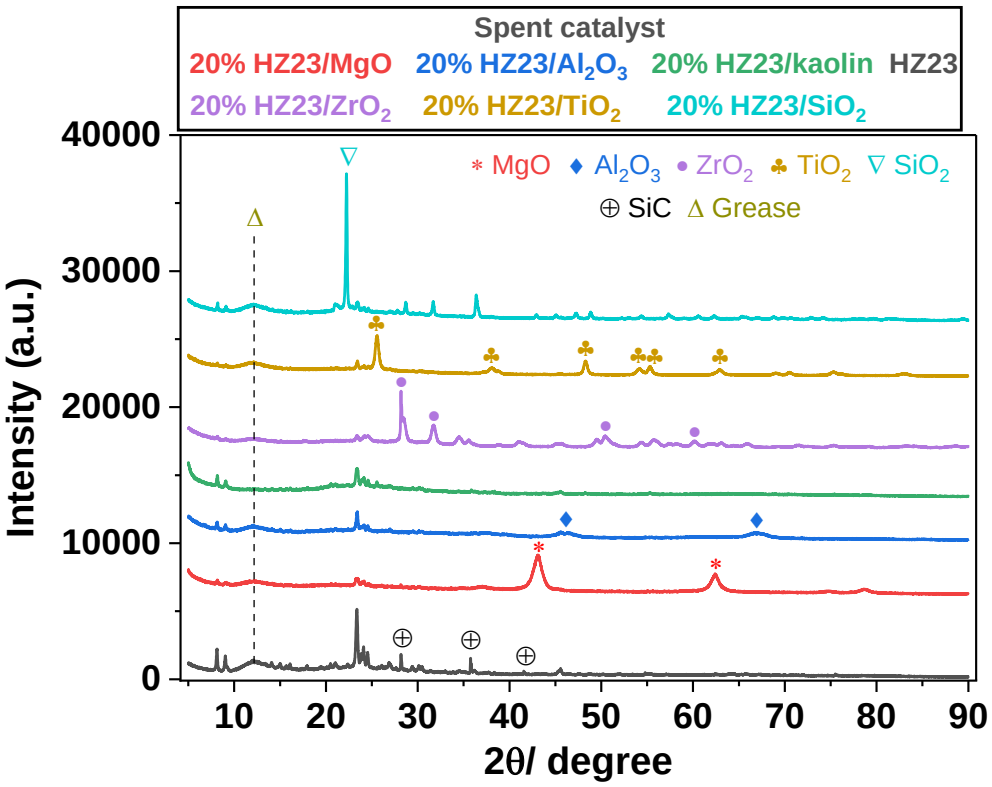


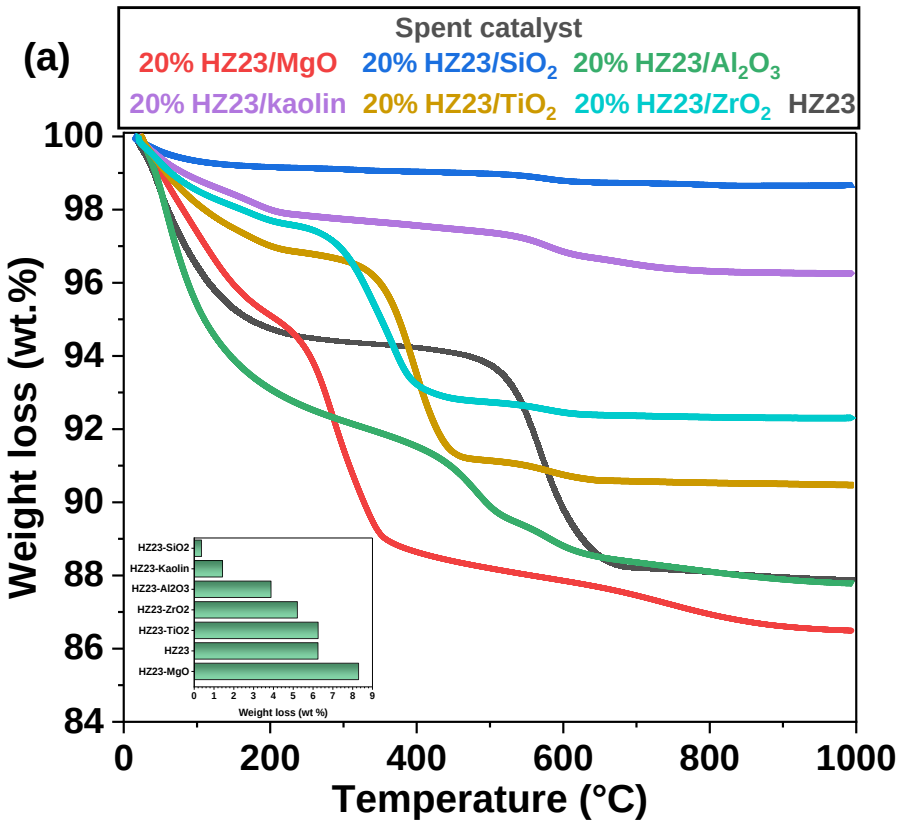
Figure 4.8. Comparison of powder X-ray diffraction patterns of the spent samples of H-ZSM-5 zeolite (HZ23), and 20 wt.% HZ23 over different supports.

4.3.3.2 Thermogravimetric measurement (TGA)

The existence of carbon residues has been established by thermogravimetric analysis (TGA) in air, despite the absence of distinct carbon diffraction peaks in the X-ray. Thermogravimetric analysis (TGA) was carried out on spent samples to find if coke/carbon was deposited on the catalyst surface after the catalytic cracking of *n*-heptane, as shown in **Figure 4.9**.

Importantly, the existence of carbon residues has been established using thermogravimetric analysis (TGA) for all the samples instead of XRD analysis (**Figure 4.8**)

due to the amorphous character of carbon material as noted earlier. The TGA curve shows two major weight losses for all the samples. The first loss stage from room temperature up to 200°C, was below 5% and is due to the loss of water and *n*-heptane remnant. The second weight loss after 200°C belong to carbon residues.



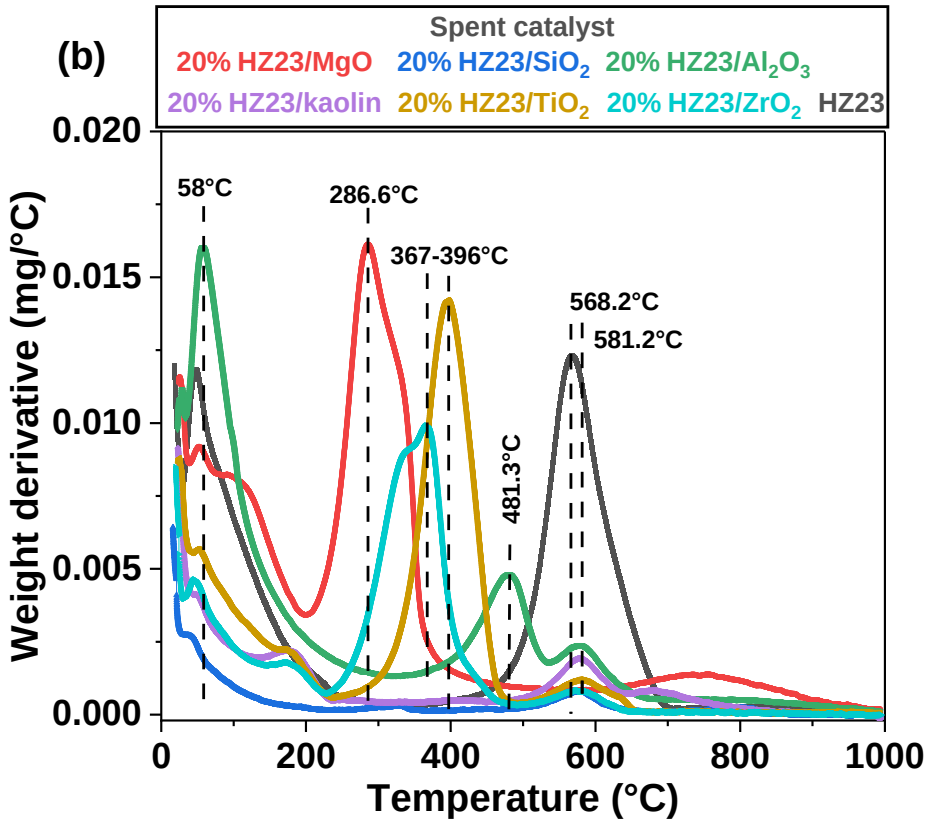


Figure 4.9. (a) TGA for spent samples under air flow for 20 wt.% HZ23 over different supports. (b) weight derivative thermogravimetry (DTG) curves of the five catalysts under air flow.

As can be seen in **Figure 4.9a**, the weight loss stage after 200℃ primarily represents the onset of the combustion of 'coke' on the spent catalyst, which is considered to be the primary reason for catalyst deactivation[47, 48]. Accordingly, the derivative thermogravimetry (DTG) profiles shows significant peak in the range 286-581℃ in **Figure 4.9b**. The results suggest that SiO_2-modified 20 wt.% HZ23 contains only 0.5 wt.% of coke, the lowest amount of coke of the studied catalyst series. The 20 wt.% HZ23/kaolin catalyst shows a slightly higher coke content (i.e., 1.5 wt.%). Interestingly, the used HZ23 catalyst showed a coke formation at the same oxidation temperature of 20 wt.% HZ23/kaolin (568℃) but a significant higher amount of coke (ca. 6.3%). A possible explanation of this observation would be that the hybrid HZ23-kaolin formulation can alter the strength of the acid sites and hence the selectivity to light olefins. The loss of acidic sites during the catalytic cracking reaction results from the coke

deposition on the cracking catalyst. The 20 wt.% HZ23/Al_2O_3 catalyst exhibits less coke production (about 3.9%) than the HZ23 sample. Two distinct peaks at 481℃ and 581℃ are showed in derivative thermogravimetry (DTG) curves, suggesting that two types of coke on the spent catalyst, as shown in **Figure 4.9b**.

Interestingly, coke deposited on the Al_2O_3 is oxidized at low temperature, between 300-500°C, whereas coke deposited on the zeolite (HZ23) is oxidized at higher temperature, typically above 500°C owing to its high strength of acid sites. However, the zeolite is still the most important catalyst component in determining the amount (and type) of coke formed. The alumina support may also have a beneficial influence on reducing coke formation. Interestingly, the amount of carbon residues on 20 wt.% HZ23/TiO_2 is similar to that on HZ23 alone (about 6.3%). However, its chemical nature is significantly different since most of coke deposited on TiO_2 (about 5.6%) burnt off at 396℃, while a small amount (about 0.7%) from zeolite (HZ23) acid sites combusted at 581℃. Similarly, the weight derivative curve for 20 wt.% HZ23/ZrO_2 has two carbon residues peaks after 200℃, representing 5.2 wt.% of coke in the sample. The broad peak at 367℃ can be assigned mainly to coke deposited on the ZrO_2 (about 4.8%), whereas the narrow and small peak at 568℃ is mainly associated with coke deposited on zeolite (HZ23) (ca. 0.4%). On the other hand, the DTG curve of 20 wt.% HZ23/MgO displays two peaks after 200℃. The first one at 286℃ (6.8 %) belongs to CO_2 release from the decarboxylation of $MgCO_3$[34] which was produced by the adsorption of CO_2 from air (**Figure 4.1A**). The small peak at about 751℃ corresponds to the combustion of coke and represents ca. 1.5%. The thermodynamics of the reaction and the mechanism both contribute to the formation of coke. In catalytic hydrocarbon transformations, the production of coke is due to a deep dehydrogenation process. This means that hydrogen is lost thermodynamically from deposited organic compounds because these various products cannot be transported out of the reaction system (i.e. vessel, reactor) in a timely manner[49].

It is also important to note that when catalyst deactivation takes place, coke tends to build along the catalyst bed in a direction that is generally opposed to the gradient of product concentration.

4.3.3.3 Brunauer-Emmentt-Teller (BET) analysis

The nitrogen physisorption of zeolite (HZ23) modified with different supports after catalytic cracking of *n*-heptane are summarized in **Figure 4.10**. All the spent catalysts, except HZ23/Al_2O_3, exhibited a lower BET surface areas compared to HZ23 with supports before catalytic cracking of *n*-heptane (**Figure 4.2**). The surface area (BET) decreases in the spent catalysts due to coke formation, so here the degree of loss of surface area depends on the supports. The BET decreased to 198 $m^2.g^{-1}$ for HZ23 compared with fresh HZ23 (ca. 355$m^2.g^{-1}$), representing a reduction of surface area of 44%. The measured surface areas of spent 20 wt.% HZ23 loading over SiO_2, MgO, kaolin, ZrO_2, TiO_2, and Al_2O_3 are 24, 53, 57, 75, 108, and 231 $m^2.g^{-1}$, respectively. In **Figure 4.11** shows the relationship between the catalyst formulation and the loss of BET surface area. Note that the loss of surface area was higher for low acidity (SiO_2) and base (MgO) metal oxides (i.e., 59 and 57 % respectively) whilst kaolin showed a loss of 40%. Supports with Brønsted acidity such as ZrO_2, TiO_2 and even Al_2O_3 showed a lower loss of surface area (i.e., 0-25%), this indicates important role of the support acidity in determining the textural and hence surface areas. It appears that the loss of surface area is therefore mainly caused by coke deposition which ultimately causes the degradation of the catalyst[50].

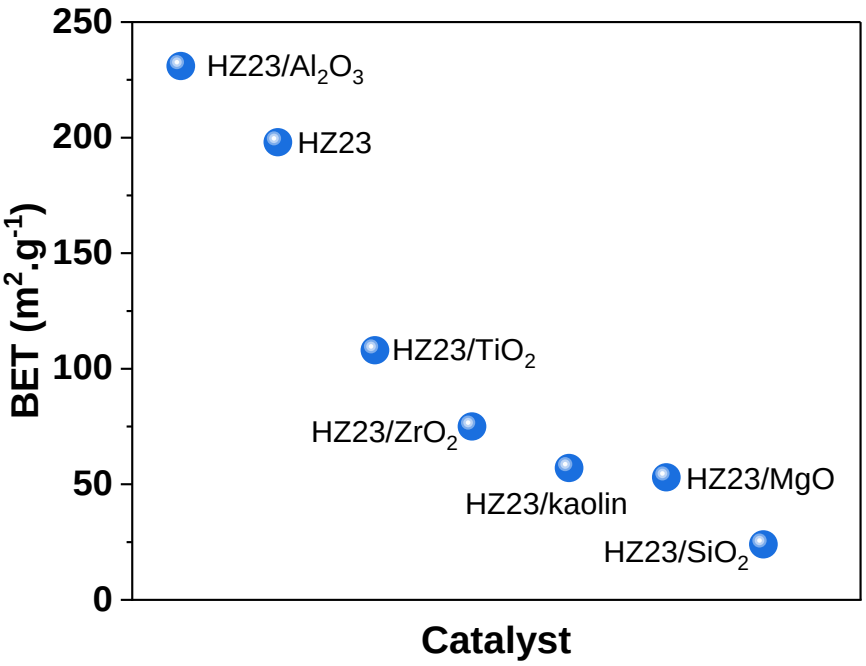


Figure 4.10. The surface area (BET) analysis of the spent 20 wt.% HZ23 on different supports for the selective cracking reaction of *n*-heptane to light olefins.

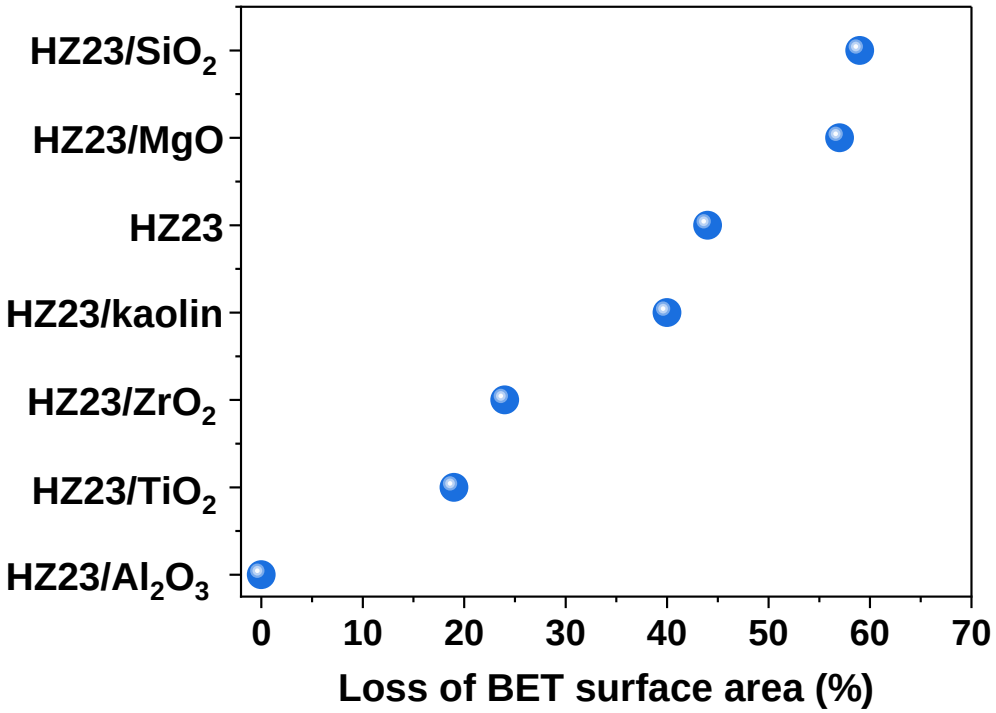


Figure 4.11. The loss of surface area of the spent hybrid of 20 wt.% HZ23 on different supports.

4.4 Conclusion

Based on the findings of this chapter, the study on 20 wt.% HZ23 on metals oxide or kaolin supports showed that all the catalysts gave an extremely high conversion (> 80%) of *n*-heptane to light olefins the exception was the HZ23/MgO catalyst which is clearly not active for catalytic cracking reaction. Moreover, all the catalysts showed a higher selectivity for light olefins than the parent HZ23 zeolite.

H-ZSM-5 are the most efficient catalysts for naphtha cracking to light olefins. Several factors affect the light olefin production. These including the zeolite acidity, the Si/Al ratios, and the temperature of the reaction. Kaolin, SiO_2, TiO_2, and ZrO_2 modified with 20 wt.% HZ23 all showed higher olefin yields (> 42 wt.%), while the HZ23/Al_2O_3 catalyst displayed about 38 wt.% due to the low acidity of Al_2O_3. The HZ23/MgO catalyst showed a low yield of light olefins (below 6 wt.%) during the thermal cracking, moreover the *n*-heptane conversion was very low compared to the other catalysts.

The X-ray results on all the hybrid catalysts before and after catalytic cracking of *n*-heptane revealed that there were no detectable changes in the diffraction peaks of all catalysts, indicating, importantly, that the catalyst structure is stable under the catalytic cracking of *n*-heptane. Despite the absence of distinct carbon diffraction peaks in the X-ray, characteristic of crystalline forms of carbon, the existence of carbon residues – inevitably amorphous - has been established using thermogravimetric analysis (TGA) analyses in air. The thermogravimetric analysis (TGA) showed that the combustion temperatures of the carbon residues are strongly dependent on the support at temperatures above 360°C.

It was found that the presence of a clay/support (such as kaolin and SiO_2) mixed with the zeolite can improve the catalytic activity in terms of olefin selectivity and yields under catalytic cracking of *n*-heptane. According to the results obtained in this chapter, the catalyst combination kaolin support mixed with HZ23 performed best and was selected for gaining

further insight into the advantages of a hybrid catalyst (i.e., HZ23-kaolin) in the cracking reaction in the next chapter.

Thus kaolin, an inexpensive, readily available, hydrothermally stable material, combined with HZ23 provides a low-cost, efficient catalyst for olefin production from naphtha or hydrocarbon feedstocks.

4.5 References

1. Gholami, Z.; Gholami, F.; Tišler, Z.; Hubáček, J.; Tomas, M.; Bačiak, M.; Vakili, M., Production of Light Olefins via Fischer-Tropsch Process Using Iron-Based Catalysts: A Review. *Catalysts*, **2022**, *12* (2), 174.
2. Védrine, J. C., Heterogeneous Catalysis on Metal Oxides. *Catalysts*, **2017,** *7* (11), 341.
3. Shinya, H.; Azusa, M.; Shuhei, W.; Ryuichi, K.; Fuyuki, Y., Catalytic conversion of light hydrocarbons to propylene over MFI-zeolite/metal-oxide composites. *Microporous and Mesoporous Materials*, **2016,** *233*, 125-132.
4. Hodoshima, S.; Motomiya, A.; Wakamatsu, S.; Kanai, R.; Yagi, F., Catalytic cracking of light-naphtha over MFI-zeolite/metal-oxide composites for efficient propylene production. *Research on Chemical Intermediates*, **2015,** *41* (12), 9615-9626.
5. Zhang, J.; Wang, L.; Zhang, B.; Zhao, H.; Kolb, U.; Zhu, Y.; Liu, L.; Han, Y.; Wang, G.; Wang, C.; Su, D. S.; Gates, B. C.; Xiao, F.-S., Sinter-resistant metal nanoparticle catalysts achieved by immobilization within zeolite crystals via seed-directed growth. *Nature Catalysis*, **2018,** *1* (7), 540-546.
6. Ning, Q.; Zhang, H.; He, Y.; Chen, Z.; Liu, S.; Ren, J., Suppression of platinum sintering on Pt–M/ZSM-22 (M = Ce, La, and Re) catalyst for *n*-dodecane isomerization. *New Journal of Chemistry*, **2019,** *43* (35), 13967-13978.
7. Rodaum, C.; Thivasasith, A.; Suttipat, D.; Witoon, T.; Pengpanich, S.; Wattanakit, C., Modified Acid-Base ZSM-5 Derived from Core-Shell ZSM-5@ Aqueous Miscible Organic-Layered Double Hydroxides for Catalytic Cracking of *n*-Pentane to Light Olefins. *ChemCatChem*, **2020,** *12* (17), 4288-4296.
8. Zeng, L.; Liu, F.; Zhao, T.; Cao, J., Superior ZSM-5@γ-Al_2O_3 Composite Catalyst for Methanol and Ethanol Coconversion to Light Olefins. *ACS Omega*, **2021,** *6* (29), 19067-19075.
9. Liu, Y.; Chen, J.-F.; Bao, J.; Zhang, Y., Manganese-Modified Fe_3O_4 Microsphere Catalyst with Effective Active Phase of Forming Light Olefins from Syngas. *ACS Catalysis*, **2015,** *5* (6), 3905-3909.
10. Wang, C.; Pan, X.; Bao, X., Direct production of light olefins from syngas over a carbon nanotube confined iron catalyst. *Chinese Science Bulletin*, **2010,** *55* (12), 1117-1119.
11. Xu, L.; Wang, Q.; Xu, Y.; Huang, J., A new supported Fe-MnO catalyst for the production of light olefins from syngas. I. Effect of support on the catalytic performance. *Catalysis Letters*, **1994,** *24* (1), 177-185.
12. Jabarullah, N. H., Production of olefins from syngas over Al_2O_3 supported Ni and Cu nano-catalysts. *Petroleum Science and Technology*, **2019,** *37* (4), 382-385.

13. Ajumobi, O. O.; Muraza, O.; Bakare, I. A.; Al Amer, A. M., Iron- and Cobalt-Doped Ceria–Zirconia Nanocomposites for Catalytic Cracking of Naphtha with Regenerative Capability. *Energy & Fuels*, **2017,** *31* (11), 12612-12623.
14. Mi-Hyun, L.; Bhari Mallanna, N.; Kwan Young, L.; Kwang-Deog, J., Dehydrogenation of alkane to light olefin over PtSn/θ-Al_2O_3 catalyst: Effects of Sn loading. *Catalysis Today*, **2014,** *232*, 53-62.
15. Wang, Y.; Li, T.; Li, C.; Lu, J.; Dai, C.; Subhan, F.; Bai, P.; Sun, H.; Feng, R.; Yan, Z., One-pot green synthesis of Fe-ZSM-5 zeolite containing framework heteroatoms via dry gel conversion for enhanced propylene selectivity of catalytic cracking catalyst. *Journal of Materials Science*, **2021,** *56* (32), 18050-18060.
16. Javaid, R.; Nanba, T., Stability of Cs/Ru/MgO Catalyst for Ammonia Synthesis as a Hydrogen and Energy Carrier. *Energies*, **2022,** *15* (10), 3506.
17. Javaid, R.; Matsumoto, H.; Nanba, T., Influence of Reaction Conditions and Promoting Role of Ammonia Produced at Higher Temperature Conditions in Its Synthesis Process over Cs-Ru/MgO Catalyst. *Chemistry Select*, **2019,** *4* (7), 2218-2224.
18. France, L. J.; Du, X.; Almuqati, N.; Kuznetsov, V. L.; Zhao, Y.; Zheng, J.; Xiao, T.; Bagabas, A.; Almegren, H.; Edwards, P. P., The effect of lanthanum addition on the catalytic activity of γ-alumina supported bimetallic Co–Mo carbides for dry methane reforming. *Applied Petrochemical Research*, **2014,** *4* (1), 145-156.
19. Roostaie, T.; Abbaspour, M.; Makarem, M. A.; Rahimpour, M. R., Synthesis and Characterization of Biotemplate γ-Al_2O_3 Nanoparticles Based on Morus alba Leaves. *Topics in Catalysis*, **2022**.
20. Aimdate, K.; Srifa, A.; Koo-amornpattana, W.; Sakdaronnarong, C.; Klysubun, W.; Kiatphuengporn, S.; Assabumrungrat, S.; Wongsakulphasatch, S.; Kaveevivitchai, W.; Sudoh, M.; Watanabe, R.; Fukuhara, C.; Ratchahat, S., Natural Kaolin-Based Ni Catalysts for CO_2 Methanation: On the Effect of Ce Enhancement and Microwave-Assisted Hydrothermal Synthesis. *ACS Omega*, **2021,** *6* (21), 13779-13794.
21. Alabdullah, M.; Shoinkhorova, T.; Rodriguez-Gomez, A.; Dikhtiarenko, A.; Vittenet, J.; Ali, O. S.; Morales-Osorio, I.; Xu, W.; Gascon, J., Composition-performance Relationships in Catalysts Formulation for the Direct Conversion of Crude Oil to Chemicals. *ChemCatChem*, **2021,** *13* (7), 1806-1813.
22. Shaobo, W.; Fangang, Z.; Yanwei, L.; Yanghao, M.; Wenjia, W.; Chang, L.; Jinglai, Z.; Hongbiao, D.; Jie, L., Preparation and application of ZrO_2–SiO_2 complex oxide for efficient biocrude generation by hydrothermal liquefaction of Spirulina. *Fuel*, **2022,** *317*, 123325.
23. Kumar, S.; Dave, V.; Krishnan, M. B.; Amudha, V.; Gomathi, S.; Soni, S.; Jeelani, S. H.; Subbiah, R.; Negash, K., Analysis of Physical, Ocular, and Aquaphobic Properties of Zirconium

Oxide Nanofilms by Varying Sputtering Pressure. *Journal of Nanomaterials,* **2022,** *2022*, 8752664.

24. Xavier, J. R., Electrochemical and dynamic mechanical properties of polyurethane nanocomposite reinforced with functionalized TiO_2–ZrO_2 nanoparticles in automobile industry. *Applied Nanoscience,* **2022,** *12* (5), 1763-1778.
25. Xueying, Z.; Wenyu, X.; Xueqing, S.; Zhuan, W.; Bo, Y.; Chao, Y.; Jide, W.; Xintai, S., An effective Ni/C co-catalyst for promoting photocatalytic hydrogen evolution over TiO_2 nanospheres. *Materials Science in Semiconductor Processing,* **2022,** *148*, 106775.
26. Lele, W.; Guogang, T.; Song, L.; Huilong, D.; Qinqin, L.; Jingfang, S.; Hua, T., Interfacial active-site-rich 0D Co_3O_4/1D TiO_2 p-n heterojunction for enhanced photocatalytic hydrogen evolution. *Chemical Engineering Journal,* **2022,** *428*, 131338.
27. Yanjie, L.; Jun, O.; Hongyou, W.; Weili, W.; Pengfei, C.; Kangning, S., Synthesis and characterization of core–shell structured SiO_2@YVO_4: Yb^{3+},Er^{3+} microspheres. *Applied Surface Science,* **2012,** *258* (8), 3689-3694.
28. Louise, S.; Aleksander, J.; Mattias, E.; Danielle, M. L.; Dong-Kyun, S.; F; Ulrich, H., Structural analysis of highly porous γ-Al_2O_3. *Journal of Solid State Chemistry,* **2014,** *217*, 1-8.
29. Xu, Y.; Li, Z.; Dervishi, E.; Saini, V.; Cui, J.; Biris, A. R.; Lupu, D.; Biris, A. S., Surface area and thermal stability effect of the MgO supported catalysts for the synthesis of carbon nanotubes. *Journal of Materials Chemistry,* **2008,** *18* (47), 5738-5745.
30. Granizo, M. L.; Blanco-Varela, M. T.; Palomo, A., Influence of the starting kaolin on alkali-activated materials based on metakaolin. Study of the reaction parameters by isothermal conduction calorimetry. *Journal of Materials Science,* **2000,** *35* (24), 6309-6315.
31. Fei, M.; Shu, C.; Yang, W.; Fang, C.; Weimin, L., Characterization of redox and acid properties of mesoporous Cr–TiO2 and its efficient performance for oxidative dehydrogenation of propane. *Applied Catalysis A: General,* **2012,** *427-428*, 145-154.
32. Xiaoliang, Y.; Yuan, L.; Binran, Z.; Zhao, W.; Yong, W.; Chang-jun, L., Methanation over Ni/SiO_2: Effect of the catalyst preparation methodologies. *International Journal of Hydrogen Energy,* **2013,** *38* (5), 2283-2291.
33. Xinyu, J.; Xiaoshan, Z.; Ning, R.; Xue, H.; Chang-jun, L., Structural effect of Ni/ZrO_2 catalyst on CO_2 methanation with enhanced activity. *Applied Catalysis B: Environmental,* **2019,** *244*, 159-169.
34. Wan Isahak, W. N. R.; Ramli, Z. A. C.; Mohamed Hisham, M. W.; Yarmo, M. A. In Magnesium oxide nanoparticles on green activated carbon as efficient CO_2 adsorbent, AIP Conference Proceedings, *American Institute of Physics,* **2013**; pp 882-889.
35. Alaba, P. A.; Sani, Y. M.; Daud, W. M. A. W., Kaolinite properties and advances for solid acid and basic catalyst synthesis. *RSC advances,* **2015,** *5* (122), 101127-101147.

36. ALlaedini, G.; Tasirin, S. M.; Aminayi, P.; Yaakob, Z.; Talib, M. Z. M., Production of multi-walled carbon nanotubes via catalytic decomposition of methane in the chemical vapor decomposition process. *International Journal of Materials,* **2015,** *2*, 48-53.
37. Wu, X.; Cao, H.; Yin, G.; Yin, J.; Lu, Y.; Li, B., $MgCO_3 \cdot 3H_2O$ and MgO complex nanostructures: controllable biomimetic fabrication and physical chemical properties. *Physical Chemistry Chemical Physics,* **2011,** *13* (11), 5047-5052.
38. Varga, G., The structure of kaolinite and metakaolinite. *Epitoanyag,* **2007,** *59* (1), 6-9.
39. Hubadillah, S. K.; Othman, M. H. D.; Matsuura, T.; Ismail, A.; Rahman, M. A.; Harun, Z.; Jaafar, J.; Nomura, M., Fabrications and applications of low cost ceramic membrane from kaolin: A comprehensive review. *Ceramics International,* **2018,** *44* (5), 4538-4560.
40. Shoinkhorova, T.; Dikhtiarenko, A.; Ramirez, A.; Dutta Chowdhury, A.; Caglayan, M.; Vittenet, J.; Bendjeriou-Sedjerari, A.; Ali, O. S.; Morales-Osorio, I.; Xu, W., Shaping of ZSM-5-based catalysts via spray drying: effect on methanol-to-olefins performance. *ACS Applied Materials & Interfaces,* **2019,** *11* (47), 44133-44143.
41. Rouholamin, B.; Bendaoud, N.; Serge, K., A facile route to synthesize mesoporous ZSM-5 with hexagonal arrays using P123 triblock copolymer. *Microporous and Mesoporous Materials,* **2020,** *298*, 110067.
42. Velthoen, M. E.; Lucini Paioni, A.; Teune, I. E.; Baldus, M.; Weckhuysen, B. M., Matrix Effects in a Fluid Catalytic Cracking Catalyst Particle: Influence on Structure, Acidity, and Accessibility. *Chemistry–A European Journal,* **2020,** *26* (52), 11995-12009.
43. Tian-Jun, R.; Jin-kai, X., The catalytic cracking activity of the kaolin-group minerals. *Materials Letters,* **2002,** *57* (2), 297-301.
44. Katsue, S.; Tadamitsu, K.; Jun, K.; Takashi, S.; Kozo, T., Acidic properties of Binary Metal Oxides. *Bulletin of the Chemical Society of Japan,* **1973,** *46* (10), 2985-2988.
45. Marek, K., Isoelectric points and points of zero charge of metal (hydr)oxides: 50 years after Parks' review. *Advances in Colloid and Interface Science,* **2016,** *238*, 1-61.
46. Al-Dughaither, A. S.; de Lasa, H., HZSM-5 Zeolites with Different SiO_2/Al_2O_3 Ratios. Characterization and NH_3 Desorption Kinetics. *Industrial & Engineering Chemistry Research,* **2014,** *53* (40), 15303-15316.
47. Milina, M.; Mitchell, S.; Crivelli, P.; Cooke, D.; Pérez-Ramírez, J., Mesopore quality determines the lifetime of hierarchically structured zeolite catalysts. *Nature Communications,* **2014,** *5* (1), 1-10.
48. Buurmans, I. L. C.; Ruiz-Martínez, J.; Knowles, W. V.; van der Beek, D.; Bergwerff, J. A.; Vogt, E. T. C.; Weckhuysen, B. M., Catalytic activity in individual cracking catalyst particles imaged throughout different life stages by selective staining. *Nature Chemistry,* **2011,** *3* (11), 862-867.

49. Guisnet, M.; Ribeiro, F. R., Deactivation and regeneration of zeolite catalysts. *Imperial College Press*, **2011**; Vol. Nine.
50. Mu, H.; Muhammad-Faryad, A.; Yue-Qin, S.; Xiao-Long, Z.; Jin An, W.; Xin-Yao, N.; Zheng, W., Study on the deactivation mechanism of HZSM-5 in the process of catalytic cracking of *n*-hexane. *Chemical Engineering Journal*, **2023,** *451*, 138793.

Chapter 5

Cracking of *n*-heptane and naphtha on HZ23-kaolin formulations

Overview

This chapter describes an investigation into the effect of natural kaolin loading on H-ZSM-5 (MFI-type, SiO_2/Al_2O_3=23) zeolite catalyst on the catalytic cracking of naphtha. The cracking properties of zeolites for the production for light alkenes are investigated using *n*-heptane as a model compound and naphtha (the actual feedstock). The combination of this natural, inert, and inexpensive clay material with the zeolite helps improve the catalyst's sustainability credentials and gives light olefins in a good yield. Various proportions of kaolin: zeolite was investigated. The formation of olefins from the catalysts was tested in a fixed-bed unit at 550°C for 4 hours and the catalyst was characterised with a range of techniques.

5.1 Introduction

Recently, researchers have become interested in improving the effectiveness of zeolites as catalysts. This can be achieved by dispersing zeolites within a matrix of natural clay that is formed into a dual component catalyst. Importantly, it has been found that these clays can affect the acidity of the HZSM-5 zeolite[1, 2]. Clays are found to be highly advantageous in influencing catalyst properties such as heat resistance, chemical and mechanical stability, and the optimal functionality of acidic sites[3, 4].

There are various types of clays that are naturally formed on earth, such as fire clay, bentonite, sagger clay, ball clay, and kaolin[5]. Clays can be classified into different classes based on their alumina content, particle size, and metal content all of which depend on their geological source and composition[6]. Kaolin is a significant type of clay that has received enormous attention due to its natural abundance, and unique physical and chemical properties such as fine particle size, attractive surface behaviour inertness, and plate-like structure[7]. It has been widely used in industry in general and the petrochemical field in particular[8-10].

Kaolin was first discovered in China in the early 17th century; it is also called china clay. It has the general formula $Al_2Si_2O_5(OH)_4$ and based on this the composition of kaolin is SiO_2, 46.54%; Al_2O_3, 39.50%; and H_2O, 13.96%. Kaolin clays generally include 10-95% kaolinite. The remainder usually contains various fragments of mica and quartz, in addition to lower percentages of anastase, illite, ilmenite, bauxite, haematite, kyanite, zircon, rutile, silliminate, montmorillonite, and graphite[11, 12].

The structure of pure kaolinite is a layered silicate with one “tetrahedral” sheet linked to an “octahedral” sheet of alumina through oxygen atoms. The sheets are continuously built upon and accumulate, forming a non-symmetrical unit cell with the tetrahedral sheet of silica on one side and the octahedral sheet of alumina on the other side. It can be seen in **Figure 5.1** that the plane of the oxygen atoms is facing the plane of hydroxyl ions in the next sheet[13, 14].

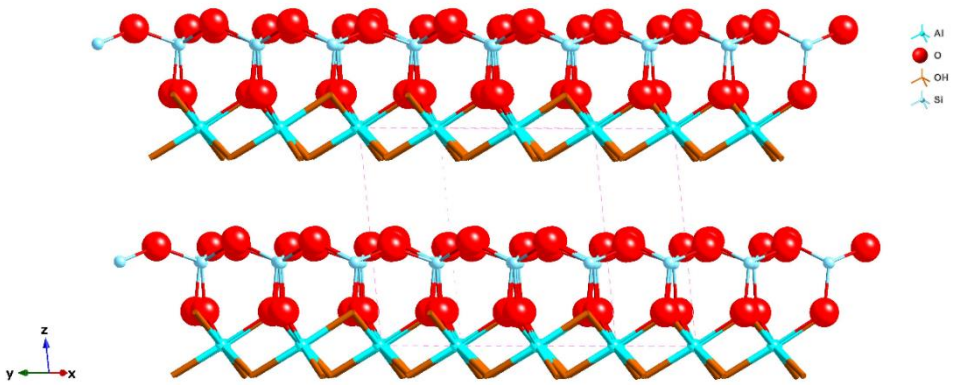


Figure 5.1. Illustration of the molecular structure of kaolinite.

Characteristics of kaolin include mechanical softness and colour (various shades of white). However, crude kaolin can appear yellow due to the presence of iron hydroxide, which can be extracted chemically to create so-called industrial kaolin[12, 15, 16].

There are also more significant characteristics of kaolin, such as acidity, pore structure, surface area and thermal stability. Minor variations in these properties can have a significant impact on the type of application. Searching the relevant literature reveals a large number of published papers involving the use of kaolin over the past few decades[6, 17].

Natural mineral clay materials have been successfully utilised in different industrial applications. Thus, kaolin is used extensively in the ceramic industry as well as in coatings, paints, agriculture, plastics, and pharmaceuticals. It has a high fusion temperature which make it the best precursor for the production of porcelain, refractors, and whiteware.

The field of olefin production has attracted huge attention in its exploitation of advanced catalytic heterogeneous materials. Several such studies utilised kaolin for promoting the enhancement of a sustainable olefin production processes[4, 18, 19]. Kaolin was used as a precursor to synthesise highly crystalline zeolite using steam-assisted conversion, followed by the incorporation of the elements: Fe, P, and Ca to enhance the catalytic stability. The experiments showed an improved performance of ZSM-5, greater stability and reduced carbon deposition. The catalytic activities indicated that zeolite with a higher Si/Al ratio favoured the production of light olefins with a 68% selectivity of C_2-C_4. Additionally, it was used to prepare SAPO-34 with higher crystallinity and a larger surface area, which helped to promote the active sites for the hydrogenation of CO_2 into light olefins over CuO-ZnO/SAPO-34 catalysts, as reported by Wang *et al.*[20]. It was also found that kaolin enhanced the catalytic lifetime, as the molecular sieves of the SAPO-34 reduced the diffusion path length of the intermediate products[20, 21].

Researchers also reported the incorporation of kaolin with zeolites as a catalytic support to enhance the performance and the reaction yield. Bachcha Lal *et al.* investigated the concentration of kaolin on the acidity of silver doped ZSM-5 zeolite. Different loadings of kaolin 15, 25, and 50 were utilised to investigate the effect of kaolin concentration on olefin production. It was found that the stronger acidic sites, which promote the conversion of lower olefins to higher olefins, are affected by an increase in the concentration of kaolin. In addition, the ion exchange and the Ag doping facilitate the dehydrogenation activities which moved the reaction towards higher selectivity for light olefins[4].

The global demand and sustainability concerns for producing light olefins encouraged researchers to look for an alternative and environmental-friendly technology able to meet the demand for light olefins in harmony with the environment. This study focuses on the catalytic cracking of light naphtha using a hybrid of kaolin and zeolite (HZSM-5) catalyst through a fixed-bed catalytic reaction configuration to produce high-quality light olefins. The aim is to develop an innovative technology to convert *n*-heptane (as a model compound) and naphtha (as the industrial feedstock) in a one-step reaction into light olefins (ethylene, propylene, and butylene) and aromatics using a catalytic cracking process in a fixed-bed reactor. The main scope of the chapter is to design, develop and optimize highly selective solid catalysts, and also to optimize the reaction conditions for converting the relatively high molecular weight hydrocarbons present in naphtha into the desired compounds. To do so; it is necessary to understand the fundamental processes occurring in the catalytic cracking of naphtha.

5.2 Experimental Methods

5.2.1 Materials

Zeolyst International (www.zeolyst.com) kindly provided the commercial zeolites examined in this study with different Si/Al ratios. Similarly, light naphtha was kindly supplied by SABIC. The model compound (anhydrous *n*-heptane, 99%), and the kaolin were bought from Sigma-Aldrich and used as purchased.

Light naphtha was analysed by GC-MS and GC-Sulphur Chemiluminescence Detector (SCD) using the standard method ASTM D5623 at Intertek and its composition is given in **Table 5.1A.** The quantification of hydrocarbon types is shown in **Table 5.2A**. Note that the main components are C_5, C_6, and C_7. The sulfur content was 0.0174 wt.%.

5.2.2 Preparation of catalysts

The catalysts used in this study were based on H-ZSM-5 (HZ23) with different kaolin loadings. The catalysts were prepared by mixing different amounts of H-ZSM-5 (SiO_2 to Al_2O_3 ratio 23 and MFI-type-zeolite) with kaolin as support material. In a typical synthesis process, NH_4-ZSM-5 was initially pre-calcined at 550℃ for 5 h using a heating rate of 3℃ min^{-1} in static air atmosphere to get the hydrogen form (H-ZSM-5), and a similar procedure was used for kaolin (Sigma-Aldrich). Such samples containing zeolite H-ZSM-5 with a SiO_2:Al_2O_3 ratio of 23 will hereafter be referred to as HZ23. The HZ23-kaolin catalysts were prepared by mixing the catalyst components in deionized water. In a typical procedure, the appropriate amount of zeolite was added to excess deionized water (water/zeolite wt. ratio ca. 5-10) and stirred at room temperature for 10 min. Kaolin was then added slowly to the suspension and stirred at room temperature for 3-4 h, followed by drying at 80-100℃ overnight (ca. 15 h). The catalysts were then calcined in a static air atmosphere at 550℃ for 2h using a heating rate of 3℃ min^{-1}. The catalysts were labelled and stored as xHZ23-kaolin, where x is the zeolite loading in the catalyst (5-30 wt.%).

5.2.3 Characterisation of catalysts

The fresh and spent catalysts were carefully characterised by a range of techniques such as X-ray powder diffraction (XRD), scanning electron microscopy (SEM), energy dispersive X-ray spectroscopy (EDX), thermogravimetric analysis (TGA), Pyridine-adsorbed Fourier Transform Infrared (FTIR) Spectroscopy to identify the nature of the acid sites and NH_3 Temperature-Programmed Desorption (TPD) to calculate total acidity, and N_2-physisoption measurements to determine surface area through the Brunauer-Emmett-Teller (BET) method.

Powder X-ray diffraction patterns were collected on Bruker-Eco D8 ADVANCE diffractometer (Cu-Kα radiation, λ = 1.5406 Å) working at 40 kV–25 mA and equipped with a Lynxeye detector. The samples were scanned in a range of 2θ from 5° to 90°.

Thermogravimetric analysis (TGA) in flowing air characterised the content and type of carbon deposited in the spent samples. The sample was heated from room temperature to 1000℃ at a heating rate of 10℃ min^{-1} under ambient atmosphere with a 100 mL min^{-1} flow rate to combust all so-called coke precursors. Between 10 and 20mg of spent sample were loaded into a small alumina crucible for the test.

The surface morphology of the sample was analysed using a scanning electron microscope (JEOL 840F). The N_2 physisorption measurements were carried out at liquid nitrogen temperature using Micromeritics Micro Active (TriStar II Plus). Before the analysis, the samples were weighed and placed in quartz tubes and then degassed under vacuum at 50ºC for 24 hours to remove impurities on the sample surface. The BET surface area was determined by nitrogen gas adsorption at -196℃ with a Micromeritics brand 3Flex model device. Adsorption and desorption points were calculated between 0 and 1 relative pressure (p/p0).

A scanning electron microscope (ZEISS EVO) was used to characterize the surface morphology of the samples before and after the catalytic cracking process. Images were taken using the Inlens detector of the Zeiss Sigma 300 Scanning Electron Microscope. The samples were poured on carbon tape and coated with a mini sputter for 300 seconds. Images were taken at 5 KV at different magnifications. The surface element concentrations were analyzed by energy-dispersive Xray spectroscopy (EDX; ZEISS EVO). EDX analysis was performed from a wide-angle general surface at 15 KV.

NH_3-TPD determines the total acidity of the catalyst samples. The analyses were carried out in a Micromeritics AutoChem II equipped with a TCD detector. Prior to the analysis, impurities were removed from the sample by heating it up to 550℃ under a He flow (50 ml.

min^{-1}) and maintaining this temperature for 45 min. Afterwards, the sample was cooled down to 150℃ and, once the TCD signal stabilized, the NH_3 was injected (150 µl.min^{-1}) until saturation. Finally, the desorption of the chemisorbed NH_3 was conducted by heating the sample up to 550℃ using a heating ramp rate of 5℃. min^{-1}.

The Fourier Transform Infrared (FTIR) spectra of samples with pyridine adsorbed allows the determination of the nature of the acid sites, i.e., Brønsted or Lewis. The spectrometer used was a Nicolet740 SX FTIR equipped with a Specac transmission catalytic cell, a temperature controller and a Vacuubrand rotary vacuum pump, for pyridine adsorption. Before pyridine injection, the sample was heated up to 550℃ under vacuum to remove impurities, and then cooled down to 150℃, at which temperature pyridine was injected. The interaction of pyridinium groups (Py) with the acid sites creates bonding which gives rise to IR bands at 1455 and 1545cm^{-1}, which are attributed to Lewis and Brønsted acid sites, respectively. The ratio of the intensity of the 2 bands provides the Brønsted/Lewis acid sites ratio.

5.2.4 Experimental conditions

The catalytic cracking tests were carried out in a fixed-bed reactor system coupled to a gas chromatography system (online GC, offline GC/MS). Typically, 0.5 g of each catalyst was mixed with 0.5g of SiC and loaded into the centre of the tube-shaped reactor, which was supported with SiC bed (Fisher, 24 grit). By help of an HPLC pump, the feed (*n*-heptane from Sigma, 99% / naphtha) was injected. Flowing N_2 carrier gas into the reactor (20 mL.min^{-1}) was used. The temperature of the catalyst bed was raised to 550°C at a rate of 5°C.min^{-1} under atmospheric pressure. In order to ensure that the catalyst was completely dehydrated for all experiments, it was left for 1 hour at 550°C under N_2 flow.

The gas and liquid products were effectively separated at the system's termination (cool water condenser used). Gaseous products were examined in a PerkinElmer, Claurs 580 GC.

The analysis was conducted through a thermal conductivity detector (TCD) for non-hydrocarbon and a flame ionisation detector (FID) for hydrocarbons every 30 minutes for four hours of time on stream (TOS) after beginning the *n*-heptane injection into the catalyst bed. Upon the reaction, liquid products were collected every 1h in the separator through the condenser and diluted in dichloromethane for the analysis in gas chromatograph-mass spectrometer instrument. Each liquid component of liquid phase was quantified (Shimadzu GC/MS-QP 2010 SE). Chapter 2 depicts the catalyst testing system and tubular design.

5.3 Results and Discussion

5.3.1 Pre-reaction analysis of catalysts

5.3.1.1 X-ray diffraction (XRD)

The combined HZ23-kaolin catalyst formulations, as well as the parent HZ23, and kaolin, were examined by X-ray diffraction (XRD) before the catalytic cracking of *n*-heptane (as a model compound) and light naphtha as shown in **Figure 5.2**.

Notably, X-ray identification of the extent of order/disorder or phase change is always challenging because of the low intrinsic crystallinity of kaolin and the various overlapping peaks and interferences by the zeolite and support. According to the literature, the peaks belonging to an MFI-type zeolite were seen in the X-ray diffraction pattern of the HZ23 sample[22]. X-ray powder diffraction of the kaolin material (**Figure 5.2**) showed an apparent phase change upon calcination at 550℃. This feature is due to the loss of hydroxyl groups from kaolin upon heat treatment of the sample[23, 24], which propagates the phase change of the kaolin and could play a vital role in the inactivity (or low activity) of this solid. The XRD pattern of kaolin treated at 550℃ exhibits broad and weak peaks between ~ 12.3 and 35º in 2θ due to its poor crystallinity. Peaks at ca 5-10º and 25º in 2θ are due to the zeolite phase, which becomes visible at 30% loading (**Figure 5.2**). The XRD profiles confirm the presence of crystalline

HZSM-5 in zeolite-kaolin combinations, particularly at zeolite compositions above 10 wt.%. The results for the powder XRD patterns of zeolite and kaolin are consistent with data obtained from literature[22, 25].

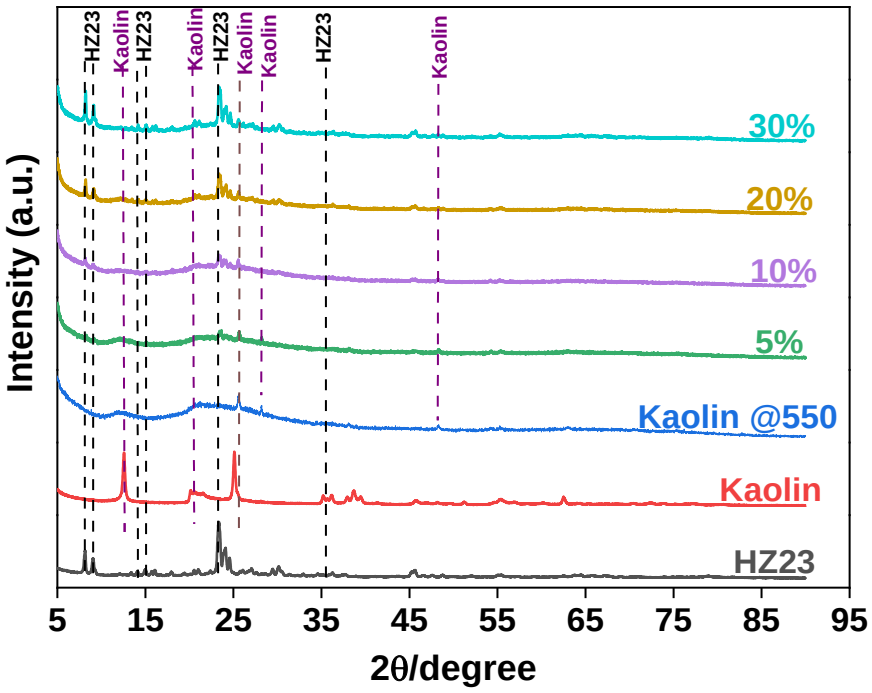


Figure 5.2. Comparison of powder X-ray diffraction patterns of the various HZ23 zeolite/kaolin combinations for fresh samples. Kaolin is as received whilst kaolin @550 is treated at 550°C.

5.3.1.2 Brunauer-Emmentt-Teller (BET) analysis

The physical properties of the surface area of fresh kaolin modified with different loadings of H-ZSM-5 (HZ23) are presented in **Table 5.1**. As indicated in the table, the zeolite component has the largest surface area with a value of ~355 m^2g^{-1} compared to the zeolite modified with kaolin, followed by the 30% HZ23-kaolin with a value of ~133 m^2g^{-1}. Moreover, the kaolin is a very dense material with a small surface area (~20 m^2g^{-1}) and a negligible pore volume[14, 26]. Therefore, the catalysts containing 5, 10, and 20 % HZ23 mixed with kaolin have a lower surface area than the parent HZ23 but a higher surface area than kaolin. This trend is

clearly associated with the increase of the HZ23 content as a consequence of its higher internal and external surface areas.

Table 5.1. Surface area of the HZ23-kaolin catalyst series tested in the selective cracking reaction of *n*-heptane and naphtha toward light olefins.

Sample	***BET ($m^2 \cdot g^{-1}$)***	***T-Plot ($m^2 \cdot g^{-1}$)***		
		External	**Internal**	**I/E**
Kaolin	20	17	3	0.2
5% HZ23-kaolin	35	20	15	0.75
10% HZ23-kaolin	51	22	29	1.3
20% HZ23-kaolin	94	44	50	1.1
30% HZ23-kaolin	133	62	71	1.2
HZ23	355	99	256	2.6

5.3.1.3 Scanning Electron Microscopy (SEM)

Scanning electron microscopy (SEM) was used to visualise the surface morphology of catalysts. **Figure 5.3** and **Figure 5.1A** display the SEM images of fresh samples with different supports. As shown in the SEM image, the HZ23-kaolin catalysts mostly consist of clusters of very fine particles, typically of dimensions 1-5 μm, as given in **Figure 5.3**. These images show a certain homogeneity in the composition of the samples based on the clearly different morphology of kaolin and the zeolite. Furthermore, **Figure 5.3** and **Figure 5.1A** clearly depicts the base shape and lamellar structure of kaolin crystals. Also, the SEM image of HZ23 zeolite showed a uniform particle size distribution, a more-or-less regular shape, a very clear crystallinity, and a narrow particle size distribution.

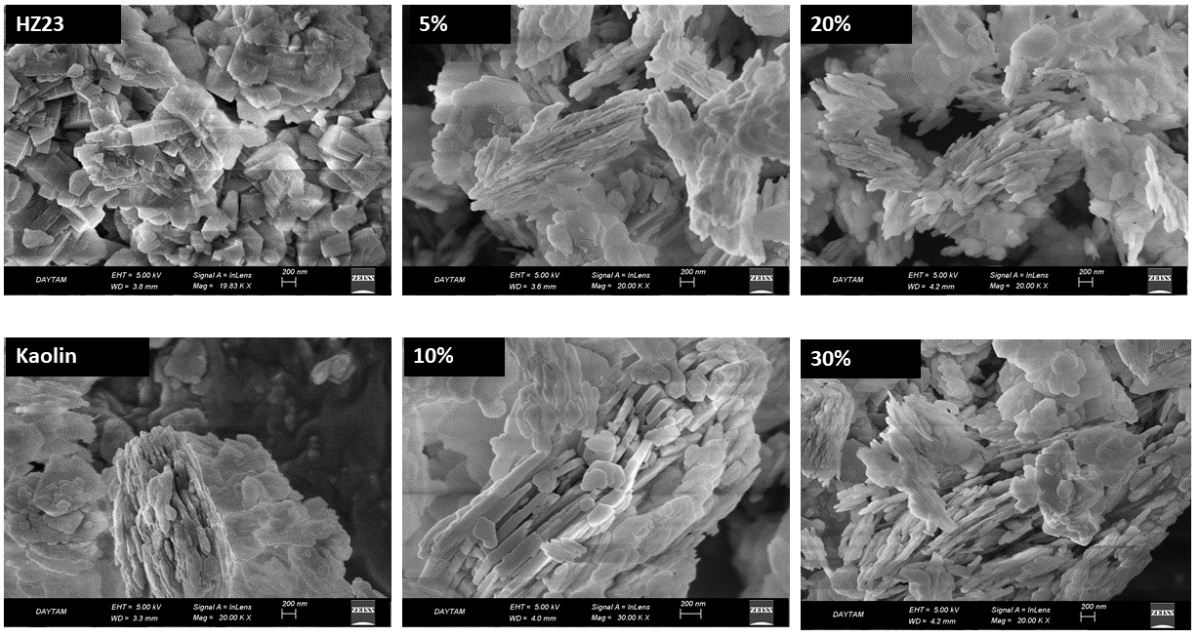


Figure 5.3. Scanning electron microscopy images (SEM) of six samples under study before the catalytic reaction. ZSM-5 (HZ23), Kaolin, 5% HZ23/Kaolin, 10% HZ23/Kaolin, 20% HZ23/Kaolin, and 30% HZ23/Kaolin.

5.3.1.4 Transmission Electron Microscopy (TEM)

The transmission electron microscopy (TEM) technique gathers information about the morphology, composition, and crystallography of samples by employing energised electrons in the analysis process. **Figure 5.4** and **Figure 5.2A** present the TEM images of a hybrid of kaolin and zeolite (HZ23) before catalytic cracking of *n*-heptane and naphtha. It can be seen in **Figure 5.4** that low percentages of HZ23 mixed with kaolin produce smaller zeolite particles with a very good dispersion (or contact) at the zeolite-kaolin interface. This promotes the selective cracking reactions by minimising the diffusion time of hydrocarbons into the zeolite channels. The high "contact points" effect is lost as the zeolite content is increased due to the aggregation of particles.

Interestingly, both the zeolite porosity and the lamellar-like structures of kaolin[3, 27] are highlighted in these TEM images. The kaolin contains some micropores, while the zeolite contains both micropores and mesopores. Upon the mixing of components, followed by drying

and calcination, some interesting structural effects are observed. It can be noted when zeolite loading is increased, the internal and external surface areas increase. That may be because the kaolin and zeolite components interact during synthesis conditions and create additional micropores compared to kaolin alone. It is particularly relevant to the sponge-like morphology of the HZ23, which enhances the diffusion of the *n*-heptane into the zeolite structure and hence the accessibility to the acid sites. **Figure 5.2A** shows a TEM image and a selected area diffraction (SAD) pattern obtained from the HZ23-kaolin catalyst indicating that the structure consists of hexagonal and lamellar shapes owing to the zeolite and clay crystal structures, respectively. The TEM images for HZ23-kaolin formulations given in **Figure 5.2A** clearly depict a flake-like morphology for kaolin, whilst zeolite (HZ23) shows an aggregated morphology.

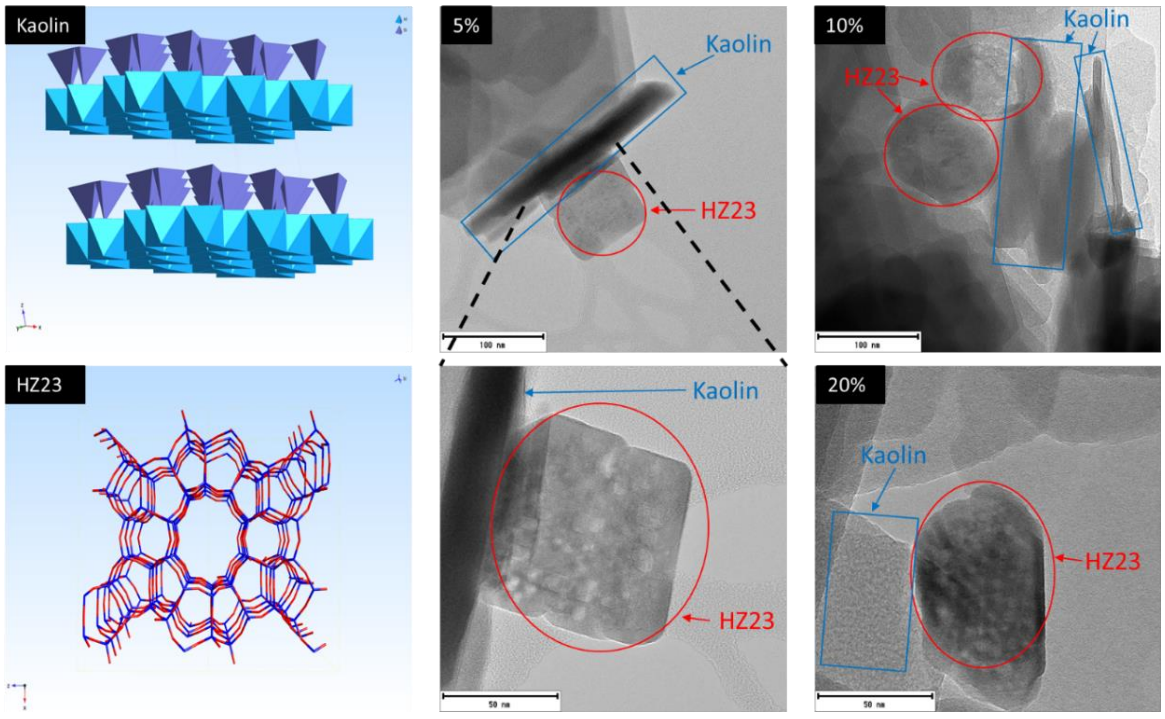


Figure 5.4. HZ23 zeolite and kaolin structures alongside TEM images of different compositions of HZ23-kaolin catalyst at two magnifications (100 and 50 nm). The percentage in the left-hand side of the photographs corresponds to the zeolite content in wt.%.

5.3.1.5 Acidity measurement

It is well-established that thermal or chemical treatment of an acid catalyst affects its acidity properties. Analysis by NH_3-TPD is routinely conducted to study the acidity of solid acid catalysts and their subsequent modification[28]. **Figure 5.3A** shows the results from NH_3-TPD of fresh catalysts. Two peaks can be distinguished in the NH_3-TPD profile for pristine HZ23 zeolite, they are associated with weak (225℃) and strong (417℃) acid sites. The addition of the kaolin reduces the contribution of both peaks, especially the sign associated with strong acid sites.

Interactions at the interface between kaolin and zeolite, together with the low content of zeolite with a high Si/Al ratio, likely play the most important roles in generating new (or optimal) acid sites able to crack *n*-heptane selectively to light olefins. It is well-known that Lewis acid sites (LAS) and Brønsted acid sites (BAS) play a critical role in catalytic cracking reactions[29, 30]. NH_3 temperature-programmed desorption (TPD) was used to determine the total acidity for the sample series, whose profiles depict the significant changes in the strength and content of acid sites at different HZ23-kaolin compositions (**Figure 5.3A)**. The Lewis, and Brønsted acidities were quantified *via* pyridine adsorption, as shown in **Table 5.2**. The zeolite is the most acidic catalyst component (526.8 $\mu mol.g^{-1}$) compared to kaolin (83.3 $\mu mol.g^{-1}$). The HZ23-kaolin catalysts with lower zeolite loading show fewer Brønsted and Lewis acidity. It is interesting to look at the Brønsted to Lewis acid ratio of the samples under study, the 5 wt.% HZ23-kaolin formulation shows a B/L ratio close to the parent zeolite. Furthermore, the catalysts that contain total acidity between 92 and 99 $\mu mol.g^{-1}$ selectively produced light olefins. It is also worth highlighting that the utilization of kaolin as catalyst matrix minimizes the content of zeolite (max. 10%) in the catalyst body and maximize the use of a cheaper natural material (kaolin), enhancing the cost of the catalyst and its sustainability credentials.

Table 5.2. Acidity of the HZ23-kaolin catalyst series.

Sample	*Total acidity, ($\mu mol_{NH3} \cdot g_{cat}^{-1}$)*	*Brønsted ($\mu mol \cdot g^{-1}$)*	*Lewis ($\mu mol \cdot g^{-1}$)*	*BAS/LAS*
Kaolin	83.3	2.3	0.3	7.7
5% HZ23-kaolin	92.3	29.8	9.3	3.2
10% HZ23-kaolin	98.6	90.7	80.4	1.1
20% HZ23-kaolin	154.5	73.1	57.7	1.3
30% HZ23-kaolin	ND	119.9	60.6	2.0
HZ23	526.8	726	191.6	3.8

*ND: Not determined measurement

The influence of the surface acidity density (SAD) over the TOFs of light alkenes and the B/L acid sites ratio was also studied, as shown in **Figure 5.5**. The TOFs for the combined HZ23-kaolin formulations are higher than those for the pristine catalysts (i.e., HZ23 and kaolin alone) regardless of the alkene considered; this indicates an optimal surface distribution of acid sites leads to maximum production of light olefins. Interestingly, the TOFs for C_3H_6 are distinctly superior for the samples with intermediate surface acidity density (i.e., ca. 1.9 - 2.6 $\mu mol_{NH_3} \cdot m^{-2}$) and containing 5 and 10 wt.% HZ23 on kaolin owing to the balance and strength of Brønsted and Lewis acid sites (i.e., BAS and LAS respectively). In fact, the 10 wt.% HZ23-kaolin formulation with the maximum TOFs for alkene production shows a BAS/LAS ratio close to unity whilst the 5 wt.% HZ23-kaolin formulation depicts about a 3-fold increase of BAS/LAS ratio. This finding suggests that the maximum TOFs for light alkenes arises as a consequence of the optimum combination of intermediate values of SAD and BAS/LAS ratio in which zeolite contributes with the most robust acid sites whilst kaolin would provide weaker acidity[31, 32]. This argument also supports the sudden diminution of the TOFs as decreasing the SAD (or increasing the HZ23 loading) in the catalyst formulation.

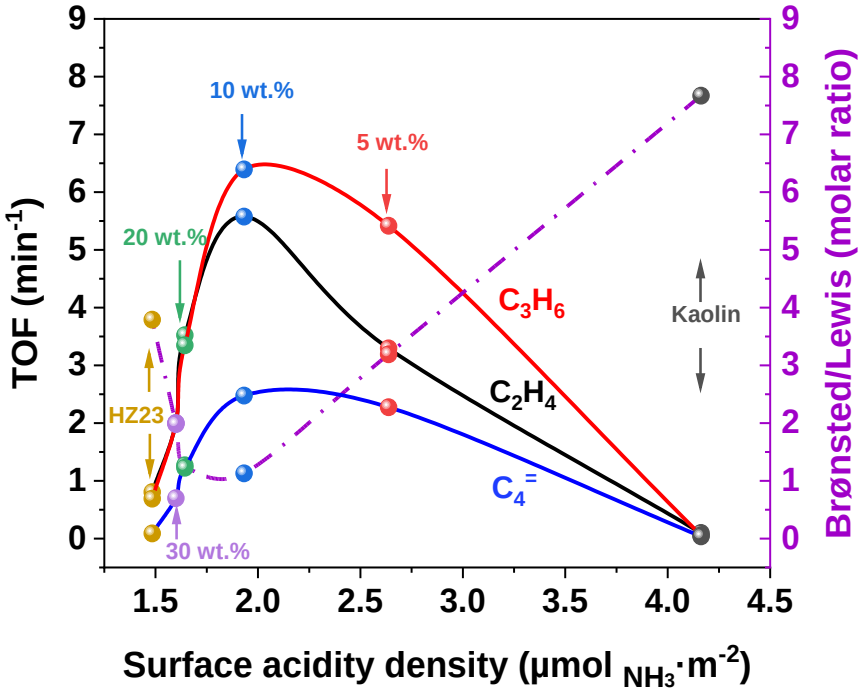
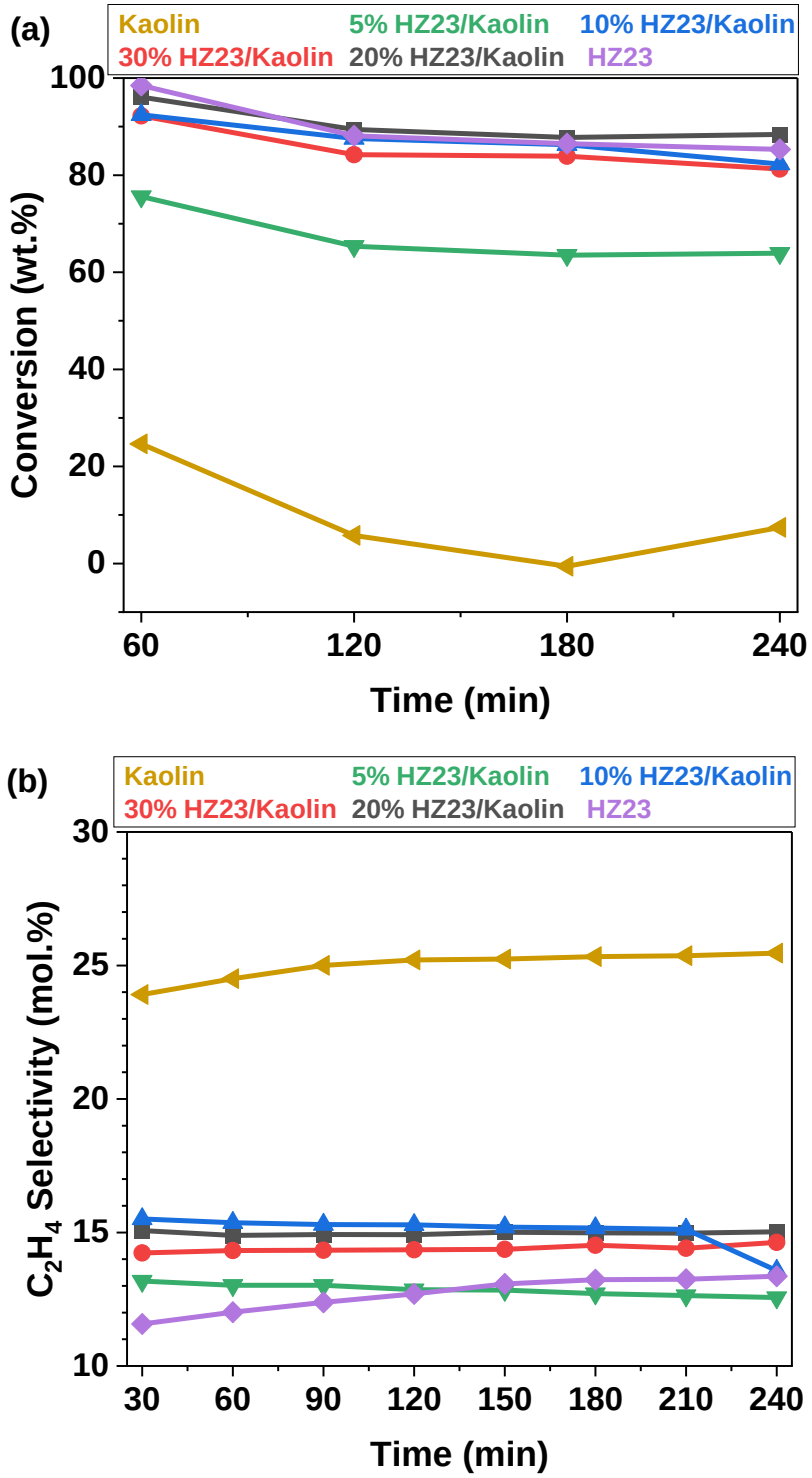


Figure 5.5. Dependence of the turnover frequencies (rates normalized to the moles of NH_3 per mass of catalyst) and Brønsted/Lewis molar ratio with the surface acidity density of HZ23-kaolin catalysts in the production of light alkenes through the cracking reaction of *n*-heptane. The TOF errors was between 3-6%.

5.3.2 Catalytic performance test

In this chapter, the focus is on the influence of kaolin as binder/matrix with HZ23 zeolite for the production of light olefins. Initially, H-ZSM-5 zeolites with SiO_2/Al_2O_3 ratios of 80 and 23 were mixed with kaolin were assessed to determine the best catalyst formulation for light olefin production. HZ23 was significantly more active and selective than the HZ80 catalyst in agreement with a previous report[25]. In order to establish the reliability of the reaction set-up, the catalytic cracking of *n*-heptane and light naphtha is evaluated over fixed bed reactor at 550°C and atmospheric pressure for 4h. Initially, the catalytic performances of a series of H-ZSM-5 (HZ23, SiO_2/Al_2O_3=23) zeolites with kaolin were evaluated to select the zeolite with the highest (optimum) yield of light olefins. The overall carbon balance for these tests was above than 90%, Including residual carbon; this value is within the expected range of cracking reactions.

5.3.2.1 Catalytic cracking of *n*-heptane on different HZ23-kaolin catalyst formulations



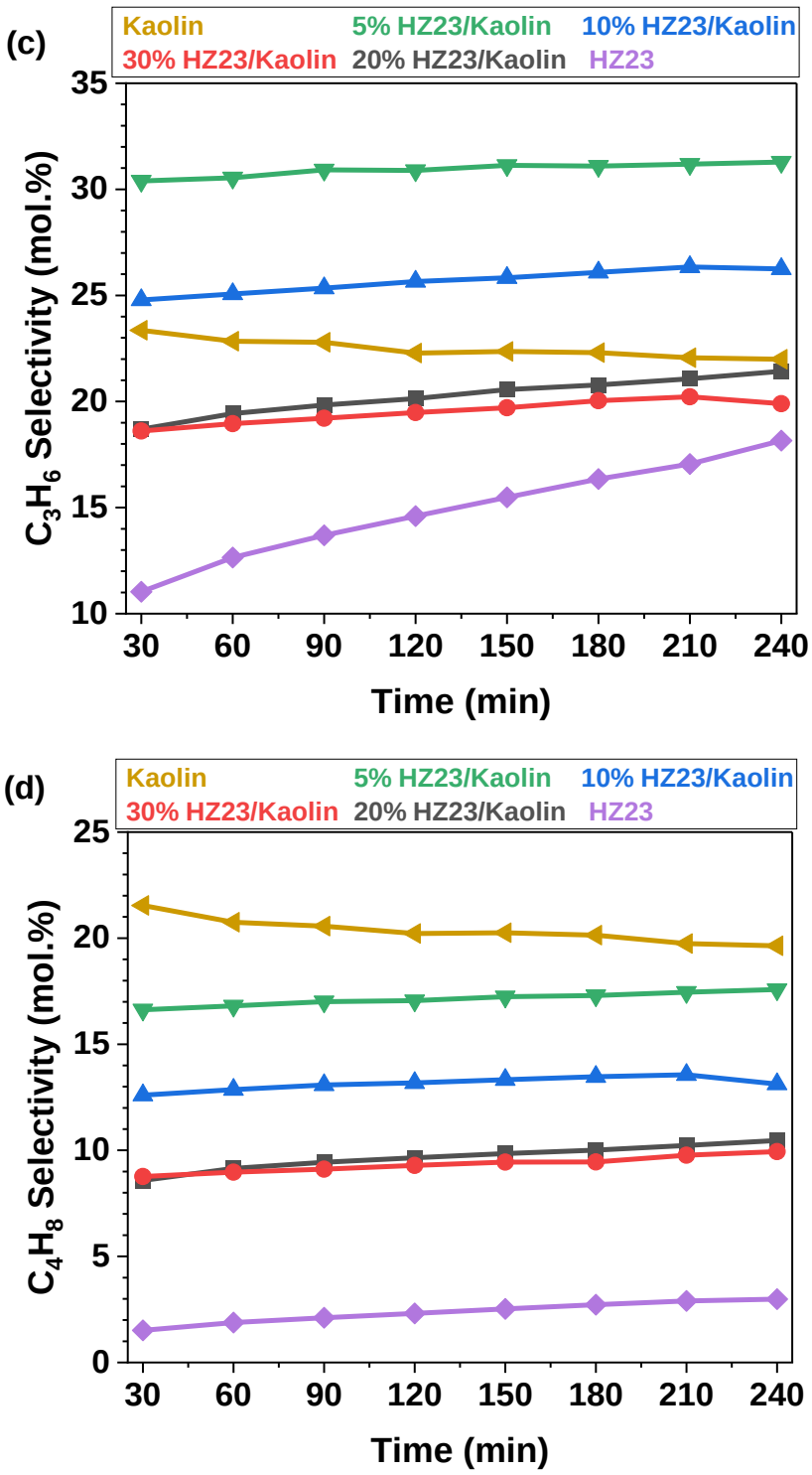


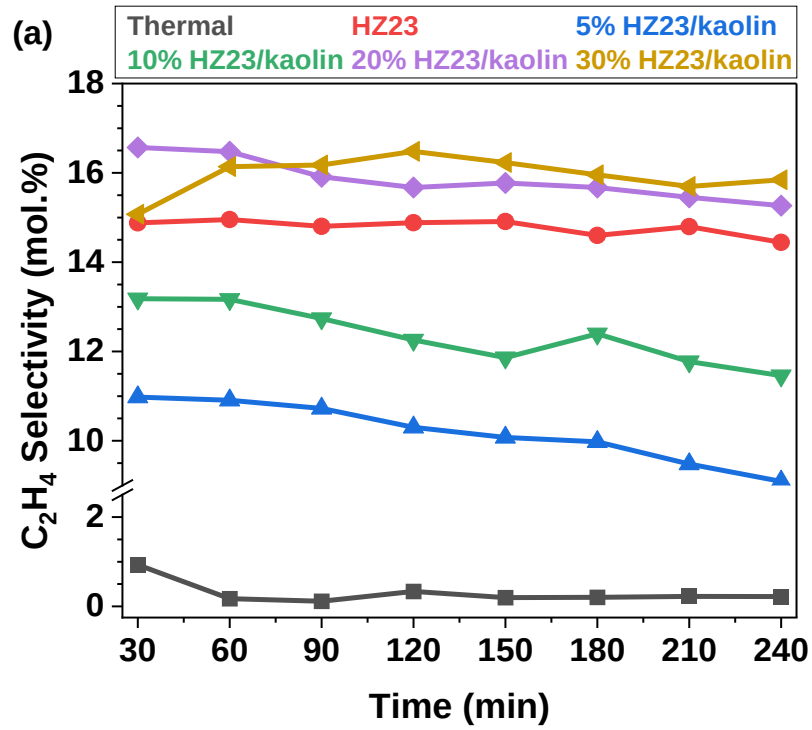
Figure 5.6. Effect of HZ23 zeolite loading on kaolin support on *n*-heptane conversion (a), C_2H_4 selectivity (b), C_3H_6 selectivity (c) and C_4H_8 selectivity (d). The reactions were conducted at 550°C, atmospheric pressure (0.1 MPa), wight hour space velocity (WHSV) 8.2 h^{-1}, and 20 ml.min-1 N_2 flow rate. The estimated error was between 3-6%.

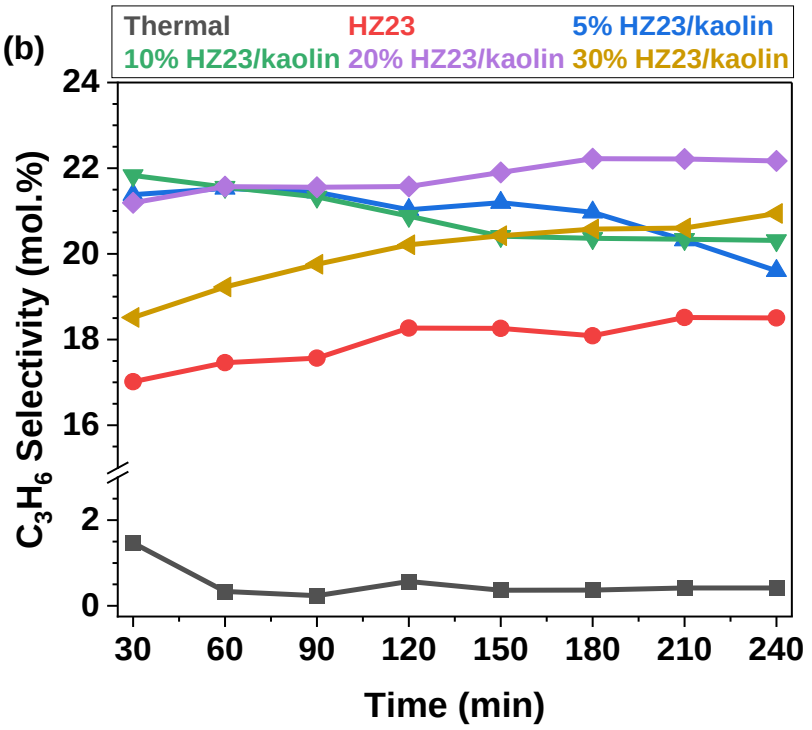
Figure 5.6 illustrates the conversion and selectivity for light olefins from the cracking reaction of *n*-heptane versus time-on-stream (TOS). The catalytic performance of unmodified HZ23 catalyst and kaolin is also included to illustrate clearly the strong influence of the support on the selectivity of olefins. Note that even small loadings of HZ23 on kaolin markedly enhance *n*-heptane conversion (**Figure 5.6a**). The parent kaolin shows higher C_2H_4 selectivity (24-25 mol.%) than the kaolin-modified HZ23 catalyst, likely due to its significant low *n*-heptane conversion (**Figure 5.6b**). However, the pristine HZ23 and kaolin-modified HZ23 catalysts exhibit quite similar C_2H_4 selectivity (i.e., about 11-15 mol.%), whilst the 5 and 10 % HZ23-containing catalysts displayed the highest propylene selectivity and catalytic stability with the time-on-stream (TOS) as given in **Figure 5.6c**. On the other hand, the kaolin containing HZ23 depicts a higher C_4H_8 selectivity (8.7-17 mol.%) than parent HZ23 (1.5-2.9 mol.%), as shown in **Figure 5.6d**. These findings clearly show the marked effect that the relatively small content of HZ23 zeolite has on the production of light olefins.

5.3.2.2 Catalytic cracking of light naphtha on different HZ23-kaolin catalyst formulations

Figure 5.7 shows the selectivity for light hydrocarbons but conversions are not reported due to the complexity of the feedstock, as reported in the literature[25]. A blank (thermal) test (without catalyst) was also conducted to compare the effect of the thermal and catalytic cracking reactions. Interestingly, thermal cracking favors the formation of mainly unsaturated C_4 compounds and could be an important pathway for the catalyst formulations with low zeolite loadings (5 and 10 % HZ23). The formulations containing 20 and 30 wt.% HZ23 show quite similar selectivity for ethylene (about 16 mol.%) than parent HZ23 zeolite (i.e., ca. 15 mol.%). In contrast, the 5 and 10% HZ23-kaolin catalysts show a vice versa trend (**Figure 5.7a**). All the catalysts exhibit propylene selectivity higher

than the parent HZ23 zeolite, as shown in **Figure 5.7b**. However, the system containing a maximum loading of 10 wt.% of zeolite in kaolin showed a high butylene selectivity of 38-48 mol.%, followed by 20 wt.% HZ23-kaolin at about 22 mol.% and 30 wt.% HZ23-kaolin and parent HZ23 (i.e., ca 19 mol.%). The formation of $C_4^=$ compounds is strongly promoted by thermal cracking reactions, as revealed by the selectivity of nearly 83 mol.% for the blank test (**Figure 5.7c**). Note that HZ23-kaolin formulations showed markedly lower alkane selectivity than pristine HZ23 catalysts (**Figure 5.7d**), owing to the efficient diminution of hydrogen transfer reactions.


(a)
Thermal
HZ23
5% HZ23/kaolin
10% HZ23/kaolin
20% HZ23/kaolin
30% HZ23/kaolin
C_2H_4 Selectivity (mol.%)
Time (min)


(b)
Thermal
HZ23
5% HZ23/kaolin
10% HZ23/kaolin
20% HZ23/kaolin
30% HZ23/kaolin
C_3H_6 Selectivity (mol.%)
Time (min)

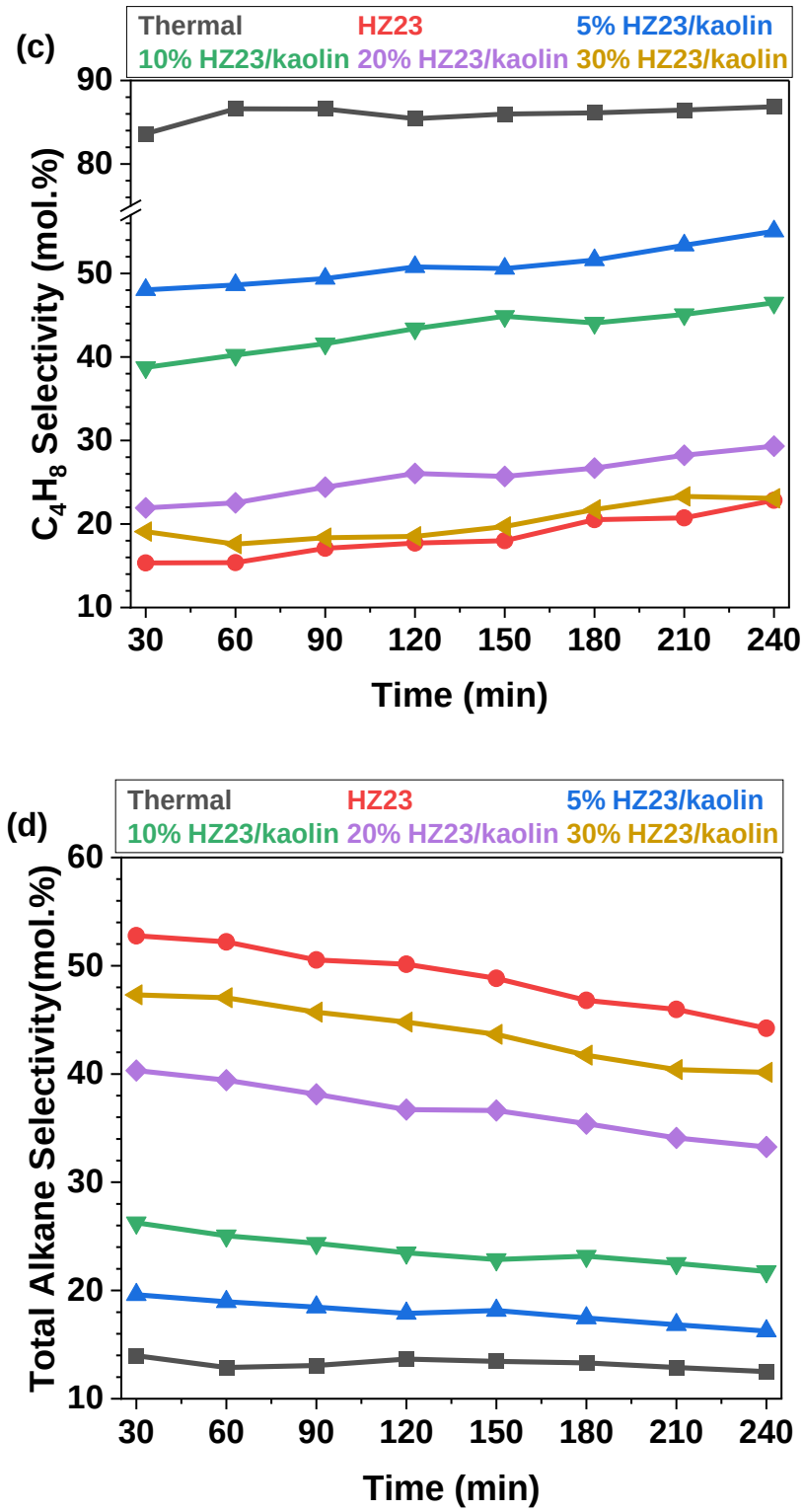


Figure 5.7. Effect of HZ23 zeolite loading of kaolin catalyst on naphtha, C_2H_4 selectivity (a), C_3H_6 selectivity (b), C_4H_8 selectivity (c), and total alkane (d). The reactions were conducted at 550°C, atmospheric pressure (0.1 MPa), wight hour space velocity (WHSV) 8.2 h^{-1}, and 20 $ml.min^{-1}$ N_2 flow rate. The estimated error was between 3-6%.

5.3.2.3 Total olefin yield for HZ23-kaolin formulation for *n*-heptane and naphtha cracking

Figure 5.8a shows the yield of light olefins (ethylene, propylene, and butylene) and the yield of BTX (benzene, toluene, and xylene) from catalytic cracking of *n*-heptane over HZ23-kaolin catalysts with different loadings of HZ23. It can be seen that, remarkably, all the HZ23-kaolin formulations have slightly higher ethylene yields, about 13-15 wt.%, than the parent HZ23, which shows about 12 wt.%. On the other hand, the HZ23-kaolin catalysts give higher yields of propylene (19-30 wt.%) and butylene (9-16 wt.%) than HZ23 alone (15 wt.% for propylene and 2.4 wt.% for butylene). However, it can see the pristine HZ23, and 30% HZ23-kaolin catalyst show higher BTX yields at about 2.7-2.8 wt.% after a 3-hour reaction due to the more extensive number of acid sites within the zeolite.

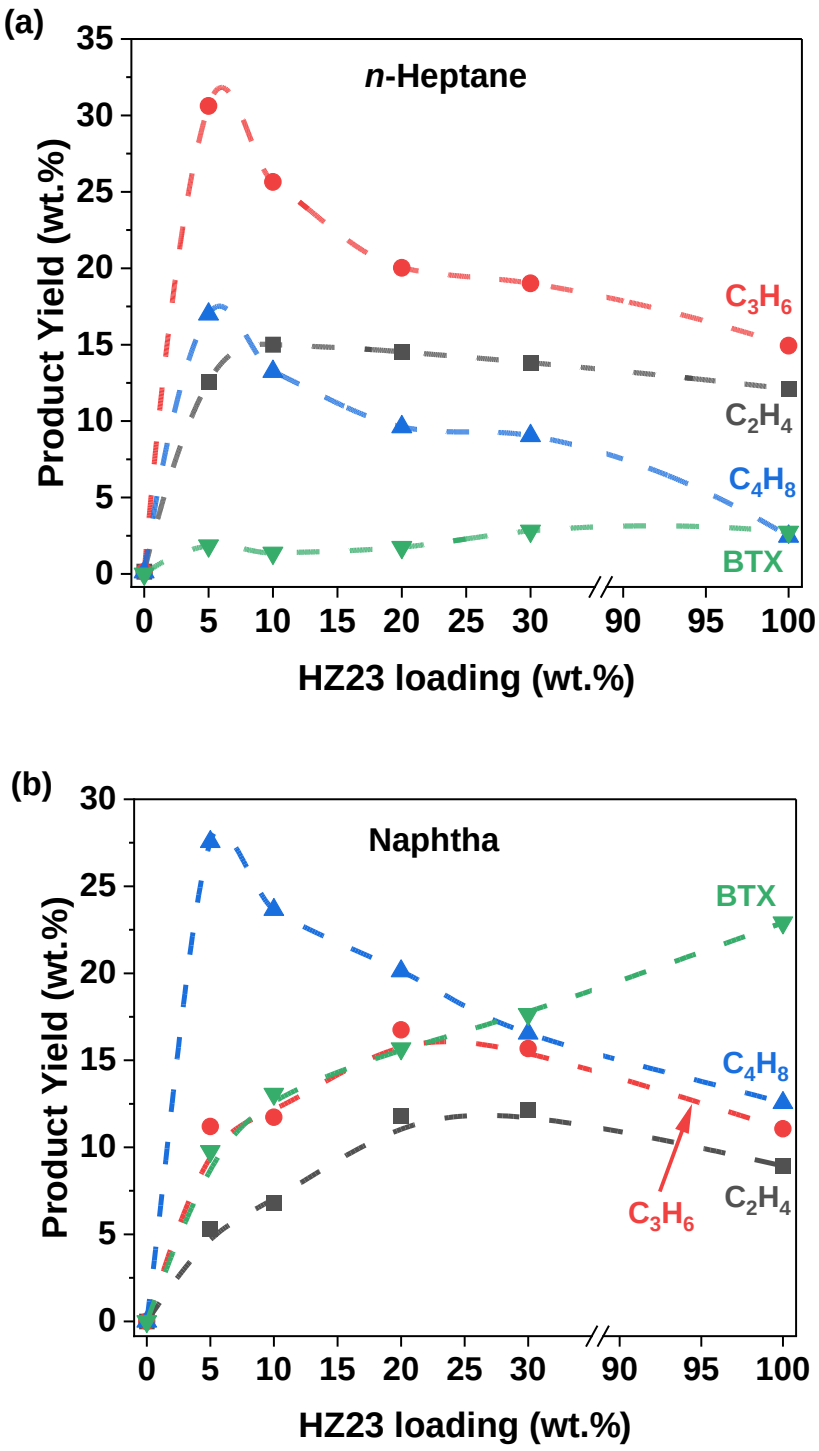


Figure 5.8. Effect of HZ23 zeolite loading over kaolin at 3-hour TOS on the *n*-heptane (a) and naphtha (b) cracking reaction for light olefins and BTX yield. The reactions were conducted at 550°C, atmospheric pressure (0.1 MPa), liquid hour space velocity (LHSV) 8.2 h^{-1}, and 20 ml min^{-1} N_2 flowrate.

On the other hand, **Figure 5.8b** displays the yields of light olefins and BTX for naphtha catalytic cracking over HZ23-kaolin catalysts with different loadings of HZ23 in the kaolin host. The enhancement of the BTX yield with increasing HZ23 loading is probably due to the conversion of cycloalkane present in naphtha into aromatics. Interestingly, the optimal catalyst formulation for maximum C_2H_4 and C_3H_6 yields from naphtha cracking was 20 wt.% zeolite (HZ23) in kaolin **(Figure 5.8b**). The zeolite loading is above that for *n*-heptane cracking owing to the broad molecular composition of naphtha (**Table 5.1A and Table 5.2A**), which demands a high density of acid sites that also facilitate the formation of BTX. In agreement with the catalytic cracking of *n*-heptane, the catalyst formulations are also able to produce higher yields of C_2H_4 and C_3H_6 than pristine HZ23 zeolite, whilst the BTX yield was markedly enhanced with increasing HZ23 content. It is noticeable that the significant yields of $C_4^=$ compounds compared to the *n*-heptane cracking reaction are due to the thermal cracking reaction of naphtha as a blank (thermal) test depicted in **Figure 5.4A**. The yield of hydrocarbon products on catalytic cracking of *n*-heptane and light naphtha on different HZ23-kaolin catalyst formulations are summarised in **Table 5.3A and 5.4A**.

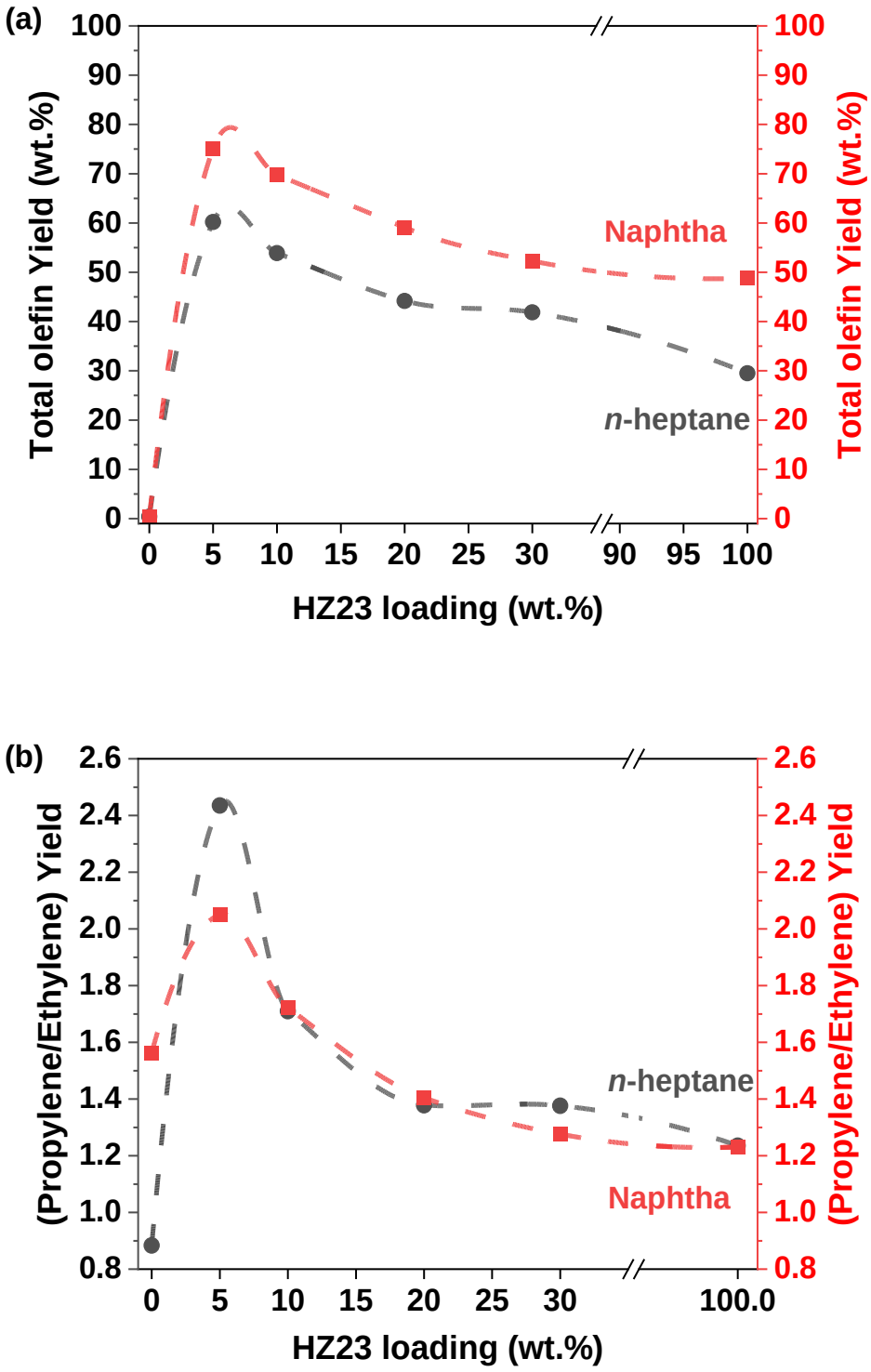


Figure 5.9. The propylene/ethylene (P/E) ratio for two feedstocks on HZ23-kaolin catalysts with different compositions.

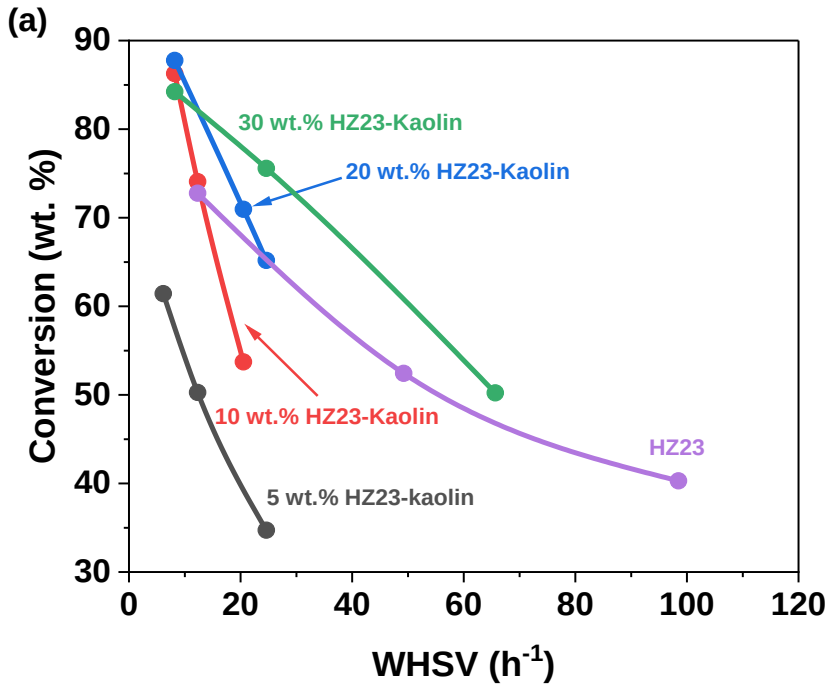
Figure 5.9a illustrates the total olefin yield during the cracking reaction of naphtha and *n*-heptane over different loadings of HZ23 dispersed within a kaolin support. Remarkably, catalyst formulations with a maximum loading of 10 wt.% HZ23 and 90 wt.% natural clay (kaolin) are able to produce higher yields of light olefins (about 53-60 wt.%) than pristine HZ23 zeolite (about 24-31 wt.%) through the catalytic cracking process.

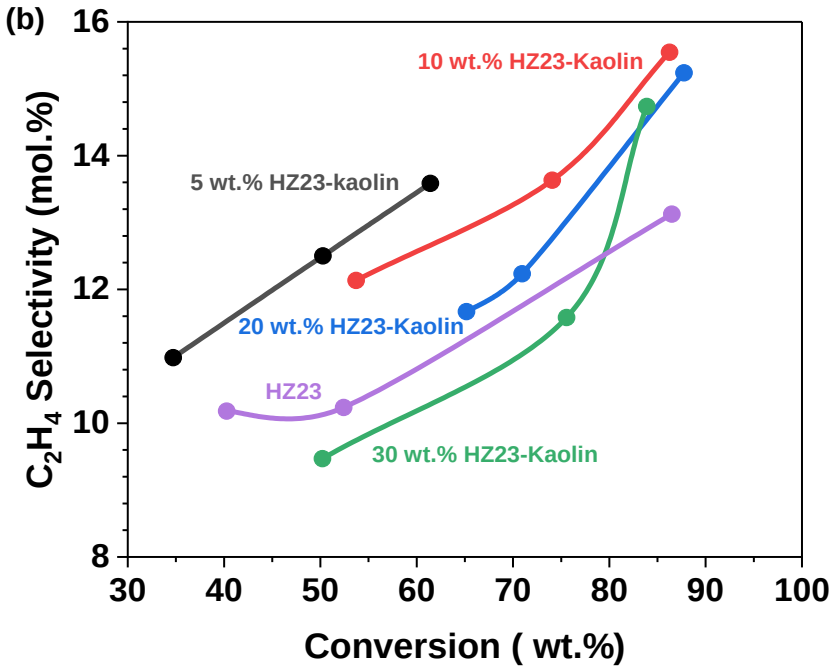
It has been proposed that the production of olefins from the catalytic cracking of *n*-heptane and naphtha proceeds *via* a monomolecular mechanism[33-36] and it was found that the total olefins yield reached a maximum of 60 to 75 wt.% respectively for a 5 wt.% HZ23-kaolin catalyst formulation.

Importantly, the loading of 5 wt.% zeolite (HZ23) in kaolin enhanced not only the yield of light olefins but also, and most importantly, the propylene to ethylene (P/E) ratio, resulting in 2 and 2.4 for naphtha and *n*-heptane respectively, whilst pristine HZ23 catalyst showed a P/E ratio close to 1.2 regardless of the feedstock, **Figure 5.9b.** This trend clearly reflects the marked effect of the molecular composition of feedstock over the olefin yields owing to the wide distribution of chemical reaction sites and accessible molecular dimensions of the hybrid catalyst system.

Alabdullah *et al.*,[25] showed a total olefin yield of 15.2 wt.% after 100 min reaction over a catalyst comprising 20 wt.% HZ23, 20 wt.% binder, and 60 wt.% kaolin for Arabian light crude oil at 570°C in a fixed bed reactor. In our investigations, we obtained a higher olefin yield (47 wt.%) for a catalyst containing 20 wt.% HZ23/kaolin for naphtha as feedstock. The different feedstocks used, and the presence or absence of binder may be responsible for the differences in total olefin yield.

5.3.2.4 Effect of different weight hourly space velocities (WHSV) on catalytic cracking of *n*-heptane into light olefins





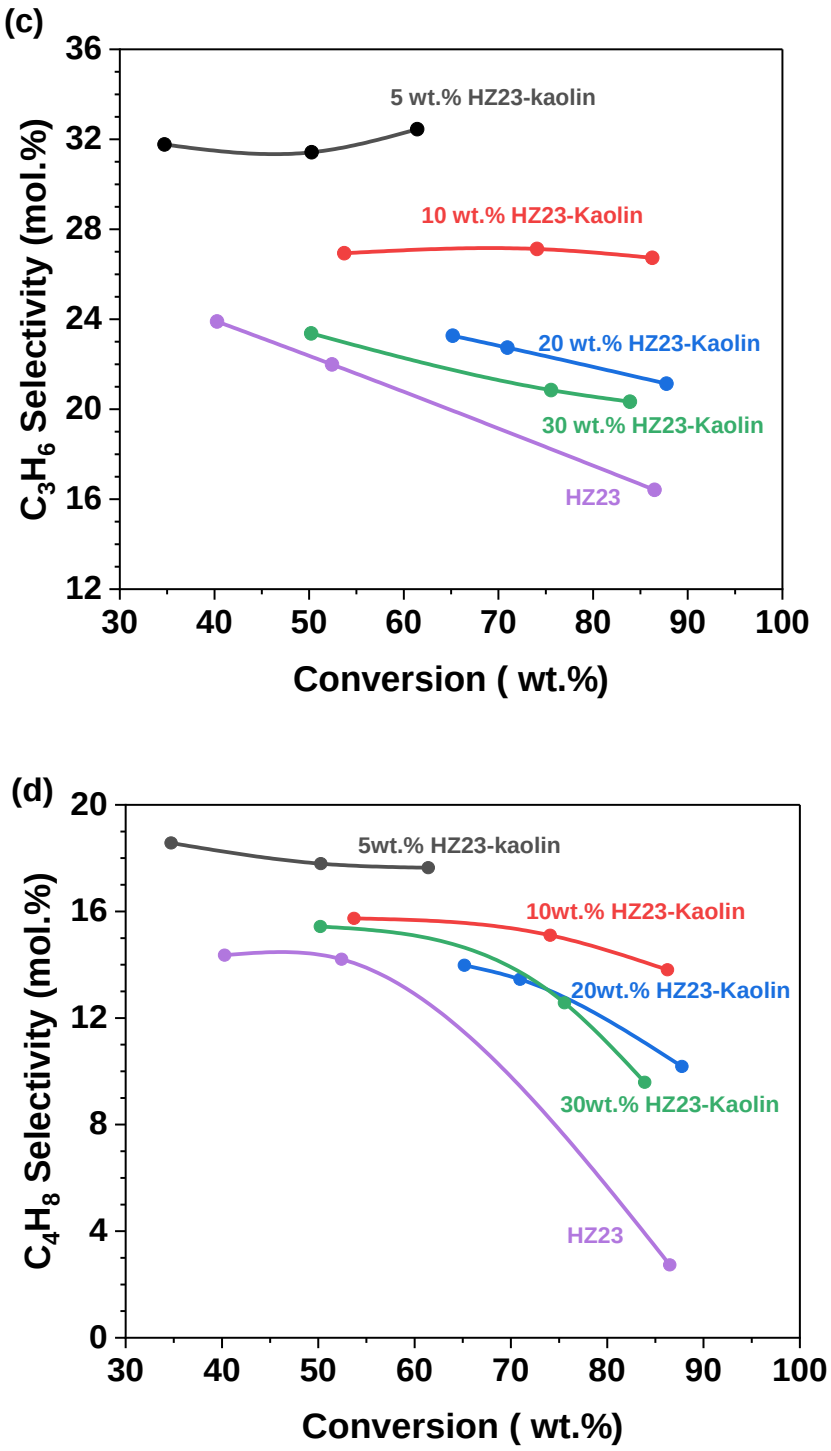


Figure 5.10. Catalytic cracking of *n*-heptane and distribution of olefins over HZ23-kaolin catalysts tested at different weight hourly space velocity (WHSV). (a) Influence of WHSV over conversion of *n*-heptane, (b) Effect of *n*-heptane conversion over ethene selectivity, (c) propene selectivity and (d) $C_4^=$ selectivity. The conversion of *n*-heptane and alkene selectivity correspond to a TOS of 3 h at 550°C, atmospheric pressure (0.1 MPa), 20 ml.min^{-1} N_2 flow rate and *n*-heptane flow rate between 0.075- and 0.8 ml.min^{-1}.

It is well-established that pretreated kaolin can be used to control coke formation and product yield during the petroleum upgrading process, minimize sulfur content and improve the metal tolerance [17]. Within this context, this section will focus on gaining further insight into the advantages of the kaolin-based support in the high catalytic performance of HZ23-kaolin formulations. Also reported is the kaolin's influence on the catalyst acidity and the rapid diffusion of *n*-heptane and light olefins to minimize secondary cracking reactions and hence maximizing the production of light olefins.

The influence of the WHSV (i.e., F_{feed}/W_{cat}) over *n*-heptane conversion in the series of HZ23-kaolin catalysts is depicted in **Figure 5.10a**. Note that the space velocity is inversely proportional to the feed contact time; hence the *n*-heptane conversion decreases as the WHSV increases. Furthermore, catalyst formulations with low content of HZ23 (e.g., 5, 10 and in less degree 20 wt.%), and in contrast to pristine HZ23 and 30 wt.% HZ23-kaolin catalysts, show a substantial diminution of *n*-heptane conversion within a narrow range of WHSV due to the rapid access of *n*-heptane to the acid sites in the zeolite framework. It is expected that thermal cracking reactions have a low contribution in the *n*-heptane conversion as verified through a blank test conducted in absence of a solid catalyst (**Figure 5.4A)**. In fact, WHSV decreases from ca. 50 h^{-1} (30 wt.% HZ23-kaolin) to about 6 h^{-1} (5 wt.% HZ23-kaolin) the HZ23 content in the HZ23-kaolin formulations is reduced at somewhat similar conversion conditions (between 60 and 65 wt.%). This trend clearly reveals the marked effect of HZ23 content over the catalyst activity and its enhancement at high zeolite content owing to the increase of the catalyst acidity. The diffusional limitations of *n*-heptane through inter and intra particles in pure HZ23 catalyst might affect the overall reaction rate since most of the acid sites in HZSM-5 are located within the porous cavities, which produce steric constrains to hydrocarbons and affect the reaction mechanism and diffusion of reactants and products[37-39].

The dependence of the selectivity of light alkenes on the *n*-heptane conversion was also explained as shown in **Figure 5.10(b-d).** There is a strong dependence of both C_2H_4 and $C_4^=$ yields on conversion whilst the C_3H_6 selectivity varied a lesser extent. Also, there is a significantly higher selectivity for alkenes with 5 and 10 wt.% HZ23-kaolin catalysts compared to the other formulations, **Figure 5.10(b-d)**. Interestingly, C_2H_4 selectivity increased with rising *n*-heptane conversion whilst $C_4^=$ and to a lesser extent that for C_3H_6 decreased. A similar trend was observed for the catalytic cracking of *n*-heptane on HZSM-5[40] and *n*-hexane on MCM-22[41], indicating that a possible chemical pathway of C_2H_4 formation would involve the cracking reaction of C_4 fragments generated from the *n*-heptane molecule. Importantly, C_3H_6 selectivity was fairly independent of *n*-heptane conversions for 5 and 10 wt.% HZ23-kaolin catalysts owing to the low diffusional constraint for *n*-heptane and the rapid diffusion and desorption of C_3H_6 product that minimize consecutive cracking reactions, **Figure 5.10c**. Obviously, the intermediate strength and the balance of Brønsted and Lewis acid sites, alongside the proximity of the catalyst components, play a main role in the maximization of light alkene production, particularly in the formation of C_3H_6. Catalyst formulations with higher zeolite content showed a diminution of the C_3H_6 selectivity due to an increase in conversion as a consequence of the high density of acid sites in closer proximity.

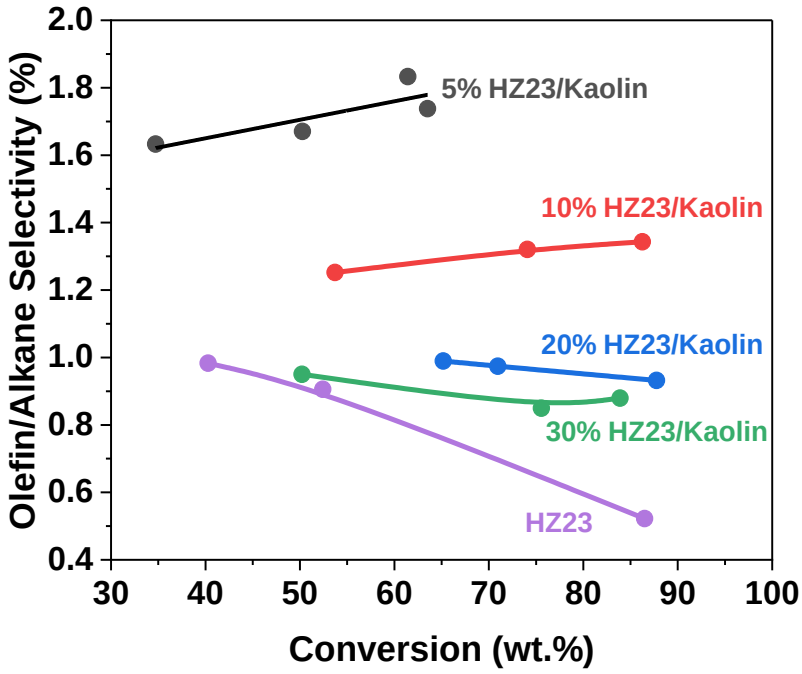


Figure 5.11. Effect of HZ23 loading on kaolin catalyst and olefins/alkane selectivity on different space velocities on the *n*-heptane conversion after 3-hour reaction.

According to the literature, a combination of both monomolecular and bimolecular mechanisms are the main pathways in the cracking of hydrocarbons[42, 43]. The Haag-Dessau (or monomolecular) mechanism involves the protonation of an alkane to produce a high-energy pentacoordinate carbonium-like ion, whose collapse produces an alkane (*via* a cracking reaction) or hydrogen (*via* dehydrogenation) and an adsorbed carbenium ion as a precursor of alkene. This reaction pathway predominates on any HZSM-5 catalyst with low acid site density and reaction temperatures above 450°C[43]. The above-described scenario is appropriate for the kaolin-enriched catalyst formulations (5 and 10 wt.% HZ23-kaolin). The alkene/alkane ratio is clearly higher (i.e., 1.2-1.8) than that for catalysts with higher zeolite contents (below 1) as shown in **Figure 5.11**.

5.3.2.5 Study of the effect of reaction temperature and lifetime of 5 wt.% HZ23-kaolin catalyst in the catalytic cracking of *n*-heptane into light olefins

The effect of temperature on 5 wt.% HZ23-kaolin catalyst on the production of light olefins using *n*-heptane as a model compound is displayed in **Figure 5.12**. It was found that the best temperatures for producing olefins, particularly propylene, are between 550°C and 650°C. The change of olefin yield and *n*-heptane conversion in catalytic cracking at different temperatures are displayed in **Figure 5.12a**. The conversion was about 7.2 wt.% at 300°C and increased with temperature to 100 wt.% at 750°C; both temperature and conversion follow a direct relationship. A similar dependency showed the ethylene yield with temperature. In fact, the ethylene yield at 300°C was 0.2 wt.% and increased to 39 wt.% when the temperature increased to 750°C. However, the propylene yield reached about 35 wt.% at temperatures between 500-650°C and dropped to 22 wt.% at 750°C. On the contrary, the butylene yield remained at ca. 21 wt.% at temperature between 300 and 600°C and started to drop at temperatures above 600°C to achieves 3.5 wt.% at 750°C. This is explained by the low activity of the catalyst due to carbon build-up on their surface, which masks the catalytically active areas. Thermal cracking rises at higher temperatures increasing carbon deposition.

The alkanes and BTX yields on 5 wt.% HZ23-kaolin in the catalytic cracking of *n*-heptane at different temperatures are depicted in **Figure 5.12b**. The yield of aromatics (BTX) reached a maximum (i.e., 4.2 wt.%) at around 600°C. However, the propane and butane yields decreased with increasing the temperature from about 27-24 wt.% to 1.2-0.2 wt.% whilst the ethane yield showed the opposite behaviour.

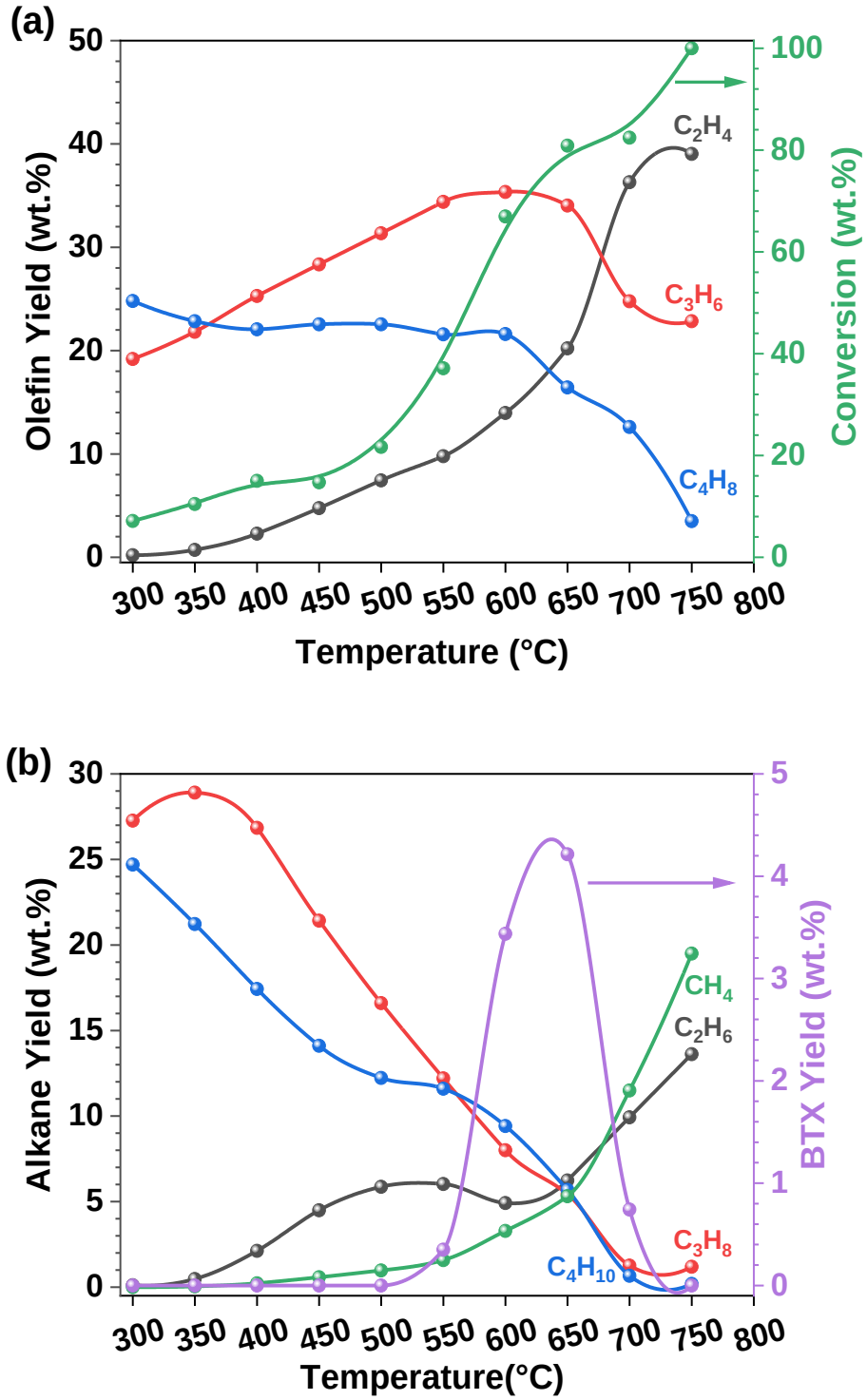


Figure 5.12. a) *n*-heptane conversion and light olefin yields (wt.%), and b) alkane and BTX yields (wt.%) over 5% HZ23-kaolin catalyst at different temperatures. The reactions were conducted at atmospheric pressure (0.1 MPa), and 20 ml.min^{-1} N_2 flowrate.

The catalytic stability of the optimal HZ23/kaolin formulation (5 wt.% of HZ23) (HZSM-5; $SiO2/Al_2O_3$ =23) over *n*-heptane for a period of 26 h was also investigated (**Figure 5.13).** The conversion reached about 60 wt.% during the first hour of reaction and steadily decreases down to ca. 52-50 % in a period of nearly 14h to keep fairly constant for the remaining 12 h of time on stream. It is much better than HZ23 alone, and longer lifetime has huge implications for industrial use.

It is noticeable that 5 wt.% zeolite-kaolin catalyst shows the highest values of C_3H_6 selectivity (i.e., about 31 mol.%), which means 14% higher C_4H_8 and C_2H_4 selectivity (**Figure 5.6A)**. Moreover, it is striking that the C_3H_6 and C_4H_8 selectivities increase with time-on-stream (TOS). In contrast, the C_2H_4 selectivity showed the opposite behaviour, indicating that the formation of C_2H_4 arises from the secondary cracking reactions of C_3 and C_4 fragments from the primary cracking of *n*-heptane.

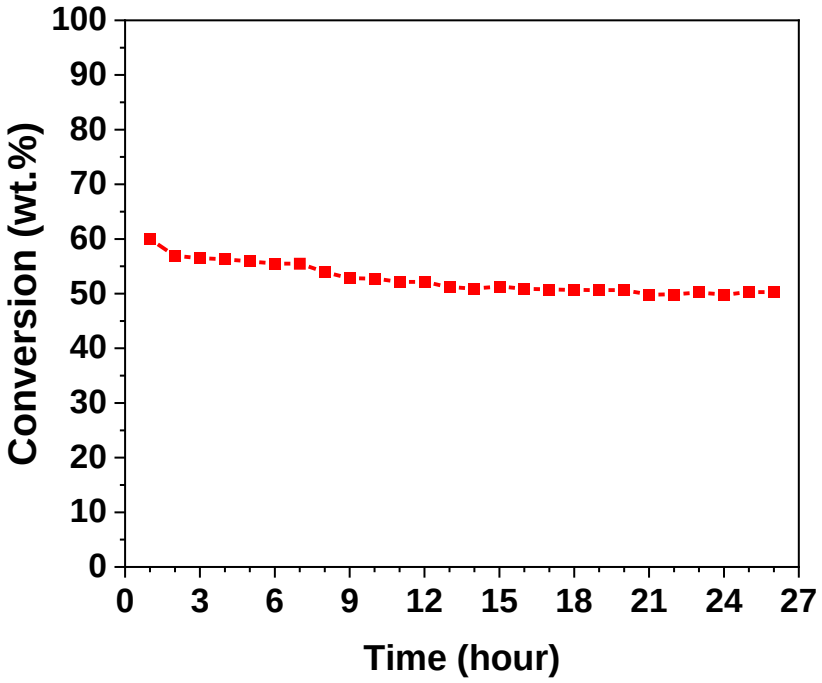


Figure 5.13. *n*-Heptane conversion over 5% HZ23 Zeolite-Kaolin catalysts in a 26-hour test reaction. The reactions were conducted at 550 °C, atmospheric pressure (0.1 MPa), and 20 $ml.min^{-1}$ N_2 flowrate.

The yields of light olefins (ethylene, propylene, and butylene) in the catalytic cracking of *n*-heptane over kaolin catalyst modified with 5 wt.% HZSM-5 (SiO_2/Al_2O_3=23) in a 26-hour catalytic test reaction are given in **Figure 5.14**. It can be seen the propylene yield for kaolin modified with 5 wt.% HZSM-5 (SiO_2/Al_2O_3=23) was higher (about 31.5 wt.%) in the first hour and then increased slowly with time-on-stream to about 33.6 wt.% with an increase rate of 0.08 wt.%.h^{-1}. However, the butylene yield increased about 15% with time-on-stream (from 18 wt.% to 20.7 wt.%), representing an activation rate of 0.11 wt.%.h^{-1}. On the contrary, this catalyst showed ethylene yields significantly lower than propylene and butylene. Note that ethylene yields were about 12.5% and decreased to 10.6 wt.% with time-on-stream and a low deactivation rate (-0.07 wt.%.h^{-1}). This means that carbon deposition is low over the 26h time frame.

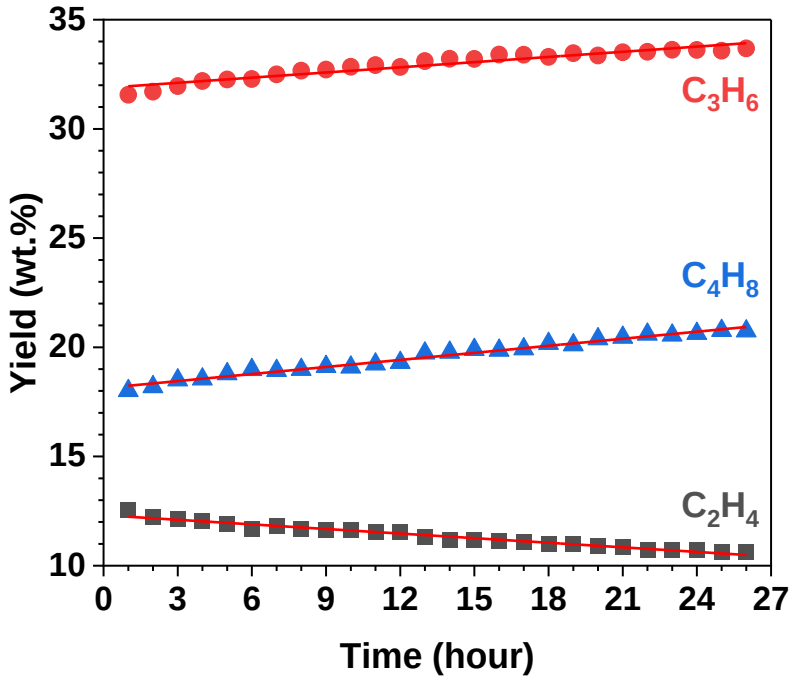


Figure 5.14. The yield of light olefins over 5% HZ23 Zeolite-Kaolin catalysts on *n*-heptane cracking in a 26-hour catalytic test reaction. The reactions were conducted at 550 °C, atmospheric pressure (0.1 MPa), and 20 ml.min^{-1} N_2 flowrate.

5.3.3 Post- reaction analysis of catalysts

5.3.3.1 X-ray diffraction analysis (XRD)

The XRD diffractograms for the spent samples (**Figure 5.15**) do not show marked changes compared to the fresh catalysts (**Figure 5.2**). In fact, when we compare the crystallite size of HZ23 and even kaolin of the fresh (**Table 5.5A**) and spent catalysts (**Table 5.6A**) the crystallite sizes are roughly comparable regardless the catalyst composition. However, kaolin shows slightly higher crystallite size than HZ23 and the increase in the crystallite size relative to HZ23 (i.e., kaolin/HZ23) enhances the total olefin yield (**Figure 5.5A**). No clear evidence of carbon deposition is shown in the XRD profiles owing to the low carbon content, and it is amorphous character. Note that the broad peak centred at ca. 12.2° in 2θ corresponds to grease used to stick the sample on the XRD sample holder. The small peak at ca. 71.9° in 2θ for 30 wt.% HZ23-kaolin is associated with SiC used a enhance the heat transfer to the catalyst bed.

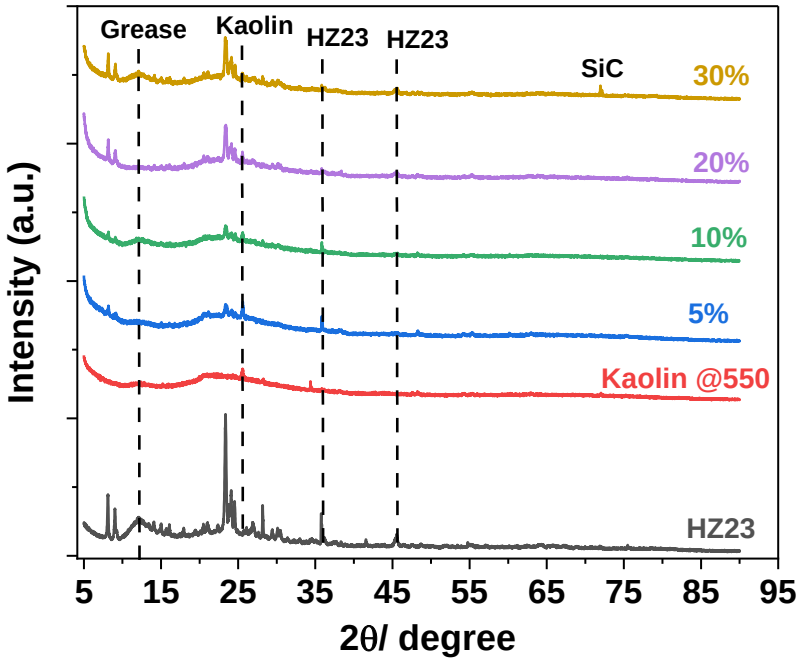


Figure 5.15. Comparison of powder X-ray diffraction patterns for used HZ23 catalyst, kaolin, and different compositions of HZ23-kaolin catalyst.

5.3.3.2 Thermogravimetric measurement (TGA)

The weight loss and derivative of the used catalysts containing different HZ23 and kaolin compositions are given in **Figure 5.16a-b**. In general, condensed *n*-heptane, light hydrocarbons product and water are weakly adsorbed on the catalyst surface and removed by heating the sample in the air in a temperature range of 50-300℃, as illustrated in **Figure 4.9a**. It is noticeable the definition of two main weight loss steps. The resulting carbon in the used catalyst has a similar oxidation temperature to ZSM-5 at 568℃, and this peak reduces as the kaolin content increases (**Figure 5.16b**) owing to the diminution of acid sites. This peak corresponds to coke-type carbon material mainly derived from zeolitic acid sites[25].

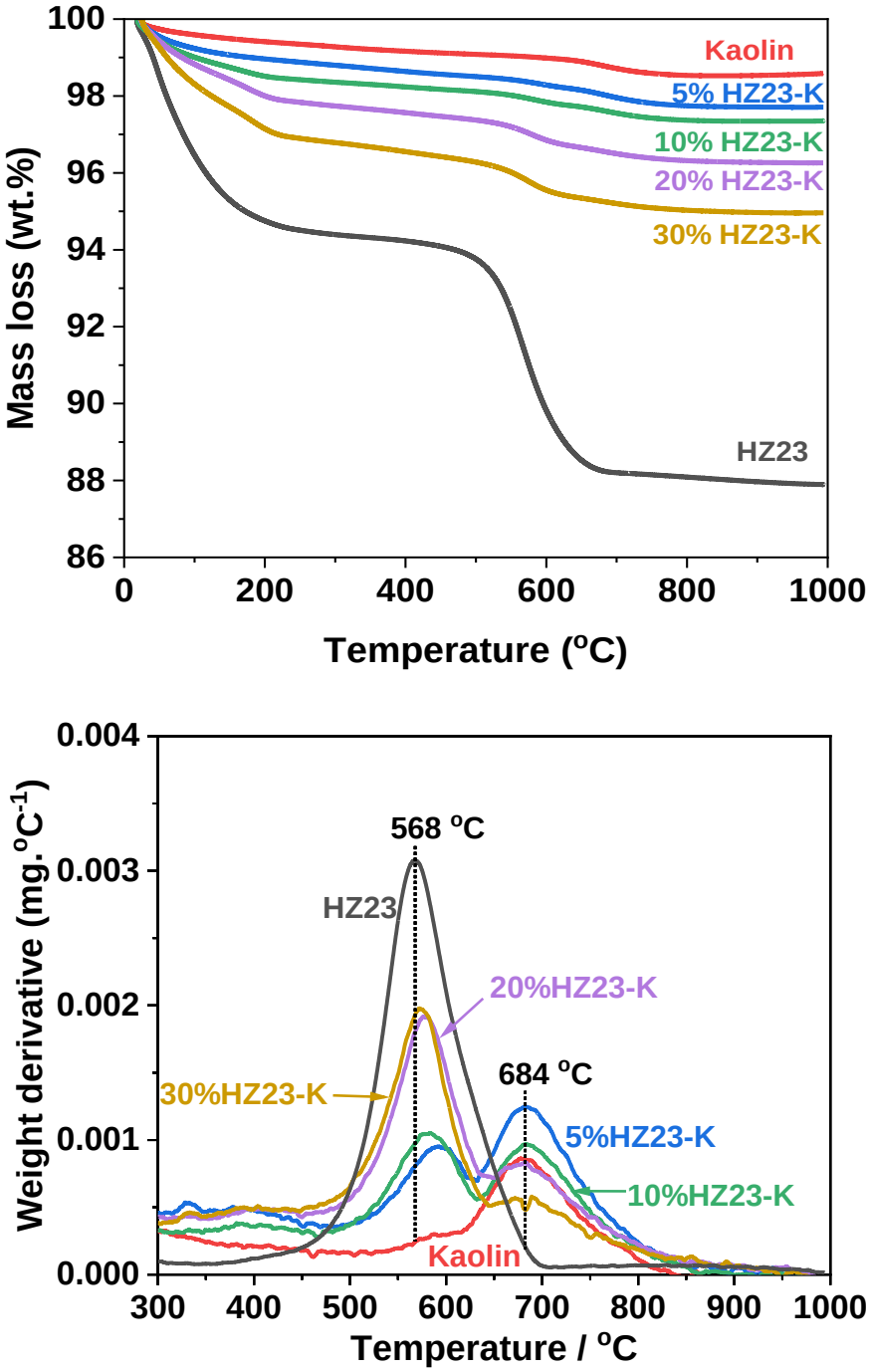


Figure 5.16. Characterization of the catalysts after the catalytic cracking of *n*-heptane. a) TGA for used samples under air flow for different HZ23-kaolin catalyst. b) weight derivative profiles of the six used catalysts under air flow. Derivative data of HZ23 curve was divided by 4 to amplify the scale of the

samples containing low loading of zeolite. The weight loss calculation considered the initial sample mass obtained at 250-300°C after the removal of adsorbed *n*-heptane.

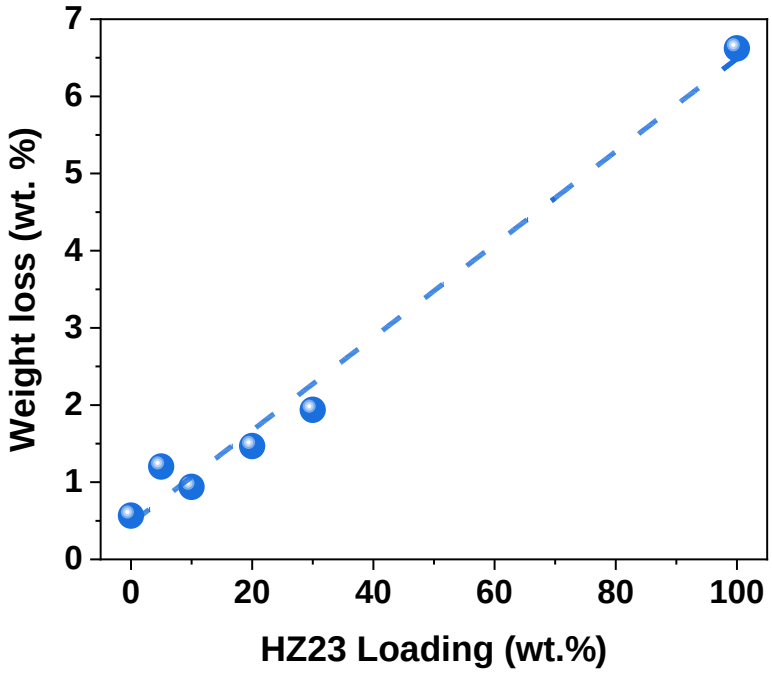


Figure 5.17. Dependence of the total weight loss of the used catalysts with HZ23 content.

Interestingly – and importantly -, this plot clearly reveals a linear dependence of the overall weight loss with the HZ23 content (**Figure 5.17**), suggesting that the content and chemical nature of deposited carbon material depend mainly upon the presence of acid sites in the zeolite catalyst. As shown **Figure 5.16b**, the hard coke includes residue deposits of extremely unsaturated species that can be burnt off at high temperatures[44, 45]. The secondary peak at 684°C is mainly associated with the complete dehydroxylation of kaolin since this slight weight loss was also observed in the kaolin sample before the catalytic reaction. It is noticeable that the used catalysts show between 3 and nearly 7-fold decrease in the content of deposited carbon compared to the used pristine HZ23 catalyst as a consequence of the significant diminution of the total acidity and specific surface area. This finding would entail an important enhancement in the catalyst lifetime due to low carbon deposition.

5.3.3.3 Brunauer-Emmentt-Teller (BET) analysis

Table 5.3 shows the surface area of the spent kaolin-zeolite hybrid catalysts. The BET results confirmed again that the catalytic cracking is very dependent on the surface area. All the spent catalysts exhibited lower BET areas compared with the fresh catalysts (**Table 5.1**) due to coke formation on the catalyst surface. On the other hand, the comparison of the BET surface area of the kaolin-zeolite hybrid catalysts before and after reaction also reveals a drastic decrease in the external surface area after the reaction, while a slight decrease was observed in the internal area, particular for the 5 wt.% HZ23-kaolin formulation. This finding might be an indication of the secondary reactions and coke production happening mainly on the external surface of the zeolite structure. On the other hand, the primary cracking reactions that produce light olefins occur rapidly and without severe diffusional limitations inside the channel of zeolites with limited participation of secondary reactions and coke production.

Table 5.3. The **s**urface area of the spent HZ23-kaolin catalyst series was tested in the selective cracking reaction of *n*-heptane toward light olefins.

Sample	***BET ($m^2 \cdot g^{-1}$)***	***T-Plot ($m^2 \cdot g^{-1}$)***		
		External	**Internal**	**I/E**
Spent 5% HZ23-kaolin	27	14	13	0.9
Spent 10% HZ23-kaolin	28	9	19	2.1
Spent 20% HZ23-kaolin	57	19	38	2.0
Spent 30% HZ23-kaolin	98	26	72	2.8
Spent HZ23	198	41	157	3.8

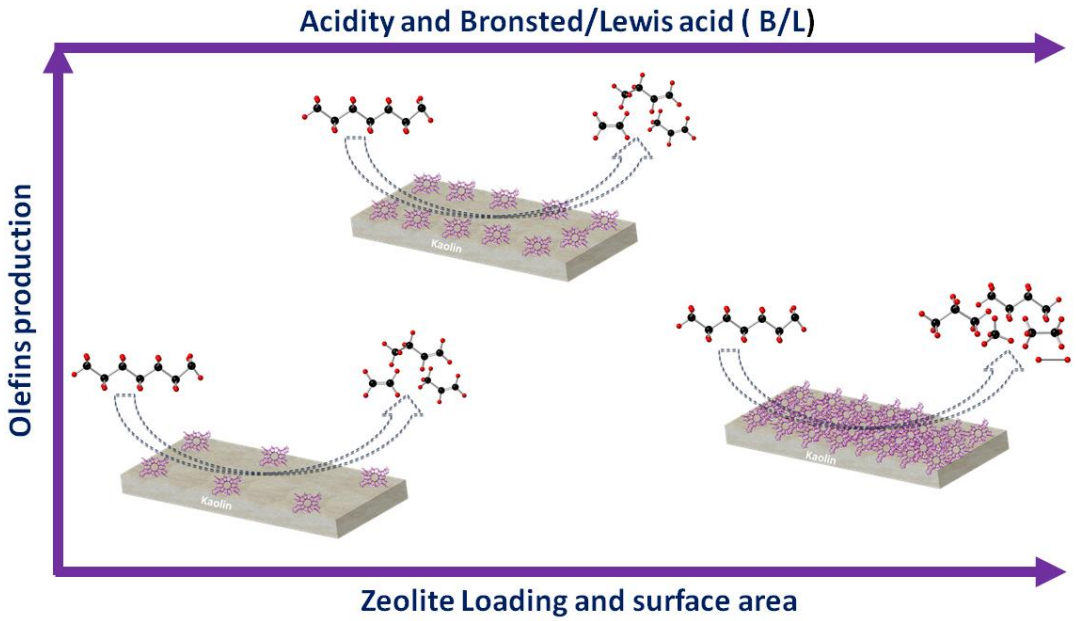


Figure 5.18. Schematic representation of the influence of HZ23-kaolin catalyst over the production of light alkenes through the catalytic cracking of *n*-heptane.

The combination of HZ23 and kaolin certainly shows a strong synergic tendency toward producing light alkenes from the catalytic cracking of *n*-heptane and even naphtha, as illustrated in **Figure 5.18**. Notably, the superior mixing of nanocrystals of HZ23 and kaolin enhances the yield of light olefins, particularly C_3H_6 followed by C_2H_4 and to a lesser extent C_4H_8. This finding is attributed to the rapid access of *n*-heptane molecule into the zeolite cavity *via* acid sites with intermediate surface acidity density that favors the partial cracking of *n*-heptane *via* a monomolecular mechanism and subsequent production of alkenes and rapid desorption to minimise secondary cracking reactions[3, 30].

5.4 A preliminary discussion of the sustainability credentials of light olefins production

Within an environmental perspective, novel technologies for producing light olefins need to minimise the CO_2 emissions associated not only with the production of process heat for powering the process but also with the generation of CO_2 as reaction product. A full

lifecycle analysis (LCA) must also consider the carbon footprint of the emitters including production and processing the feedstock, distribution, application, recycling and minimization of waste. Interestingly, according to Ismaël *et al.*,[46] steam cracking (SC) is the most environmental friendly technology for producing light olefins despite requiring the highest reaction temperatures (above 800°C) relative to the oxidative coupling of methane (OCM), methanol to olefin (MTO) and Fischer-Tropsch Synthesis. Furthermore, the utilization of coal as raw material for olefins' production increases between 7 and 9 times the total CO_2 emissions compared to SC of naphtha or ethane. A similar trend should be expected for the FCC process since the catalyst after a reaction cycle requires a reactivation stage in which the induced coke is burnt-off with the consequent emissions of CO_2[47]**.** In fact, we have previously proposed that a significant total CO_2 emission reduction of the FCC process can be obtained through the development of advanced FCC catalysts based on the analysis via the Catalyst Sensitivity Index (CSI) of a series of different technologies[48].

Importantly, our catalytic cracking process, on the other hand, favors the production of light olefins at temperatures (500-600°C) substantially lower than that for the SC process and does not produce CO_2 during the catalytic reaction, indicating that the carbon fingerprint is substantially reduced relative to the SC of naphtha. Our advance minimises the utilization of expensive zeolite catalyst and maximises the production of light olefins thereby enhancing its potential impact in the transition to a more sustainable future for producing petrochemicals and conversion technologies. Further studies of this important facet of these advances are underway through a complete LCA =incorporated in the Catalyst Sensitivity Index approach.

5.5 Conclusion

Our approach of zeolite dilution with kaolin described in this chapter not only minimizes the use of zeolite (max. 20 wt.%) it also maximizes the use of a natural based inexpensive material (kaolin), enhancing the cost efficiency of the catalyst and its sustainable characteristics. The catalytic system containing a maximum loading of 10 wt.% of zeolite in kaolin showed the best performance for producing light alkenes from *n*-heptane (as a model compound), whilst for naphtha cracking (an industrial feedstock) the best performance was for the 20 wt.%. HZ23-Kaolin catalyst owing to the wide molecular distribution present in this feedstock.

The combination of HZ23 and kaolin enhances the production of light alkenes from the catalytic cracking of *n*-heptane and light naphtha. The optimal distribution of HZ23 with a large contact with the kaolin improves the yield of light olefins, particularly C_3H_6, followed by C_2H_4 and to a smaller extent $C_4^=$ olefins owing to the rapid access of *n*-heptane molecules into the zeolite microporous through acid sites with intermediate surface acidity density. These acid sites assist the cracking reaction of *n*-heptane *via* the monomolecular mechanism and subsequent production of alkenes, whose high diffusion and rapid desorption minimises the secondary cracking reaction.

Low contents of HZ23 mixed with kaolin produce a large distribution of zeolite-kaolin interfaces that selectively catalyze the cracking reactions by maximizing access of hydrocarbons into the zeolite channels. The combined HZ23-kaolin formulations after cracking reaction show low levels of deposited carbon particularly on the internal surfaces when compared to the used HZ23 catalyst due to their lower total acidity. The deposited carbon is formed by unsaturated carbonaceous species (hard coke) that require high combustion temperatures as a consequence of the high strength of acid sites from the higher content of zeolite. Interestingly, the secondary reactions and coke production happening mainly on the

external surface of the zeolite structure whilst the primary cracking reactions that produce light olefins occur rapidly and without severe diffusional limitations inside the channel of zeolite.

The optimal formulations for the production of mainly C_2H_4 and C_3H_6 from the catalytic cracking of *n*-heptane resulted in 5 wt.% HZ23-kaolin followed by 10 wt.% HZ23-kaolin catalyst, which maximizes the formation of $C_4^=$ from the catalytic cracking of naphtha. Catalyst formulations with higher zeolite contents (20 and 30 wt.% HZ23-kaolin) enhance the yields of C_2H_4 and C_3H_6 whilst decreasing the formation of $C_4^=$ compounds. This reveals that depending upon the chemical composition of the feedstock, different catalyst formulations will be required to optimize the catalyst performance and thereby maximizing the yield of light olefins, particularly propene.

5.6 References

1. Al-Dughaither, A. S.; de Lasa, H., HZSM-5 zeolites with different SiO_2/Al_2O_3 ratios. Characterization and NH_3 desorption kinetics. *Industrial & Engineering Chemistry Research,* 2014, *53* (40), 15303-15316.
2. Dorado, F.; Romero, R.; Cañizares, P., Influence of Clay Binders on the Performance of Pd/HZSM-5 Catalysts for the Hydroisomerization of *n*-Butane. *Industrial & Engineering Chemistry Research,* **2001,** *40* (16), 3428-3434.
3. Velthoen, M. E. Z.; Lucini Paioni, A.; Teune, I. E.; Baldus, M.; Weckhuysen, B. M., Matrix Effects in a Fluid Catalytic Cracking Catalyst Particle: Influence on Structure, Acidity, and Accessibility. *Chemistry – A European Journal,* **2020,** *26* (52), 11995-12009.
4. Lal, B.; Pal, D. B.; Rathoure, A. K.; Singh, A., Studies on acidity and activity of kaolin-supported Ag-doped HZSM–5 in methanol to olefins process. *Biomass Conversion and Biorefinery,* **2021**, 1-15.
5. Rhodes, D., Clay and Glazes for the Potter. *Ravenio Books,* **2015**.
6. Siti Khadijah, H.; Mohd Hafiz Dzarfan, O.; Takeshi, M.; Ismail, A. F.; Mukhlis, A. R.; Zawati, H.; Juhana, J.; Mikihiro, N., Fabrications and applications of low cost ceramic membrane from kaolin: A comprehensive review. *Ceramics International,* **2018,** *44* (5), 4538-4560.
7. Gualtieri, A.; Norby, P.; Artioli, G.; Hanson, J., Kinetics of formation of zeolite Na-A [LTA] from natural kaolinites. *Physics and Chemistry of Minerals,* **1997,** *24* (3), 191-199.
8. Ebrahim, M.; Yusuf Makarfi, I.; Masikana, M. M.; Nonyameko, S.; David, K.; Themba, T., Synthesis of ZSM-5 from impure and beneficiated Grahamstown kaolin: Effect of kaolinite content, crystallisation temperatures and time. *Applied Clay Science,* **2016,** *119*, 213-221.
9. Khatamian, M.; Irani, M., Preparation and characterization of nanosized ZSM-5 zeolite using kaolin and investigation of kaolin content, crystallization time and temperature changes on the size and crystallinity of products. *Journal of the Iranian Chemical Society,* **2009,** *6* (1), 187-194.
10. Kovo, A.; Hernandez, O.; Holmes, S., Synthesis and characterization of zeolite Y and ZSM-5 from Nigerian Ahoko Kaolin using a novel, lower temperature, metakaolinization technique. *Journal of Materials Chemistry,* **2009,** *19* (34), 6207-6212.
11. Emam, E. A., Clays as catalysts in petroleum refining industry. *ARPN Journal of Science and Technology,* **2013,** *3* (4), 356-375.
12. Hartati; Prasetyoko, D.; Santoso, M.; Qoniah, I.; Leaw, W. L.; Firda, P. B. D.; Nur, H., A review on synthesis of kaolin-based zeolite and the effect of impurities. *Journal of the Chinese Chemical Society,* **2020,** *67* (6), 911-936.
13. Deng, C.; Xie, X.; Han, J.; Tang, Y.; Gao, J.; Liu, C.; Shi, X.; Zhou, J.; Liang, S., A Sieve-Functional and Uniform-Porous Kaolin Layer toward Stable Zinc Metal Anode. *Advanced Functional Materials,* **2020,** *30* (21), 2000599.

14. Aimdate, K.; Srifa, A.; Koo-amornpattana, W.; Sakdaronnarong, C.; Klysubun, W.; Kiatphuengporn, S.; Assabumrungrat, S.; Wongsakulphasatch, S.; Kaveevivitchai, W.; Sudoh, M.; Watanabe, R.; Fukuhara, C.; Ratchahat, S., Natural Kaolin-Based Ni Catalysts for CO_2 Methanation: On the Effect of Ce Enhancement and Microwave-Assisted Hydrothermal Synthesis. *ACS Omega*, **2021,** *6* (21), 13779-13794.
15. Dewi, R.; Agusnar, H.; Alfian, Z. In Characterization of technical kaolin using XRF, SEM, XRD, FTIR and its potentials as industrial raw materials, Journal of Physics: Conference Series, *IOP Publishing*, **2018**; p 042010.
16. Prasad, M. S.; Reid, K. J.; Murray, H. H., Kaolin: processing, properties and applications. *Applied Clay Science*, **1991,** *6* (2), 87-119.
17. Hui, W.; Hongfei, L.; Ying, Z.; Siauw, N.; Hilary, B.; Yu, X., Kaolin-based catalyst as a triglyceride FCC upgrading catalyst with high deoxygenation, mild cracking, and low dehydrogenation performances. *Catalysis Today*, **2019,** *319*, 164-171.
18. Mohiuddin, E.; Isa, Y. M.; Mdleleni, M. M.; Key, D., Synthesis and Application of Porous Kaolin-Based ZSM-5 in the Petrochemical Industry. In Nanofluid Flow in Porous Media, *IntechOpen*, **2018**.
19. Lal, B.; Singh, A., Effect of Kinetic Parameters on Activity of Kaolin and Silver Modified HZSM–5 Zeolite in the Methanol-to-Olefins (MTO) Process. *Journal of Materials and Environmental Science*, **2021,** *12* (5), 656-663.
20. Wang, P.; Zha, F.; Yao, L.; Chang, Y., Synthesis of light olefins from CO_2 hydrogenation over (CuO-ZnO)-kaolin/SAPO-34 molecular sieves. *Applied Clay Science*, **2018,** *163*, 249-256.
21. Pan, F.; Lu, X.; Zhu, Q.; Zhang, Z.; Yan, Y.; Wang, T.; Chen, S., Direct synthesis of HZSM-5 from natural clay. *Journal of Materials Chemistry A*, **2015,** *3* (7), 4058-4066.
22. International Zeolite Association. http://www.iza-structure.org/databases/.
23. Shoinkhorova, T.; Dikhtiarenko, A.; Ramirez, A.; Dutta Chowdhury, A.; Caglayan, M.; Vittenet, J.; Bendjeriou-Sedjerari, A.; Ali, O. S.; Morales-Osorio, I.; Xu, W.; Gascon, J., Shaping of ZSM-5-Based Catalysts via Spray Drying: Effect on Methanol-to-Olefins Performance. *ACS Applied Materials & Interfaces*, **2019,** *11* (47), 44133-44143.
24. Varga, G., The structure of kaolinite and metakaolinite. *Epitoanyag*, **2007,** *59* (1), 6-9.
25. Alabdullah, M.; Shoinkhorova, T.; Rodriguez-Gomez, A.; Dikhtiarenko, A.; Vittenet, J.; Ali, O. S.; Morales-Osorio, I.; Xu, W.; Gascon, J., Composition-performance Relationships in Catalysts Formulation for the Direct Conversion of Crude Oil to Chemicals. *ChemCatChem*, **2021,** *13* (7), 1806-1813.
26. Granizo, M. L.; Blanco-Varela, M. T.; Palomo, A., Influence of the starting kaolin on alkali-activated materials based on metakaolin. Study of the reaction parameters by isothermal conduction calorimetry. *Journal of Materials Science*, **2000,** *35* (24), 6309-6315.

27. Tian-Jun, R.; Jin-kai, X., The catalytic cracking activity of the kaolin-group minerals. *Materials Letters,* **2002,** *57* (2), 297-301.
28. Shafei, E. N.; Albahar, M. Z.; Aljishi, M. F.; Aljishi, A. N.; Alnasir, A. S.; Al-Badairy, H. H.; Sanhoob, M. A., Naphtha catalytic cracking to olefins over zirconia–titania catalyst. *Reaction Chemistry & Engineering,* **2021,** *7*, 123-132.
29. Il-Ho, C.; Hye-Jin, L.; Geun-Bae, R.; Dong-Hyun, C.; Kyong-Hwan, L.; Kyung-Ran, H., Catalytic hydrocracking of heavy wax from pyrolysis of plastic wastes using Pd/Hβ for naphtha-ranged hydrocarbon production. *Journal of Analytical and Applied Pyrolysis,* **2022,** *161*, 105424.
30. Whiting, G. T.; Chowdhury, A. D.; Oord, R.; Paalanen, P.; Weckhuysen, B. M., The curious case of zeolite–clay/binder interactions and their consequences for catalyst preparation. *Faraday Discussions,* **2016,** *188* (0), 369-386.
31. Xia, X.; Bing, S.; Peng, W.; Xiaoqiang, F.; Lian, K.; Zean, X.; Bonan, L.; Zhen, Z., Tuning the density of Brønsted acid sites on mesoporous ZSM-5 zeolite for enhancing light olefins selectivity in the catalytic cracking of *n*-octane. *Microporous and Mesoporous Materials,* **2022,** *330*, 111621.
32. Bok, T.; Andriako, E.; Ivanova, I., Effect of Binder Content on the Properties of Nanocrystalline Zeolite BEA-based Catalysts for Benzene Alkylation with Propylene. *Petroleum Chemistry,* **2021,** *61* (8), 901-907.
33. Fu, J.; Feng, X.; Liu, Y.; Shan, H.; Yang, C., Mechanistic Insights into the Pore Confinement Effect on Bimolecular and Monomolecular Cracking Mechanisms of N-Octane over HY and HZSM-5 Zeolites: A DFT Study. *The Journal of Physical Chemistry C,* **2018,** *122* (23), 12222-12230.
34. Anh, T. T.; Daniel, E. R., Hydride transfer between a phenolic surface pool and reactant paraffins in the catalytic cracking of m-cresol/hexanes mixtures over an HY zeolite. *Journal of Catalysis,* **2015,** *329*, 57-68.
35. Fajun, Z.; Yongjian, L.; Ning, L.; Tianxiao, X.; Guangmeng, Z.; Kai, W., A review on upgrading and viscosity reduction of heavy oil and bitumen by underground catalytic cracking. *Energy Reports,* **2021,** *7*, 4249-4272.
36. Shafei, E. N.; Masudi, A.; Yamani, Z. H.; Muraza, O., Acidity modifications of nanozeolite-Y for enhanced selectivity to olefins from the steam catalytic cracking of dodecane. *RSC Advances,* **2022,** *12* (28), 18274-18281.
37. Jones, A. J.; Iglesia, E., The Strength of Brønsted Acid Sites in Microporous Aluminosilicates. *ACS Catalysis,* **2015,** *5* (10), 5741-5755.
38. Zheng, J.; Huang, L.; Wei, P.; Li, Q.; Fan, X.; Qin, Y.; Song, L., Molecular Insights into Adsorption and Diffusion Mechanism of *n*-Hexane in MFI Zeolites with Different Si-to-Al Ratios and Counterions. *Catalysts,* **2022,** *12* (2), 144.

39. Roque-Malherbe, R.; Wendelbo, R.; Mifsud, A.; Corma, A., Diffusion of aromatic hydrocarbons in H-ZSM-5, H-Beta, and H-MCM-22 zeolites. *The Journal of Physical Chemistry*, **1995,** *99* (38), 14064-14071.
40. Kohei, K.; Hajime, I.; Seitaro, N.; Akira, I., Selective formation of light olefin by *n*-heptane cracking over HZSM-5 at high temperatures. *Microporous and Mesoporous Materials*, **2012,** *149* (1), 126-133.
41. Yong, W.; Toshiyuki, Y.; Seitaro, N.; Junko, N. K.; Takashi, T., Catalytic cracking of n-hexane for producing propylene on MCM-22 zeolites. *Applied Catalysis A: General*, **2015,** *504*, 192-202.
42. Kotrel, S.; Knözinger, H.; Gates, B. C., The Haag–Dessau mechanism of protolytic cracking of alkanes. *Microporous and Mesoporous Materials*, **2000,** *35-36*, 11-20.
43. Blay, V.; Louis, B.; Miravalles, R.; Yokoi, T.; Peccatiello, K. A.; Clough, M.; Yilmaz, B., Engineering Zeolites for Catalytic Cracking to Light Olefins. *ACS Catalysis*, **2017,** *7* (10), 6542-6566.
44. Alaba, P. A.; Sani, Y. M.; Ashri Wan Daud, W. M., Kaolinite properties and advances for solid acid and basic catalyst synthesis. *RSC Advances*, **2015,** *5* (122), 101127-101147.
45. Qian, S.; Peng, W.; Huiping, T.; Riyuan, Y.; Yan, S.; Jun, L., Study of the application of structural catalyst in naphtha cracking process for propylene production. *Catalysis Today*, **2009,** *147*, S347-S351.
46. Ismaël, A.; Laurien, A. V.; Kevin, M.; Guy, B. M., New Trends in Olefin Production. *Engineering*, **2017,** *3* (2), 171-178.
47. Faisal, M. A.; Sergio, G.-C.; Mohammed, F. A.; Tiancun, X.; Hamid, A.-M.; Guidong, Y.; Peter, P. E., Enhancing the production of light olefins from heavy crude oils: Turning challenges into opportunities. *Catalysis Today*, **2018,** *317*, 86-98.
48. Xiao, T.; Shirvani, T.; Inderwildi, O.; Gonzalez-Cortes, S.; AlMegren, H.; King, D.; Edwards, P. P., The Catalyst Selectivity Index (CSI): A Framework and Metric to Assess the Impact of Catalyst Efficiency Enhancements upon Energy and CO_2 Footprints. *Topics in Catalysis*, **2015,** *58* (10), 682-695.

Chapter 6

Conclusions and Future Research

This chapter highlights the main results in this thesis and also suggests possible future research in the field of catalytic cracking of hydrocarbons.

6.1 Concluding remarks

The global demand and sustainability concerns for light olefin production encouraged researchers to look for an alternative and sustainable feedstock. This thesis has focused on the catalytic cracking of naphtha and *n*-heptane as model compound for naphtha through fixed-bed catalytic reaction, at 550℃ and atmospheric pressure, to produce good yields of light olefin. This work has been carried out as part of the KACST-Oxford Project at Inorganic Chemistry Laboratory (ICL) of the University of Oxford under the supervision of Prof. Peter P. Edwards.

The work described in chapter 3 reveals that, for these catalytic processes using zeolites, the SiO_2/Al_2O_3 ratio has some impact on the performance of the catalyst. Although it does not affect the MFI zeolite type structure. As the SiO_2/Al_2O_3 ratio increased, the crystallinity of H-ZSM-5 type zeolites also increased. The zeolites with higher SiO_2/Al_2O_3 ratios (HZ80 and HZ280) were more selective (i.e., about 40 and 52 mol.% from HZ280 and HZ80, respectively) toward light olefin (ethene, propene, and butene) formation, but produced less BTX yield (below 2 wt.%) than H-ZSM-5 type zeolites with a lower SiO_2/Al_2O_3 ratio.

According to the TGA analysis in dry air, after the *n*-heptane catalytic cracking at 550℃ the zeolites with lower SiO_2/Al_2O_3 ratios shows a higher amount of coke compared with the zeolite before reaction. Comparative tests suggested that the zeolite with an SiO_2/Al_2O_3 ratio of 80 (designated throughout the thesis as HZ80) produced higher olefin yield and was modified with Cr oxide in subsequent experiments.

As previously stated, our objective was to make further modifications to the zeolites to increase their catalytic performance and increasing the yield of light olefins from the naphtha cracking process. Alteration of the Si/Al ratio had a relatively limited impact on catalytic

activity. Therefore, the effects of Cr oxide introduced by different preparation methods were explored for improvement of catalytic cracking using zeolites.

The work described in Chapter 3 showed that zeolite modification using chromium oxide (Cr_2O_3) indeed has a very positive effect on the selectivity for light olefins. Furthermore, Cr_2O_3 loading on HZ80 *via* the impregnation method (IMP) has a higher positive impact into the production (yield) of total olefin and *n*-heptane conversion than a similar catalyst formulation prepared by mechanical mixture (MM).

The large surface area of HZ80 is affected by loading Cr oxide, particularly *via* impregnation, due to its potential blocking of pores. Another possible effect can be acidity diminution when increasing the Cr oxide loading and type of Cr oxide species dispersed onto the zeolite.

The optimum amount of Cr loading (i.e., 10 wt.%) in the IMP-prepared catalysts resulted in an increase in selectivity and yield toward olefins. It is interesting, the Cr_2O_3 loaded onto the zeolite by mechanical mixing produced a lower amount of coke. However, the selectivity and yield of olefins were lower than IMP catalyst. In addition, according to the XRD results, the Cr_2O_3 loaded by mechanical mixing showed a bigger particle size than by IMP, indicating that Cr_2O_3 is located on the external surface of the zeolite channel. However, the catalyst prepared by impregnation (IMP) was superior to the mechanical method (MM) approach in terms of yield of olefins.

Comparative tests suggested that the zeolite with an SiO_2/Al_2O_3 ratio of 23 (designated throughout the thesis as HZ23) showed higher conversion of *n*-heptane so it was used in subsequent experiments for modification with different supports.

The effect of combining different metal oxides such as Al_2O_3, TiO_2, ZrO_2, MgO, SiO_2 and kaolin with 20 wt.% zeolite (HZ23, SiO_2/Al_2O_3= 23)) in the cracking of naphtha into light olefins was also explored. The hybrid catalysts were prepared *via* the impregnation method

through a suspension mixture was dried and then calcined at 550℃. These catalysts were tested for the catalytic cracking of *n*-heptane into light olefins at 550℃ for 4 hours. For comparison, the parent zeolite (HZ23) was also tested under similar operating conditions. The powder X-ray patterns showed that the structure of MFI-type zeolite (HZ23) did not change after combining with the different supports measurements of the surface area confirmed the drop in BET areas by 20 wt.% HZ23 over metal oxide or kaolin, however, the kaolin has a lower surface area (about 20 $m^2.g^{-1}$) than the oxides, and it increased when mixed with 20 wt.% HZ23 to 94 $m^2.g^{-1}$. All fresh catalysts exhibited similar weight losses compered to pure zeolite (HZ23) in TGA in air except the 20 wt.% HZ23/MgO catalyst due to additional weight losses for the dehydroxylation and decarbonization reactions from magnesium hydroxycarbonate phase. The 20 wt.% HZ23/metal oxide formulations showed high capability to convert *n*-heptane into light olefins through the catalytic cracking reaction. Furthermore, all the catalysts, except the MgO-containing catalyst, showed higher olefins yield than the pure zeolite (HZ23). Secondary cracking reactions play essential role in the generation of coke when acid supports such as TiO_2, ZrO_2 and Al_2O_3 are used. The amount of coke in spent samples showed the following descending order: HZ23> HZ23/TiO_2 > HZ23/ZrO_2 > HZ23/Al_2O_3 > HZ23/ MgO > HZ23/kaolin > HZ23/SiO_2. It is interesting, the kaolin and SiO_2-containing catalysts had the lowest coke content, whereas the more acidic supports produced higher content of coke.

Under the conditions of catalytic cracking of *n*-heptane, the addition of clay or binder (such as kaolin or SiO_2) in combination with zeolite has the potential to boost the catalytic activity in terms of olefin selectivity as well as yields. In light of the findings presented in this thesis, the kaolin support was chosen for further study due to its good all round performance. It was hoped that this would generate a deeper understanding of the benefits offered by such a hybrid catalyst in the cracking reaction.

When clay is added to zeolite, it modifies dramatically the way the zeolites perform, which shows up in the increased formation of olefins. It is remarkable the effect that the zeolite-kaolin combination has on the design of advanced catalytic cracking for producing light olefins. For instance, the dilution of zeolite with kaolin minimizes the use of zeolite (max. 10 or 20 wt.%, depending on the feedstock) and maximizes the use of a cheaper natural material (kaolin), reducing the cost of the catalyst and enhancing its sustainability characteristics. According to the catalytic results in this thesis, the system containing a maximum loading of 10 wt.% of zeolite in kaolin showed the best performance for producing light olefins from *n*-heptane, as a model compound, and the naphtha using a fixed bed reactor.

The total olefins from the catalytic cracking of *n*-heptane and naphtha reach a maximum of 60 and 75 wt.% respectively on a 5 wt.% HZ23-binder catalyst formulation. Furthermore, the loading of 5 wt.% zeolite (HZ23) mixed with kaolin enhances the propylene to ethylene (P/E) ratio, resulting in 2 and 2.4 for naphtha and *n*-heptane respectively. This trend clearly reflects the marked effect of the nature of the feedstock on the olefin yields owing to the wide distribution of chemical reactivity and molecular dimensions. The benzene, toluene, and xylenes (BTX) yield did not change markedly (below 2.5 wt.%) when the HZ23 loading over kaolin was increased. On the other hand, the transformation of cycloalkanes contained in naphtha (more than 17 wt.%) and converted into aromatic compounds is likely the cause of the slight improvement in BTX yield when increasing the HZ23 loading. Also, the effect of weight space velocities (WHSV) on *n*-heptane catalytic cracking to light olefins was studied for all the hybrid kaolin and zeolite (HZ23) catalysts. It was found that the space velocity, which is inversely proportional to the feed contact time, affects markedly the product distribution, particularly in hybrid catalysts that contain high loading of HZ23.

Zeolite crystallinity was maintained through the modification with kaolin, particularly when the zeolite loading is increased. An overall analysis of the surface areas for the clay-

zeolite hybrid catalysts reveals an increase in the area compared to parent clay (kaolin) owing to the significant high surface area of the zeolite (HZ23).

At low percentages of HZ23 in kaolin, smaller zeolite particles are obtained with a very good dispersion on the kaolin matrix structures that catalyses selectively cracking reactions. This high dispersion effect is lost on increasing the zeolite content. There is evidence of a decrease in dispersion and an increase in particle size at 20 and 30% HZ23-kaolin. Interestingly, the transmission electron microscopy (TEM) and the scanning electron microscopy (SEM) analysis display the base shape and lamellar structure of kaolin crystals as well as the porosity and crystallite structure of H-ZSM5 zeolite.

The acidity measurements provide further insight into the capability of the HZ23-kaolin catalysts for the catalytic cracking of *n*-heptane and naphtha. The total acidity Brønsted (B), and Lewis (L) was lower for the kaolin compared with hybrid catalysts. All the hybrid catalysts showed a lower B/L ratio compared with zeolite alone except the hybrid with 5 wt.% HZ23/kaolin, where the B/L ratio was close to that for pure zeolite (HZ23).

A hybrid catalyst enhances the reactivity for the catalytic cracking of hydrocarbons, which produces high activity and selectivity towards light olefins. These catalysts change the acidity distribution in the zeolite, which can also hinder the hydrogen transfer reactions and thereby enhancing the light olefins production. Furthermore, the Kaolin -zeolite hybrid reduces coke formation, improving catalyst life. An optimal composition (max. 10 or 20 wt.% HZ23, depending on the feedstock) between the zeolite and kaolin is crucial to maximizing the catalytic performance of light olefins.

6.2 Future perspectives

It is generally accepted that the catalytic cracking of hydrocarbons is an extensive topic, in which a great number of advancements are needed to overcome the current enviromental limitations.

First of all, the future work will be focused on the combination of Cr_2O_3 with H-ZSM-5 at different SiO_2/Al_2O_3 ratios to try to enhance further the yield of olefins and the hydrocarbon conversion.

Further measurements of physical and chemical properties of the Cr oxide/HZ80 catalysts such as specific surface area, surface acidity and type of CrO_x species present by techniques such as Raman spectroscopy need to be undertaken to gain further insight into the effects of adding chromium oxide to the HZ80.

The interface between zeolite and different supports, alongside the small content of zeolite with a high Si/Al ratio, likely plays the most important role in generating new (or optimal) acid sites able to crack selectively *n*-heptane to light olefins. It is well-known that Lewis acid centers (L) and Brønsted acid centers (B) play a critical role in catalytic cracking reactions. Therefore, the acidity analysis using NH_3 temperature programmed desorption (TPD) to determine the strength and distribution of acid sites in the kaolin-ZSM-5 catalysts will give further insights into the catalytic generation of light olefins, as hybrid catalysts show promising performance for *n*-heptane catalytic cracking.

Reaction parameters such as contact time, catalyst-to-hydrocarbons ratio and cracking temperature above the catalytic cracking conventional range are some of the main factors that need to be optimised considering the chemical nature of the catalytic cracking feedstock. It is also worth exploring the effect of steam over the catalytic performance of hybrid formulations.

This thesis work used *n*-heptane and naphtha as feedstocks for catalytic cracking experiments on H-ZSM-5 zeolite-based catalysts. Another worthwhile investigation might be the utilization of different feedstocks over zeolite catalysts, particularly hybrid formulations. It might also be useful to use methanol as feedstock to investigate the activity, selectivity, and stability of hybrid catalysts to produce light olefins.

In terms of the catalyst testing, it will also be important to use an Advanced Cracking Evaluation (ACE) unit and pilot plant reaction system to assess the hybrid catalyst performance when larger volumes and various compositions of feedstocks are processed.

Investigating and contrasting the efficacy of several alternative ways of preparation, such as precipitation, sol-gel synthesis, and hydrothermal synthesis, with the impregnation approach, could be a fruitful area to explore. Moreover, it is worth studying the effect of different zeolites in hybrid catalysts using different contact times of feedstock and reaction temperature to gain further understating of the reaction kinetics and the roles of additives on different reaction pathways to produce olefins.

To the best of my knowledge, there are as yet no reports in the literature of applying hybrid zeolite catalyst formulations to the catalytic cracking of hydrocarbons into olefins using a fixed bed reactor. Therefore, it is possible to draw the conclusion that there are enormous opportunities in making use of materials such as oxides and clays as support for zeolites in the petrochemical field in general, and for the production of olefins in particular.

Appendix

Estimation of Errors

The assessment of the catalytic test error in all measured values is crucial to all investigations. If a single measurement is taken, any error estimate may be grossly inaccurate. This is the reason the scientific method becomes more robust as large is the number of measurements.

In addition to the inherent accuracy of the specific experimental method, there may be a significant human or inadvertent error that need also be considered.

Throughout the course of the investigation, numerous measurements of the same catalytic test were taken to assist decrease or disclosing inadvertent errors.

For instance, if x_0 units are measured n times and recorded as $x_1, x_2, x_3, \ldots., x_n$ units, one may write:

$$x_r = x_0 + e_r \qquad \text{(A-1)}$$

Where e_r is the error in the measurement x_r

The arithmetic mean $\bar{x}$ of n (the number of times a measurement is taken) is then

$$\bar{x} = \frac{x_1 + x_2 + x_3 + x_n}{n} = x_0 + \frac{e_1 + e_2 + e_3 + e_n}{n} \qquad \text{(A-2)}$$

Consequently, the value of $(\frac{e_1 + e_2 + e_3 + e_n}{n})$ may be very tiny if some of the errors $e_1, e_2, e_3, \ldots. e_n$ are positive and others are negative.

$(\frac{e_1 + e_2 + e_3 + e_n}{n})$ must always be numerically lower than the largest value of the separated errors.

Consequently, if e represents the greatest numerical error in any of the measurements, we get:

$$\left|\frac{e_1 + e_2 + e_3 + \cdots + e_n}{n}\right| \leq e \qquad \text{(A-3)}$$

And consequently $|\bar{x} - x_0| \leq e$

In general, $\bar{x}$ will be close to x_0, and the "best or real" value of the measured quantity that the measurements offer may be used.

Thus, in general, the longer the value of n, the closer $\bar{x}$ (the arithmetic mean) approaches x_0 (the "optimal" value of the quantity).

Repeated measurements of the same amount may compensate for unintentional errors to some extent, but systematic errors cannot be entirely out (since they are related to the inherent error in the instrument itself).

As a result, accuracy is defined as how near the measurements are to the "true" or "real" value of any physical quantity, while precision refers to the degree to which the catalytic test results are accurate. Precision is used to show the degree to which measurements agree with one another regardless of the presence of systematic error.

In this thesis, the catalytic tests are carried out between 2 and 4 times and all the experimental results with error between 3 and 6%. The percentage errors were calculated by following eq (A-4):

$$Percentage\ error = \frac{\bar{e}}{\bar{x}} \times 100\% \qquad \text{(A-4)}$$

References

1- Taylor, J., Introduction to error analysis, the study of uncertainties in physical measurements. *University Science Books*, **1997.**

2- Topping, J., Errors of observation and their treatment, 4th Edition, **1972**, *Chapman and Hall*, Great Britain

Supplementary Information for Chapter 3

ZEOLYST INTERNATIONAL

Product Analysis Sheet

Product Code	CBV 28014
Zeolite Type	ZSM-5
Lot #	2493-136
Chemical Analysis	
Na_2O, wt.%	<0.04
SiO_2/Al_2O_3, molar ratio	322
XRD Crystallinity, %	97
Average Particle Size (D_{50}), µm	2.0
LOI, wt.%	1.4
Surface Area, m^2/g	437

ZEOLYST INTERNATIONAL

Product Analysis Sheet

Product Code	CBV 8014
Zeolite Type	ZSM-5
Lot #	2493-78
Chemical Analysis	
$\%Na_2O$ (wt.%)	0.00
SiO_2/Al_2O_3 (molar ratio)	88.2
XRD	
% Crystallinity	89
Surface Area	
Multi Point (m^2/g)	480
Physical Properties	
Median Particle Size	1.9µ
LOI, % wt	6.9

ZEOLYST INTERNATIONAL

Product Analysis Sheet

Product Code	CBV 3024E
Zeolite Type	ZSM-5
Lot #	2493-117
Chemical Analysis	
Na_2O, wt. %	<0.01
SiO_2/Al_2O_3, molar ratio	33.1
XRD Crystallinity, %	88
Surface Area, m^2/g	443
Particle Size (D_{50}), µm	3.4
LOI, wt. %	9.7

ZEOLYST INTERNATIONAL

Product Analysis Sheet

Product Code	CBV 2314
Zeolite Type	ZSM-5
Lot #	2493-128
Chemical Analysis	
Na_2O, wt. %	0.05
SiO_2/Al_2O_3, molar ratio	22.0
XRD Crystallinity, %	92
Surface Area, m^2/g	439
Particle Size (D_{50}), µm	6.8
LOI, wt. %	7.3

ZEOLYST INTERNATIONAL

Product Analysis Sheet

Product Code	CBV 8524G
Zeolite Type	ZSM-5
Lot #	2493-6
XRF	
$\%Na_2O$ (wt.%)	0.01
SiO_2/Al_2O_3 (molar ratio)	87
XRD	
% Crystallinity	88
LOI	7.9
Surface Area	
Multi Point (m^2/g)	450

Figure 3.1A. Composition of zeolite according to supplier (Zeolyst).

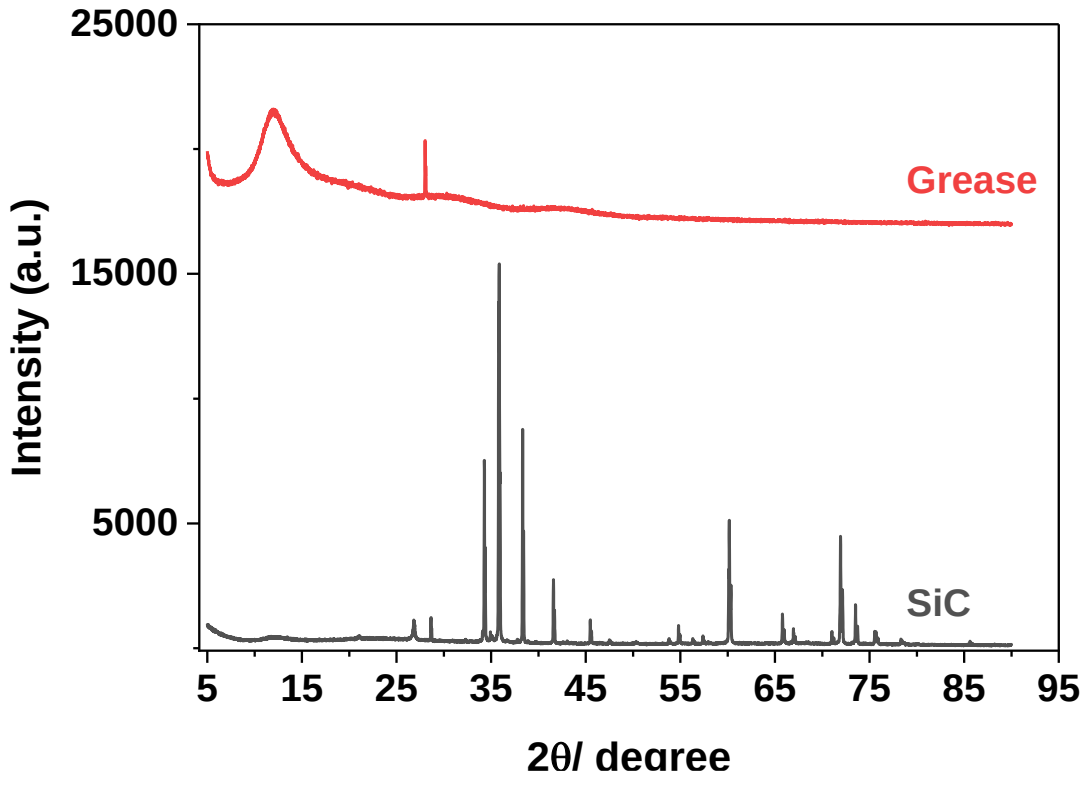


Figure 3.2A. The powder X-ray diffraction patterns of the SiC and grease.

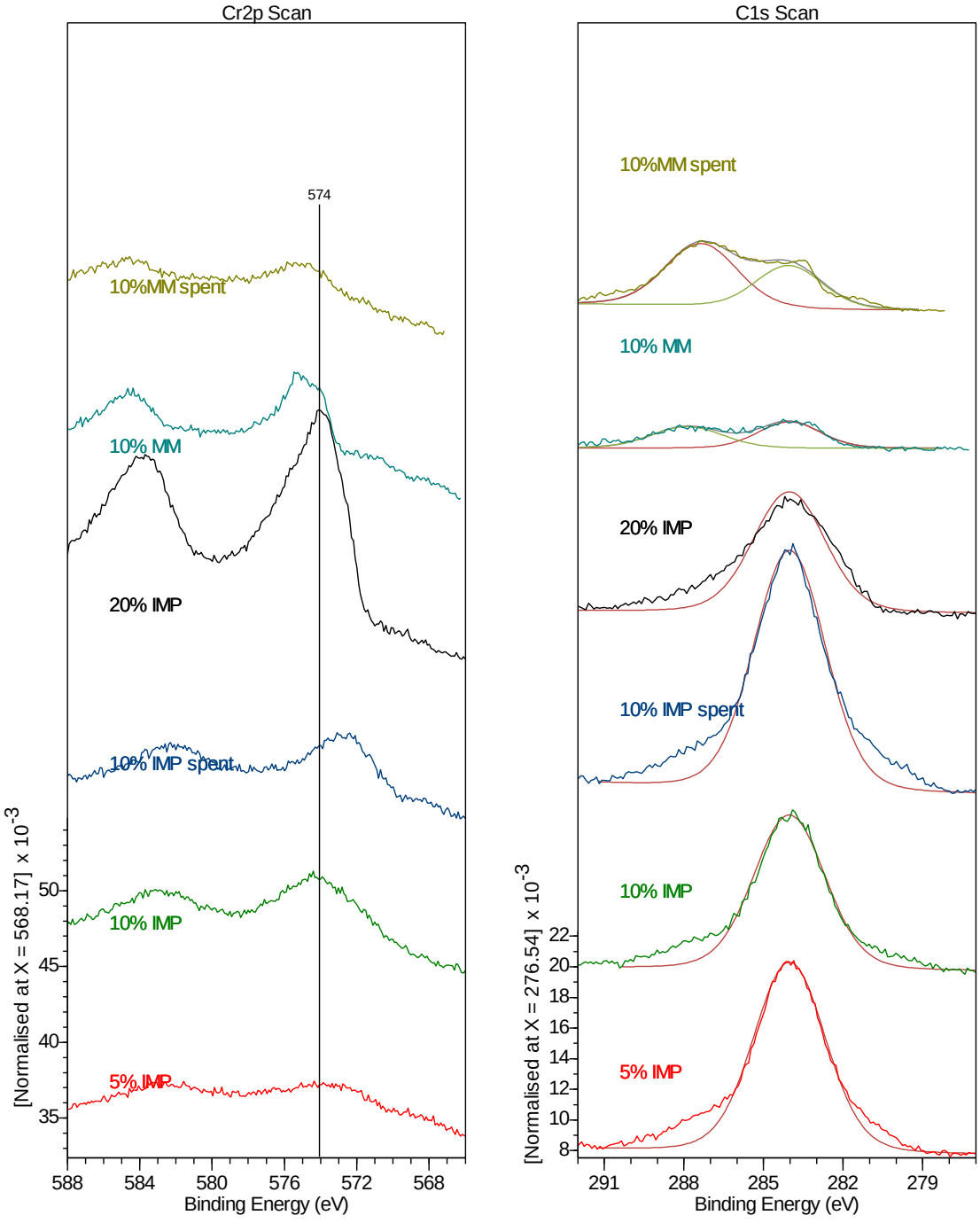


Figure 3.3A. XPS peak of Cr 2p and C 1s species of HZ80 zeolite modified with Cr_2O_3 synthesis by different methods.

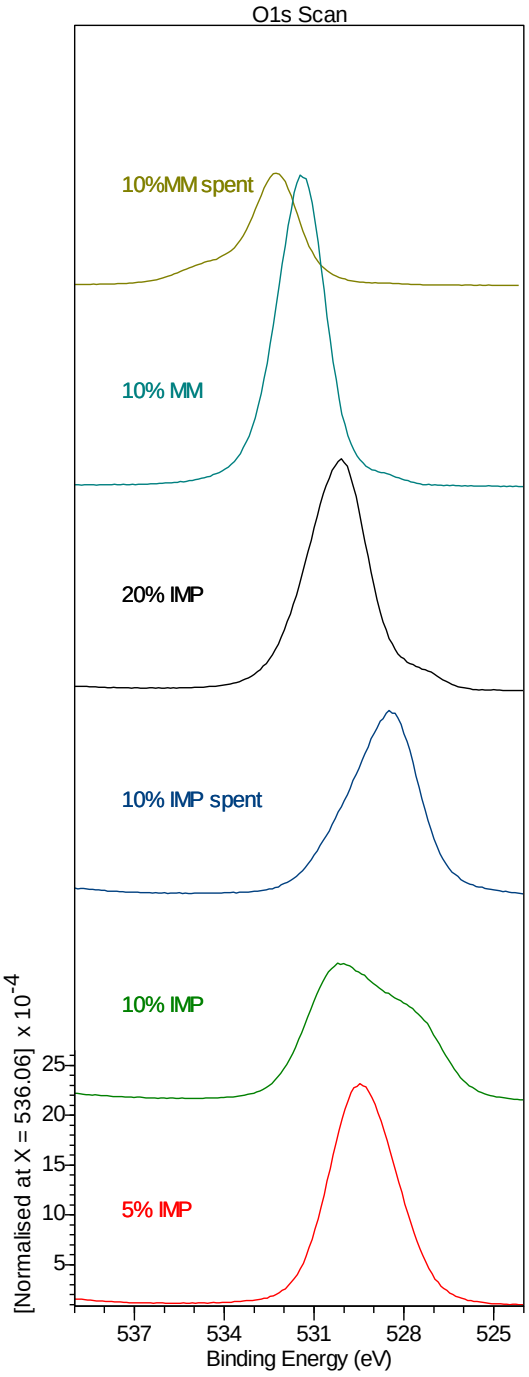


Figure 3.4A. XPS peak of O 1s species of HZ80 zeolite modified with Cr_2O_3 synthesis by different methods.

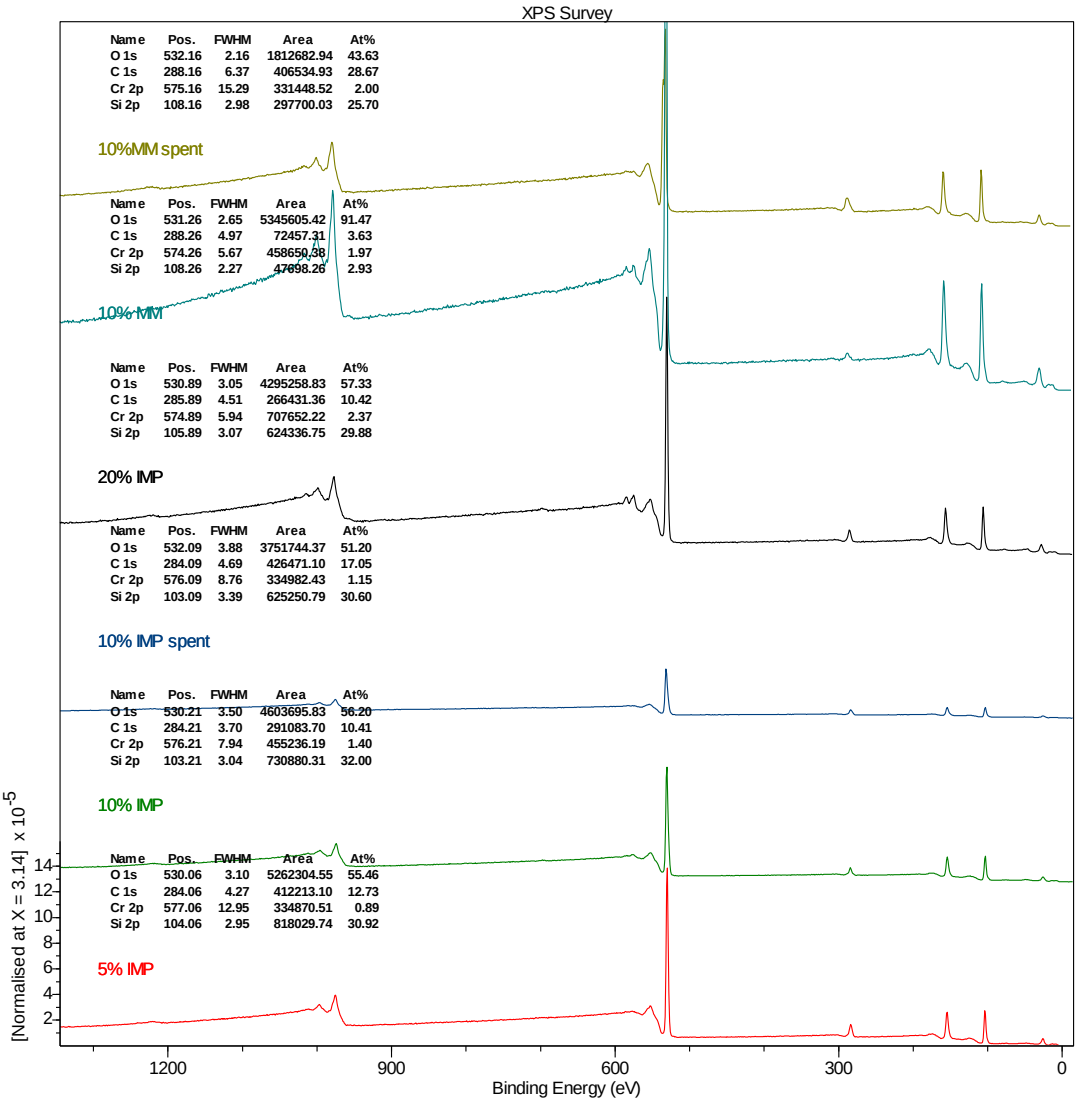


Figure 3.4A. Survey XPS spectra of the Cr_2O_3-HZ80 catalyst.

Supplementary Information for Chapter 4

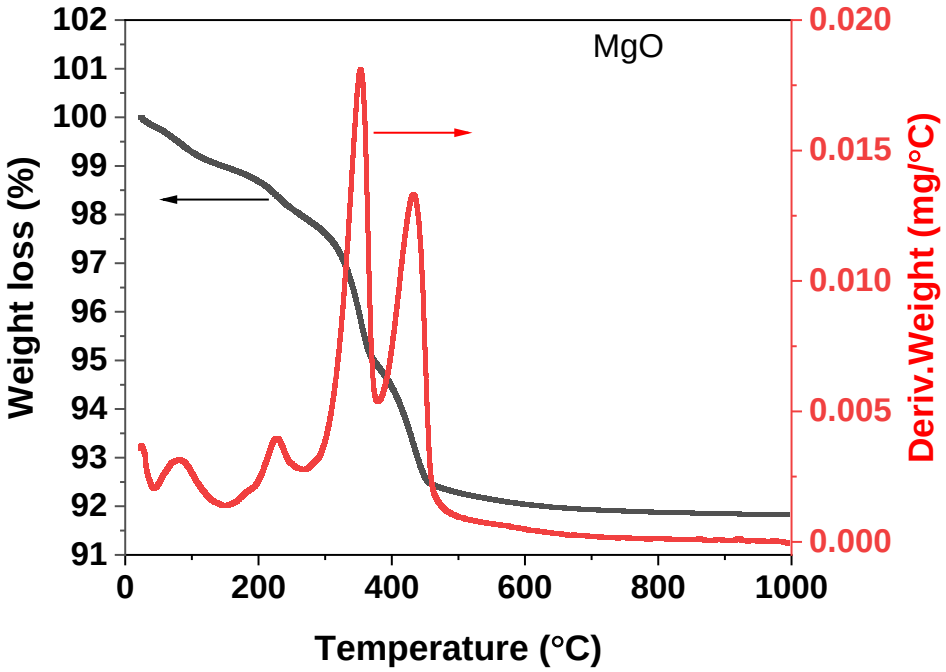


Figure 4.1A. TGA-DTG curve for fresh MgO.

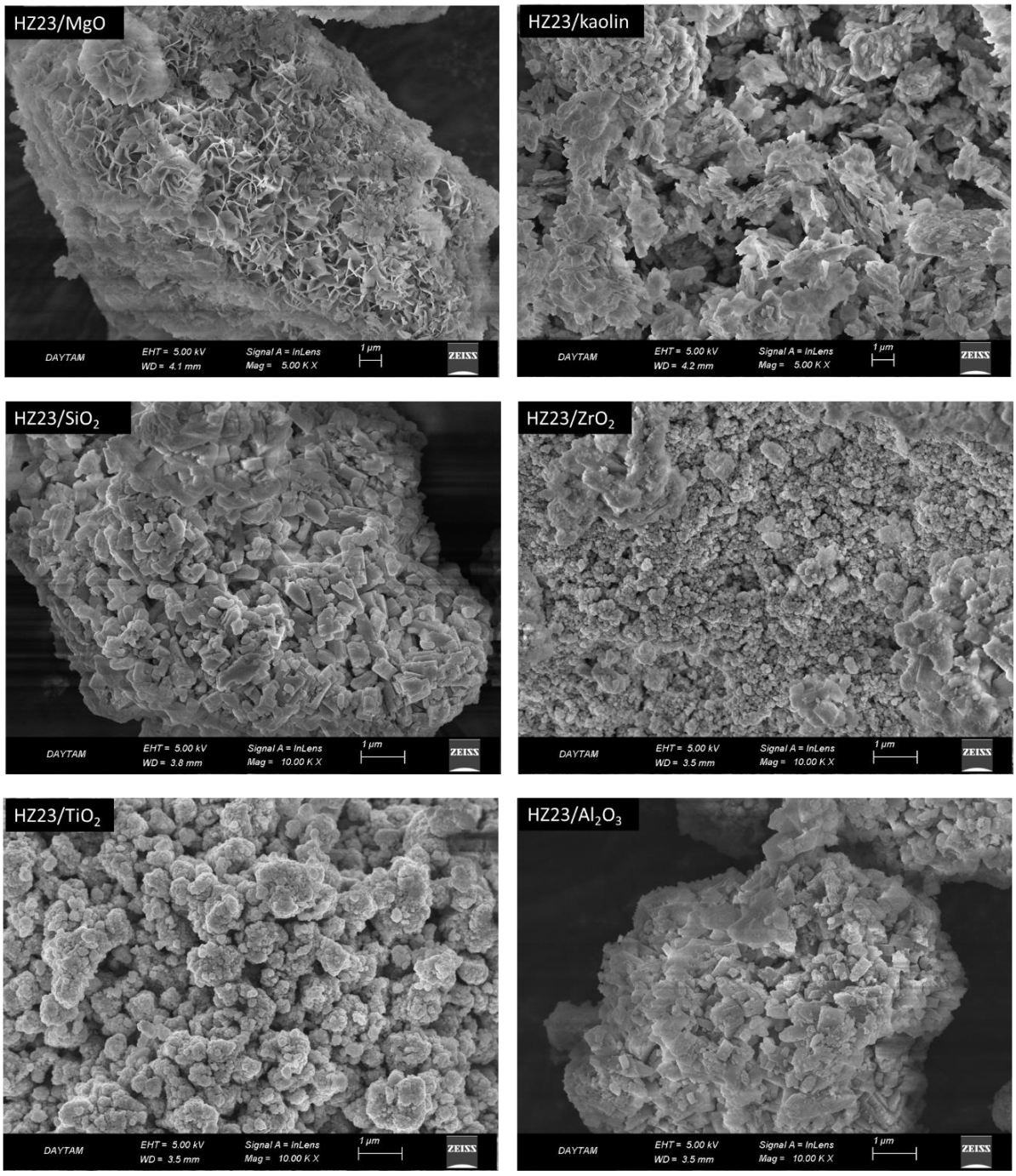


Figure 4.2A. Scanning electron microscopy (SEM) images of 20 wt.% H-ZSM-5(HZ23) over different supports catalysis.

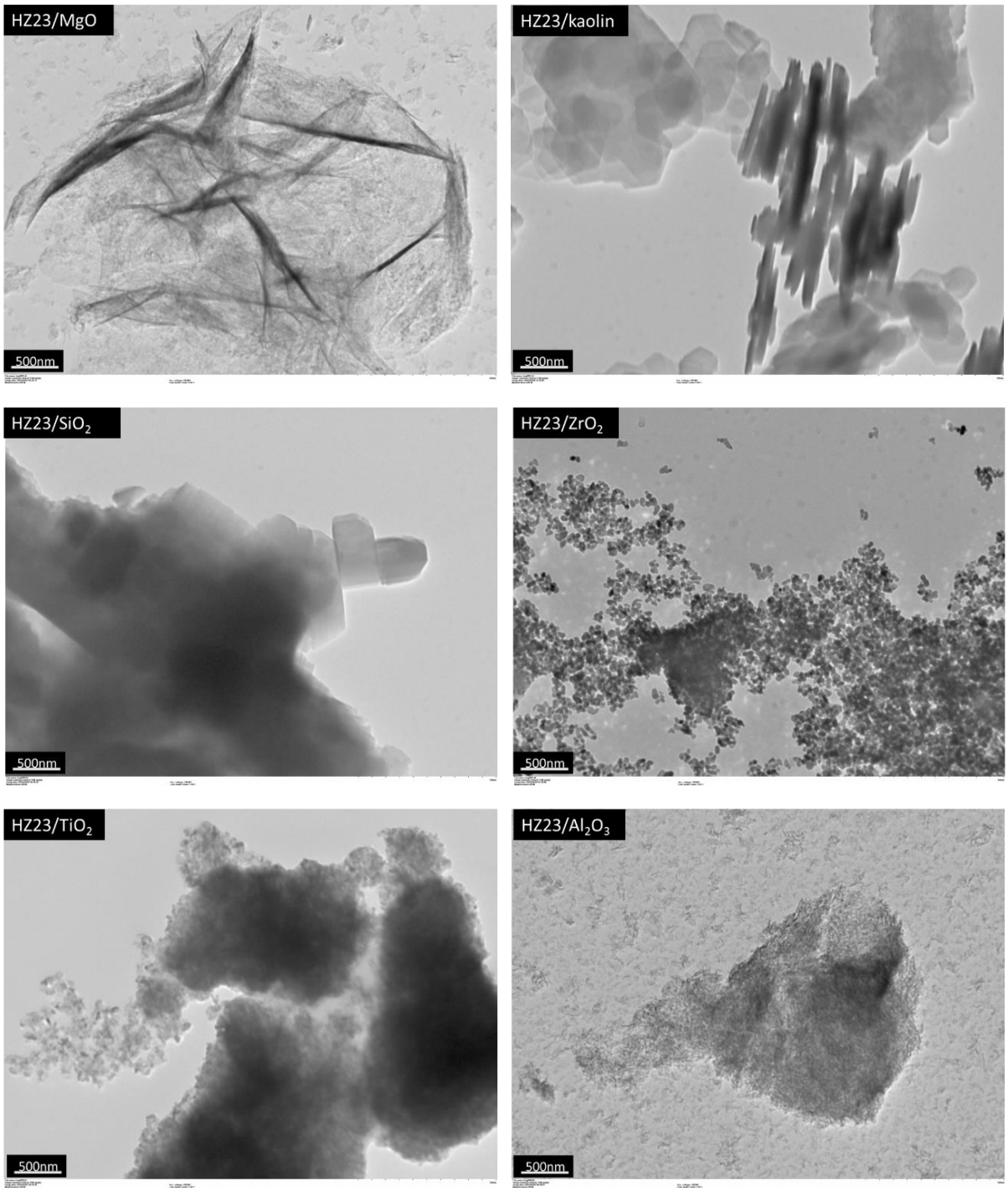


Figure 4.3A. Transmission Electron Microscopy (TEM) image of 20 wt.% HZ23 over different supports.

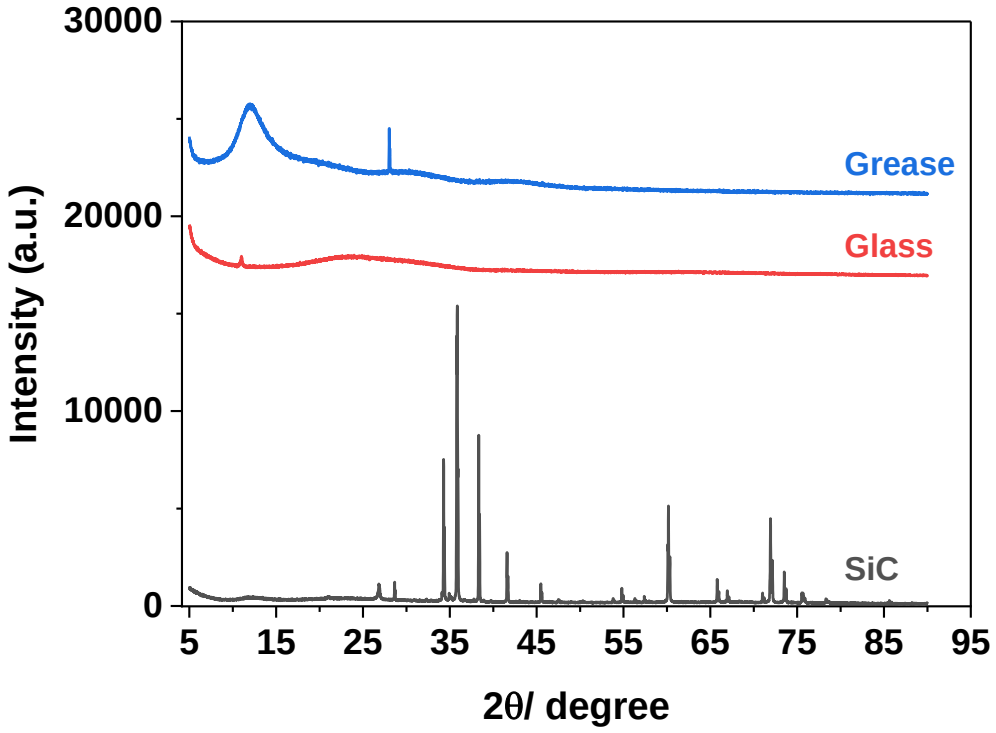


Figure 4.4A. The powder X-ray diffraction patterns of the SiC, Glass, and Grease.

Supplementary Information for Chapter 5

Table 5.1A. Summary of light naphtha composition.

Test	*Result*
Density at 15°C	0.688 g. ml^{-1}
Sulphur Content	0.017 wt.%
Mercaptan Sulphur	54 ppm
IBP	23°C
FBP	173°C

Table 5.2A. The quantification of hydrocarbon type (wt.%) in light naphtha.

Carbon Number	*Cyclo-alkane*	*i-Paraffin*	*n-paraffin*	*Cyc-Olefin*	*i-Olefin*	*n-Olefin*	*Aromatic*	*Total*
4	-	0.32	2.05	-	-	0.02	-	2.4
5	3.32	12.77	16.23	0.28	1.60	0.71	-	34.92
6	10.57	10.82	8.87	0.01	0.01	-	2.02	32.29
7	5.57	5.51	3.60	-	0.01	-	1.01	15.70
8	2.97	2.79	2.04	-	-	-	1.00	8.80
9	1.64	1.36	1.37	-	-	-	0.37	4.74
10	0.21	0.17	0.75	-	-	-	-	1.13
11	-	-	0.03	-	-	-	-	0.03
12+	-	-	-	-	-	-	-	-
Poly	-	-	-	-	-	-	-	-
Total	24.29	33.75	34.94	0.29	1.62	0.73	4.39	100.00

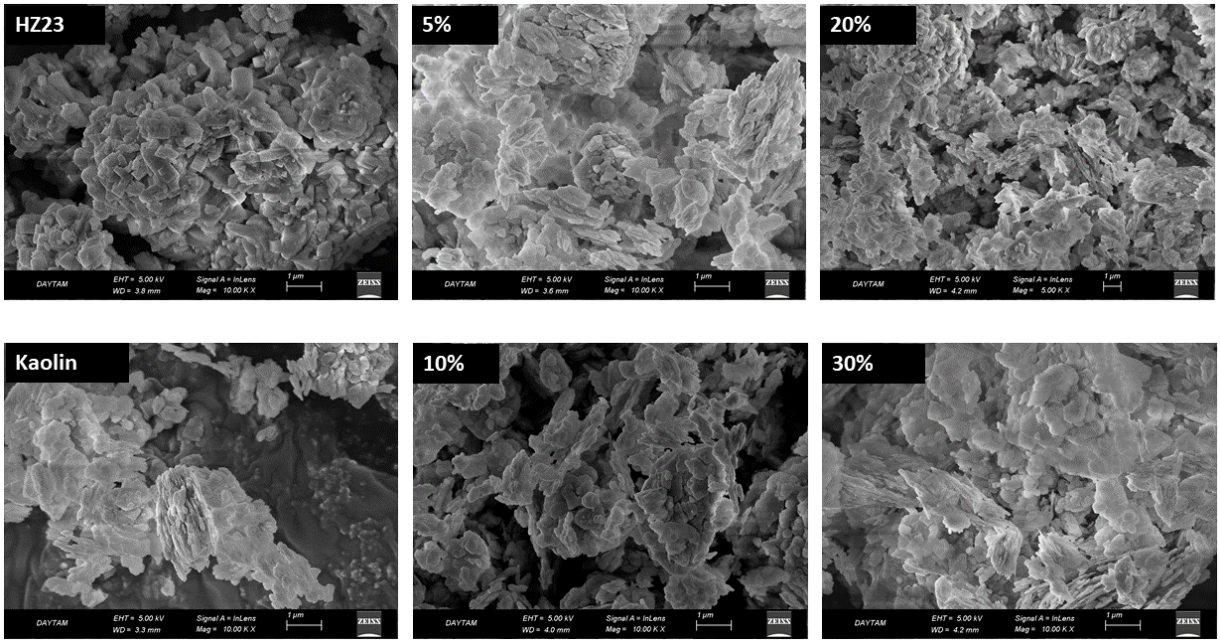


Figure 5.1A. Scanning electron microscopy images (SEM) of six samples under study before the catalytic reaction. ZSM-5 (HZ23), Kaolin, 5% HZ23/Kaolin, 10% HZ23/Kaolin, 20% HZ23/Kaolin, and 30% HZ23 HZ23/Kaolin.

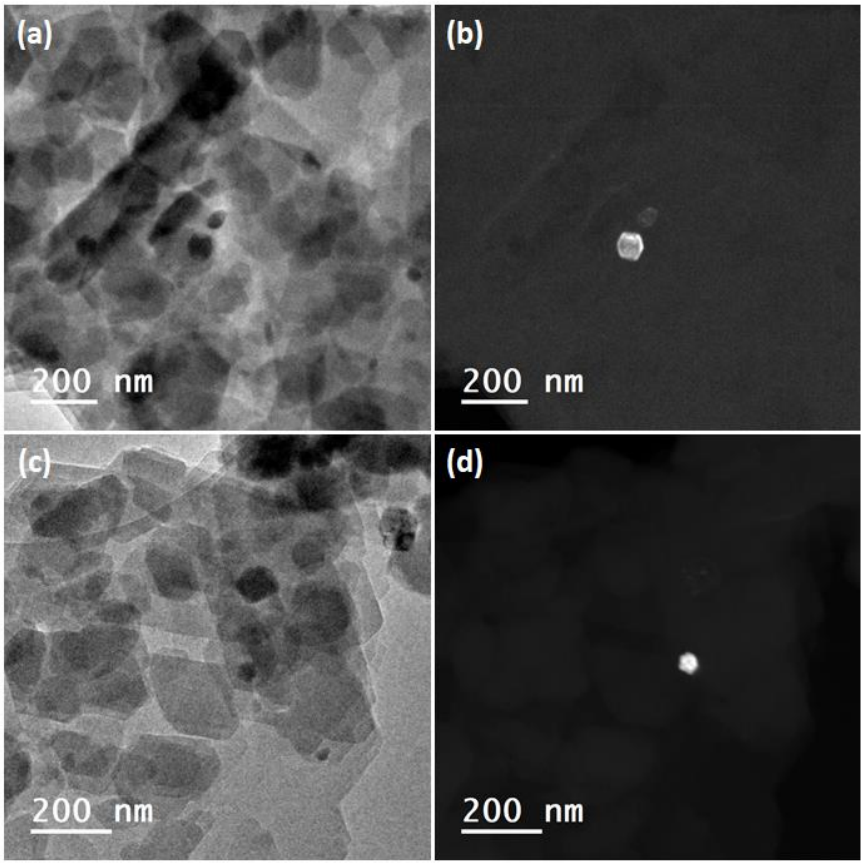


Figure 5.2A. TEM images obtained from HZ23-kaolin catalyst: (a) and (c) two-beam bright field images, (b) and (d) dark-field images formed using Zeolite 110 reflections from the areas shown in (a) and (c), respectively.

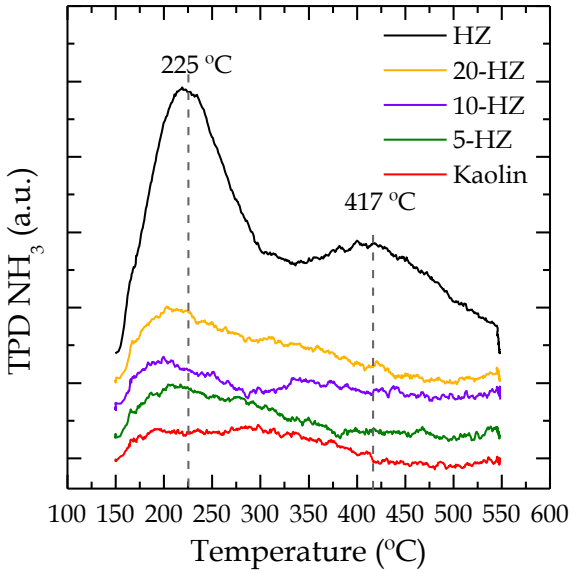
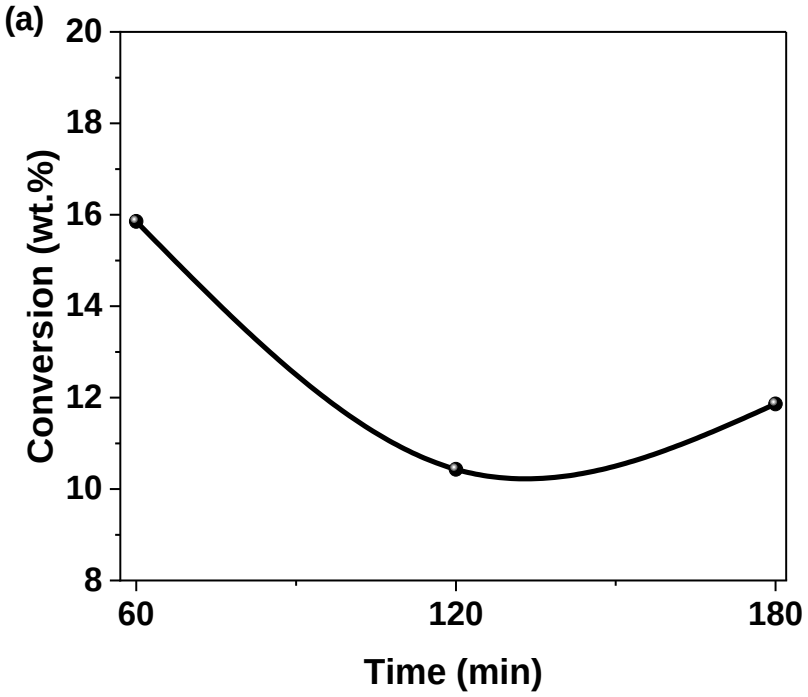
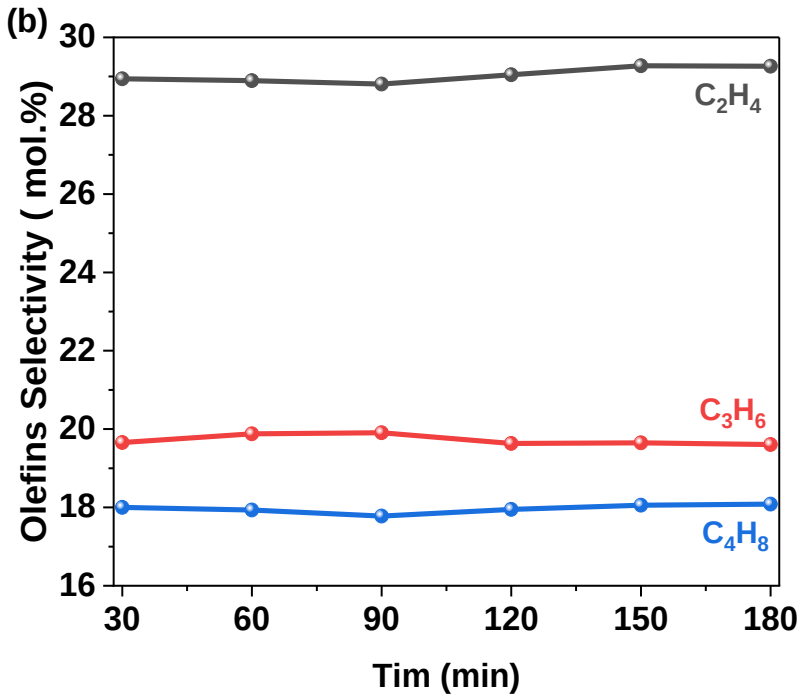


Figure 5.3A. NH_3-TPD profiles for HZ23-kaolin formulation with different compositions.


(a)
Conversion (wt.%)
20
18
16
14
12
10
8
60
120
180
Time (min)


(b)
Olefins Selectivity (mol.%)
30
28
26
24
22
20
18
16
30
60
90
120
150
180
Tim (min)
C2H4
C3H6
C4H8

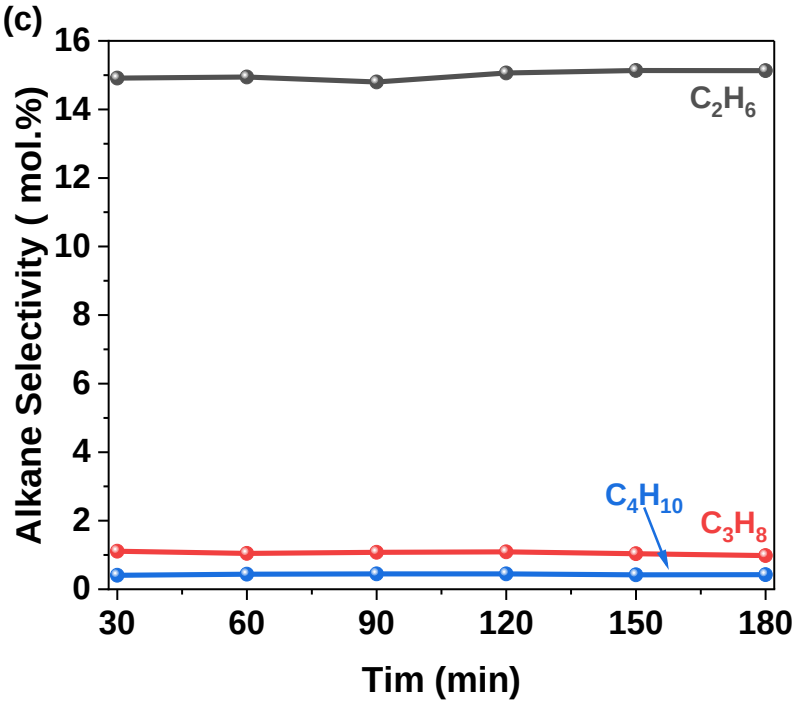


Figure 5.4A. Effect of the thermal cracking on *n*-heptane conversion (a), Olefin selectivity (b), Alkane selectivity (b). The reactions were conducted at 550°C, atmospheric pressure (0.1 MPa), wight hour space velocity (WHSV) 8.2 h^{-1}, and 20 ml min^{-1} N_2 flow rate.

Table 5.3A. Yield of hydrocarbons products on light naphtha cracking on different HZ23-kaolin catalyst formulations. The reactions were conducted at 550°C, atmospheric pressure (0.1 MPa), wight hour space velocity (WHSV) 8.2 h^{-1} and 20 ml.min^{-1} N_2 flow rate. The estimated error was between 3 and 6%.

Samples	*Time (min)*	*Products Yield (wt.%)*				
		C_2H_4	C_3H_6	C_4H_8	Alkane*	BTX
HZ23	60	14.1	16.2	14.4	53.1	2.2
	240	12.4	15.7	18.5	41.0	12.4
Thermal	60	0.5	0.8	73.5	12.0	13.2
	240	0.2	0.3	68.7	10.5	20.3
5% HZ23/kaolin	60	10.2	20.0	45.0	19.0	5.8
	240	8.4	18.1	49.2	15.8	8.5
10% HZ23/kaolin	60	12.5	20.5	37.4	25.8	3.8
	240	10.6	18.7	41.8	21.4	7.5
20% HZ23/kaolin	60	15.9	20.6	21.4	40.7	1.4
	240	14.3	20.6	26.7	33.1	5.3
30% HZ23/kaolin	60	14.9	18.0	17.6	47.9	1.6
	240	14.5	19.2	21.4	39.5	5.4

*Total alkane (CH_4+C_2H_6+C_3H_8+C_4H_{10})

Table 5.4A. Yield of hydrocarbons products on *n*-heptane cracking on different HZ23-kaolin catalyst formulations. The reactions were conducted at 550°C, atmospheric pressure (0.1 MPa), wight hour space velocity (WHSV) 8.2 h^{-1} and 20 $ml.min^{-1}$ N_2 flow rate. The estimated error was between 3 and 6%.

Samples	*Time (min)*	*Products Yield (wt.%)*				
		C_2H_4	C_3H_6	C_4H_8	Alkane*	BTX
HZ23	60	10.7	11.3	1.6	76.3	0.0
	240	13.0	16.3	1.7	65.4	3.6
5% HZ23/kaolin	60	13.0	30.2	16.6	38.9	1.3
	240	12.4	30.8	17.2	37.6	2.0
10% HZ23/kaolin	60	15.5	24.9	12.7	46.9	0.0
	240	14.1	25.9	12.7	45.6	1.7
20% HZ23/kaolin	60	14.8	18.8	8.7	57.7	0.0
	240	14.6	20.7	10.1	53.1	1.5
30% HZ23/kaolin	60	13.9	18.3	8.7	58.4	0.7
	240	10.0	17.3	11.6	57.6	3.5

*Total alkane (CH_4+C_2H_6+C_3H_8+C_4H_{10}), kaolin showed products yield close to 0%.

Table 5.5A. The Crystallite size of fresh HZ23 catalyst from XRD peaks at 23.3º in 2θ, and kaolin at 25.5º in 2θ at different compositions of HZ23-kaolin catalyst.

Sample	*Crystallite size of HZ23 [nm]*	*Crystallite size of Kaolin [nm]*
HZ23	32.2	--
5 wt.%	24.0	66.8
10 wt.%	24.0	66.8
20 wt.%	73.1	49.4
30 wt.%	66.5	49.4
Kaolin	--	39.2

Table 5.6A. The Crystallite size of spent HZ23 catalyst from XRD peaks at 23.3º in 2θ, and kaolin at 25.5º in 2θ at different compositions of HZ23-kaolin catalyst.

Sample	*Crystallite size of HZ23 [nm]*	*Crystallite size of Kaolin [nm]*
HZ23	43.4	--
5 wt.%	49.2	56.5
10 wt.%	24.0	66.8
20 wt.%	35.3	40.1
30 wt.%	65.4	49.4
kaolin	--	66.8

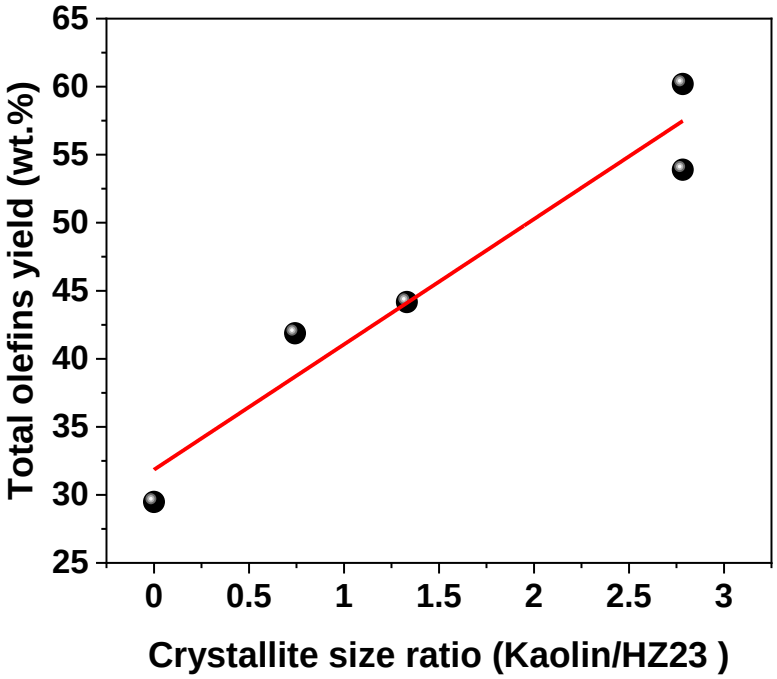


Figure 5.5A. The relation between crystallite size ratio (Kaolin/HZ23) and total olefins production for fresh catalyst in *n*-heptane catalyst cracking.

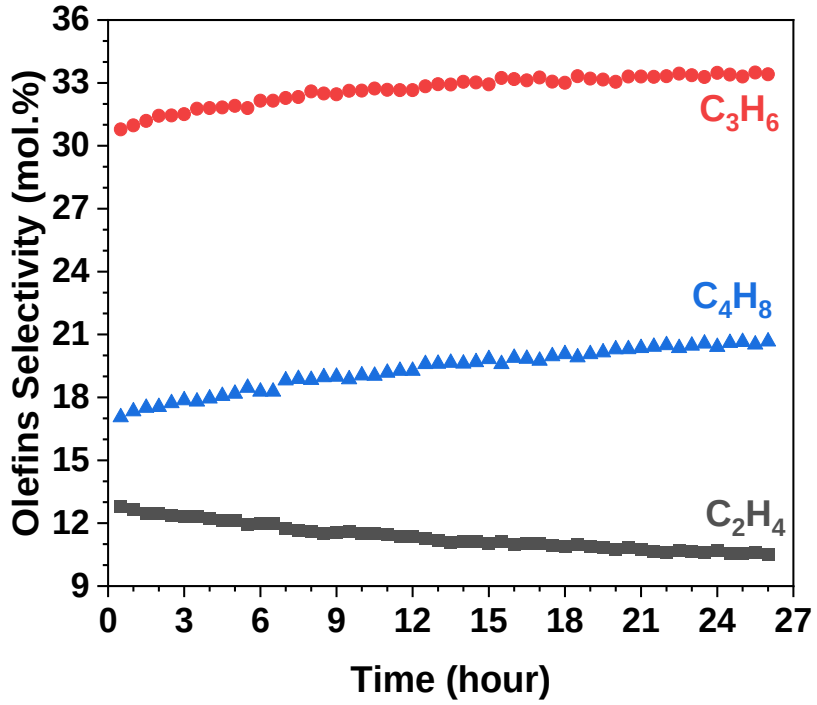


Figure 5.6A. The olefin selectivity (mol.%) over 5% HZ23 Zeolite-Kaolin catalysts in a 26-hour *n*-heptane catalytic test reaction. The reactions were conducted at 550 °C, atmospheric pressure (0.1 MPa), and 20 ml.min^{-1} N_2 flowrate.